

Geometry controlled phase behavior in nanowetting and jamming

Walter Mickel

▶ **To cite this version:**

Walter Mickel. Geometry controlled phase behavior in nanowetting and jamming. Other [cond-mat.other]. Université Claude Bernard - Lyon I; Institut für Paläontologie (Erlangen, Allemagne), 2011. English. NNT : 2011LYO10151 . tel-00868861

HAL Id: tel-00868861

https://theses.hal.science/tel-00868861

Submitted on 2 Oct 2013

HAL is a multi-disciplinary open access archive for the deposit and dissemination of scientific research documents, whether they are published or not. The documents may come from teaching and research institutions in France or abroad, or from public or private research centers.

L'archive ouverte pluridisciplinaire **HAL**, est destinée au dépôt et à la diffusion de documents scientifiques de niveau recherche, publiés ou non, émanant des établissements d'enseignement et de recherche français ou étrangers, des laboratoires publics ou privés.

N° d'ordre 151-2011 Année 2011

THESE DE L'UNIVERSITE DE LYON

délivrée par

L'UNIVERSITE CLAUDE BERNARD LYON 1

et préparée en cotutelle avec

FRIEDRICH-ALEXANDER UNIVERSITÄT ERLANGEN-NÜRNBERG

ECOLE DOCTORALE
ED52-PHAST

DIPLOME DE DOCTORAT

(arrêté du 7 août 2006 / arrêté du 6 janvier 2005)

soutenue publiquement le 30 septembre 2011

par

M MICKEL, Walter

TITRE :
GEOMETRY CONTROLLED PHASE BEHAVIOR IN NANOWETTING AND JAMMING

Directeurs de thèse : BIBEN, Thierry et MECKE, Klaus

JURY : M. Prof. Thierry BIBEN (Directeur de thèse)
M. Prof. Klaus MECKE (Directeur de thèse)
M. Prof. Lydéric BOCQUET (Examinateur)
M. Prof. Roland ROTH (Examinateur)
M. Prof. Hartmut LÖWEN (Rapporteur)

M. Prof. Ignacio PAGONABARRAGA (Rapporteur)

Zusammenfassung

Diese Dissertation befasst sich mit geometrischen und morphologischen Aspekten bei Benetzungsproblemen und bei Packungsproblemen harter Kugeln. In den ersten Kapiteln wird der Einfluss geometrischer Nanorauhigkeit auf den Benetzungswinkel untersucht. In den letzten Kapiteln werden geometrsische Effekte bei amorphen Systemen diskutiert.

Superhydrophobizität, d.h. sehr große Benetzungswinkel, sind von besonderem Interesse bei der Entwicklung von micro- und nanofluidischen Anwendungen, um Durchflussraten zu erhöhen und den Durchflusswiderstand zu reduzieren. Hierfür werden typischerweise zwei Einflussgrößen optimiert. Einerseits kann die Oberfläche geometrisch strukturiert werden, andererseits wird über die Auswahl der chemischen Paarung von Flüssigkeit und Substrat der Benetzungswinkel beeinflusst. Simulationen von Oberflächen mit Nanostrukturen gepaart mit makroskopischen Tropfen ist im Allgemeinen eine besondere Herausforderung, da die Längenskalen von Tropfen und Rauhigkeit sehr verschieden sind. Im ersten Teil wird daher eine sogenannte Phasen-Feld-Simulations-Methode spezifiziert und getestet, die speziell diesen Längenskalenunterschied mit einbezieht und Phasenübergänge in in der Nähe der rauhen Oberfläche berücksichtigt.

Mit dieser Methode werden statische, wie z.B. Benetzungswinkel, und dynamische Eigenschaften, wie z.B. Reibung, untersucht. Im Widerspruch zu der klassischen Cassie-Baxter-Wenzel Theorie, zeigen diese Simulationen, dass auch auf einfach strukturierten Oberflächen, d.h. Oberflächenstrukturen ohne Überhänge, Omniphobizität erreicht werden kann. D.h. weitgehend unabhängig von der chemischen Paarung bilden alle Tropfen entnetzende Kontaktwinkel aus. Es wird gezeigt, dass linienförmige Spannungsanteile an nadel- und klingenförmigen Oberflächenstrukturen zur Omniphobizität führen. Dynamische Simulationen erlauben das Verständnis von metastabilen Benetzungszuständen und Durchflussoptimierung. Insbesondere Lufteinschüsse, die durch Nanostrukturierung erzeugt werden, vermindern den Reibwiderstand enorm. In kürzlich durchgeführten Experimenten wurde Omniphobizität auf nanometrisch geätzten amorphen Siliziumoberflächen gefunden. Die durchgeführten Simulationen dienen dem Verständnis solcher Experimente.

Geometrische Effekte sind von großer Bedeutung beim Verständnis von glasartigen und jamming Systemen, z.B. bei amorphen Packungen von harten Kugeln im Limes hoher Drücke. Ein solches System wird arretiert beim sogenannten jamming. In dieser Arbeit wird gezeigt, dass die lokale Struktur in solchen Systemen universal ist,

d.h. unabhängig vom Verfahren zur Erzeugung der amorphen Packung. Hierfür werden robuste Ordnungsparameter benötigt - sogenannte Minkowski-Tensoren. Es wird gezeigt, dass diese Methoden die Probleme (Mangel an Robustheit) von Standardordnungsparametern beheben. Dies führt letztendlich zu einem verallgemeinerten Bild von lokalen Ordnungsparametern, die auf geometrisch basierten Prinzipien beruhen. Desweiteren wird mit dieser Methode gezeigt, dass Kristallisierung bei Packungsdichten jenseits von der sogenannten RCP-Packungsdichte (random close packing) eintritt.

Résumé

Cette thèse porte sur différents aspects géométriques et morphologiques concernant des problèmes de mouillage et d'empilement de sphères. Les premiers chapitres traitent du lien entre la rugosité nanométrique d'un substrat et l'angle de contact du liquide placé au dessus, les derniers chapitres abordent les effets géométriques dans les systèmes amorphes.

La superhydrophobicité (angles de contact très élevés) est une propriété très importante en micro ou nanofluidique car elle permet de réduire considérablement la friction d'un liquide sur une paroi, et d'augmenter ainsi le débit dans le système. Cette propriété est obtenue de manière classique en combinant traitements chimiques et structuration géométrique de la surface. La simulation numérique d'une goutte macroscopique placée sur une surface texturée à l'échelle nanométrique est une tache notoirement difficile a cause de l'énorme différence dans les échelles de longueur. La première partie est ainsi dédiée à l'élaboration et au test d'une nouvelle méthode de simulation : un modèle de champ de phase en lien avec la théorie de la fonctionnelle de la densité dynamique. Cette méthode permet d'étudier les transitions de phases au voisinage d'un substrat rugueux, et d'évaluer les angles de contact d'une goutte infiniment grande. Nous étudions les propriétés statiques (mouillage) mais aussi dynamiques (friction). Contrairement à la théorie macroscopique de Cassie-Baxter-Wenzel, nous montrons qu'une surface monovaluée, i.e. sans constrictions, peut produire un comportement omniphobe c'est à dire repousser tous les liquides. Nous avons étudié de manière systématique l'influence des paramètres géométriques de la surface sur l'omniphobicité et nous montrons que cet effet est contrôlé par les énergies de pointes. Des études dynamiques sont conduites pour évaluer les effets de métastabilité et pour mesurer le glissement introduit par ces structures en pointes, qui peuvent soutenir le liquide en laissant un coussin d'air entre le liquide et la surface, même si la surface est mouillante. Des expériences récentes on montré l'existence de ce type de surfaces fabriquées à partir de silicium amorphe gravé.

La géométrie a également un effet considérable dans les milieux vitreux ou bloqués, comme les empilements de sphères dures dans la limite de pression infinie. Ces empilements de sphères conduisent à des état bloqués ("jamming") et nous montrons que la structure locale de ces systèmes est universelle, c'est à dire indépendante de la méthode de préparation. Pour cela, nous introduisons des paramètres d'ordre - les tenseurs de Minkowski - qui suppriment les problèmes de robustesse qu'ont les paramètres d'ordre utilisés classiquement. Ces nouveaux paramètres d'ordre conduisent à une vision unifiée, basée sur des principes géométriques. Enfin, nous montrons grâce

aux tenseurs de Minkowski que les empilements de sphères se mettent à cristalliser au delà du point d'empilement aléatoire le plus dense ("random close packing").

Contents

1. Introduction **11**

1.1. Wetting, omniphobicity and simulation methods 12

1.2. Jamming, local geometry, order and disorder characterization 14

2. Phase-field models, DFT and dynamical DFT **17**

2.1. Density functional theory 17

2.2. Phase-field models 21

2.3. Dynamical density functional theory 25

2.4. PF/DDFT model for nanofluidics 28

2.4.1. Thermodynamic properties 29

2.4.2. Dynamics of the density profile 31

2.4.3. Hydrodynamic transport equation 33

2.4.4. The numerical implementation 37

2.4.5. Comparison with lattice Boltzmann 48

2.4.6. Comparison with molecular dynamics 49

2.4.7. Discussion (limits, interfaces, wall-interaction) 49

3. Nanowetting and omniphobicity **51**

3.1. Classical wetting theory 52

3.1.1. Wenzel theory 52

3.1.2. Cassie-Baxter theory 53

3.1.3. Multivalued surfaces and omniphobicity 54

3.1.4. Metastability of the Cassie-Baxter state and superhydrophobicity 55

3.2. Experimental findings 60

3.2.1. Superhydrophobicity 60

3.2.2. Multivalued omniphobicity 61

3.2.3. Monovalued omniphobicity 61

3.3. Simulations in the literature 63

3.4. PF simulations 66

3.4.1. Randomness 75

3.5. Metastabilities 78

3.6. Conclusion . . . 80

4. Slip on nanorough substrates **81**
4.1. Experiments and simulations . . . 83
4.1.1. Simulations . . . 84
4.1.2. PF simulations . . . 86
4.2. Apparent slip vs. intrinsic slip . . . 90
4.3. Capillary rise: Lucas-Washburn-law . . . 92
4.3.1. PF model test . . . 92
4.4. Contact angle hysteresis . . . 94
4.4.1. PF simulations . . . 97
4.4.2. Conclusion . . . 102

5. Minkowski functionals and Minkowski tensors **103**
5.1. Minkowski functionals . . . 104
5.1.1. Integral geometry of Minkowski tensors . . . 105
5.1.2. Computation of Minkowski functionals . . . 108
5.2. Minkowski tensors . . . 108
5.2.1. Algorithm . . . 111
5.2.2. Invariants and shape descriptors . . . 114
5.3. Spinodal decomposition . . . 117
5.3.1. Introduction to spinodal decomposition . . . 118
5.3.2. Morphology . . . 118
5.3.3. Discussion . . . 130

6. Local structure analysis and anisotropy in particulate matter **133**
6.1. $\beta_\nu^{r,s}$ as local order parameter . . . 135
6.2. Alternative commonly used local order parameters . . . 141
6.3. Jamming in athermal dissipative HS systems . . . 152
6.3.1. Anisotropy of jammed bead packs . . . 154
6.3.2. Random ellipsoid packings . . . 160
6.3.3. Conclusion . . . 160
6.4. Crystallization onset at RCP . . . 162
6.4.1. Crystallization identification with Minkowski tensors . . . 165
6.4.2. Conclusion . . . 175

7. Spherical normal Minkowski tensors and bond order parameters **177**
7.1. Irreducible tensors . . . 178
7.2. Cartesian irreducible tensors . . . 179

7.3. Spherical Minkowski tensors 181
7.4. Spherical Minkowski tensors and normal orientation order parameters (NOO) 185
7.5. NOO of triply periodic minimal surfaces 187
7.6. Discussion 190

8. Summary **193**
8.1. Nanowetting, nanoslip 193
8.2. Jamming, RCP, defects 196

A. Details on the Parameters of the PF Model **199**

B. Experiments and simulations of particulate matter **203**
B.1. Monte-Carlo simulations 203
B.2. Molecular dynamics simulations 203
B.3. Supercooled liquids-MD simulations 204
B.4. Lubachevsky-Stillinger 204
B.5. Monte-Carlo simulations of nearly jammed 205
B.6. DEM-simulations 205
B.7. Dry acrylic experiments 206
B.8. Fluidized bed experiments 206

C. Minkowski tensors **209**
C.1. MT algorithm 209
C.2. Clebsch-Gordan transformation matrices for $W_1^{0,r}$ 212
C.3. Normal vectors 214

1. Introduction

This thesis deals with geometrical aspects in several domains of soft matter physics. In the last decades, many experimental techniques and industrial processes appeared to control surface structures on smaller and smaller scales, with a broad range of interesting technological applications. From this, microfluidics emerged to a leading interdisciplinary domain, bridging from physics over chemistry to engineering. The smaller the structures become the more dominant are the surface properties, yielding to new challenges when going beyond microsized devices to nanometric scales. New subtleties breeze in, trying to apply macro- and mesoscopic rules on microscales. To work out mainly geometrical effects from the complex interplay between fluids and nanopatterned substrate we shall employ statistical mechanics tools in the first part of this work. Systematical investigations of the geometry impact onto important fluid dynamics quantities are performed, like contact angles, slip properties which allow for flow enhancement and contact angle hysteresis. We shall show, how well-known strategies to gain superhydrophobicity, i.e. strong water repellency, can be advanced to yield omniphobicity or even superomniphobicity; this means liquid repellency, no matter its chemistry. In the second part we go the other way round and shall see how geometrical subtleties appears coming from microscale to macroscale. As new experimental techniques become available, more detailed information on the nature of the fluid state can be accessed. While in former years the local fluid structure was only known from computer simulations, new scattering experiments reveal the local ordering of fluids and confocal microscopy allows for individual particle tracking in colloidal systems. Computed tomography provides structural data of even millimeter sized particles, which got stuck in so-called jammed states. We shall exploit and refine novel geometrical methods in order to get robust measures which allow for detailed structure description of fluids, glasses and amorphous materials on all length scales. Purely geometrical effects cause for example crystallization in particulate ensembles beyond a certain packing fraction.

1.1. Wetting, omniphobicity and simulation methods

In nano- and microfluidic devices it is favorable to lower the friction for liquid transport as much as possible. In particular the liquid–solid interface friction at the boundaries of the capillaries strongly contributes to the dissipation, due to the large surface contact area per volume. It was recognized long time ago that high contact angles mostly support efficient transport [77]. In nature the lotus effect, i.e. superhydrophobic behavior, was found in 1977 and studied by biologists [25, 26, 226]. Nowadays, hundreds of examples in flora and fauna are known [226, 98], where extremely high contact angles and low contact angle hysteresis appear, e.g. to yield self-cleaning surfaces [245]. For two decades now, nature is mimicked in microfluidic devices [38]. Superhydrophobicity arise from a combination of microstructured surface topographies with water repellent materials. Spreading water on a rough surface with pillars or ridges may result in a penetrated homogeneous wetting state, where liquid enters the grooves or a heterogeneous fakir state with air-pockets suspending the liquid above. The former is referred to as Wenzel state [311], the latter as Cassie-Baxter state [58] (see fig. 1.1). On micronic scales this behavior is very well described with the Wenzel and Cassie-Baxter laws. According to this theory hydrophobic materials are needed to obtain superhydrophobic states due to the roughness induced amplification of hydrophobicity. Indeed, the air-supported wetting configuration is realized on superhydrophobic substrates, like the lotus leaf.

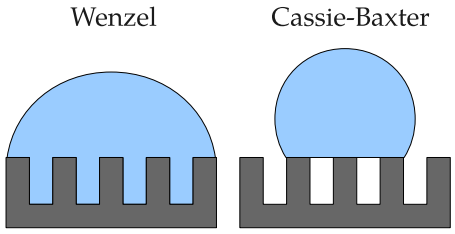


FIGURE 1.1. *Wenzel- and Cassie-Baxter wetting*

In recent years, many experiments showed that even omniphobic behavior can be achieved on appropriate surface structures [327, 154, 300, 301, 65, 66, 19, 142]. Marmur [198] and Herminghaus [125, 126] gave explanations of these experiments within the assumptions of the classical wetting theory of Wenzel and Cassie-Baxter. Overhangs of the corrugations are needed, which hamper liquid intrusion into the indentions of the roughness. More recently Ramos et al. [250] reported an experiment, which apparently

does not fit in this explanation scheme, since the roughness seems not to provide sufficient overhangs. On a randomly rough etched hydrophobic substrate, even oil drops displayed large contact angles. In chapter 3 we shall review this experiment under the assumption of an overhang-free topography with simulations. To tackle this problem, one have to account for the roughness of the etched structure, whose length scale goes down to nanometers, while the drops are millimetric. To study generic wetting properties widely used simulation methods may not be suitable. For example standard lattice Boltzmann (LB) methods do not account for nanoscopic roughness [63]. Molecular dynamics (MD) are to heavy if large drops are used.

We use therefore a so-called phase-field model approach, which is not as common as MD and LB, but allows us to study infinite drops on surfaces with corrugation length scales of only a few atomic diameters. This generic model is refined and tested in chapter 2. With this model we can explain several wetting phenomena which might appear in Ramos' experiment, notably the wetting inversion, which is necessary for omniphobicity. From our simulations we conclude, that the wetting inversion is also found in the Wenzel state, contradicting the classical Wenzel law. This effect is rooted in a subtle geometric effect which we shall call needle tip effect.

Our model allows also to study dynamic behaviors, connected to the flow enhancement and friction reduction. In hydrodynamic descriptions, which are applicable to surprisingly small scales [41], one has to assume a certain boundary condition between the fluid and the wall. We shall demonstrate in chapter 4, that the thermodynamically stable Wenzel state does not significantly contribute to large slip lengths. Slip is considered to enhance flow rates. On the other hand our metastability analysis of these phenomena in chapter 3 show, that the favorable Cassie-Baxter state is supported. Chapter 4 is completed by a study of contact angle hysteresis on corrugated substrates. Due to the roughness, a drop can take a whole range of contact angles. Line pinning leads to energy barriers between adjacent ridges. At sufficiently high driving forces, the former sticking drop starts to move in a heterogeneous motion: slip—stick—jump.

A detailed introduction to each of these phenomena can be found in the mentioned chapters.

1.2. Jamming, local geometry, order and disorder characterization

A very common model of a simple fluid is the hard sphere model. Individual classical particles are supposed to be non interacting at a distance larger than the sum of their radii r_1 and r_2. Distances smaller than $r_1 + r_2$ are not allowed, due to the hard repulsion at contact. This model has the merit, that the only relevant state variable is the packing fraction ϕ, which is the volume occupied by spheres per volume of the confining container. This purely geometrical based model already shows a first order phase transition in 3D [106] [1], due to entropy. This microscopic model system can be extended to macroscopic dissipative hard spheres, i.e. collisions lead to a loss of momentum and spheres in contact are subject to solid–solid friction. We shall discuss the geometrical effects onto the local arrangements in large ensembles of frictional and frictionless spheres in chapter 6. To do so, we use a rather novel class of morphometric descriptors—the so-called Minkowski tensors [209, 28], which are introduced in chapter 5.3. This class is validated against widely used methods, which—we shall show—lack robustness. In particular in amorphous media the former methods might lead to artefacts in the structure description.

In 1983 Steinhardt et al. [289] has proposed the widely used q_l orientation order parameter family as 3D generalization of the ψ_6 hexatic order parameter in 2D [289]. q_l and its derivates have become a fruitful instrument in identifying different crystalline phases, notably fcc, hcp and bcc [294, 227, 319, 177, 302, 155, 308] or icosahedral nuclei [309, 158, 133]. They have been used to study melting transitions [309, 59, 54] and fluids [59, 127] too. In the literature of glasses and supercooled fluids q_6 has arisen to the most prominent order parameter [159] searching for glass-transitions [135, 220, 293] and crystalline clusters [181, 227, 266, 158, 304, 155]. Similar to the bond-orientation order parameter, most local parameter depend crucially on a definition of nearest neighbor sites. Such local structure descriptors include the Edwards tensor [88] in granular systems and texture tensors in cellular materials [86]. In crystallography the number of nearest neighbors (also called coordination number) is used directly or combined with other parameters to localize crystal defects [156, 2, 94].

We shall show in chapter 6 how these measures suffer from the nearest neighbor definition when applied to amorphous media. The Minkowski tensors are an alternative approach, which we shall show is closely related to the Edwards tensor (chap. 6) and the bond orientation order parameters (chap. 7) but omits the robustness deficien-

[1] the case in 2D is less clear

cies. Such robust order parameters are needed to characterize geometrical subtleties in jammed hard sphere packings, i.e. an ensemble of spheres, where each sphere is fixed by its neighboring spheres, so that no further motion is possible.

While fluids of spherical particles are usually globally isotropic, the local environments of the particles may be anisotropic. Our Minkowski analysis of jammed packs reveals an universal local anisotropy. It is well-known that ellipsoidal particles pack randomly denser than spherical ones [82]. We suppose that higher packing fractions in ellipsoid packings can be understood by more efficient exploitation of the elongated void space by elongated particles. The universal anisotropy is astonishing since each jamming process is out of equilibrium and therefore a priori history dependent. These findings are reported in chapter 6.

Bernal and Mason [33] pointed out—half a century ago—that packings of hard spheres exhibit a critical packing fraction density around 0.64, widely referred to in the literature as *random close packing* (RCP). They have made the conjecture that this packing fraction must be mathematically determinable like e.g. the Kepler's conjecture packing fraction proofed by Hales in 1998 [120]. Up to date a mathematical theory is lacking. Since Bernal and Mason many studies have found a packing fraction limit, when compactifying spheres densely, with a large variety of protocols [17, 278, 228, 244]. Up to now not even one experimental finding show densification beyond RCP, except when nucleation seeds for crystallization were implanted [228]. Most simulation algorithms are also hampered to overcome RCP when trying to densify hard sphere systems, except of two. The Jodrey-Tory algorithm [144, 145] and the Lubachevsky- Stillinger algorithm [281]. Results from the latter one inspired Torquato and others in a widely cited paper [297] to the conjecture that RCP is not well defined, rather maximally random jammed (MRJ) configurations have to be taken into account, which should be located at similar packing fraction around 0.64. This conjecture is still heavily debated [247, 150, 149].

Recently several studies—experimental [228] and numerical [181, 8, 319] and theoretical [247, 11]—have conjectured that RCP is an onset of crystallization, but stringent verification is missing. The resolution of these question relies on suitably defined order parameters to quantify structural properties of the sphere configurations—like the Minkowski tensors. We investigate and confirm this crystallization onset at a packing fraction around 0.649 in chapter 6.

In chapter 7 we analyze the Minkowski tensor method in the framework of irreducible tensors, and we demonstrate, that this novel method is a generalization of a special case of the Steinhardt order parameter family, which strips off robustness deficiencies and obeys all the strong theorems, which render the Minkowski tensors so powerful.

This work is structured as follows: Chapters 2 provide the theoretical background for chapters 3 4 and 5.3, where applications of the phase field model onto geometrical wetting phenomena is discussed. Chapter 5 gives a theoretical introduction to Minkowski functionals and tensors, and shows examples of applications in continuum fluid simulations. Applications of the Minkowski method are discussed in chapters 5.3 and 6. In chapter 7 the calculus of spherical irreducible Minkowski tensors is demonstrated. Chapter 8 is left for the conclusions and summary and outlook.

2. Phase-field models, density functional theory and dynamical density functional theory

In this chapter we explain the theoretical background of our phase field model. Indeed, this model borrows concepts from density functional theory (DFT), classical phase field models (PF) and dynamical density functional theory (DDFT). For this, sections 2.1 to 2.3 describe some important aspects of these theories in order to establish a basis for the wetting phase field model, which is explained in 2.4. Static properties are tested there too, in order to study wetting phase diagrams in the following chapter. Dynamic properties of our model are tested in chapter 4, right before we look at the dynamical behavior of nanocorrugated surfaces.

2.1. Density functional theory

In this section we will give a brief introduction to the density functional theory (DFT) since it shares a lot of similarities with phase field models. DFT was invented in the 1960s to study non-uniform liquids/fluids [92, 122]. Non-uniform means in this context, that the translational symmetry is broken—by an interface for example. It turned out that the theory is very successful also to describe uniform liquids, which means the bulk behavior [122].

This section aims to point out some key features of DFT and follows in great parts introductions from Evans [92] and the textbook of Hansen and MacDonald [122]. Let us consider a fluid with the N-particle phase-space distribution $f^{(N)}(\mathbf{r}^{(N)}, \mathbf{p}^{(N)}, t)$. The reduced phase-space distribution of $n < N$ particles is obtained by integrating out the degrees of freedom (DOF) of $N - n$ particles

$$f^{(n)}(\mathbf{r}^{(n)}, \mathbf{p}^{(n)}, t) = \frac{N!}{(N-n)!} \int \mathrm{d}\mathbf{r}^{(N-n)} \mathrm{d}\mathbf{p}^{(N-n)} f^{(N)}(\mathbf{r}^{(N)}, \mathbf{p}^{(N)}, t) \tag{2.1}$$

The one particle (space) distribution is recovered by integrating the phase space distribution over all momenta DOF and all but one spatial coordinates

$$\rho(\mathbf{r},t) = \rho(\mathbf{r}_1,t) = \int \mathrm{d}\mathbf{p}_1 f^{(1)}(\mathbf{r}_1,\mathbf{p}_1,t). \tag{2.2}$$

The $N-$ particle Hamilton function H is assumed to have the form:

$$H(\mathbf{r}^{(N)},\mathbf{p}^{(N)}) = \hat{T}(\mathbf{p}^{(N)}) + \hat{V}_{\mathrm{ext}}(\mathbf{r}^{(N)}) + \Phi(\mathbf{r}^{(N)}), \tag{2.3}$$

so that H can be decomposed in a kinetic part $\hat{T} = \sum_{i=1}^{N} \mathbf{p}_i^2/m$, where m is the particle mass, a particle-particle interaction part $\Phi = \frac{1}{2}\sum_{i=1}^{N}\sum_{j=1}^{N} \varphi(\mathbf{r}_i,\mathbf{r}_j)$ and an external potential $\hat{V}_{\mathrm{ext}} = \sum_{i=1}^{N} V_{\mathrm{ext}}(\mathbf{r}_i)$. The grand canonical potential of the system Ω_0 in equilibrium can be derived from the partition function Ξ'

$$\Xi' := \sum_{N=0}^{\infty} \frac{1}{N!} \int \mathrm{d}\mathbf{r}^{(N)} \mathrm{d}\mathbf{p}^{(N)} \exp(-\beta(H-\mu N)) = \mathrm{Tr}' \exp(-\beta(H-\mu N)), \tag{2.4}$$

$$\Omega_0 = -\beta \ln \Xi', \tag{2.5}$$

where $\beta = 1/k_{\mathrm{B}}T$, T is the temperature and k_{B} is the Boltzmann constant. The index 0 denotes equilibrium quantities, the prime indicates the full phase space quantities. Since one wants to obtain functionals of the particle density, it is convenient to switch to quantities which depend only on $\mathbf{r}^{(N)}$ rather than $(\mathbf{r}^{(N)},\mathbf{p}^{(N)})$. From the full partition function Ξ' one can integrate out the momentain order to gain a reduced partition function, which contains all real-space informations

$$\Xi := \sum_{N=0}^{\infty} \frac{1}{N!} \int \mathrm{d}\mathbf{r}^{(N)} \exp(-\beta(\Phi + \hat{V}_{\mathrm{ext}} - \mu N)) = \mathrm{Tr} \exp(-\beta(\Phi + \hat{V}_{\mathrm{ext}} - \mu N)). \tag{2.6}$$

In the full description, the equilibrium phase space distribution is given by

$$f_0' = f_0'(\mathbf{r}^{(N)},\mathbf{p}^{(N)}) = \Xi' \exp(-\beta(H-\mu N)), \tag{2.7}$$

and in the spatial coordinates it reads

$$\rho_0 = \rho_0(\mathbf{r}^{(N)}) = \Xi \exp(-\beta(\Phi + \hat{V}_{\mathrm{ext}} - \mu N)), \tag{2.8}$$

with the N particle distribution operator

$$\rho_N = \rho_N(\mathbf{r}^{(N)}) = \sum_{i=1}^{N} \delta(\mathbf{r}_i - \mathbf{r}). \tag{2.9}$$

The equilibrium distribution can be recasted as follows:

$$\rho_0 = \Xi \exp(-\beta(\Phi + \int (V_{\mathrm{ext}}\rho_N - \mu\rho_N)\,\mathrm{d}^3 r)). \tag{2.10}$$

Comparing this formula with an uniform system, one recognizes its similarity when defining the intrinsic chemical potential as the term in the brackets

$$\mu_{\text{in}}(\mathbf{r}) = \mu - V_{\text{ext}}(\mathbf{r}). \tag{2.11}$$

The internal energy U in bulk thermodynamics is a function of $U(S, V, N)$, where S is the entropy, V the confining volume and N the particle number. The volume can be interpreted as a confining external potential, which is 0 inside the system and infinite everywhere else. Thus, the external potential $V_{\text{ext}}(\mathbf{r})$ generalizes the volume V in non-uniform systems.

Starting with a functional of the phase space distribution f' in the presence of an external potential V_{ext}

$$\Omega'[f] = \text{Tr}' f' \left(H - \mu N + \beta^{-1} \ln f' \right) \tag{2.12}$$

it can be shown that

$$\Omega'[f_0'] = -\beta^{-1} \ln \Xi = \Omega_0, \tag{2.13}$$

where Ω_0 is the grand canonical potential. Note, that H contains the external potential. And further it can be shown that (see ref. [92] or [213] for proves)

$$\Omega'[f'] > \Omega'[f_0'] = \Omega_0; \qquad \forall f' \neq f_0'. \tag{2.14}$$

This important theorem is constructive to find the grand canonical potential Ω_0 by minimizing Ω'. As shown for example in ref. [92] Ω' is minimized by minimizing the spatial part only: Ω.

The equilibrium particle density ρ_0 is the ensemble average $\rho_0 = \langle \rho_N \rangle = \text{Tr}\rho_N$. Clearly this density ρ_0 is a function of the external potential V_{ext}, since f_0' is a function of the external potential. Furthermore one can show (see ref. [92] for a prove) that f_0' is a functional of ρ_0. The idea is to prove that for a given interaction potential Φ and known ρ_0, $\hat{V}_{\text{ext}}$ is uniquely determined, if existent. And $\hat{V}_{\text{ext}}$ determines f_0'. This powerful theorem (which is equivalent to the Hohenberg-Kohn theorem in quantum density functional theory) states an one-to-one correspondence between the one-particle density and the external potential.

The free energy F_0 can be written in a form

$$F = \mathcal{F}[\rho_0] + \int \rho_0 V_{\text{ext}} \, \mathrm{d}^3 r, \tag{2.15}$$

where $\mathcal{F}$ is the bulk free energy contribution. Inductive reasoning gives the free energy functional

$$F[\rho] = \mathcal{F}[\rho] + \int \rho V_{\text{ext}} \, \mathrm{d}^3 r. \tag{2.16}$$

A deductive way can be found e.g. in ref. [92]. Eventually, we can write the grand canonical potential functional as

$$\Omega[\rho, \mu] = F[\rho] - \int \rho \mu \mathrm{d}^3 r. \tag{2.17}$$

From (2.16) classical thermodynamics ($N = \int \rho \mathrm{d}^3 r$) yield the important result

$$V_{\text{ext}} - \frac{\delta \mathcal{F}[\rho]}{\delta \rho(\mathbf{r})} = \mu, \tag{2.18}$$

and we define

$$\mu_{\text{in}}[\rho, \mathbf{r}] = \frac{\delta \mathcal{F}[\rho]}{\delta \rho(\mathbf{r})}. \tag{2.19}$$

Although this derivation is exact by now, in practice the functionals $\mathcal{F}[\rho]$ are not known and approximations have to be used. Commonly used in liquid state theory [31, 122] are functionals, which have the form

$$\mathcal{F}[\rho] = \mathcal{F}_{\text{id}}[\rho] + \mathcal{F}_{\text{hs}}[\rho] + \mathcal{F}_{\text{att}}[\rho] = \mathcal{F}_{\text{id}}[\rho] + \mathcal{F}_{\text{ex}}[\rho], \tag{2.20}$$

where $\mathcal{F}_{\text{id}}[\rho]$ describes a non-interacting ideal gas term, $\mathcal{F}_{\text{hs}}[\rho]$ a repulsive part term approximated by a hard sphere system (an accurate functional is known [257]) and an attractive part $\mathcal{F}_{\text{att}}[\rho]$, which has to be adjusted to the system under consideration. Another common decomposition is to write $\mathcal{F}_{\text{ex}}$ as the excess part of the intrinsic free energy functional, which corrects the (local) ideal gas term. A merit of DFT is that it describes features of liquids in the vicinity of a wall in a proper way (depending on the choice of the intrinsic functionals and the external potential), i.e. a layering effect is observed, that means in the vicinity of a substrate the density oscillates till it reaches a bulk average apart from the wall [122]. This behavior is described by correlations of the density, which can be derived from DFT too. We start from the partition function in (2.6) and write the terms Φ and V_{ext} in the Hamiltonian seperatately. This allows for extraction of μ_{in} in Ξ. Using (2.14) one obtains

$$\begin{aligned} \frac{\delta \Omega}{\delta \mu_{\text{in}}(\mathbf{r})} &= -\Xi \sum_{N=0}^{\infty} \frac{1}{N!} \int \mathrm{d}\mathbf{r}^{(N)} \exp(-\beta(\Phi - \int \rho_N \mu_{\text{in}} \, \mathrm{d}^3 r)) \\ &= -\mathrm{Tr} \exp(-\beta(\Phi - \int \rho_N \mu_{\text{in}} \, \mathrm{d}^3 r)) \\ &= -\langle \rho_N \rangle = -\rho_0. \end{aligned} \tag{2.21}$$

Differentiating again yields after some manipulations the density–density correlation function

$$\mathrm{Y}^{(2)}(\mathbf{r}_1,\mathbf{r}_2) = -\beta^{-1}\frac{\delta^2\Omega[\rho]}{\delta\mu_{\mathrm{in}}(\mathbf{r}_1)\delta\mu_{\mathrm{in}}(\mathbf{r}_2)} = \beta^{-1}\frac{\delta\rho_0(\mathbf{r}_1)}{\delta\mu_{\mathrm{in}}(\mathbf{r}_2)} = -\rho_0(\mathbf{r}_1)\rho_0(\mathbf{r}_2) + \langle\rho_N(\mathbf{r}_1)\rho_N(\mathbf{r}_2)\rangle. \tag{2.22}$$

$\mathrm{Y}^{(2)}(\mathbf{r}_1,\mathbf{r}_2)$ can be expressed with the total correlation function $h^{(2)}(\mathbf{r}_1,\mathbf{r}_2)$

$$\mathrm{Y}^{(2)}(\mathbf{r}_1,\mathbf{r}_2) = \rho_0(\mathbf{r}_1)\rho_0(\mathbf{r}_2)h^{(2)}(\mathbf{r}_1,\mathbf{r}_2) + \rho_0(\mathbf{r}_1)\delta(\mathbf{r}_1-\mathbf{r}_2), \tag{2.23}$$

where δ is the Dirac δ-function. The total correlation function $h^{(2)}(\mathbf{r}_1,\mathbf{r}_2)$ is connected to the the two particle distribution function $g(\mathbf{r}_1,\mathbf{r}_2)$ by

$$h^{(2)}(\mathbf{r}_1,\mathbf{r}_2) = g(\mathbf{r}_1,\mathbf{r}_2) - 1. \tag{2.24}$$

Finally, the Ornstein-Zernike equation relates the total correlation function $h^{(2)}(\mathbf{r}_1,\mathbf{r}_2)$ to the direct correlation function $c^{(2)}(\mathbf{r}_1,\mathbf{r}_2)$.

$$h^{(2)}(\mathbf{r}_1,\mathbf{r}_2) = c^{(2)}(\mathbf{r}_1,\mathbf{r}_2) + \rho_0\int \mathrm{d}^3r_3\ \ c^{(2)}(\mathbf{r}_1,\mathbf{r}_3)h^{(2)}(\mathbf{r}_2,\mathbf{r}_3). \tag{2.25}$$

The direct correlation function can expressed as a functional derivative of the excess free energy, similar to the density–density correlation in eq. (2.21) [122]

$$c^{(2)}(\mathbf{r}_1,\mathbf{r}_2) = -\beta\frac{\delta^2\mathcal{F}_{\mathrm{ex}}[\rho]}{\delta\rho(\mathbf{r}_1)\delta\rho(\mathbf{r}_2)}. \tag{2.26}$$

DFT proved to be an useful tool to study e.g. the phase diagram of liquid crystals [183], colloidal systems [46] capillary condensation or evaporation [225], liquid–solid interfaces [191] and wetting [31].

2.2. Phase-field models

It is a notoriously demanding task to tackle problems which involve undergoing phase transitions. On microscopic level molecular dynamics (MD) can be used to simulate systems with interfaces between two thermodynamic phases. But on larger scales, where the computer power is not sufficient to explore the system with molecular simulations, one has to use continuum models. This leads to moving interface problems—so-called Stefan-type problems—due to phase transitions. This is mathematically difficult and an evolution equation for the boundary has to be derived. The complete description of the problem needs a coupled description of the thermodynamics of

the phase transition with the large scale transport equations. In the 1980s by Fix, Langner [113, and references therein], Collins and Levine [69] a new class of models were proposed to omit this difficult moving boundary problem; the so-called phase-field models (PF). The advantage of this models is that the location of the interface is not modeled separately but obtained from the solution. This advantage is most welcome when topological changes of the interface occur or the moving boundary is a 2D manifold in 3 dimensions [113]. Furthermore, numerical treatment of the partial differential equations (PDE) in PF models are simpler than in sharp interface descriptions [113, 37].

PF models are a class of very versatile models and used to study dentritic growth [36], solidification from undercooled melt [69], phase-transitions in binary alloys [6, 42], pure substances [6] and growth of liquid crystals [184]. There is also a wide literature on PF models to study fluid-fluid interfaces like viscous fingering [104, 105], Maragoni convections [45], drop and vesicle dynamics [37].

In the reminder of this section, the principle ingredients of a PF model are introduced. For this reason a simple melting scenario serves as an example.

A phase field model consists of two ingredients, first a thermodynamic model of the phase transition and interfaces and second a model for the dynamics of the system from out off equilibrium to equilibrium or to a steady state [69]. The thermodynamic model is in the simplest case based on a scalar order parameter $\phi = \phi(\mathbf{r}, t)$ which indicates one of either phases; e.g. $\phi = -1$ defines a solid phase and $\phi = 1$ a liquid phase. Both phases are separated by an interface with a finite thickness κ, where ϕ varies smoothly between $-1 < \phi < 1$. Of course, such a description is an approximation of the real microscopic nature of the system and is called a coarse-grained free energy functional [242]. A thermodynamic potential, e.g. the free energy F, is modeled as a functional of $\phi(\mathbf{r}, t)$. A widely used choice for the bulk free energy f_{bulk} is the ϕ^4 model

$$f_{\text{bulk}} = b(\phi^2 - 1)^2 + c(T)\phi, \tag{2.27}$$

where c is called a diffusion field. c is proportional to the temperature difference w.r.t. the melting temperature $c \propto (T - T_{\text{m}})$. It is thus a model parameter to favor one of both phases (see fig. 2.1). And b is a positive model parameter. The interface is commonly modeled with a square gradient term [22, 303]

$$f_{\text{interface}} = a \left|\nabla\phi\right|^2. \tag{2.28}$$

The interfacial thickness κ is related to the positive parameter a and the former parameter b, as we shall see below. This model is referred to as Ginzburg-Landau free

energy model [116, 242, 129].

We shall show the connection of the free energy ansatz

$$F[\phi] = \int \left[f_{\text{bulk}} + f_{\text{interface}} \right] \mathrm{d}^3 r \,, \tag{2.29}$$

with the surface tension γ of a planar interface and the corresponding density profile in thermal equilibrium, i.e. $c(T) = 0$.

A minimal free energy profile of the density ϕ_0 obeys the equation

$$\phi_0 = \tanh\left(\sqrt{\frac{b}{a}} (x - x_0) \right) \tag{2.30}$$

for the boundary conditions $\phi(z \to \infty) = 1$ and $\phi(z \to -\infty) = -1$. This solution of the order parameter profile is presented in fig. 2.1 in panel *b)* and the bulk free energy f_{bulk} in panel *a)*. The surface tension is then defined as the excess free energy due to the interface of ϕ_0:

$$\gamma = \int_{-\infty}^{\infty} a \left(\frac{\mathrm{d}\phi_0(z)}{\mathrm{d}z} \right)^2 + b \left(\phi_0^2(z) - 1 \right)^2 \mathrm{d}z. \tag{2.31}$$

Using eq. (2.30) we get

$$\gamma = \int_{-1}^{1} \sqrt{4ab(\phi^2 - 1)^2} \mathrm{d}\phi = \frac{8}{3} \sqrt{ab}. \tag{2.32}$$

The thickness of interfacial region is in the order of $\kappa = \sqrt{a/b}$.

Several dynamical models are used for phase field equations. We shall first discuss the commonly used "Model A"-type evolution equation [129], which is often referred to as Ginzburg-Landau evolution equation or Allen-Cahn dynamics. It reads like

$$\Gamma^{-1} \frac{\partial \phi}{\partial t} = -\frac{\delta F}{\delta \phi}, \tag{2.33}$$

where F is the free energy from eq. (2.63).

An elemantary variation $\delta\phi$ produces a variation δF given by

$$\delta F[\phi] = \int \left[f'(\phi) \delta\phi + 2\kappa \nabla\phi \delta\nabla\phi \right] \mathrm{d}^3 r \tag{2.34}$$

$$= \int \left[f'(\phi) \delta\phi + 2\kappa \nabla^2 \phi \right] \delta\phi \mathrm{d}^3 r \tag{2.35}$$

and leads to

$$\frac{\delta F}{\delta \phi} = f'(\phi) - 2\kappa \triangle \phi \tag{2.36}$$

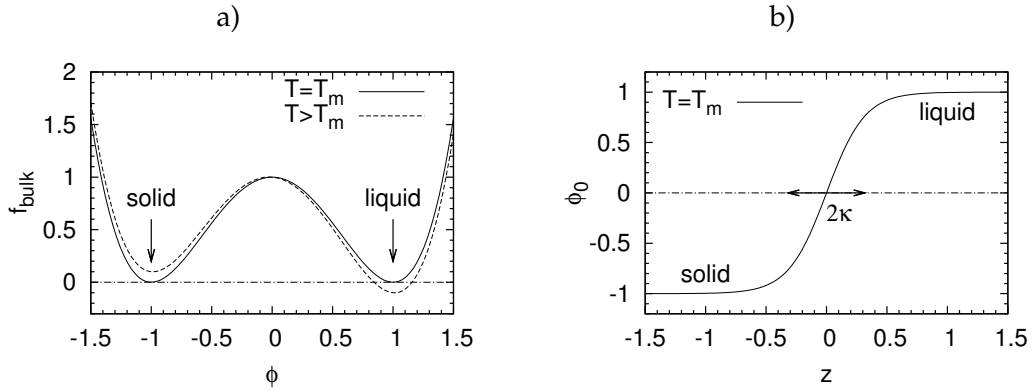


FIGURE 2.1. a) ϕ^4 *or* W*-potential* b) *density profile at two phase coexistence* $T = T_\mathrm{m}$. *The diffuse interface thickness in the order of* $\kappa = \sqrt{a/b}$.

for the functional derivative.

In thermal equilibrium the condition $\delta F[\phi]/\delta\phi = 0$ is obeyed, and the relaxation into the equilibrium is modeled with eq. (2.33) which can be written as

$$\Gamma^{-1}\frac{\partial\phi}{\partial t} = -\frac{\delta F}{\delta\phi} = 2\kappa\triangle\phi - f'(\phi), \tag{2.37}$$

where Γ^{-1} corresponds to the time-scale of the relaxation process. This is the simplest form of an evolution equation, where the free energy necessarily decreases [242]:

$$\begin{aligned}\frac{\mathrm{d}}{\mathrm{d}t}F &= \int\frac{\delta F}{\delta\phi}\frac{\partial\phi}{\partial t}\mathrm{d}^3r &(2.38)\\ &= \Gamma\int\left(\frac{\delta F}{\delta\phi}\right)^2\mathrm{d}^3r &(2.39)\\ &\leq 0. &(2.40)\end{aligned}$$

This model has no conserved variables and thus has not any hydrodynamic mode [129]. It is used for example for the kinetic Ising model [112].

Another common model for the dynamics is described by the ϕ-conserving Cahn-Hilliard equation

$$\Gamma^{-1}\frac{\partial\phi}{\partial t} = \triangle\frac{\delta F}{\delta\phi} = \triangle\left(f'(\phi) - 2\kappa\triangle\phi\right). \tag{2.41}$$

Let us assume for the moment that the order parameter ϕ is proportional to the particle density ρ. Starting from the continuity equation [116]

$$\frac{\partial\rho}{\partial t} = -\nabla\cdot\mathbf{u}, \tag{2.42}$$

where $\mathbf{u}$ is a particle flux related to a chemical potential μ

$$\mathbf{u} = -\lambda \nabla \mu. \tag{2.43}$$

The chemical potential is derived from the functional derivative of the free energy $F[\phi]$ and thus $\mu = \mu(\mathbf{r}, t)$:

$$\mu = \frac{\delta F[\rho]}{\delta[\rho]}. \tag{2.44}$$

Using eq. (2.41) yields the Cahn-Hilliard equation

$$\frac{\partial \rho}{\partial t} = \Gamma \triangle \frac{\delta F[\rho]}{\delta[\rho]}. \tag{2.45}$$

Although the mass/particle density is used here as an order parameter to derive the Cahn-Hilliard equation any conserved order parameter ϕ can be used in this model equivalently ($\frac{\mathrm{d}}{\mathrm{d}t} \int \phi \mathrm{d}^3 r = 0$).

Like the Allan-Cahn model, the evolution equation is of the simplest form to preserve a steady decrease of the free energy [242], which obeys the conservation of the order parameter:

$$\begin{aligned}
\frac{\mathrm{d}}{\mathrm{d}t} F &= \int \frac{\delta F}{\delta \phi} \frac{\partial \phi}{\partial t} \mathrm{d}^3 r && (2.46)\\
&= -\int \left(\frac{\delta F}{\delta \phi} \nabla \cdot \Gamma \nabla \frac{\delta F}{\delta \phi} \right) \mathrm{d}^3 r && (2.47)\\
&= -\int \Gamma \left(\nabla \frac{\delta F}{\delta \phi} \right)^2 \mathrm{d}^3 r && (2.48)\\
&\leq 0. && (2.49)
\end{aligned}$$

The right-hand side in eq. (2.46) makes use of the conservation equation written in an Eulerian frame. This model was first suggested by Cahn and Hilliard [52] to study the process of spinodal decomposition.

2.3. Dynamical density functional theory

Many studies of fluids are done with continuum mechanics. Indeed, hydrodynamics works very well even at rather small length scales, ignoring that the fluid consists of individual particles [41]. In systems where the particle diameters are at the same length scale as the typical length scale of the imposed geometry the dynamics are not well described by the Navier-Stokes equation. Thus other approaches are needed.

These limits are first reached when describing colloids in a suspension or blood cells in capillaries [286]. During the last decade theories tackling this problem were developed and the first dynamical density function theory (DDFT) was formulated by Marconi and Tarazona [194, 195] for Brownian particles suspended in a solvent and neglecting hydrodynamic interactions. In the last years, also molecular fluids were widely discussed in that framework [9, 193, 196]. We shall make a brief description of these approaches in this section.

First the DDFT for Brownian particles is discussed here, as it was derived by Marconi and Tarazona [194, 195]. Afterwards DDFT shall be discussed following recent studies concerning molecular fluids.

Starting from a system with N Brownian particles at position $\mathbf{r}_i(t)$ and momentum $\mathbf{p}_i(t)$ $(1 \leq i \leq N)$. The microscopic equations of motion reads

$$\frac{\mathrm{d}\mathbf{p}_i}{\mathrm{d}t} = -\gamma \mathbf{p}_i - \nabla \varphi_i(\mathbf{r}_i, \mathbf{r}_j) - \nabla V_{\mathrm{ext}}(\mathbf{r}_i, t) + \eta_i(t) \tag{2.50}$$

$$\frac{\mathrm{d}\mathbf{r}_i}{\mathrm{d}t} = \frac{\mathbf{p}_i}{m}, \tag{2.51}$$

where $\varphi_i(\mathbf{r}_i, \mathbf{r}_j)$ describes the inter-particle potential, $V_{\mathrm{ext}}(\mathbf{r}_i, t)$ the external potential, which is probably time-dependent, and a random noise force η_i, which is connected to the friction term $\gamma \mathbf{p}_i$ by the fluctuation-dissipation theorem:

$$\langle \eta_{i,k}(t) \rangle = 0 \tag{2.52}$$

$$\langle \eta_{i,k}(t) \eta_{j,l}(t') \rangle = 2\gamma m k_{\mathrm{B}} T \delta_{ij} \delta_{kl} \delta(t - t'), \tag{2.53}$$

where i, j denotes the particle i resp. j and k, l run over x, y, z. Note that the ensemble averages are taken over the realizations of the noise, since the system is not necessarily in equilibrium [194]. Hydrodynamic interactions are not included in the Langevin equation (2.50). In the limit of large γ, where the dynamics become overdamped, the momenta are proportional to the instantaneous forces, thus $\mathrm{d}\mathbf{p}_i/\mathrm{d}t$ vanishes [9]. And eq. (2.50) simplifies to

$$\gamma m \frac{\mathrm{d}\mathbf{r}_i}{\mathrm{d}t} = -\nabla \left[\varphi_i(\mathbf{r}_i, \mathbf{r}_j) + V_{\mathrm{ext}}(\mathbf{r}_i, t) \right] + \eta_i(t). \tag{2.54}$$

Eq. (2.54) can be reformulated as a stochastic differential equation (SDE). Therefore the density operator

$$\rho_N(\mathbf{r}, t) := \sum_{i=1}^{N} \delta(\mathbf{r}_i(t) - \mathbf{r}) \tag{2.55}$$

is needed, and following ref. [195] it obeys

$$\begin{aligned}\gamma m\frac{\partial \rho_N}{\partial t} &= \nabla\cdot\Big[T\nabla\rho_N(\mathbf{r},t)+\rho_N(\mathbf{r},t)\nabla V_{\text{ext}}\\ &\quad+\int\rho_N(\mathbf{r},t)\rho_N(\mathbf{r}',t)\nabla\varphi(\mathbf{r},\mathbf{r}')\,\mathrm{d}^3r'\\ &\quad+\eta(\mathbf{r},t)\rho_N^{\frac{1}{2}}(\mathbf{r},t)\Big].\end{aligned}\tag{2.56}$$

$\eta(\mathbf{r},t)$ is a so-called global noise field (not to be confused with of the random force $\eta_i(t)$ of particle i). The global noise field has zero mean and is uncorrelated in time and space

$$\langle\eta(\mathbf{r},t)\eta(\mathbf{r}',t')\rangle = 2\gamma m k_{\text{B}}T\delta(\mathbf{r}-\mathbf{r}')\delta(t-t').\tag{2.57}$$

Averaging over the noise (ensemble average) eq. (2.56) gives

$$\begin{aligned}\gamma m\frac{\partial \rho}{\partial t} &= \nabla\cdot\Big[T\nabla\rho(\mathbf{r},t)+\rho(\mathbf{r},t)\nabla V_{\text{ext}}\\ &\quad+\int\langle\rho_N(\mathbf{r},t)\rho_N(\mathbf{r}',t)\rangle\nabla\varphi(\mathbf{r},\mathbf{r}')\,\mathrm{d}^3r'\Big],\end{aligned}\tag{2.58}$$

where $\rho(\mathbf{r},t)$ is the one particle density ($\langle\rho_N(\mathbf{r},t)\rangle = \rho(\mathbf{r},t)$). Eq. (2.58) connects the one particle density ρ to the two particle density $\rho^{(2)} = \langle\rho_N(\mathbf{r},t)\rho_N(\mathbf{r}',t)\rangle$. Hence an assumption for $\rho^{(2)}$ is needed to close this equation.

This local equilibrium approximation [252] is the cornerstone of the Brownian-DDFT. The idea comes from the equilibrium-DFT, since it exists an one-to-one correspondence of the density profile in equilibrium and the external potential V_{ext}. The external potential, in turn, contributes to the excess part of the free-energy functional $F[\rho]$. Assuming, that the two particle density at time t in the non-equilibrium system with instantaneous one particle density $\rho(t)$ is the same as the equilibrium two particle density in a system with the equilibrium one particle density $\rho(t)$, the eq. (2.58) can be closed with eq. (2.23) [194]. One obtains

$$\int -\rho_{\text{eq}}^{(2)}\nabla\varphi\mathrm{d}^3r' = k_{\text{B}}T\rho\frac{\partial c_{\text{eq}}^{(2)}}{\partial\mathbf{r}} = -\rho\nabla\frac{\delta\mathcal{F}_{\text{ex}}}{\delta\rho},\tag{2.59}$$

where $c_{\text{eq}}^{(2)}$ is the direct correlation function, as defined in (2.26).

The first two parts on the right hand side of eq. (2.58) can also be recasted with the other terms of the free energy functional F. The final equation reads than [194]

$$\gamma m\frac{\partial\rho}{\partial t} = -\nabla\cdot\left(\rho\nabla\frac{\delta F[\rho]}{\delta\rho}\right).\tag{2.60}$$

It is noteworthy to mention that the assumption of overdamped dynamics (large γ) implies that the system equilibrates on short time-scales, justifying the local equilibrium assumption (which uses equilibrium descriptions from DFT).

In the development of a DDFT for molecular liquids, where the fluid is not damped by a solvent (implying a Langevin-thermostat) this chain of arguments do not hold any longer. However, there are recent contributions, e.g. from Archer [9, 193] to build a DDFT for molecular fluids. Some of these results shall be discussed in the following section.

2.4. PF/DDFT model for nanofluidics

In this section we formulate a model to study nanofluidic devices. As microscopic simulations with molecular dynamics (MD) or Monte Carlo (MC) [107] algorithms are used to study dynamical behavior in systems of a few nanometers, the droplets in these studies are considered nanometric too. Length scales of microns are inaccessible with standard computer power and time scales are also limited up to nanoseconds. On the other side, macroscopic behavior of wetting is often studied with lattice Boltzmann (LB) methods. In such studies, the roughness length scale is typically micrometric and drops are one (up to two) orders of magnitude larger. However, systematically, there is a gap in length scales of the roughness L between LB and MD methods.

Thus the model which is used in this study aims to bridge this gap between the roughness length scale and the drop diameter. It takes explicitly account for a liquid-vapor phase transition in the vicinity of a corrugated wall. While the roughness is microscopic (Angstroms or nanometers) the drops might be much larger. For this purpose the complex features of a solid-fluid interaction can not be treated as a simple contact potential, neglecting a finite range of the wall potential. More realistic coupling mechanisms are needed. Furthermore, the objective of such a PF model is to include both: static behavior and dynamical behavior. The former is needed to study wetting properties while the latter is needed for slip, contact angle hysteresis and other features in nanofluidic devices. In hydrodynamic descriptions at short length scales, slippage is an important issue [40]. While no-slip boundary conditions work rather well for macroscopic systems, partial-slip is found in some microscopic setups [174]. For the microscopic understanding it is thus required to define solid-liquid interfaces without a macroscopic boundary condition. Combining methods from DFT, PF and DDFT allows us to formulate such a model, as described below.

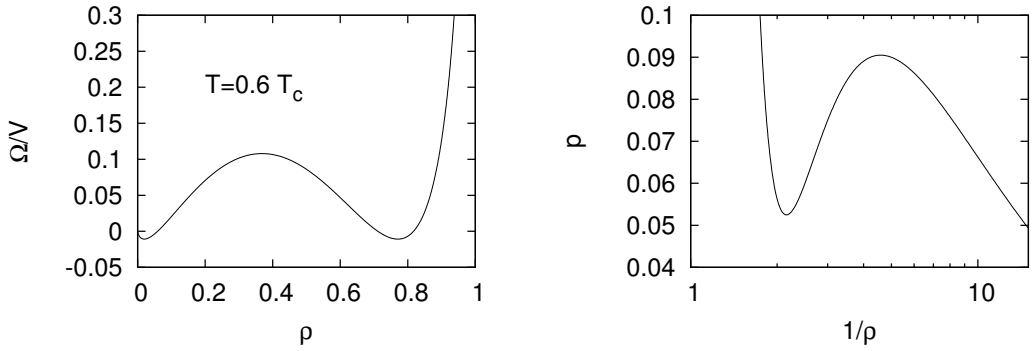


FIGURE 2.2. *Grand potential $\Omega = F - \mu N$ and $p - v$ diagram ($v = 1/\rho$) of van der Waals fluid. $T = 0.9T_c$*

2.4.1. Thermodynamic properties

DFT describes the thermal equilibrium density profiles in an external potential, like a solid wall. This framework provides in principle generic and exact access to wetting properties, such as contact angles. Although this theory is free of approximations in its roots, in practice the grand canonical potential functional $\Omega[\rho]$ is approximated for all real systems. The simplest density functional theory for heterogeneous systems is the square gradient theory, which accounts for phase boundaries [303, 258]. Together with a bulk free energy ansatz the square gradient term is convenient to describe a diffuse interface problem. This thickness w of the interface is in the order of a few Angstroms. And the square gradient term gives a monotonic smooth change from one phase to another (see fig. 2.3 on page 41). More complex functionals demonstrate, that the real interface can be oscillatory [122]. This theory can therefore be considered as a mean field theory for phase boundaries in general. Such a mean field description is sufficient for the investigation of generic wetting properties. Specific systems might need other functionals, which could be introduced in this model too. A widely used fluid model, which exhibits liquid-vapor coexistence is the one-species van der Waals gas. The free energy reads

$$f_{\text{bulk}}(\rho) := k_{\text{B}}T\left(\ln\left(\frac{\rho\Lambda^3}{1-\rho b}\right) - 1,\right) - a\rho^2 \tag{2.61}$$

where k_{B} is the Boltzmann constant, T the temperature and Λ the thermal de Broglie wavelength. The constant a effectively accounts for the attractive forces between the particles in a mean field way and the constant b models the excluded volume of one particle. The particle density ρ is taken as a function of $\mathbf{r}$.

Figure 2.2 shows the van der Waals grand canonical potential as a function of the density in the left panel and the $p - v$-diagram. The phenomenological constants a and b can be substituted with the critical point temperature T_c ($k_B T_c = 8a/27b$) and the definition $b = \sigma^3$ is used to rescale the variables in eq. (2.61) dimensionless. σ is in the order of a few Angstroms and corresponds roughly to the particle diameter. This bulk term is also called local density approximation, and the combination with the square gradient term

$$f_{\text{interface}} = \frac{W^2}{2} |\nabla \rho(\mathbf{r})|^2 \tag{2.62}$$

provides a simple model for phase coexistence with interfaces.

$$F\left[\rho(\mathbf{r})\right] = \int \left(f_{\text{bulk}} + f_{\text{interface}}\right) \mathrm{d}^3 r + F_{\text{wall}}[\rho], \tag{2.63}$$

where F_{wall} is the solid-fluid contribution to the free energy, if a substrate is present. For the interaction between fluid particles and solid particles a 12-6 Lennard-Jones interaction is assumed.

$$V_{\text{LJ}}(|\mathbf{r} - \mathbf{r}'|) = \varepsilon_{\text{LJ}} \left(\frac{\sigma^{12}}{|\mathbf{r} - \mathbf{r}'|^{12}} - \frac{\sigma^6}{|\mathbf{r} - \mathbf{r}'|^6} \right), \tag{2.64}$$

where σ is the interaction range and ε_{LJ} is the interaction strength. For simplicity we connect σ with the excluded volume b from the bulk term via $\sigma^3 = b$. We have therefore only 2 intrinsic length scales in the system: the interaction range σ and the interfacial thickness W. Both are of the same order. With the Lennard-Jones potential F_{wall} reads

$$F_{\text{wall}}\left[\rho(\mathbf{r})\right] = \int \int \rho_{\text{wall}-\text{fluid}}(\mathbf{r}, \mathbf{r}') V_{\text{LJ}}(|\mathbf{r} - \mathbf{r}'|) \mathrm{d}^3 r' \, \mathrm{d}^3 r, \tag{2.65}$$

where $\rho_{\text{wall}-\text{fluid}}(\mathbf{r}, \mathbf{r}')$ is the two particle distribution function of fluid and wall particles.

We can rewrite the two particle distribution function using the pair-correlation-function $g_{\text{wall}-\text{fluid}}(\mathbf{r}, \mathbf{r}')$

$$\rho_{\text{wall}-\text{fluid}} = \rho\left(r\right) \rho_{\text{wall}}\left(r'\right) g_{\text{wall}-\text{fluid}}\left(r, r'\right) \tag{2.66}$$

and we know that $g_{\text{wall}-\text{fluid}} \to 1$ when $r \to \infty$ and $g_{\text{wall}-\text{fluid}} \to 0$ for $r \to 0$ in such a way that

$$\int \mathrm{d}^3 r' \rho_{\text{wall}}\left(r'\right) g_{\text{wall}-\text{fluid}}\left(r, r'\right) V_{LJ}\left(|\mathbf{r} - \mathbf{r}'|\right) < \infty \tag{2.67}$$

everywhere. The $\mathbf{r}'$ integral represents the effective wall potential V_{wall}. We assume therefore a finite value V_0 of the wall potential V_{wall} inside the wall. For numerical

reasons this can be treated with a cut off radius r_c in the wall–fluid Lennard-Jones interaction

$$V_{\mathrm{LJ}}^{\#} = \begin{cases} V_c = V_{\mathrm{LJ}}(r_c) & \text{if } r < r_c \\ V_{\mathrm{LJ}} & \text{if} r > r_c. \end{cases} \tag{2.68}$$

Thus

$$F_{\mathrm{wall}} = \int \rho\left(\mathbf{r}\right) V_{\mathrm{wall}}\left(\mathbf{r}\right) \mathrm{d}^3 r. \tag{2.69}$$

with $V_{\mathrm{wall}}(\mathbf{r}) = \int \rho_{\mathrm{wall}}(\mathbf{r}') V_{\mathrm{LJ}}^{\#}(|\mathbf{r} - \mathbf{r}'|)\, \mathrm{d}^3 r$. Eventually the free energy reads in a dimensionless form

$$F^*\left[\rho\right] = \quad = \quad \int \left[f_{\mathrm{bulk}}^* + \frac{w^2}{2} |\nabla^* \rho^*|^2 + \rho^* V_{\mathrm{wall}}^* \right] \mathrm{d}^3 r^*, \tag{2.70}$$

where * denotes dimensionless quantities and $w = W/\sqrt{\sigma^3 k_{\mathrm{B}} T_{\mathrm{c}}}$. Rescaling removes dimensions from the bulk free energy $f_{\mathrm{bulk}}^* = \frac{\sigma^3}{k_{\mathrm{B}} T_{\mathrm{c}}} f_{\mathrm{bulk}}$, the wall potential $V_{\mathrm{wall}}^* = \frac{1}{k_{\mathrm{B}} T_{\mathrm{c}}} V_{\mathrm{wall}}$ and the density $\rho^* = \sigma^3 \rho$. For ease of notation, * is droped below. The grand canonical potential reads

$$\Omega[\rho] = F[\rho] - \mu \int \rho \mathrm{d}^3 r, \tag{2.71}$$

where μ is the chemical potential of the system. For a given substrate potential, which is entirely defined by ρ_{wall} and $\varepsilon_{\mathrm{LJ}}$, the density profile in thermodynamically stable states is obtained by minimizing Ω. The global minimum yields the equilibrium state, local minima represent metastable states. Chemically homogeneous substrates are modeled with a wall density ρ_{wall} taken as $1/\sigma^3$ inside the wall and 0 elsewhere. Other system control parameters are the temperature T, the interface thickness w and the chemical potential μ to tune the average density.

2.4.2. Dynamics of the density profile

In this paragraph the dynamical equations for the fluid density field $\rho(\mathbf{r}, t)$ and the velocity field $\mathbf{v}(\mathbf{r}, t)$ are developed. First we shall focus on the evolution equation for the density profile. The formulation takes several forms depending on thermodynamic constraints.

Isothermal and mass conserving dynamics To work at isothermal conditions (in space and time) with a fixed number of particles the evolution equation reads [9, 252]

$$\begin{aligned}\frac{\partial \rho}{\partial t} &= -\nabla\cdot(\rho\mathbf{v}) + \nabla\cdot\left[G^{\mathrm{DDFT}}\rho\nabla\left(\frac{\delta\Omega[\rho]}{\delta\rho}\right)\right] \\ &= -\nabla\cdot(\rho\mathbf{v}) + \nabla\cdot\left[G^{\mathrm{DDFT}}\rho\nabla\left(\frac{\delta F[\rho]}{\delta\rho}\right)\right].\end{aligned} \tag{2.72}$$

The second equality comes from the fact that $\frac{\delta F[\rho]}{\delta\rho}$ and $\frac{\delta\Omega[\rho]}{\delta\rho}$ only differs by the constant μ. We recognize the convective flux $-\nabla\cdot\mathbf{j}_{\mathrm{hydro}} = -\nabla\cdot\rho\mathbf{v}$ at the right hand side terms, as known from the continuity equation. The second term in this description is less usual. It is known from the above discussed DDFT and accounts for a coupling to a thermostat. In MD simulations often thermostats are used to equilibrate the system faster. Several methods are used in the literature to fix the temperature [107]: Rescaling of velocities with Nosé-Hover thermostat, effective friction or Langevin random forces. The so-called shadow theorem ensures, that the precise method of thermostatting is not very important to describe the collective behavior of the fluid at equilibrium. Only the trajectories are strongly sensitive to forces of the thermostat, but not the ensemble averages [107, 251]. Actually, this is the reason, why molecular simulations work so well. The second terms on the right hand side models one method to thermalize the system, and we expect therefore no influence of the precise method of thermostatting onto the collective behavior of ρ and $\mathbf{v}$. When the local equilibrium is reached $\frac{\delta F}{\delta\rho}$ vanishes and we recover at large time scale the actual hydrodynamic transport equations $\frac{\partial\rho}{\partial t} = -\nabla\cdot\rho\mathbf{v}$.

Indeed, this second term we can interpret as a flux $\mathbf{j}_{\mathrm{thermo}} = -G^{\mathrm{DDFT}}\rho\nabla\left(\frac{\delta F[\rho]}{\delta\rho}\right)$. The continuity equation reads

$$\frac{\partial\rho}{\partial t} = -\nabla\cdot\mathbf{j}. \tag{2.73}$$

And we decompose $\mathbf{j} = \mathbf{j}_{\mathrm{hydro}} + \mathbf{j}_{\mathrm{thermo}}$. At molecular scales the local thermalization process is very fast (in the order of picoseconds) and the $\mathbf{j}_{\mathrm{thermo}}$ plays only a role in a short transient non-equilibrium regime, until the Ω is locally minimized. Microscopically, this is equivalent to the assumption of a local Maxwellian phase-space distribution

$$f^{(1)}_{\text{local eq.}}(\mathbf{r},\mathbf{p},t) = \frac{\rho(\mathbf{r})}{(2\pi k_{\mathrm{B}}T)^{3/2}}\exp\left(-\frac{(\mathbf{p}-\overline{\mathbf{p}}(t))^2}{(2mk_{\mathrm{B}}T)}\right), \tag{2.74}$$

where $\overline{\mathbf{p}}(t) = m\mathbf{v}(t)$ [9]. Thus the correct long-time behavior is recovered $\mathbf{j} = \mathbf{j}_{\mathrm{hydro}}$. Quite recently it has been shown from microscopic considerations that the relaxation dynamics of an ensemble in contact with a heat reservoir can be remarkably well described using equation (2.72) [9]. Equations like that one are now the corner stone

of DDFT, as described above. One has to mention, that these equations fail to predict subtle local arrangements (roughly comparable to the glassy cage effect) of fluids with a pronounced hard core behavior in narrow confinements [252]. This is so, because fast transients to equilibrium are assumed, which do not hold in glassy systems. Since the typical confinement of our systems is in the order of ten or more particle diameters. We do not expect such subtleties to appear when applying the DDFT thermostat. The constant G^{DDFT} describes the relaxation time scales to local equilibrium. In usual PF models $G^{\mathrm{DDFT}}\rho$ is taken to be constant and the thermostat term reads $\triangle(G^{\mathrm{CH}}\delta F/\delta\rho)$, where the superscript CH reminds to the similarity with the Cahn-Hilliard equation described above. We used this ansatz here for the sake of simplicity and we choose G^{CH} to reproduce the self-diffusion constant of water molecules. The time scale τ of the local relaxation dynamics are therefore fixed by $\tau = \sigma^2/G^{\mathrm{CH}}$. One can check, that e.g. an amplification of τ by one order of magnitude does not effect the long time behavior. We use τ to define dimensionless times.

Isothermal dynamics and coupling to a particle reservoir Equations like (2.72) are useful for two reasons. First, applying the thermodynamic constraints is convenient and it takes explicitly the fast relaxation dynamics on small length scales into account. To explore the phase diagram of a system, the DDFT or Cahn-Hilliard thermostat is exchanged by a non-conserving Allen-Cahn thermostat, which couples the system to a particle reservoir at chemical potential μ

$$\frac{\partial\rho}{\partial t} = -\nabla\cdot(\rho\mathbf{v}) - G^{\mathrm{AC}}\left(\frac{\delta\Omega[\rho]}{\delta\rho}\right). \tag{2.75}$$

With this prescription, we can investigate phase coexistences quite easily by tuning the chemical potential μ. Although the relaxation dynamics does not correspond to a real system, the equilibrium states satisfy the macroscopic transport equation (2.73) and the steady velocity field obtained in this case corresponds to the true hydrodynamic flow. Quantities such as slip lengths can thus be obtained with this method as well. The framework presented here is thus very generic and allows to model various physical problems.

2.4.3. Hydrodynamic transport equation

The hydrodynamic transport is described by the momentum equation

$$m\frac{\partial\rho\mathbf{v}}{\partial t} + \nabla\cdot(\rho m\mathbf{v}\mathbf{v}) = \nabla\cdot\mathbf{\Sigma} - \rho\nabla\left(\frac{\delta\Omega[\rho]}{\delta\rho}\right) + \mathbf{f}_{\mathrm{wall}} + \mathbf{f}_{\mathrm{ext}}, \tag{2.76}$$

where $\mathbf{\Sigma} = \eta\left(\nabla\mathbf{v} + (\nabla\mathbf{v})^{\,t}\right) + (\zeta - 2/3\eta)(\nabla\cdot\mathbf{v})\delta$ is the viscous stress tensor (with the first/shear viscosity η, the second/bulk viscosity ζ and the unit matrix δ). The extra contribution $-\rho\nabla\left(\frac{\delta\Omega[\rho]}{\delta\rho}\right) = \mathbf{f}_{\text{thermo}}$ accounts for both: the pressure tensor and the capillary force. The external force terms $\mathbf{f}_{\text{wall}} + \mathbf{f}_{\text{ext}}$ are discussed afterwards.

Thermodynamic force field We shall derive this force field applied by the fluid distribution ρ onto the flow by considering the free-energy variation due to a virtual displacement of the fluid distribution. Using conserved dynamics constraints we denote the displacement field, which is applied to the fluid $\delta\mathbf{r}'(\mathbf{r})$. With the conservation constraint, the proper thermodynamic potential is the free energy F and the corresponding variation $\delta\rho(\mathbf{r})$ of the density field is a conservation law

$$\delta\rho(\mathbf{r}) + \nabla\cdot(\rho(\mathbf{r})\delta\mathbf{r}'(\mathbf{r})) = 0. \tag{2.77}$$

The free-energy variation of the full system is given by

$$\delta F = \int \frac{\delta F[\rho]}{\delta\rho(\mathbf{r})}\delta\rho(\mathbf{r})d\mathbf{r}. \tag{2.78}$$

Using eq. (2.77) in (2.78) yields

$$\delta F = -\int \frac{\delta F[\rho]}{\delta\rho(\mathbf{r})}\nabla\cdot(\rho(\mathbf{r})\delta\mathbf{r}'(\mathbf{r}))d\mathbf{r}. \tag{2.79}$$

An integration by part (assuming vanishing values of $\delta\mathbf{r}'(\mathbf{r})$ at the boundaries of the system or periodic boundary conditions as in our simulations) leads to

$$\delta F = \int \rho(\mathbf{r})\nabla\left(\frac{\delta F[\rho]}{\delta\rho(\mathbf{r})}\right)\delta\mathbf{r}'(\mathbf{r})d\mathbf{r}. \tag{2.80}$$

The functional derivative of F with respect to $\mathbf{r}'(\mathbf{r})$ is found to be

$$\frac{\delta F}{\delta\mathbf{r}'(\mathbf{r})} \equiv \rho(\mathbf{r})\nabla\left(\frac{\delta F[\rho]}{\delta\rho(\mathbf{r})}\right) \tag{2.81}$$

and the resulting force field as:

$$\begin{aligned}\mathbf{f}_{\text{thermo}}(\mathbf{r}) = -\tfrac{\delta F}{\delta\mathbf{r}'(\mathbf{r})} &= -\rho(\mathbf{r})\nabla\left(\tfrac{\delta F[\rho]}{\delta\rho(\mathbf{r})}\right)\\ &= -\rho(\mathbf{r})\nabla\left(\tfrac{\delta\Omega[\rho]}{\delta\rho(\mathbf{r})}\right)\end{aligned}. \tag{2.82}$$

Pressure and Laplace Force obtained from the thermodynamic force field In this paragraph it is proven that the thermodynamic force field $-\rho\nabla\left(\frac{\delta\Omega[\rho]}{\delta\rho}\right)$ accounts for both: the volume pressure contribution $-\nabla P$ and the surface capillary force $-\mathcal{H}\gamma\hat{\mathbf{n}}$, where $\mathcal{H}$ is the local mean curvature of the interface (with the convention that it is positive for a sphere), $\hat{\mathbf{n}}$ is the normal vector (pointing outside) and γ the liquid-vapor surface tension.

First, the pressure tensor is extracted, using the identity

$$-\rho(\mathbf{r})\nabla\left(\frac{\delta\Omega[\rho]}{\delta\rho(\mathbf{r})}\right) \equiv -\rho(\mathbf{r})\nabla\left(\frac{\delta F[\rho]}{\delta\rho(\mathbf{r})}\right) \equiv -\nabla\cdot\mathbf{P}. \tag{2.83}$$

The meaning of the first equality sign is already discussed (the functional derivatives of F and Ω differs only by a constant) and the second equality states the definition of the pressure tensor $\mathbf{P}$. For the square gradient theory

$$F[\rho] \equiv \int\left\{f_{\text{bulk}}(\rho) + \frac{W^2}{2}|\nabla\rho|^2\right\}\mathrm{d}^3r, \tag{2.84}$$

and therefore the functional derivative reads

$$\frac{\delta F[\rho]}{\delta\rho(\mathbf{r})} = f'_{\text{bulk}}(\rho) - W^2\Delta\rho. \tag{2.85}$$

An ansatz for the pressure tensor [6]:

$$\mathbf{P}_{ij} = \left(\rho\frac{df_{\text{bulk}}}{d\rho} - f_{\text{bulk}} - W^2\rho\Delta\rho - \frac{W^2}{2}|\nabla\rho|^2\right)\delta_{ij} + W^2\nabla_i\rho\nabla_j\rho \tag{2.86}$$

satisfies the second identity in eq. (2.83). The pressure tensor can be rewritten as

$$\mathbf{P}_{ij} = P_n\delta_{ij} + W^2\left(\nabla_i\rho\nabla_j\rho - |\nabla\rho|^2\delta_{ij}\right), \tag{2.87}$$

where $P_n = \rho\frac{df_{\text{bulk}}}{d\rho} - f_{\text{bulk}} - W^2\rho\Delta\rho + \frac{W^2}{2}|\nabla\rho|^2$ is the normal pressure (i.e. in the direction of $\nabla\rho$). For a planar interface, P_n is constant across the interface, but there is a jump when the interface is curved. Plugging this last equation in the definition (2.83) yields decomposition into the bulk pressure and the Laplace force

$$-\rho(\mathbf{r})\nabla\left(\frac{\delta\Omega[\rho]}{\delta\rho(\mathbf{r})}\right) = -\nabla P_n + W^2(\nabla\rho\cdot\nabla(\nabla\rho) - \Delta\rho\nabla\rho). \tag{2.88}$$

The latter has not yet been proved. Let us denote tentatively $\mathbf{L} \equiv W^2(\nabla\rho\cdot\nabla(\nabla\rho) - \Delta\rho\nabla\rho)$ as the Laplace force. Since ρ varies in the normal direction only (by definition), this force is normal by construction. The normal vector field reads

$$\hat{\mathbf{n}} \equiv \frac{\nabla\rho}{|\nabla\rho|}, \tag{2.89}$$

where the local curvature $\mathcal{H}$ of the interface is defined as

$$\mathcal{H}(\mathbf{r}) = \nabla \cdot \hat{\mathbf{n}} = \frac{\Delta\rho}{|\nabla\rho|} - \frac{\nabla\rho \cdot (\nabla\rho \cdot \nabla)(\nabla\rho)}{|\nabla\rho|^3}, \tag{2.90}$$

which is positive for a spherical drop. This expression can be rewritten as

$$\mathcal{H}(\mathbf{r}) = -\frac{\hat{\mathbf{n}}}{|\nabla\rho|^2}.\,(\nabla\rho \cdot \nabla(\nabla\rho) - \Delta\rho\nabla\rho) = -\frac{\hat{\mathbf{n}} \cdot \mathbf{L}}{W^2|\nabla\rho|^2} \tag{2.91}$$

from which we deduce that $\mathbf{L}$ is

$$\mathbf{L} = -\mathcal{H}(\mathbf{r})W^2|\nabla\rho|^2\hat{\mathbf{n}}\,. \tag{2.92}$$

To identify the Laplace force, we need to recall that for a planar interface the surface tension can be written [258]:

$$\gamma = \int W^2|\nabla\rho|^2 dz, \tag{2.93}$$

where z is the normal coordinate. Equation (2.92) is thus a local expression for the Laplace force.

External force fields We come back to the remaining forces in eq. (2.76). The term $\mathbf{f}_{\text{ext}}$ can be gravity for instance or any other driving force. Such driving power is dissipated in a system with a solid substrate by two types of non-reversible processes: first by friction with the walls and second viscous dissipation due to shear and compression. While the latter effect is covered by the viscous stress tensor in (2.76), the former is modeled by the term $\mathbf{f}_{\text{wall}}$. This is a continuous force field applied by the walls, which move with $\mathbf{v}_{\text{wall}}$ (to simulate shear, e.g. the bottom wall is fixed and the top wall has a constant velocity $\mathbf{v}_{\text{wall}} = v_{\text{top}}$, the wall-speed field is therefore discontinuous). A heuristic friction ansatz is thus

$$\begin{aligned}\mathbf{f}_{\text{wall}}(\mathbf{r}) = \quad & -k\varepsilon_{\text{LJ}}\rho(\mathbf{r})\,(\mathbf{v}(\mathbf{r}) - \mathbf{v}_{\text{wall}}(\mathbf{r}))\times \\ & \int \mathrm{d}\mathbf{r}'\left(\rho_{\text{wall}}(\mathbf{r}')\tfrac{1}{\sqrt{\pi}^3\sigma^3}\mathrm{e}^{-\frac{(\mathbf{r}'-\mathbf{r})^2}{\sigma^2}}\right)\end{aligned}, \tag{2.94}$$

where k is phenomenological parameter, which has to be adjusted to the requirements. This force is proportional to the interaction energy ε_{LJ} of the fluid-solid interaction potential and this prescription allows for correct intrinsic slip behavior reported in MD studies [23, 24, 40]. In particular, we obtain a continuous change from an intrinsic no-slip boundary condition (BC) in a wetting situation ($\theta \sim 0°$) to a partial slip BC with a slip length $b \sim 10$nm (depending on the value of k) in a non-wetting situation ($\theta \sim 120°$). Details shall be discussed in chapter 4.

2.4.4. The numerical implementation

This paragraph is dedicated to the numerical implementation of the nanofluidics PF model. This model is solved with a mixed scheme of finite difference methods and Fourier methods. Among a huge number of possible formulations for the differential operators most lead to numerically unstable algorithms. Therefore, this paragraph displays a compilation of robust schemes to solve equations (2.72)/(2.75) and (2.76).

The square gradient grand canonical potential/free energy variation can be computed from equation (2.71)

$$\frac{\delta\Omega[\rho]}{\delta\rho} = f'_{\text{bulk}}(\rho(\mathbf{r})) + V_{\text{wall}}(\mathbf{r}) - W^2\Delta\rho(\mathbf{r}) - \mu, \tag{2.95}$$

where $f'_{\text{bulk}}(\rho(\mathbf{r}))$, the derivative of the bulk free-energy with respect to ρ, which is known analytically. To simplify the algebra, let us define:

$$\omega'_{\text{local}}(\mathbf{r}) = f'_{\text{bulk}}(\rho(\mathbf{r})) + V_{\text{wall}}(\mathbf{r}) - \mu \tag{2.96}$$

The density field Using (2.96) and (2.95)

$$\frac{\partial\rho}{\partial t} - GW^2\Delta\rho(\mathbf{r}) = -\nabla\cdot(\rho\mathbf{v}) - G\omega'_{\text{local}}(\mathbf{r}) \tag{2.97}$$

(with $G = G^{\text{AC}}$ or $-G^{\text{CH}}\Delta$). From here we derive a semi-implicit scheme

$$\frac{\rho^{t+\mathrm{d}t} - \rho^t}{\mathrm{d}t} - GW^2\Delta\rho^{t+\mathrm{d}t}(\mathbf{r}) = -\nabla\cdot(\rho\mathbf{v})^t - G\left(\omega'_{\text{local}}(\mathbf{r})\right)^t, \tag{2.98}$$

where the notation ^{t} indicates the time at which the quantity is evaluated. Rearranging the terms leads to

$$(1 - \mathrm{d}tGW^2\Delta)\rho^{t+\mathrm{d}t} = \rho^t - \mathrm{d}t\left[\nabla\cdot(\rho\mathbf{v})^t + G\left(\omega'_{\text{local}}(\mathbf{r})\right)^t\right]. \tag{2.99}$$

The operator in front of $\rho^{t+\mathrm{d}t}$ can be transformed into Fourier space, and the equation solved for $\rho^{t+\mathrm{d}t}$

$$\rho^{t+\mathrm{d}t}_{\mathbf{k}} = \frac{\rho^t_{\mathbf{k}} - \mathrm{d}t\left[\nabla\cdot(\rho\mathbf{v})^t + G^{\text{AC}}\left(\omega'_{\text{local}}(\mathbf{r})\right)^t\right]_{\mathbf{k}}}{1 + \mathbf{k}^2G^{\text{AC}}W^2\mathrm{d}t}, \tag{2.100}$$

where the quantity between the brackets is evaluated in the direct space, and Fourier transformed afterwards. For conserved dynamics, G needs to be replaced by $-G^{\text{CH}}\Delta$ and the final expression writes

$$\rho^{t+\mathrm{d}t}_{\mathbf{k}} = \frac{\rho^t_{\mathbf{k}} - \mathrm{d}t\left[(\nabla\cdot(\rho\mathbf{v}))^t_{\mathbf{k}} + G^{\text{CH}}\mathbf{k}^2\left(\omega'_{\text{local}}(\mathbf{r})\right)^t_{\mathbf{k}}\right]}{1 + \mathbf{k}^4G^{\text{CH}}W^2\mathrm{d}t}. \tag{2.101}$$

These schemes give quite a robust numerical stability.

Unfortunately this scheme does not strictly ensure positivity of $\rho(\mathbf{r})$ at time $t + \mathrm{d}t$. While this is no problem when the occurring densities are sufficiently large at low temperature in the vapor phase or in the vicinity of the substrate negative ρ can occur. To prevent negative values in $\rho(\mathbf{r})$ at each time step the semi-implicit scheme written above provides an initial guess for $\rho^{t+\mathrm{d}t}(\mathbf{r})$ that we call $\rho^{t+\mathrm{d}t}_{\text{implicit}}(\mathbf{r})$. From this intermediate step the actual value is generated with

$$\rho^{t+\mathrm{d}t}(\mathbf{r}) = \rho^{t}(\mathbf{r}) \exp\left(\frac{\rho^{t+\mathrm{d}t}_{\text{implicit}}(\mathbf{r})}{\rho^{t}(\mathbf{r})} - 1\right). \tag{2.102}$$

This first order finite difference scheme ensures the positivity, due to the exponential term. When $\rho^{t+\mathrm{d}t}_{\text{implicit}}(\mathbf{r})/\rho^{t}(\mathbf{r})$ is close to 1 (which is true for sufficiently small time steps) a Taylor expansion yields $\rho^{t+\mathrm{d}t}(\mathbf{r}) \simeq \rho^{t+\mathrm{d}t}_{\text{implicit}}(\mathbf{r})$ as the leading order in $\Delta\rho(\mathbf{r})/\rho^{t}(\mathbf{r})$, where $\Delta\rho(\mathbf{r}) \equiv \rho^{t+\mathrm{d}t}_{\text{implicit}}(\mathbf{r}) - \rho^{t}(\mathbf{r})$.

The velocity field To simulate shear the velocity field $\mathbf{v}$ is decomposed in two parts

$$\mathbf{v} = \mathbf{u} + \mathbf{v}_{\text{applied}}, \tag{2.103}$$

where $\mathbf{v}_{\text{applied}}$ is the applied velocity profile. A jump of $\mathbf{v}_{\text{applied}}$ at one boundary of the simulation box emulates shear. The remaining part is called $\mathbf{u}$. Without gravity the transport equation reads

$$m\frac{\partial \rho \mathbf{v}}{\partial t} + \nabla \cdot (\rho m \mathbf{v}\mathbf{v}) = \nabla \cdot \boldsymbol{\Sigma} - \rho \nabla \left(\frac{\delta \Omega[\rho]}{\delta \rho}\right) + \mathbf{f}_{\text{wall}}, \tag{2.104}$$

which can be recasted as

$$\begin{aligned} \rho m \tfrac{\partial \mathbf{v}}{\partial t} + \mathbf{v}\tfrac{\partial \rho m}{\partial t} + \quad & \mathbf{v}\nabla \cdot (\rho m \mathbf{v}) + (\rho m \mathbf{v} \cdot \nabla)(\mathbf{v}) \\ & = \nabla \cdot \boldsymbol{\Sigma} - \rho \nabla \left(\tfrac{\delta \Omega[\rho]}{\delta \rho}\right) + \mathbf{f}_{\text{wall}}. \end{aligned} \tag{2.105}$$

Multiplying the transport equation for the density with the molecular mass m, we get

$$m\frac{\partial \rho}{\partial t} + \nabla \cdot (\rho m \mathbf{v}) = -mG\left(\frac{\delta \Omega[\rho]}{\delta \rho}\right). \tag{2.106}$$

Plugging this equation into (2.105) yields

$$\begin{aligned} \rho m \tfrac{\partial \mathbf{v}}{\partial t} + (\rho m \mathbf{v}.\nabla)\mathbf{v} \quad & = \mathbf{v} m G\left(\tfrac{\delta \Omega[\rho]}{\delta \rho}\right) \\ & + \nabla \cdot \boldsymbol{\Sigma} - \rho \nabla \left(\tfrac{\delta \Omega[\rho]}{\delta \rho}\right) + \mathbf{f}_{\text{wall}}. \end{aligned} \tag{2.107}$$

Since the applied velocity field is constant in time, $\partial \mathbf{v}/\partial t = \partial \mathbf{u}/\partial t$. We divide (2.107) by ρm

$$\begin{aligned} \frac{\partial \mathbf{u}}{\partial t} \equiv \frac{\partial \mathbf{v}}{\partial t} = \quad & -\mathbf{v}.\nabla(\mathbf{v}) + \mathbf{v}\frac{G}{\rho}\left(\frac{\delta\Omega[\rho]}{\delta\rho}\right) \\ & + \frac{1}{\rho m}\left\{\nabla\cdot\mathbf{\Sigma} - \rho\nabla\left(\frac{\delta\Omega[\rho]}{\delta\rho}\right) + \mathbf{f}_{\text{wall}}\right\}. \end{aligned} \tag{2.108}$$

When the local thermodynamic equilibrium is reached, $\delta\Omega[\rho]/\delta\rho(\mathbf{r})$ vanishes and the usual Navier-Stokes equation is recovered. This equation is solved in mixed direct and Fourier space scheme. For first order differential operators isotropic stencils from ref. [240] are used, i.e. the truncation error is quadratic in $\Delta\mathbf{r}$. Furthermore it has been found that solving the second derivatives numerically is more stable in the Fourier space. Periodic boundary conditions are applied at the edges of the simulation box for the density field $\rho(\mathbf{r})$ and the $\mathbf{u}(\mathbf{r})$ component of the velocity field.

Surface tension In this paragraph, the PF model and its implementation is analyzed with respect for the wetting properties of a flat substrate and the liquid-vapor surface tension. First, we follow a calculation of ref. [258] to obtain an analytic description for the liquid-vapor surface tension γ of a planar phase boundary, where the capillary force vanishes. It is also assumed, that the phase boundary does not move and both phases coexist at equilibrium. The normal pressure is therefore constant in the entire system and reads $P = -f'_{\text{bulk}}(\rho) + \mu\rho$ in either bulk phases. Minimizing $F[\rho]$ under the constraint of fixed number of particles yields

$$\frac{\partial f_{\text{bulk}}}{\partial \rho_{\text{eq}}} - W^2\Delta\rho_{\text{eq}} = \mu. \tag{2.109}$$

ρ_{eq} is the equilibrium profile normal to the interface, and let us orientate the normal to the z axis.

In this case the Laplacian reduces to $\Delta\rho_{\text{eq}} = d^2\rho_{\text{eq}}/dz^2 \equiv \rho''_{\text{eq}}$. Multiplying (2.109) with ρ'_{eq} and few manipulations leads to

$$\frac{\mathrm{d}}{\mathrm{d}z}\left\{f_{\text{bulk}}(\rho_{\text{eq}}) - \frac{W^2}{2}|\nabla\rho_{\text{eq}}|^2 - \mu\rho_{\text{eq}}\right\} = 0 \tag{2.110}$$

and thus

$$f_{\text{bulk}}(\rho_{\text{eq}}) - \frac{W^2}{2}|\nabla\rho_{\text{eq}}|^2 - \mu\rho_{\text{eq}} = -P, \tag{2.111}$$

where P is the bulk pressure. Using eq. (2.109), we can eliminate μ

$$P = \frac{\partial f_{\text{bulk}}}{\partial \rho_{\text{eq}}}\rho_{\text{eq}} - f_{\text{bulk}}(\rho_{\text{eq}}) - W^2\rho_{\text{eq}}\Delta\rho_{\text{eq}} + \frac{W^2}{2}|\nabla\rho_{\text{eq}}|^2 = P_{\text{n}} \tag{2.112}$$

	γ in $k_B T_c/\sigma^2$ units
Theoretical expectation	0.34203
$h = 0.5w$	0.34251
$h = 0.25w$	0.34202
$h = 0.125w$	0.34200

TABLE 2.1. *Comparison between the theoretical expectation of γ and the values obtained from the numerical minimization of the grand canonical potential. The numerical values are obtained for three different lattice spacing h. The difference between all these values is less than 0.2% (and even 0.01% if we exclude $h = 0.5w$). These results are for $T = 0.6\,T_c$ and $\sigma = 0.75w$*

.

This expression equals the normal pressure P_n, which we already found in (2.86). The surface tension is defined as the excess grand-potential at the interface

$$\gamma = \int_{-\infty}^{+\infty} \left(f(\rho_{eq}) + \frac{W^2}{2} |\nabla \rho_{eq}|^2 - \mu \rho_{eq} + P \right) \mathrm{d}z \tag{2.113}$$

for a planar interface. From 2.111 we obtain

$$f_{bulk}(\rho_{eq}) - \mu \rho_{eq} + P = \frac{W^2}{2} |\nabla \rho_{eq}|^2 \tag{2.114}$$

and thus

$$\gamma = \int_{-\infty}^{+\infty} W^2 |\nabla \rho_{eq}|^2 \mathrm{d}z. \tag{2.115}$$

Substituting $W|\nabla \rho_{eq}|$ with $\sqrt{2(f_{bulk}(\rho_{eq}) - \mu \rho_{eq} + P)}$ from (2.114) one gets

$$\gamma = \int_{-\infty}^{+\infty} W \sqrt{2(f_{bulk}(\rho_{eq}) - \mu \rho_{eq} + P)} \left| \frac{d\rho_{eq}}{dz} \right| dz, \tag{2.116}$$

where $\left|\frac{d\rho_{eq}}{dz}\right| dz$ can be replaced by $d\rho_{eq}$. The gradient is taken positive. Finally one ends up with

$$\gamma = W \int_{\rho_V}^{\rho_L} \sqrt{2(f_{bulk}(\rho) - \mu \rho + P)} d\rho, \tag{2.117}$$

where ρ_V is the vapor density and ρ_L the liquid one. This integral can be evaluated without knowing the precise shape of ρ_{eq}. The value computed from this expression can be compared to the value determined by a direct minimization of the functional,

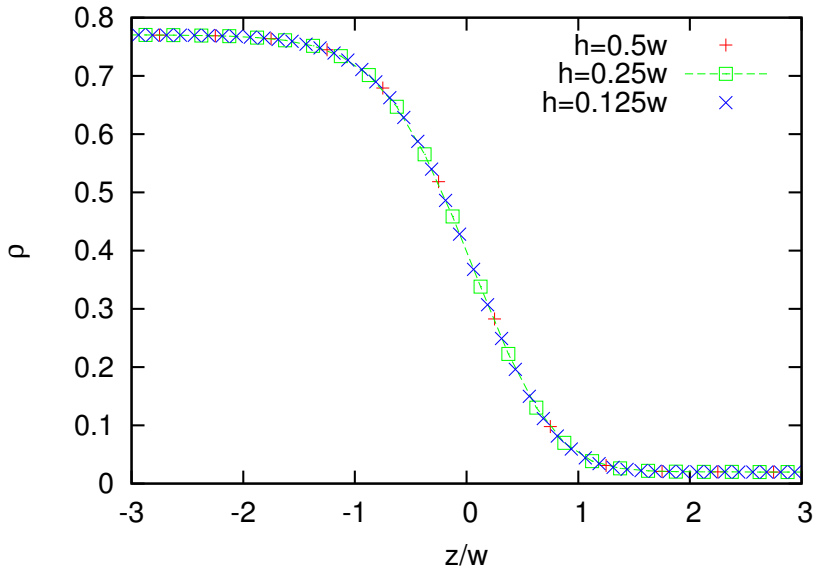


FIGURE 2.3. *Density profile for liquid vapor interface for different resolutions.* $T = 0.6T_c$.

using explicitly $\rho(\mathbf{r})$ and eq. (2.111). The latter numerical scheme is only very weakly grid resolution dependent. The differences between the theoretical value and the simulation result is less than 0.2% for a grid spacing $h = 0.5w$ and temperature $T = 0.6k_BT_c$ (see Tab. 2.1).

Next we want to establish a scheme for computing the fluid-solid surface tension for a flat surface at equilibrium. Thus the fluid is either in the liquid-like or the vapor-like state. As the surface tension is the excess of the grand canonical potential Ω due to the interface, we write

$$\Omega_V = -PV + \gamma_{\text{planar}}A \Longleftrightarrow \gamma_{\text{planar}} = \frac{\Omega_V + PV}{A}, \tag{2.118}$$

where γ_{planar} represents the solid-fluid surface tension. In concrete cases this is denoted either γ_{SL} or γ_{SV} for solid-liquid and solid-vapor phase boundaries resp. P is again the bulk pressure of the fluid phase and V the volume. In practice, a box (aligned with the interface and with volume V) is taken to determine γ_{planar} (see sketch fig. 2.4). Since the diffuse interface with the typical thickness w, the box height L_z must be sufficiently large to separate the bulk phases (solid and fluid). A is the surface area of the interface. In order to gain a more explicit equation for the numerical integration one can derive from (2.118) by extending L_z to infinity:

$$\gamma_{\text{planar}} = \int_{-\infty}^{\infty} \{P + \omega(\rho(z))\}\, \mathrm{d}z. \tag{2.119}$$

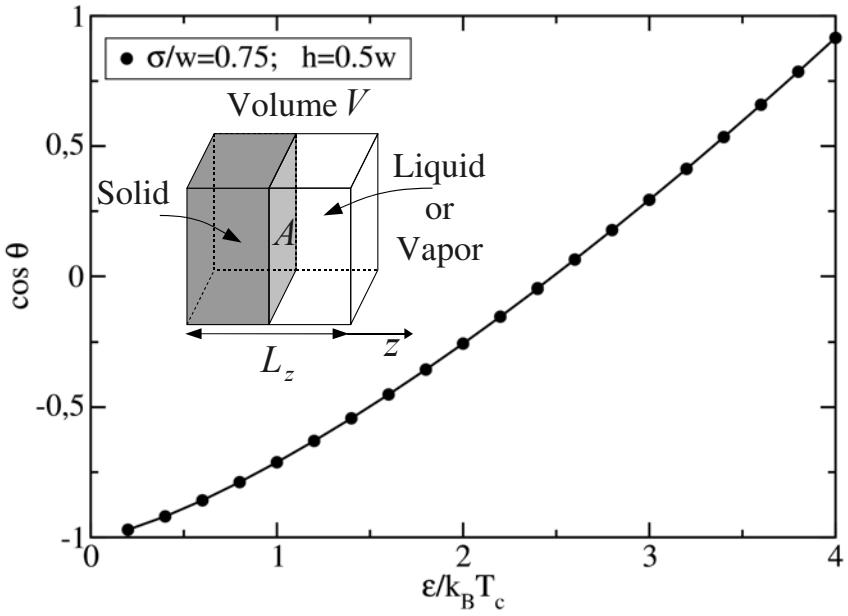


FIGURE 2.4. *Intrinsic contact angle* $\Gamma = \cos\theta$ *as a function of* ε

where

$$\begin{aligned}\omega(\rho(z)) &= \omega_{\text{local}}(\rho(z)) + \frac{W^2}{2}\left|\nabla\rho(z)\right|^2 \\ &= f_{\text{bulk}}(\rho(z)) + \frac{W^2}{2}\left|\nabla\rho(z)\right|^2 + \rho(z)V_{\text{wall}}(z) - \mu\rho(z) \qquad (2.120)\end{aligned}$$

is the grand-canonical potential density. Eq. (2.120) shows, that the surface tension γ_{planar} can be computed from the equilibrium profile $\rho(z)$ and the bulk pressure (measured far away from the wall). This is done by minimization of Ω (as explained above) for a box which is sufficiently large. Actually, box sizes much smaller than the drop size are sufficient. To model a macroscopic drop with radius $R \to \infty$ a thick film is simulated, and L_z is chosen around $20w$ or larger. The contact angle θ at the triple line is computed from the Young equation

$$\Gamma = \cos\theta = \frac{\gamma_{\text{SV}} - \gamma_{\text{SL}}}{\gamma}. \qquad (2.121)$$

Therefore γ, γ_{SV} and γ_{SL} are determined separately for the same substrate. Since γ only depends on w and does not depend on the external potential, this value can be precomputed. For computing the surface tension with eq. (2.118) correctly it is also needful to use the same scheme for the gradient term as in eq. (2.99). The contact

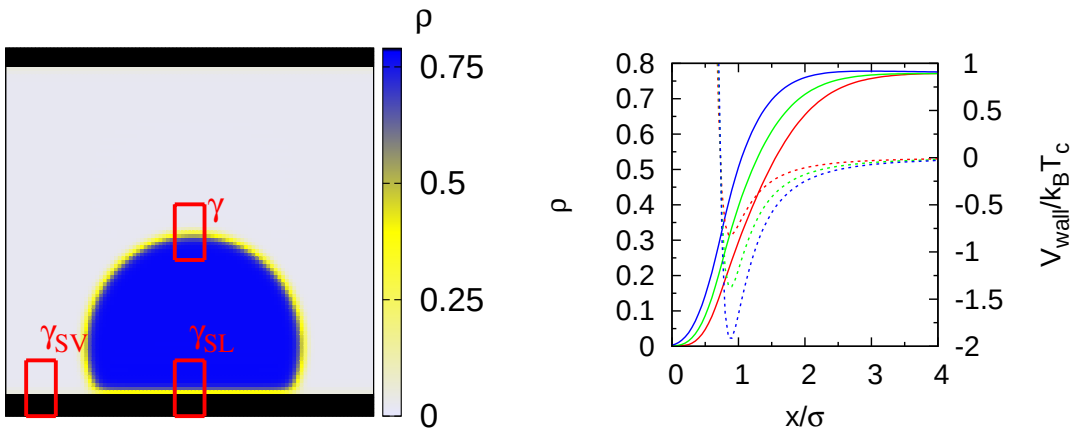


FIGURE 2.5. Left: *Density profile of a cylindrical drop. Using the Young equation is the most efficient way to compute the contact angles θ and θ_{eff}. The surface tensions are evaluated with eq. 2.121. The boxes are only schematic sketches, γ can be precomputed in the absence of a wall potential. The substrate ($V_{\text{wall}} > 0$) is drawn black.* Right: *fluid density ρ (solid lines) and wall potential V_{ext} of a planar wall (dashed lines) for three different* $\cos\theta \approx -0.5, 0.1, 0.7$ *(red, green, blue resp.)*

angle θ depends besides w also on σ and ε_{LJ} (and formally on V_0). In fig. 2.4 we show the dependence of $\Gamma = \cos\theta$ as a function of ε_{LJ} for fixed w and σ. Since the numerical scheme is in principle grid spacing h dependent, it has to be checked, that the combinations of w, σ, V_0 and h lead to robust contact angles (in fig. 2.4: $V_0 = 2k_{\text{B}}T_{\text{c}}$, $h = 0.5w$ and $\sigma = 0.75w$). This is discussed below. One have also to check, that the measured Young contact angle meets the observed contact angle. Indeed, both methods produce the same results, but the former has the merit of much smaller computational effort, since small boxes compared to the drop are sufficient (see fig. 2.5).

Adjusting parameters As discussed above, it is necessary to adjust several parameters in the model to obtain simply tunable contact angles with ε_{LJ}. There is also one parameter for the dynamical slip behavior, which have to be adjusted to recover correct intrinsic slip behavior. The latter adjustment is discussed in chapter 4.

Among the five parameters, which have an influence onto the contact angle θ, the potential cutoff V_0 is introduced only for numerical simplicity of the scheme, and should thus have no large impact to the wetting in a certain range of values. Indeed, low values of V_0 lead to unrealistic systems, where a significant amount of fluid en-

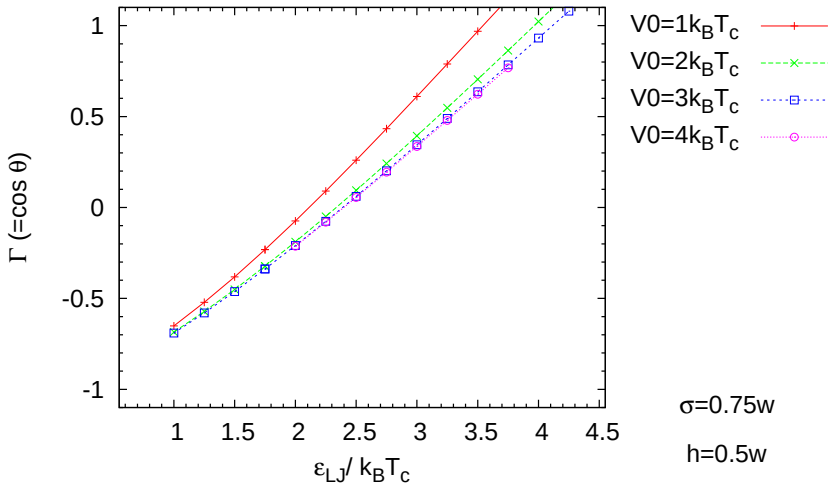


FIGURE 2.6. $\cos\theta$ *as a function of* $\varepsilon_{\mathrm{LJ}}$. *The potential cutoff is changed* V_0 *from* $1k_{\mathrm{B}}T_{\mathrm{c}}$ *to* $4k_{\mathrm{B}}T_{\mathrm{c}}$. $T = 0.6T_{\mathrm{c}}$.

ters the space, which is occupied by the wall. Very high values result in numerical instabilities, because of the nearly vanishing fluid densities at wall lattice sites. Thus, it is favorable to tune V_0 so that ρ inside the wall is some orders of magnitude lower than in vapor phase but large enough ($\approx 10^{-4}$) to prevent instabilities. In fig. 2.6 the $\cos\theta$ is shown as a function of $\varepsilon_{\mathrm{LJ}}$ for various V_0. This diagram shows nicely that the contact angles converges fast to a V_0 independent curve for high values of V_0. On the other hand, the computation time grows, since the time steps have to be shortened to prevent instabilities. As a compromise we fix V_0 to $2k_{\mathrm{B}}T_{\mathrm{c}}$.

The grid spacing has no noticeable influence onto the liquid-vapor interface in the absence of an external field (see fig.2.3). This was already indicated by the comparison of the surface tension with the analytic expression (2.117) (see Tab. 2.1). In contrary, in the vicinity of a wall, the resolution becomes more important. Figure 2.8 shows the density profile of a liquid phase on a solid substrate with $\varepsilon_{\mathrm{LJ}} = 4$ (strongly wetting) for three different resolutions. Deviations are clearly visible. A careful check of the physical quantities is therefore needed.

The discretization scheme enters at several levels in the simulations. The wall potential $V_{\mathrm{wall}}(\mathbf{r}) = \int_V \rho_{\mathrm{wall}}(\mathbf{r}')V_{\mathrm{LJ}}^{\#}(|\mathbf{r}-\mathbf{r}'|)\,d\mathbf{r}'$ is precomputed in Fourier space using the convolution theorem. fig. 2.7 shows the potential obtained with three different discretization and the theoretical prediction of the $9-3$ Lennard-Jones potential, which

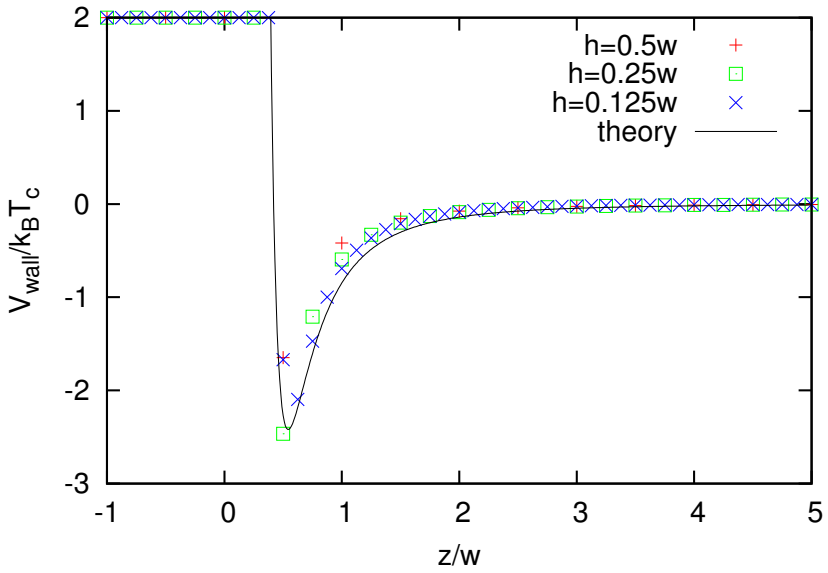


FIGURE 2.7. *Wall potential profile for liquid vapor interface for different resolutions.*

results from an integration of the $12-6$ LJ potential over one half space filled with solid. We clearly see deviations from the theoretical prediction. Unfortunately we can not make use of the theoretical prediction for corrugated surfaces. Thus, we consider the planar discrete potential as the real potential and compare it to corrugated wall potentials with the same discretization scheme. This method captures fairly well the nanometric features of rough surfaces consisting of single atoms as discussed later (see fig. 3.16 on page 72). Other discretization effects are part of the minimization scheme, and fig. 2.8 displays the results of the fluid density profile at a liquid-solid interface at small contact angle ($\varepsilon_{\mathrm{LJ}} = 4$). Again, discretization errors are visible. Since this errors makes it difficult to compare data for several resolutions, as a function of the remaining tuning parameter $\varepsilon_{\mathrm{LJ}}$ one should rather compare results for the same θ for different resolutions. To predict experiments more precisely with more realistic free energy functionals one needs more care about the discretization. At this level of wetting description a robust set of fixed parameters and one tuning parameter is sufficient.

Capillary condensation Since this model is made for nanoscopic devices, consisting of cavities in the nanometer range, it has to account for capillary condensation. Therefore, we check the model in a slit geometry against the macroscopic theory. Starting

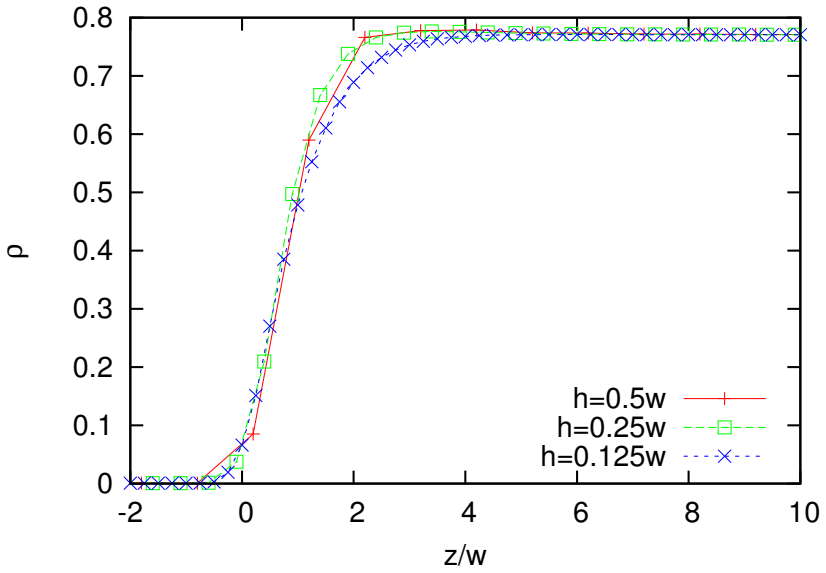


FIGURE 2.8. *Density profile of the liquid-solid interface for different resolutions.* $T = 0.6T_c$, $\sigma = 0.75w$, $V_0 = 2k_BT_c$ *and* ε_{LJ}.

form the Gibbs-Duhem relation

$$-S\mathrm{d}T - V\mathrm{d}P + N\mathrm{d}\mu = 0, \tag{2.122}$$

where S is the entropy and N the number of molecules in the system, it follows for constant T ($\rho = N/V$)

$$\left.\frac{\partial\mu}{\partial P}\right|_T = \frac{1}{\rho}. \tag{2.123}$$

Integrating from the saturated quantities to the quantities in the vapor and the liquid phase we obtain

$$\mu_L - \mu_{sat} = \frac{1}{\rho_L}\left(P_L - P_{sat}\right) \tag{2.124}$$

and

$$\mu_V - \mu_{sat} = k_BT \ln\frac{P_V}{P_{sat}}. \tag{2.125}$$

To get the first equation we assumed that the liquid is incompressible, for the second we used the ideal gas equation of state. Since the triple line contact angle has to fulfill the Young equation, the Laplace pressure ($P_{Laplace} = 2\gamma\mathcal{H}$, $\mathcal{H}$ is the mean curvature) in a slit with thickness D, reads

$$P_V - P_L = \frac{2\gamma\cos\theta}{D}. \tag{2.126}$$

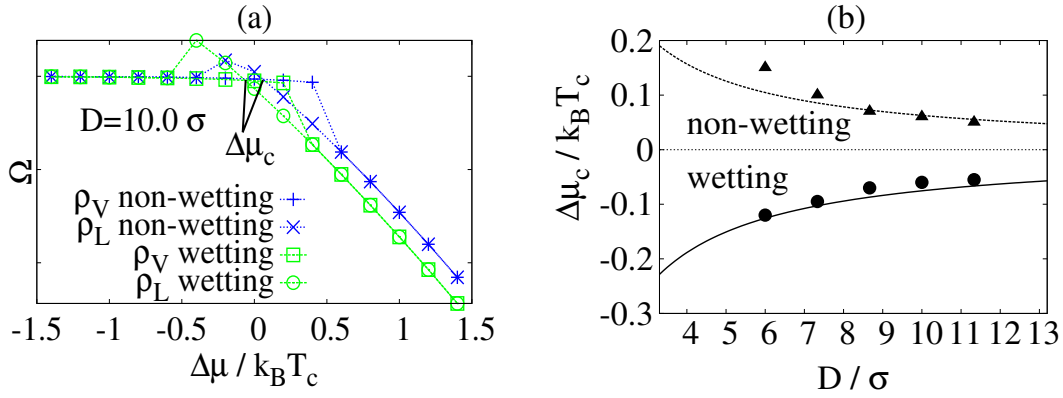


FIGURE 2.9. (a)*Grand canonical potential* Ω *over* $\Delta\mu \equiv \mu - \mu_{sat}$ *for two values of the intrinsic contact angle:* $\cos\theta = -0.5$*, the non-wetting case, and* $\cos\theta = 0.6$ *the wetting situation. For each case, the horizontal branch corresponds to a vapor-phase and the falling branch to a liquid-phase inside the slit. The crossover of the two branches determines the capillary condensation point* $\Delta\mu_c$*. For an intermediate range of* $\Delta\mu$ *there are strong metastabilities observed.*
(b) $\Delta\mu_c$ *over the thickness* D *of the slit. The positive values correspond to* $\cos\theta = -0.5$ *and the negative ones to* $\cos\theta = 0.6$*. for each case, the solid lines are the theoretical expression* $\Delta\mu_c = -2\gamma_{LV}\cos\theta/\rho_L D$ *while the points correspond to the simulations.*

We use the approximation $P_\mathrm{L} \gg P_\mathrm{V} \gtrsim P_\mathrm{sat}$

$$P_\mathrm{V} - P_\mathrm{L} \approx P_\mathrm{sat} - P_\mathrm{L} = -\rho_L \Delta\mu = \frac{2\gamma_\mathrm{LV}\cos\theta}{D} \tag{2.127}$$

$$D_\mathrm{crit} = -\frac{2\gamma_\mathrm{LV}\cos\theta}{\rho_\mathrm{L}\Delta\mu}. \tag{2.128}$$

$\mu_\mathrm{V}(P_\mathrm{V}) = \mu_\mathrm{L}(P_\mathrm{L}) = \mu = \mu_\mathrm{sat} + \Delta\mu$ is defined as the offset from the chemical potential to the saturation $\mu_\mathrm{sat} = \left(\frac{\partial F_\mathrm{bulk}(\rho)}{\partial\rho}\right)_T\Big|_{\rho=\rho_\mathrm{V}}$ [60, 138]. Capillary condensation occurs when D becomes smaller than a critical distance D_crit which depends on the wetting angle θ of the confining surfaces [60].

With non-conserved Allen-Cahn dynamics the PF model can be used to study this transition. The left panel of fig. 2.9 shows the grand canonical potential of a fluid in a slit. The green lines correspond to a wetting state ($\cos\theta = 0.6$) whereas the blue lines correspond to a non-wetting situation ($\cos\theta = -0.5$). The points are simulation results with either a vapor-phase as initial state or a liquid phase for various $\Delta\mu$. The branches

on the right belong to a liquid equilibrium state whilst the branches on the left to a vapor one. In between these two regimes one could probe metastable states (points above the two branches). The cross-over between the regime where the liquid phase is favored and the regime where the vapor-phase is favored is interpolated by the crossing point $(D, \Delta\mu_c)$ of the connecting lines. The right panel shows $\Delta\mu_c$ for several slit-widths D. For large D there is a good agreement with the theoretical curves where as for very small $D < 6\sigma$ the macroscopic theory assuming sharp interfaces become insufficient. However it is remarkable that the macroscopic theory compares so well to the simulations for values of D as small as 8σ, i.e. 8 particle diameters.

2.4.5. Comparison with lattice Boltzmann

In this paragraph we shall briefly discuss the lattice Boltzmann (LB) methods, which play an important role in fluid dynamics—in particular in microfluidics—as a very versatile and computationally efficient method. We omit recalling the details but rather discuss same basic features. As LB is founded on kinetic theory it is different from other approaches like continuum hydrodynamics simulations. First, the dynamics are solved step wise, i.e. a streaming process is succeeded by collision process at each time step. Second, the streaming process, which corresponds to the convection is linear in phase space, and not quadratic as in the Navier-Stokes equation. Nevertheless, the combination with the collision step allows for non-linear advection through multi-scale expansions. Third, the velocity space is discrete, i.e. only some velocities in some directions are possible. This allows for simplified transformations of the phase space distribution. Last but not least, in contrast to simple incompressible Navier-Stokes descriptions, the pressure is modeled with an equation of state [63, 30, 62, 325]. Multiphase methods invented, e.g. by Shan and Chen [280] or by Swift and Yeomans [291, 49, 50], are used to study contact angles hysteresis [168], capillary imbition to pores [166, 218], drop collapse [164], small drop wetting [114], macroscopic wetting [265], and apparent slip [29]. Despite that the LB method is one of the most common simulation methods in microfluidics, with a lot of adaptions for special problem available, it has up to now some drawbacks that render it less useful for certain systems. First, in many studies the density contrast between the gas and the liquid is rather limited [164, 167], second the solid-fluid contact is typically modeled as an effective contact potential without finite range into the fluid phase. This particular point limits LB to macro- and mesoscopic problems. The microscopic details of the wall potentials are not covered. A priori a no-slip boundary condition (BC) at the walls is used, i.e. the tangential speed $\mathbf{v}_\perp$ at the wall is zero. In microfluidics a partial slip can be

important. However, partial slip $\mathbf{v}_\perp \neq 0$ can be implemented, but only in a limited range [124, 162]. Thus, LB is somehow limited to macroscopic systems down to scales of microns. On the other hand, large system sizes and long simulation time-scales are accessible.

2.4.6. Comparison with molecular dynamics

Going to very small length scales, molecular simulations provide a versatile toolbox to study bulk properties and non-uniform problems in nanofluidics at scales of ten or less nanometers and time scales of hundreds of picoseconds. The aim of MD simulations is to solve numerically Newton's equation for classical particles allows for either equilibrium investigations or studies of non-equilibrium problems, e.g. driven steady state flows [107, 251]. To ensure isothermal conditions a variety of thermostatting methods are available [107]. As in the other presented methods in this chapter, MD deals with classical systems neglecting quantum mechanical details. MD is also useful to study complex fluids and complex systems, with polymers or steric molecules. So-called Boltzmann iteration methods allows for grouping monomers to accelerate calculation with coarse graining [222]. MD is therefore used in plenty of studies to investigate water flows or hydrocarbons with complex hydrogen bondings [76, 180]. Intrinsic wetting [136] and apparent wetting [188, 189, 190, 180, 321] is studied with MD as well as intrinsic [130] and apparent slip [73, 74, 148, 322]. While MD takes into account all the molecular details a major drawback of MD simulations is the small size limits of the simulations box, due to nowadays computer power limits. Therefore, in lots of MD studies droplets are at the same scale as roughness length scales and applied flows are at similar velocities as the thermal velocities.

2.4.7. Discussion (limits, interfaces, wall-interaction)

The PF model bridges a gap between the microscopic MD simulations and the macroscopic LB simulations, in a sense, that the substrate is modeled with the essential features of molecular theory and the fluid allows for phase transitions, diffuse interfaces and explicit relaxation processes. Modeling the free energy as a functional of ρ gives direct access to the free energy or grand canonical potential landscape and easy access to thermodynamic quantities like surface tensions. Therefore, we can easily probe macroscopic drops, modeled as an infinite thick film and make use of the Young equation to get contact angles.

Although we do not model the molecular details of the fluid, which would cause e.g. layering effects of oscillating density at the wall, this details could be in principle added. For the sake of simplicity we use the mean field square gradient model. Instead of applying a thermostat in the density transport equation, one could also use a thermostatting term in the momentum transport equation, which is usually applied as fluctuating stress tensor. This was tested also, but it is less stable in combination with the wall boundary condition. Furthermore the analysis of slip and wetting angles is much easier, when deterministic thermalization is used. Dropping the thermostat term and adding temperature and energy flux equations, this model can be also enhanced to study heat transfer mechanisms, but this is out of the scope of this work.

While the PF model is formulated as a fully 3 dimensional model, with available computer power parallel codes are needed to solve 3 dimensional systems. Throughout this work, we assume a translation invariant system in one spatial direction, so that it is sufficient to solve an effective 2D problem. We shall use a serial solver for this model to study nanowetting in chapter 3, dynamics in nanochannels in chapter 4 and the morphology of spinodal decomposition in section 5.3.

3. Nanowetting and omniphobicity

Designing omniphobic (or superhygrophobic) surfaces is a true challenge since usual surfaces have affinities either for polar liquids like water or for non-polar liquids like oils. Building a surface that repels all liquids requires therefore a careful adjustment of its physico-chemical properties [300]. Among the possible ingredients which can be used to control the wetting properties of surfaces is the geometry. This strategy has already been used to amplify wetting and to design superhydrophobic surfaces [245, 290] thanks to the Wenzel-Cassie-Baxter wetting/dewetting transition that occurs when the roughness becomes large [58, 311]. In such a case, the surface energy becomes very large due to the large contact area between the liquid and the substrate, and the system prefers to expel the liquid from the surface. The liquid then floats on the tips of the roughness, and this Cassie-Baxter state is often referred to as a "fakir" state [245]. Natural superhydrophobic surfaces like lotus leaves are indeed working in this way, and synthetic substrates made of pillars or ridges are widely used in microfluidics thanks to the lubricating effect produced by the gas layer trapped between the surface and the liquid [40, 237, 67, 148, 322]. However, the Cassie-Baxter-Wenzel framework does not allow for a wettability inversion. Roughness only amplifies the natural wetting properties of a surface in this model. Beyond this classic theory Herminghaus explored the possibility of self-affine surfaces to become hydrophobic, whatever their natural wetting properties are [125, 126], taking advantage of the metastable states. Combining roughness at various scale with surface chemistry and/or playing with electric fields allowed experimental advances in the control of repellency by many authors [300, 3, 56, 327]. Recently, the possibility of wettability inversion based on geometry has been discussed by Tuteja et al. [300] and by Marmur [198] who showed that multivalued surfaces (re-entrant surfaces) are good candidates for omniphobicity. These surfaces can indeed trap the gas phase inside the re-entrant cavities, by pinning the triple contact line at the overhangs. The Cassie-Baxter states can thus become metastable in a large region of the wetting diagram, in particular in the wetting region ($\theta < 90°$), which is a possible mechanism for wetting inversion [147].

More intriguing are recent experimental observations that surfaces made by ion etching techniques are able to produce wetting inversion, but their structure is not pre-

senting multivalued cavities, as far as AFM measurements could show [250]. These etched surfaces have fractal character. Berim et al. [31] also pointed out in a DFT study that for nanowetting the Wenzel theory need not to be hold. Daub et al. [76] and recently Leroy et al. [180] report similar results from MD simulations. Each of these simulations deal with regular corrugations of the solid interface. It is the purpose of this chapter to investigate the possibility of wetting inversion for monovalued surfaces. In particular we have two experimental setups in mind which may described by PF simulations: substrates made of tips, like carbon nanotube coated surfaces, or substrates made of ridges, like the one obtained by ion-etching techniques. By playing with various geometrical parameters (thickness, width, depth, disorder, ...) we investigate the wetting diagram of these surfaces and we discuss the contribution of geometry to the metastability of the Cassie-Baxter states and to the Wenzel wetting inversion. Rather than studying wetting on fractal surfaces, we shall focus on the smallest physical length scales in the hierachy of length scales on real fractal surfaces.

3.1. Classical wetting theory

3.1.1. Wenzel theory

The classical wetting theory of Wenzel [311] and Cassie-Baxter [58] describes macroscopic wetting situations, where a large drop is spread over a corrugated surface. The term macroscopic here specifies the lengthscale L of the roughness, i.e. microns and larger. Also it is assumed that the drop radius R_d is much larger than the roughness lengthscale L [198, 200, 203]. Further, it is assumed that line tensions are negligible. The roughness factor r describes the ratio of the actual wetted surface A_0 by the projected surface A_p in the homogeneous wetting regime. Under the assumption, that r is homogeneous everywhere on the substrate, the Wenzel law can be derived from the Young-Dupré equation for a flat surface $\gamma\cos\theta = \gamma_\mathrm{SV} - \gamma_\mathrm{SL}$, where θ is the contact angle on a flat and homogeneous substrate, γ the liquid-vapor surface tension and γ_SV and γ_SL are the solid-vapor solid-liquid surface tensions resp. The right-hand term describes the energy needed to remove the solid-vapor interface and to build up solid-liquid interface per unit area of the flat surface. For a rough wall the energy is amplified by $r > 1$, since the total wetted surface area A_0 is larger than the projected surface area A_p [311, 200, 245] and classical Wenzel wetting angle is given by $\cos\theta^\mathrm{W}_\mathrm{eff} = r\cos\theta$ (see left panel in fig. 3.1).

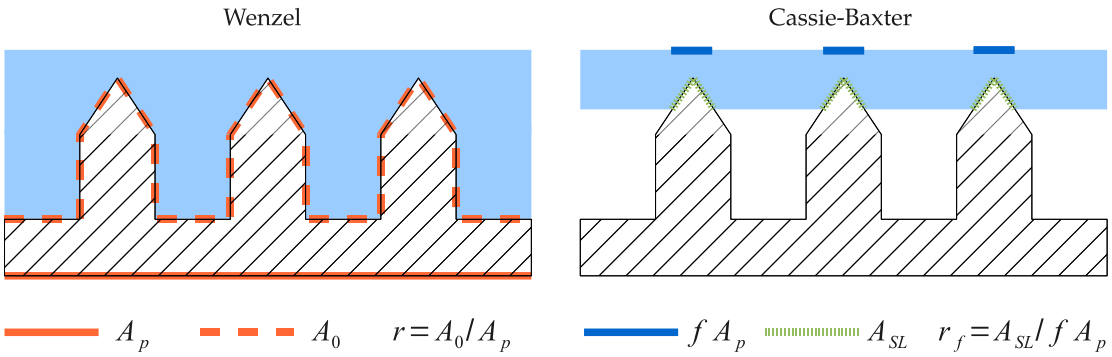


FIGURE 3.1. *Corrugated substrate geometry: A_0 is the total substrate surface area, A_p its projection, f is the fraction of the projected area, which is wetted, the total roughness factor $r = A_0/A_p$ and the wetted roughness factor r_f describes the roughness of the wetted part only.*

3.1.2. Cassie-Baxter theory

On some rough substrates there exist also heterogeneous Cassie-Baxter wetting states ("fakir"-states). In this regime the parameter f denotes the fraction of the projected area A_p which is wetted. In terms of the total wetted area A_{SL} the roughness of the wetted surface fraction is $r_f = A_{SL}/(fA_p)$. From Laplace's equation it follows that the meniscus radius inside the roughness valleys is the same as the drop radius R_d (assuming that the vapor pressure in the air pockets equals the ambient pressure). Since R_d is much larger than L the liquid-vapor interface can be estimated by a flat surface patch. Thus $1-f$ is the fraction of the projected area A_p which is non-wetted and thus $c_{1-f}(1-f)$ is the total area of the liquid-vapor interface below the drop. The prefactor c_{1-f} takes an inclined liquid-vapor surface into account. Thus the energy needed to build up a heterogeneous wetting state spreading a drop on the surface is $r_f f\gamma\cos\theta - c_{1-f}(1-f)\gamma$ [200]. For simple regular pillars there is only one heterogeneous state possible with $r_f = 1 = c_{1-f}$ and we get the well-known Cassie-Baxter equation $\cos\theta_{\text{eff}}^{\text{CB}} = (\cos\theta + 1)f - 1$. We shall denote the effective (apparent) wetting angle θ_{eff} $\theta_{\text{eff}}^{\text{W}}$ for homogeneous resp. $\theta_{\text{eff}}^{\text{CB}}$ for heterogeneous wetting states, when distinction is necessary. The right panel of fig. 3.4 shows a schematic wetting diagram of a monovalued substrate.

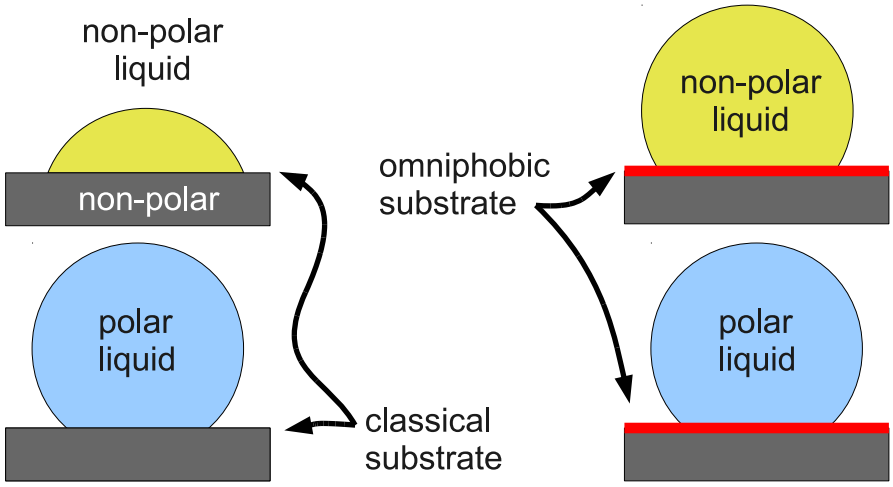


FIGURE 3.2. *Illustration of omniphobicity. A flat and chemically homogeneous surface of e.g. a non-polar substrate material exhibits intrinsic contact angles (CA) θ less than 90° for non-polar liquids and CA greater than 90°. An omniphobic substrate is supposed to exhibit repellent behavior for both types of liquids, described by the effective/apparent contact angle.*

3.1.3. Multivalued surfaces and omniphobicity

Figure 3.2 illustrates the generic properties of an omniphobic substrate. A homogeneous substrate made of, for example, a non-polar material has a contact angle (CA) less than 90° for a non-polar liquid, and larger than 90° for polar liquids (left states). Apparent contact angles of a heterogeneous substrates typically enhance the intrinsic wetting behavior, but do not show a wetting inversion, i.e. different signs of the $\cos\theta$ and $\cos\theta_{\text{eff}}$. However, certain surface treatments may render the surface omniphobic, i.e. the apparent contact angles are larger than 90° for both types of liquids (right states).

In the Wenzel- and Cassie-Baxter theory, it was presumed that the corrugation of the substrate is monovalued, i.e. points on the projected area A_{p} correspond to an unique point of the rough interface, or to a vertical wall. Multivalued surfaces exhibits overhangs as it is illustrated in fig. 3.3. At the sharp corners of an overhang pinning can appear. Inclined side walls with an overhang angle $\beta < \pi/2$ the flat liquid-vapor interface has to be enlarged during the intrusion. E.g. for a symmetric multivalued groove with angle β the energy to wet a surface patch dl at the side wall of a ridge is $(\gamma_{\text{SV}} - \gamma_{\text{SL}})\text{d}l$ while the energy to increase the liquid-vapor interface is $\gamma\cos\beta\text{d}l$.

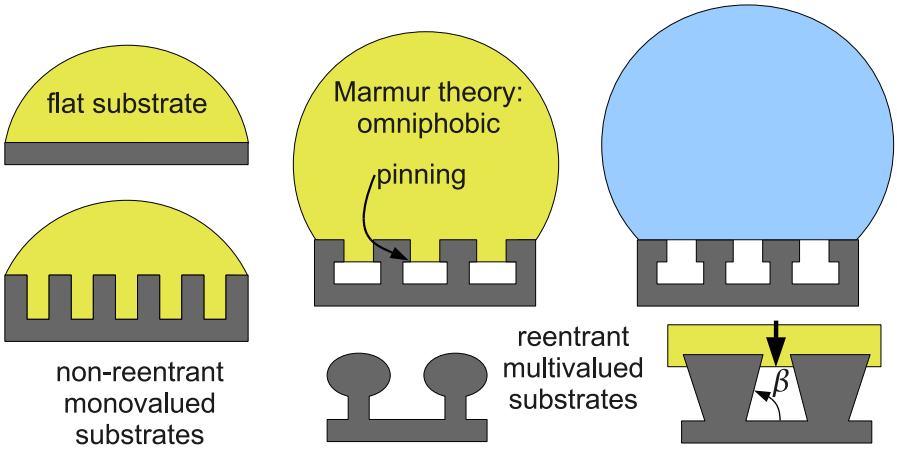


FIGURE 3.3. *Examples of mono- and multivalued substrate geometries. Metastability is exploited to gain omniphobicity with multivalued geometries.*

Thus intrusion is hampered when $\cos\beta < \cos\theta$. We call this states fakir-states, too. Comparing the energies of fakir states and the homogeneous wetting state shows that fakir-states are metastable when $\cos\theta > 0$ for all substrate-shapes, as we shall demonstrate below. Figure 3.4 (right panel) is a schematic wetting diagram of a multivalued substrate. The metastable CB branch is prolonged to positive $\cos\theta$. Since intrusion is blocked, the breakdown of the fakir state is driven by a nucleation process [147] at some small CA $\theta = \theta_m \ll \pi/2$.

3.1.4. Metastability of the Cassie-Baxter state and superhydrophobicity

The classical wetting theories mentioned above, were extended by Marmur [200, 198] to answer the question whether a heterogeneous wetting state is possible or not. Starting from the Gibbs energy of a drop (in analogy to the derivation of the Young equation)

$$G = \gamma A_{LV} + \gamma_{SL} A_{SL} + \gamma_{SV} A_{SV}, \tag{3.1}$$

where the surface areas A_{LV}, A_{SL}, A_{SV} depend on the Young angle θ and the wetted fraction f (see the left panel fig. 3.5). The latter is a representation of the intrusion depth. As before, the roughness factor r_f is a function of f. The wetting state is

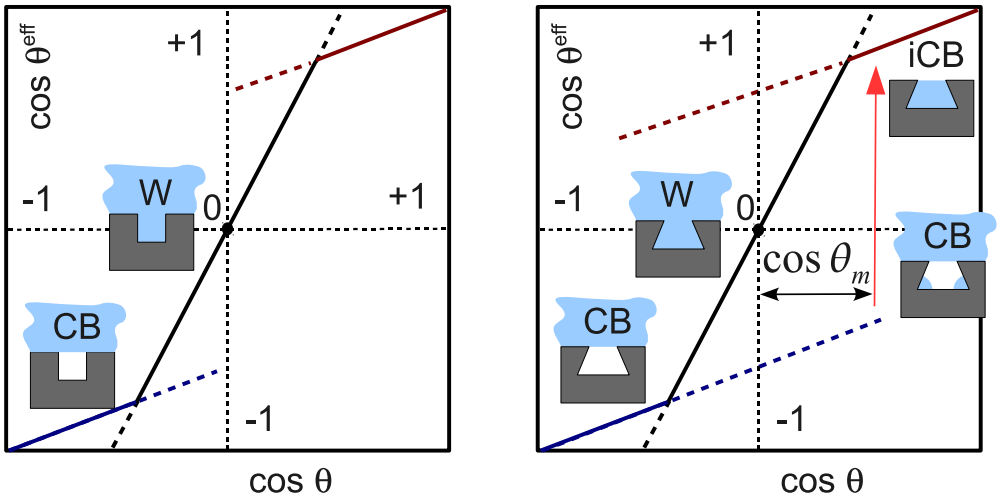


FIGURE 3.4. Left: *The diagram shows a prototype of a wetting diagram for corrugated substrates (non omniphobic/monovalued), which connects the effective contact angles to the intrinsic one. The solid line in the center of the diagram is described by the Wenzel (W) law* $\cos\theta_{\text{eff}} = r\cos\theta$ *for homogeneous wetting states. On the left bottom quarter the solid line (blue) obeys the Cassie-Baxter (CB) law* $\cos\theta_{\text{eff}} = r_f f\cos\theta + f - 1$*, which describes the heterogeneous wetting situations. In the top right quarter, the red solid line corresponds to an inverse Cassie-Baxter state. Dotted lines describe metastable wetting states.* Right: *Schematic wetting diagram of multivalued substrate (cf. Figure 3.2). Nucleation in the grooves spawn a breakdown of the fakir state at some wetting angle* θ_{m}*. In the inverse Cassie-Baxter regime (iCB) crenels are filled liquid, independently whether a drop is spread above or not.*

therefore a function of f and θ_{eff}

$$\begin{aligned} A_{\text{LV}} &= 2\pi R^2(1-\cos\theta_{\text{eff}}) + (1-f)\pi R^2\sin^2\theta_{\text{eff}} \\ A_{\text{SL}} &= \pi R^2 r_f f \sin^2\theta_{\text{eff}} \\ A_{\text{SV}} &= -2\pi R^2\sin^2\theta_{\text{eff}} + r_{1-f}(1-f)\pi R^2\sin^2\theta_{\text{eff}} + \text{const.} \end{aligned} \tag{3.2}$$

Plugging this into (3.1) one obtains a minimization problem in the two variables f and θ, where the case $f = 1$ corresponds to the homogeneous wetting regime. The heterogeneous CB-states are local minima or a border minimum at $\theta_{\text{eff}} = \pi$. Marmur proofed that the existence of such a local minimum if $\frac{\mathrm{d}^2 r_f f}{\mathrm{d}f^2} > 0$, $\theta_{\text{eff}} < \pi$ and the Cassie-Baxter equation can be fulfilled [200]. In the case $\frac{\mathrm{d}^2 r_f f}{\mathrm{d}f^2} < 0$ no CB-states exists

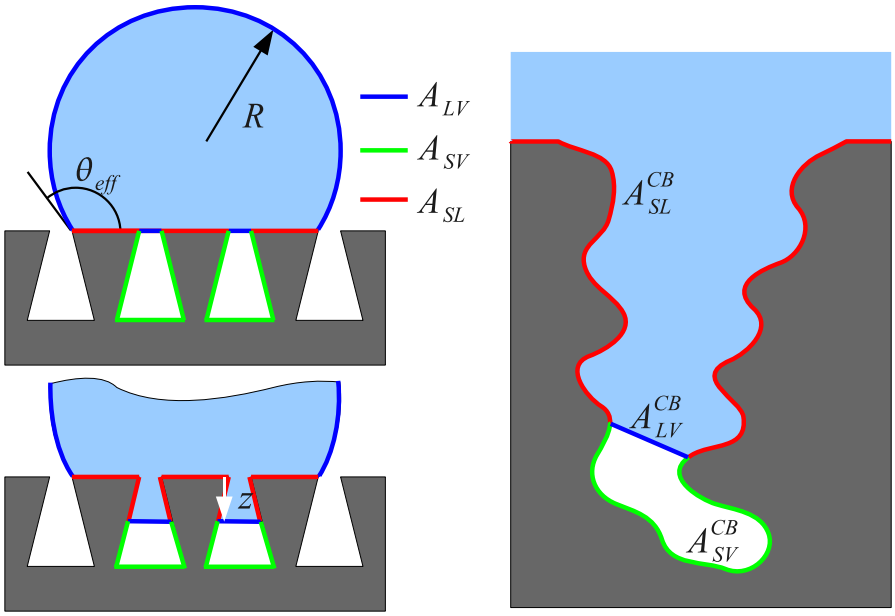


FIGURE 3.5. Left: *Schematic sketch of the geometry in the heterogeneous wetting regime. Note that in the Cassie-Baxter theory the drop is assumed to be much larger than the length-sclaes of the roughness.* Right: *Heterogeneous wetting situation in an arbitrary rough substrate.* $A_{\mathrm{SL}}^{\mathrm{CB}} + A_{\mathrm{SV}}^{\mathrm{CB}} = A_0$

for $\theta_{\mathrm{eff}} < \pi$. Finally the often discussed case $\frac{\mathrm{d}^2 r_f f}{\mathrm{d}f^2} = 0$ (e.g. crenels) is particular. Thus the quantity $r_f f$ plays an important role, whether superhydrophobic CB-states are supported or not.

In a 2008 paper Marmur extended this theory to multivalued surfaces [198]. Marmur derived the necessary condition for the existence of heterogeneous states at hydrophilic Young angle θ as

$$\frac{\mathrm{d}^2 f}{\mathrm{d}z^2} - \cos\theta \frac{\mathrm{d}^2 (r_f f)}{\mathrm{d}z^2} > 0, \tag{3.3}$$

where z is the intrusion depth of the meniscus, f is again the fraction of the wetted projected area and $(r_f f)$ is the totally wetted area. In this study, for some examples it was found that the Wenzel state is favored for hydrophilic intrinsic contact angles, while the heterogeneous state is metastable.

Indeed, one can demonstrate, that in the classical wetting theory the homogeneous W state is stable with respect to the heterogeneous CB state— whatever the geometry is—when $\cos\theta$ is positive (under the assumptions of section 3.1.1). To check whether

the homogeneous wetting state is stable, one have to compare the Gibbs energies $G = A_{SL}\gamma_{SL} + A_{SV}\gamma_{SV} + A_{LV}\gamma$ of all possible states. For the homogeneous wetting state (only solid-liquid interface) the Gibbs energy is simply:

$$G^W = A_{SL}^W \gamma_{SL} = A_0 \gamma_{SL}. \tag{3.4}$$

The heterogeneous wetting state (fakir-states only) Gibbs energy writes

$$G^{CB} = A_{SL}^{CB}\gamma_{SL} + A_{SV}^{CB}\gamma_{SV} + A_{LV}^{CB}\gamma. \tag{3.5}$$

Using the Young equation $\cos\theta = (\gamma_{SV} - \gamma_{SL})/\gamma$ and the geometrical identity $A_{SL}^{CB} + A_{SV}^{CB} = A_0$ (see fig. 3.5), we get an equation to compare the unique homogeneous state with all possible heterogeneous states:

$$g := \frac{G^W - G^{CB}}{\gamma} = A_0\frac{\gamma_{SL}}{\gamma} - A_{SL}^{CB}\frac{\gamma_{SL}}{\gamma} - A_{SV}^{CB}\frac{\gamma_{SV}}{\gamma} - A_{LV}^{CB} \tag{3.6}$$

Minimizing the Gibbs energy in the thermal equilibrium state tells, that the homogeneous state is stable, if $g < 0$:

$$g = A_{SV}^{CB}\frac{\gamma_{SL}}{\gamma} - A_{SV}^{CB}\frac{\gamma_{SV}}{\gamma} - A_{LV}^{CB} \tag{3.7}$$

$$g = A_{SV}^{CB}(-\cos\theta) - A_{LV}^{CB} \tag{3.8}$$

$$0 > -\frac{A_{SV}^{CB}}{A_{LV}^{CB}}\cos\theta - 1 \tag{3.9}$$

A stable W state has to be favored over all heterogeneous states, therefore we define

$$\tau_{max} := \max(A_{SV}^{CB}/A_{LV}^{CB}) > 1, \tag{3.10}$$

maximized over all heterogeneous states. In the intrinsically partially non-wetting states ($\cos\theta < 0$) it follows that $1 > -\frac{A_{SV}^{CB}}{A_{LV}^{CB}}\cos\theta$ and finally we get that the homogeneous wetting state is the stable state, if τ_{max} is small, so that

$$1 > -\tau_{max}\cos\theta \tag{3.11}$$

is obeyed. If $\cos\theta > 0$ then the inequality (3.11) is always fulfilled, i.e. the homogeneous state is stable.

Fractal surfaces Herminghaus [125] proposed fractal surfaces to gain omniphobic behavior. Supposing, that at very small length-scales the substrate consists of grooves or holes (protrusions would be also possible), so that a Cassie-Baxter state can be formed (see left panel of fig. 3.6). As discussed above, overhangs are needed in the case $\theta < \pi/2$. We shall discuss wetting on self-affine structures, i.e. similar grooves appear at different length-scales. Two of this iterations are sketched in fig. 3.6. Herminghaus assumed for the first member of the hierarchy roughly molecular dimensions so that one can span several orders of magnitude up to the capillary length [125].

The Young contact angle is denoted $\theta_0 = \theta$ as the first member in a hierarchy of apparent contact angles. The CB equation for a flat substrate with different Young angles θ_i, due to the chemical nature of the substrate reads

$$\cos\theta_{\text{eff}}^{\text{CB}} = \sum_i f_i \cos\theta_i, \tag{3.12}$$

where $\sum_i f_i = 1$ and i runs over all substrate patch types with different chemical properties. The geometrical CB equation is obtained in the case, where
$i \in \{\text{liquid} - \text{air}, \text{solid} - \text{liquid}\}$ and the wetting angles $\theta_i \in \{\pi, \theta\}$. The CB-equation of the grooves at the smallest length scales is

$$\cos\theta_1 = f_0 \cos\theta_0 + (1 - f_0), \tag{3.13}$$

where f_0 denotes the wetted fraction of the surface. At the next level, it is argued, that the wetting angle of the drop at the coarse-grained fraction of the wetted area f_1 exhibits θ_1 as "intrinsic" contact angle, and so on. On each level, the apparent contact angle is therefore

$$\cos\theta_{n+1} = f_n \cos\theta_n + (1 - f_n). \tag{3.14}$$

This sequence is monotonic, when $0 \leq f_n \leq 1$ and converges (since $0 \leq \cos\theta_n \leq 1$) to $\cos\theta_\infty = -1$. Herminghaus showed also that for sufficiently large $\cos\theta_n$, the sequence converges exponentially fast [125]. On the other hand, if $\theta < \pi/2$ one can construct a recursion relation for the inverse Cassie-Baxter states. This results to a perfect wetting limit $\cos\theta_n \to 1$. This is consistent to experiments, where liquid is pressed into the grooves of superhydrophobic leaves. The soaked leaves showed a wetting angle close to 1 [125]. Fractal surfaces and wetting is a long-standing topic with theoretical contributions [68], simulation studies [321] and experiments [250].

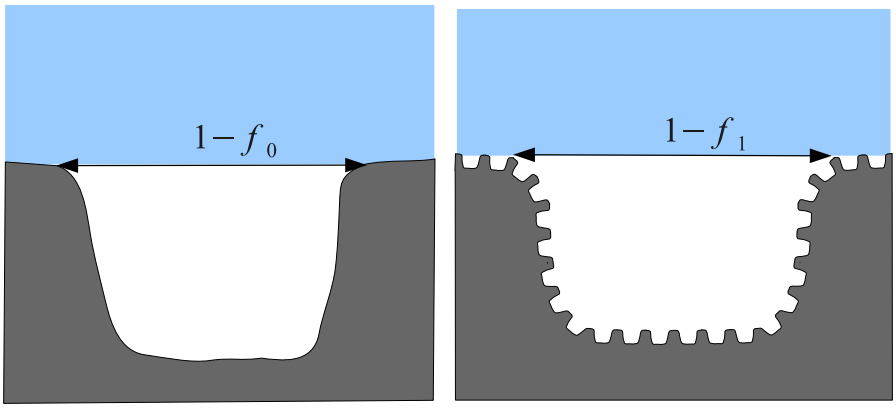


FIGURE 3.6. *Self-affine substrate: Similar corrugation appears at several length-scales, from molecular lengths to capillary length.*

3.2. Experimental findings

In this section the experimental findings are briefly reviewed, starting with studies of superhydrophobic behavior and the famous Lotus effect to more recent studies of omniphobic substrates, either multivalued or monovalued.

3.2.1. Superhydrophobicity

First the Lotus effect i.e. superhydrophobic behavior was found in nature in 1977 and studied by biologists [25, 26, 226]. For around two decades it is mimicked on artificial substrates [38, 245]. While superhydrophobicity is connected to large contact angles and small contact angle hysteresis, in this paragraph only the large contact angles are considered, because these effects are captured by the Wenzel and Cassie-Baxter equations, while no consistent theory for the contact angle hysteresis exists [201] (see chapter 4). Lafuma and Quéré confirmed the low adhesion in the CB state [171] reflecting the typical low contact angle hysteresis.

There is a discussion in several papers, arguing that Wenzel- and Cassie-Baxter-laws fail to predict experimental findings [109, 108, 93], while Marmur [201] and McHale [203] resolved this misinterpretation of experiments. The experiments were made with drops of sizes comparable to the lengths of the corrugations or chemical heterogeneities. The classical wetting laws therefore are not applicable to these problems. On the other side Oener measured the maximal length scale of $32\mu m$ for superhydropho-

bicity [236]. In a nice paper of Barbieri et al. [21] the authors investigate systematically the CB and W coexistence and transition on microstructured superhydrophobic substrates. We are not aware of earlier studies confirming both laws as accurately.

3.2.2. Multivalued omniphobicity

Feng et al. [96] found for the first time omniphobic behavior with aligned carbon nanotubes (CNT), which exhibit a multivalued surface. In a considerable amount of experimental papers authors proposed a wide range of methods to produce multivalued structures and verified their omniphobic features. Tuteja et al. [300, 301] proposed disordered polymer-fiber networks and micro-hoodoos (T-shaped silica posts), Chhatre and co-authors [65] proposed woven fiber-networks as cheap re-entrant substrates and studied the break-through behavior as a function of pressure. Others produced multivalued cellulose surfaces and showed the repellency for several liquids [19, 142]. Nanonails and honeycombs with overhangs were produced by Ahuja et al. [3] and omniphobic features of such substrates were checked with electro wetting. Silica nanonails are also used in works of Karlsson [154]. Porous silica films with special etching techniques were presented in a papers of Cao and others [56, 55]. Coaxial electrospinning is used by Han and Steckl [121]. And Zimmermann et al. [327] exploited silica coated nanofilament networks to demonstrate omniphobicity.

On probably multivalued surfaces Feng et al. [97] report the so-called petal effect, i.e. drops exhibit a quite repellent apparent contact angle of more than 150°, but with high adhesion, so that drop sticks up side down. This was found on petals of red roses (rosea Rehd).

3.2.3. Monovalued omniphobicity

One recent experiment differs quite a lot from those mentioned above. Ramos et al. [250] report omniphobicity on probably monovalued surfaces and the apparent contact angles are systematically studied for a variety of liquids. Figure 3.7 shows AFM images of the fractal surface under consideration, which were obtained from amorphous silica, treated with an iron-etching method. Then, the surface was grafted with perfluorooctyltrichlorisilan (PFOTS), so that it became hydrophobic. From a former Ramos et al. paper [249] it is known that this surface is superhydrophobic with an apparent water contact angle of 158°. Oil drops were deposited on top and the apparent contact angle was measured optically. The intrinsic contact angles were measured

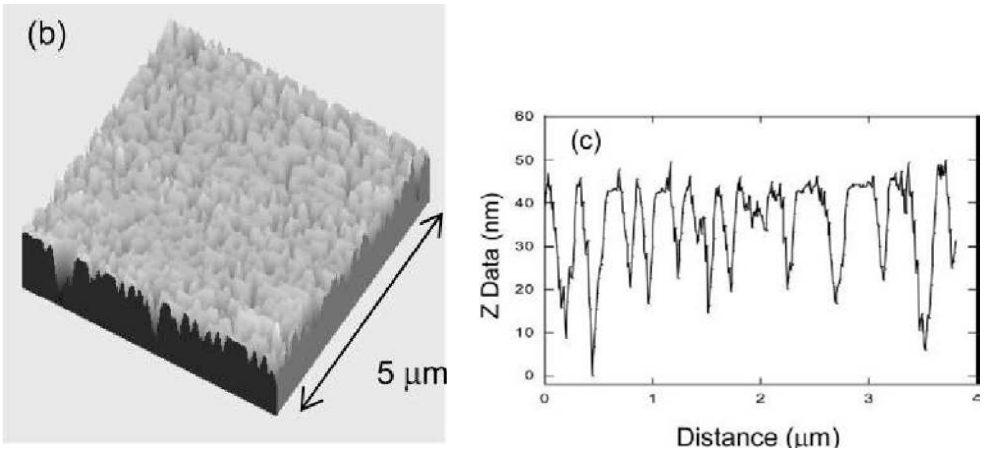


FIGURE 3.7. *Roughness profiles of the Ramos experiments. Figures taken from ref. [250].*

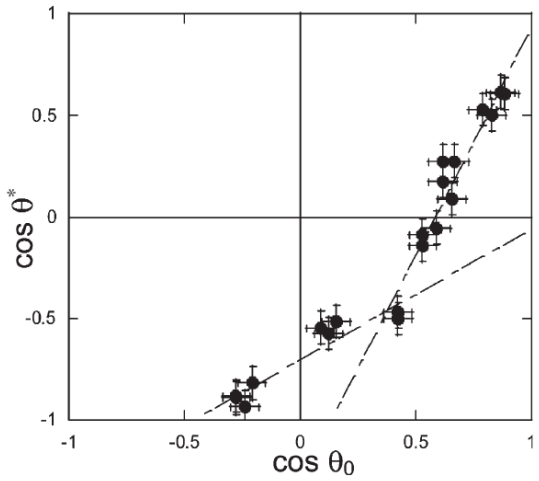


FIGURE 3.8. *Wetting diagram of superhydrophobic and omniphobic fractal surface from the Ramos experiment. Figure taken from ref. [250].*

independently and the wetting diagram is reported. It is presented in fig. 3.8. It is shown that a CB-like branch exists, even in the oleophilic part of the diagram and a strong change of the slope indicates W-like states. It is concluded, that probably omniphobic behavior is explained by re-entrent (multivalued) surface structures. Though multivalued topologies cannot be found with AFM measurements. Further, Ramos refers that no condensation process is observed, but a progressive emergence of mixed CB-W states is most likely. This intriguing results leaves the question, if a random rough surface without re-entrant features can exhibit omniphobicity?

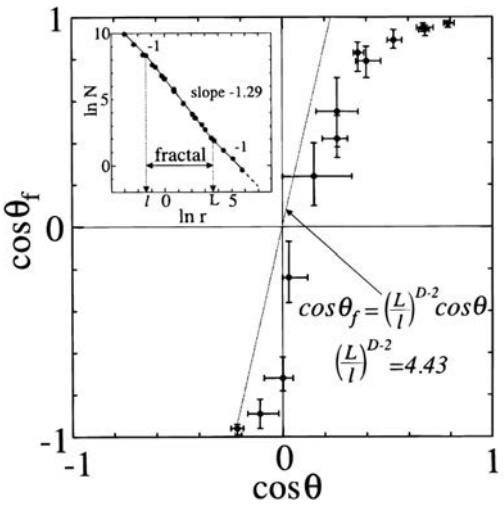


FIGURE 3.9. *Wetting diagram of alkylketene dimer fractal surfaces. Figure taken from ref. [235]. Note, the apparent contact angle is denoted θ_f here.*

Another paper discussing alkylketene dimer fractal surfaces was published by Onda et al. [235]. Interestingly they present a wetting diagram with a smooth transition to a Wenzel-like branch from both sides (see fig. 3.9). Further, one might guess that their wetting diagram shows a slight Wenzel wetting inversion.

3.3. Simulations in the literature

DFT simulations Berim and Ruckenstein [31] published a 2D DFT analysis of nanodrops on chemically rough and also on geometrically rough surfaces. A free energy functional for modeling Lennard-Jones like fluids were used, together with a Lennard-Jones like fluid-solid coupling. Such an approach recovers also the layering effects in the vicinity of the wall. The Wenzel and Cassie-Baxter equations were tested against roughness variations, by changing the height of the ridges. The width of the pillars a were fixed to 2σ and the spacing in between was 4σ. Nanodroplets were used and the contact angle was determined by geometrical methods; a complex dependence of the apparent contact angle on the nanodrop volume is reported. Intervals of the roughness parameters were found, where the Wenzel contact angle increases, despite the hydrophilic nature of the smooth interface.

MD and MC simulations Most studies use nanodroplets and a geometric method to find the contact angle [324, 188, 128, 160, 189, 190]. Ingebrigsten et al. [136] found that even on smooth surfaces (9-3 Lennard-Jones potential) finite size effects (line tensions) of the Young contact angle play a role, in particular on hydrophilic substrates. Werder et al. [312] studied the SPC/E water model on graphite surfaces and report finite size effects too.

A recent paper by Daub et al. [76] studies water molecules (SPC/E model) on top of a (111) graphite layer with and without molecular asperity decoration on a broad range of surface coverage factor f. The Cassie-Baxter law is checked. The roughness depth is quite small with $h \approx 1 - 3\sigma$ and the drops are nanometric consisting of 2000/4000 atoms, which lead to drops bridging 2-5 times the periodicity length L of the patterns. It is reported, that water cannot penetrate the grooves, when the spacing is less than 10Å which is the size of a few water molecules. A clear impact of the corrugation topology is reported, i.e. different topologies with the same f can exhibit different apparent contact angles in heterogeneous states. However, qualitative agreement with the CB law was found. Quantitative agreement cannot be expected due to small size effects. Also, hydrogen-bonding effects are discussed, stating that individual asperity atoms are covered, similar to small solutes. With MD simulations one could also observe thermal motion of nanodrops, and interestingly the motion diffusivity increases with hydrophilicity.

To overcome limits of nanodrops a very recent paper of Leroy et al. [180], applies a so-called phantom wall method to perform a thermodynamic integration to obtain the surface tension [178, 179]. They showed that at nanometric scale the details of the corrugations are much more important, thus the Wenzel law cannot be applied anymore and the CB equation only holds qualitatively. For this study, the SPC/E water model was used, and the wall was made of graphite with certain regular defects, bridging the parameter f from 0.5 to 1. Although only 2790 water molecules were used, finite drop size effects (e.g. line tensions at the triple line or curvature dependent pressure) is not at play, since the thermodynamic integration method leads directly to surface tensions, similar to our approach. Furthermore, several realizations of $f = 0.75$ topographies were checked against the CB equation. Wenzel states are found on certain topographies. It was further reported, in agreement with Daub's findings, that perturbations of the hydrogen bond network have a strong impact to the surface tensions. While most of the MD studies on wetting are performed for highly specific systems, we are not aware of any generic study of apparent contact angles at the scales under consideration.

Grzelak et al. [115] report in an MC study on the applicability of the Wenzel law at nanoscale. A sinusoidal wall of distinct atoms interacting via a Lennard-Jones cutoff potential with the fluid particles (the fluid is also modeled as Lennard-Jones fluid). From the free energy the contact angle is recovered, so that they can work without triple lines, similar two the latter MD study above. The authors state that Wenzel's equation underestimate the contact angle on small scale rough substrates. One have to be aware, that the distinct wall atom configuration in a sinusoidal substrate leads to heterogeneous "intrinsic" structures, which might have an impact to an effective roughness factor in the Wenzel formula. Effective roughness and geometrical roughness cannot be defined on molecular scales without arbitrariness. A study of the contact angle dependence of the Wenzel equation is not performed in this study.

LB simulations LB simulations are widely used to study two and three dimensional wetting problems on scales of microns. Recently a LB model has become popular, which takes into account a diffuse interface term, which is compareable to the square gradient description in our model [164, 167, 291, 50, 49]. The wall interaction in this LB model is described by a contact potential at the lattice adjacent to the wall. This model is able to recover macroscopic wetting properties as well as dynamical behavior like contact angle hysteresis. In the lattice Boltzmann equations, typically isothermal conditions are assumed and the number of particles is conserved. Thus, the wetting relaxation of drops is with respect of its volume. Often, this finite drop volumes create additionally metastable states. Kusumaatmaja et al. [164] studied for example the collapse transitions of small drops on superhydrophobic surfaces during quasistatic evaporation. Two distinct collapse scenarios are reported. Either only few posts support the drop or the meniscus touches the ground surface. The same authors studied in [169] the wetting and contact angle hysteresis in asymmetric corrugated stripes, where partially suspended states occur. Further works have been done on 3D drops on grooved substrates, reporting anisotropic drop shapes [167]. Interestingly they found that parallel to the stripes, where no pinning occurs the Wenzel law holds, while perpendicular metastabilities lead to large contact angle hysteresis and the well-known wetting laws can not applied. In ref. [265], Sbragaglia and others discuss LB applications of flows in nanochannels. A Shan-Chen multiphase description is used, and the authors demonstrates that under the conserved-dynamics constraints the wetting state is controlled by the pressure. Since the focus is more on apparent slip in that paper, we shall come back to it, when we discuss slippage.

3.4. PF simulations

In this section we shall discuss—based on findings in PF simulations—that omniphobicity can be found also on monovalued substrates. This phenomena can be explained with line tensions, which are not included in the theories above. It will be shown that these line-contributions can be easily added to the Wenzel-law.

Random-rough surface simulations Monovalued random rough surfaces (RRS) geometries show a large variety of wetting phenomena. We present as an example in fig. 3.10 a wetting diagram of simulated RRS (open symbols) and experimental RRS from ref. [250] (solid dots). Comparing the simulation data and the experimental results with the typical wetting diagram—shown in the insert—one notices that the change from the apparent non-wetting ($cos\theta_{\text{eff}} < 0$) substrate to the apparent wetting substrate ($cos\theta_{\text{eff}} > 0$) is found at quite small intrinsic wetting angles—far away from $\theta = \pi/2$. From the data it remains unclear whether the experiments show two branches (W and CB) with a sharp transition or with a smooth change from one to the other. Either hypothesis remains plausible from the experimental data. In the main panel of fig. 3.10 the open squares represent the wetting states for the RRS geometry (S1) that mimics experimental surfaces from ref. [250]. Details on the definition of S1 and S2 can be found in the appendix A. Although this choice (specified in app. A) is simplistic, it reveals the physical phenomena observed in the experiments. From three realizations of (S1) we estimate an error of $\Delta(\cos\theta_{\text{eff}}) = 0.05$. The geometry (S2) is a simplified version with regular pillars and random distributed crenel width chosen in a way that the W branch of the S1 wetting diagram is reproduced. We can check in fig. 3.10 that the wetting diagram of S1 is fairly well reproduced by S2. As it is a much simpler geometry we shall use S2 and regular crenels for further investigation. Three interesting features in the diagram are highlighted with boxes which we shall discuss later in detail.

A: This box highlights the change from non-wetting to wetting ($\cos\theta^{\text{W}}_{\text{eff}}$) which is displaced from the origin. We call this effect Wenzel wetting inversion. It is in contrast to Cassie-Baxter wetting inversion, which makes use of the metastability as discussed above. The simulation results (S1, S2) indicate a change at the crossover contact angle $\cos\theta^{\text{W}}_{\text{c}} \approx 0.35$ (inversion contact angle). The experiments of ref. [250] show even a larger $\cos\theta_{\text{c}} \approx 0.6$. *B*: S1: The transition from CB to W is smooth (due to the roughness). The two branches follow the same curve in a quite broad interval. But a distinct transition still exists as we shall discuss later. We call this a hidden wetting transition. *C*: While at large θ the CB branch is stable, the W states exhibit a strongly

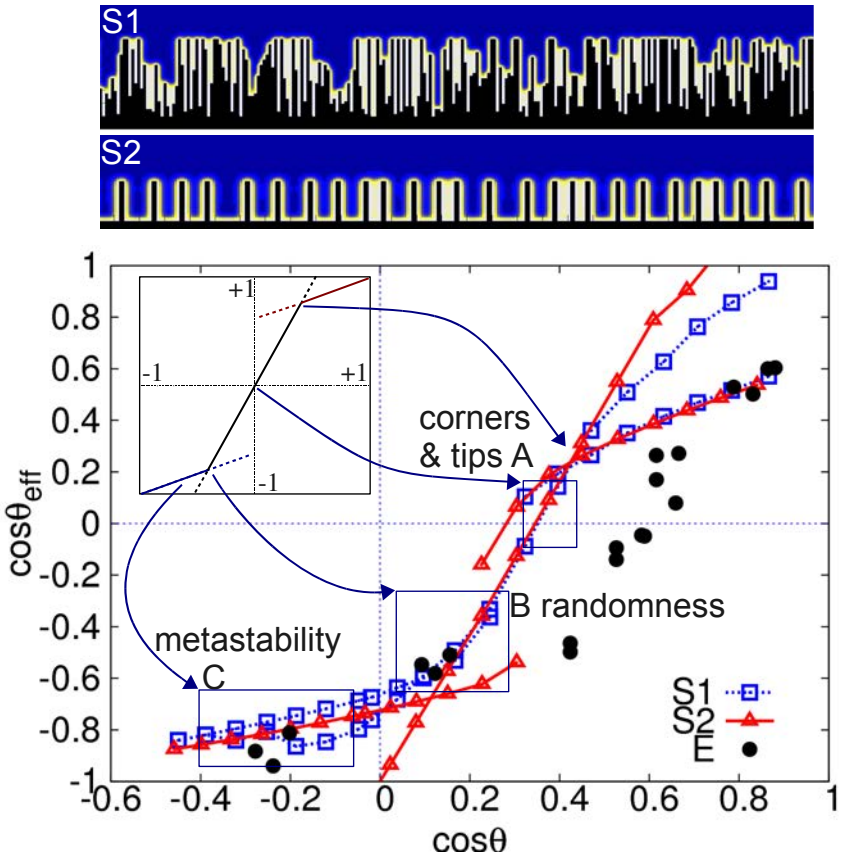
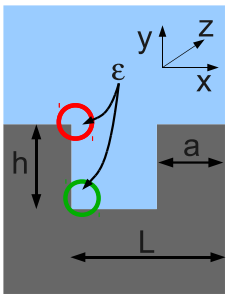


FIGURE 3.10. *Wetting diagram of monovalued S1 and S2 substrate geometries—obtained with the PF model. The black dots are experimental results from ref. [250]. Three nanowetting phenomena of the simulation results are highlighted and compared to the typical wetting diagram of fig. 3.2:* A*: The change from non-wetting to wetting ($\theta^{W}_{eff} = 0$) is found at hydrophilic intrinsic contact angles θ (wetting inversion).* B*: For intermediate contact angles θ, a smooth transition from the CB branch to W branch is observed. The wetting transitions itself is hidden by the fact that both branches follow nearly the same curve whilst the wetting situation is quite different.* C*: For large intrinsic contact angles θ the CB state is stable and the W states show a strong roughness dependent metastable behavior.*

roughness dependent metastable behavior. The first two effects are focused in this section the latter in the next section.

Corner energy In this paragraph we focus on the Wenzel wetting inversion for monodisperse pillars. The Wenzel wetting inversion angle θ_c is defined as the root of W branch ($\cos\theta^W_{\text{eff}}(\theta_c) = 0$) in the wetting diagram. The contact angle of the heterogeneous wetting state is given by the Young-Dupré equation using the effective surface tensions ($\gamma^{\text{eff}}_{\text{SV}}$: situation *d* in fig. 3.12 and $\gamma^{\text{eff}}_{\text{SL}}$: situation *a* ib.).



$$\begin{aligned} \cos\theta_{\text{eff}} &= r\cos\theta + 2\frac{\varepsilon}{L\gamma} \\ r &= 1 + 2h/L \\ \varepsilon &= \varepsilon_{\text{U}} + \varepsilon_{\text{D}} \end{aligned} \tag{3.15}$$

FIGURE 3.11. Corner Energies ε *(line tensions) occur in W states. On mesoscopic scales* ($\lesssim$ 100 *particle diameters) a significant contribution to the W wetting angle occurs [35].*

We computed the wetting diagrams of crenels as a function of the nanometric pillar widths a (for the geometry see fig. 3.11) and measured the inversion contact angle θ^W_c. This is shown in fig. 3.12. The main panel presents the W branches for various nanometric pillar widths a and the experimental data from ref. [250]. As we can see the smallest pillar width roughly corresponds to the experimental findings, but the W wetting inversion decreases rapidly with increasing pillar width. The insert displays the W wetting inversion angle as a function of a.

Apparent contact angles on mesoscopic scales ($\approx$ 15-100 atomic diameters) already show some mismatch to the classical Wenzel law $\cos\theta_{\text{eff}} = r\cos\theta$. This can be understood as a line tension along the edges of the grooves [35]. In homogeneous wetting state the liquid is convexly curved at the bottom corners and concavely curved at the edges of the pillars. Compared to flat substrate the wall potential is less attractive at an outer edge and more attractive at an inner corner (see fig. 3.11). Quantitatively these line tensions can be estimated in the PF simulations in several ways. First we notice that there are two distinct corner energies: ε_{U} at the upper corner and ε_{D} at the lower corner.

These line tension can be interpreted as the "microscopic" correction to the "macroscopic" grand-canonical potential. Unfortunately the definition of the of the "macro-

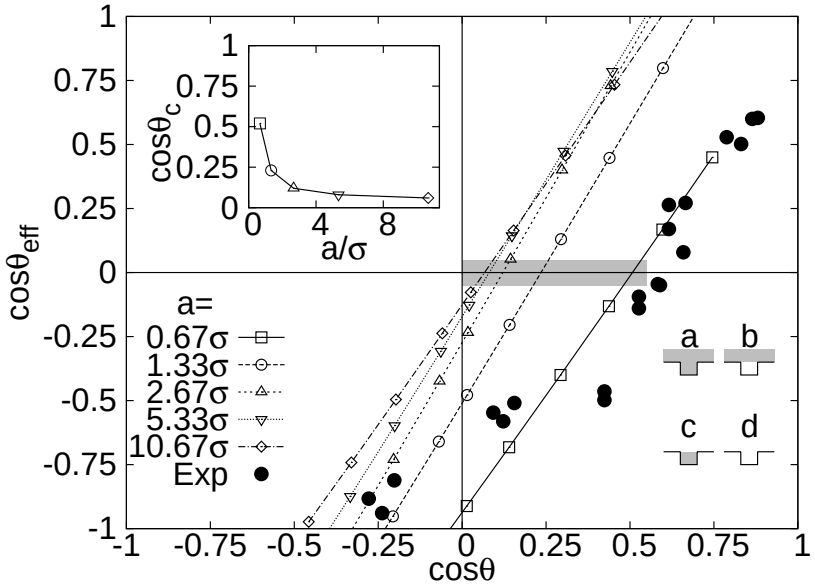


FIGURE 3.12. *Wetting diagram: W branches of monodisperse pillars with pillar width* $a = (0.67, 1.33, 2.67, 5.33, 10.67)\sigma$*; (*$L - a = h = 13.3\sigma$*). The insert shows the intrinsic* $\cos\theta$*, where the substrate changes from non-wetting to wetting* ($\cos\theta_c^W$) *as a function of the pillar width a. For pillars with only atomic thickness the Wenzel wetting inversion angle* θ_c^W *is comparable to the experimental findings of ref. [250] (solid dots).*

scopic" grand potential is somewhat difficult. There are two microscopic effects: Deviations due to the confinement and more important, the line tensions at the corners. We used three different methods to measure this excess energies. First, if the crenel is sufficiently large one can measure the "macroscopic" grand-potential in the middle of the crenel flank and extrapolate it to the corners as sketched in fig. 3.14 (*panel a*) We use this extrapolated grand-canonical potential (*panel b*) as a reference field and subtract the real one. The excess-field (*panel a-b*) can be integrated around the edges to obtain the corner energies ε_U and ε_D. Upper corners are repellent ($\varepsilon_U > 0$) and the lower corners are attractive ($\varepsilon_D < 0$). Interestingly, these energies are θ-dependent and the overall effect varies from attractive for large θ to repellent for small θ (see fig. 3.14). To ensure that the corners are sufficiently large in fig. 3.14 three different values for the corner heights h are used and no deviation for $d/L = 3/4$ and $d/L = 1$ are visible [35].

A second way to define the corner energies is to use the Euclidean distance map $EDM(\mathbf{r})$. This is a mapping of each point $\mathbf{r}$ in the Euclidean space $\mathbb{E}$ (here the simu-

lation box) to its (smallest) distance to the substrate. Then, on a planar wall the EDM is mapped onto the grand canonical potential density $\omega(\mathbf{r}) = \omega(e)$, where e is the distance to the substrate. Using the EDM method in the corrugated system yields a reference field, which is independent of the confinement inside the crenels. Subtraction from the real grand-canonical potential gives the excess energy, which is again integrated over subpatches to define the corner energies ε_{U} and ε_{D}. This method give virtually the same results as the first method, but it is also useful in more complicated geometries.

A third method is to use the classical Wenzel law as a reference and to subsume the corner-energies as a deviation from the measured W contact angle to the ideal one in a sufficiently large crenelated system. Using eq. (3.15) yields the total corner energies ε. This handy method is useful only when no distinction between lower and upper corners is necessary.

In fig. 3.15 the Wenzel-law plus the corner-energies (measured with the first (extrapolation) method) is compared to the PF simulation results. The solid line is the enhanced Wenzel-law (3.15), while the dotted lines show the classical Wenzel law. Clearly, the agreement is significantly enhanced. These effects are already visible in

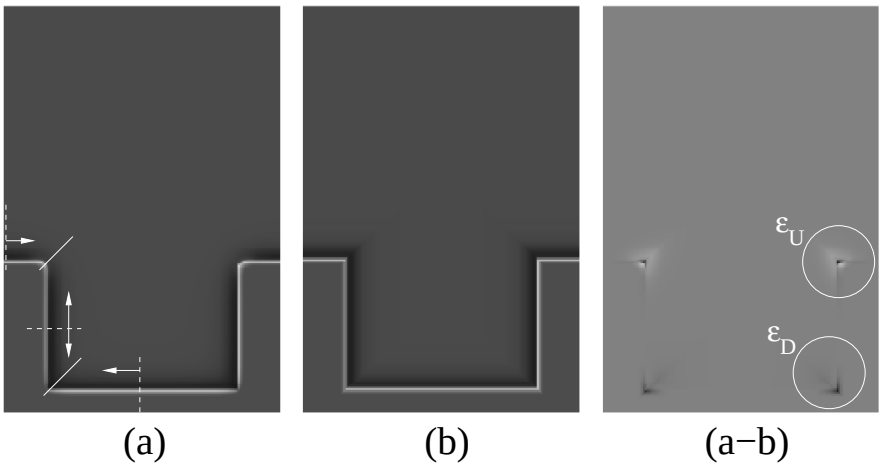


FIGURE 3.13. *Corner energies. (a) Excess grand-canonical potential, as measured at equilibrium; (b) Expected excess grand-canonical potential from macroscopic considerations (a-b) difference between the two: white means positive values, black corresponds to negative values. The gray background in all figures is the zero level. The dashed lines in (a) represent the grand canonical potential profiles that are propagated in the direction of the arrows to construct (b) [214].*

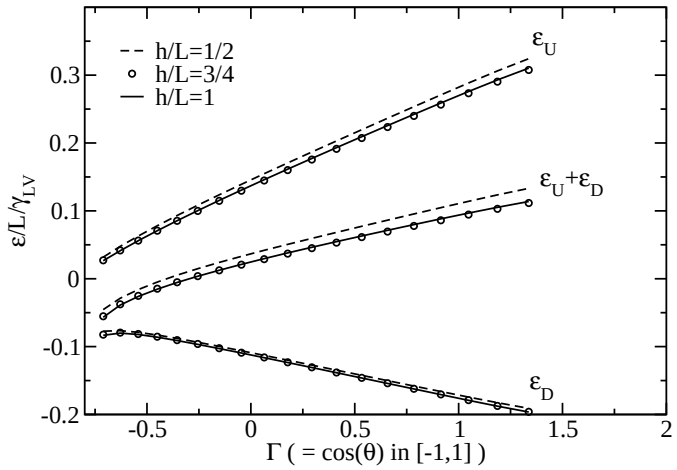


FIGURE 3.14. *Corner line energies as a function of the intrinsic wettability of the surface.*

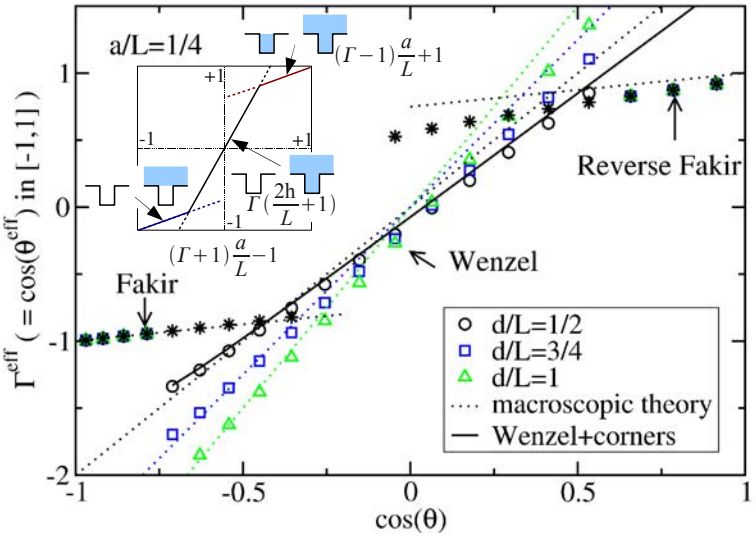


FIGURE 3.15. *Measured wetting diagram for crenelated surfaces.*

the wetting diagram for mesoscopic structures. Their quantitative contribution is quite weak, when the corner density is small, as it is supposed for macroscopic structured systems (i.e. the corner contributions scale like $1/L$, where L is the periodicity of the structure). Thus corner energies ε weakly contribute to the observed W wetting inversion.

Needle tip effect

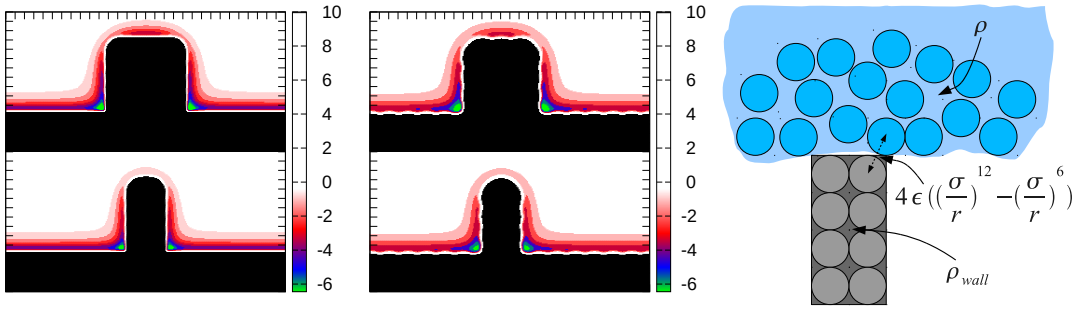


FIGURE 3.16. *Attractive parts of the wall potential:* Left: *potential of the PF model, obtained from a continuous wall particle density,* Middle: *microscopic potential of discrete wall atoms. Repulsive parts are black colored.* Top: *pillar width* $a \approx 3\sigma$ Bottom: $a \approx 1\sigma$ Right: *The continuous wall potential is a mean field model of wall particles with density* ρ_{wall} *which interact via a Lennard-Jones potential with the fluid particles distributed with density* ρ.

For microscopic/nanometric pillars ($a \approx 1\sigma$) there is an extra energy penalty which can be even larger than the corner energy for mesoscopic pillars. This non-linear effect is strong enough to render a substrate with an intrinsic contact angle of $\theta \approx 60°$ non-wetting. One may think that this effect results from a less attractive interaction potential at both sides of a thin pillar compared to a thick one. In that case the effect should strongly be height-dependent. As we only observe weak h dependence (see insert of fig. 3.18) we conclude that the energy penalty is mainly located at the needle tip. It is noteworthy that this is not an effect of the higher surface tension for a curved interface as it is described by the Tolman length δ [295]. δ is the distance between the equimolar surface and the surface of tension and is connected to the leading correction term of the surface tension for small curvature radii and can be written as $\gamma_R = \gamma(1 - \delta/R + \ldots)$. For small pillars the curvature diameter $2R$ of the liquid phase is in the order of the crenel width a (see sketch in fig. 3.17 and one realization of S2 in fig. 3.10). The extra energy at the pillar top associated to the Tolman δ can be written as $(\gamma_R - \gamma)\pi R$ when assuming a half circle shaped liquid-solid interface. Thus the $1/R$ scaling is canceled by R in the arc length πR leading to a curvature independent correction $+\gamma\delta\pi$ which is already included in the corner energy term ε.

Thin lines in fig. 3.17 with dots show the simulation results from the homogeneous wetting state for three different pillar widths a. After subtracting the corner energies ε one gets the thick lines presenting the macroscopic plus the needle tip contributions.

The displacement of the Wenzel branch root out of the origin stems from the needle tip effect. The tip effect vanishes when the pillar width exceeds $a \geq 2.7\sigma$. In fig. 3.16 we compare the wall potential of discrete atoms, which would be used in microscopic simulations like MD with the wall potential used in the PF model. For pillars of one atomic diameter there is a depletion layer of the attractive wall potential on the needle tip (only bright red needle tip potential), which vanishes for slightly larger pillars. Large pillars still have a depletion zone on the upper edges.

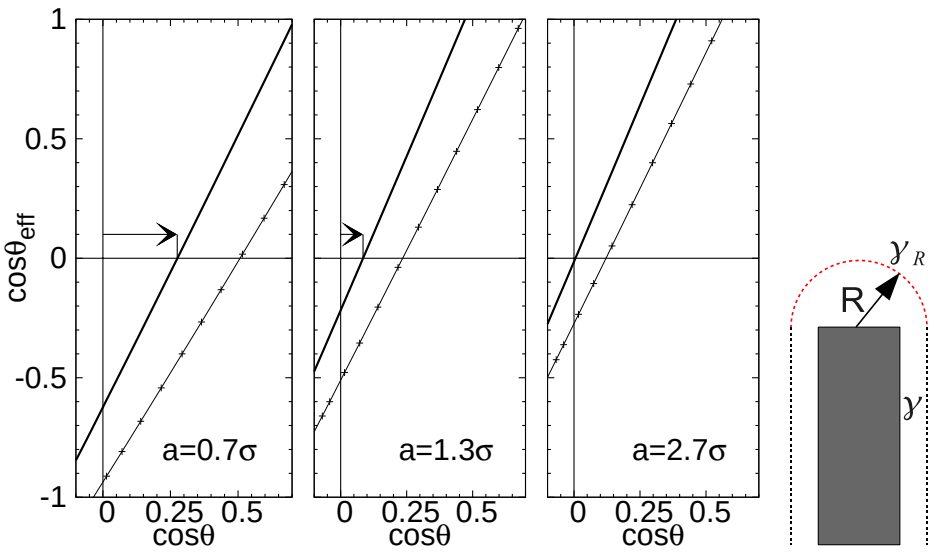


FIGURE 3.17. *Wetting diagram of regular crenel with $L - a = h = 13.3\sigma$. Thin lines with crosses show the simulation results. After subtracting the corner energies one gets the thick lines presenting the macroscopic plus the needle tip contributions. The displacement between the origin and the thick lines stems from the needle tip effect. The tip effect vanishes as soon as the pillar width exceeds $a \geq 2.7\sigma$. The sketch on the right-hand side illustrates the surface tension γ_R on curved substrates. The Tolman contribution is included in the corner energies.*

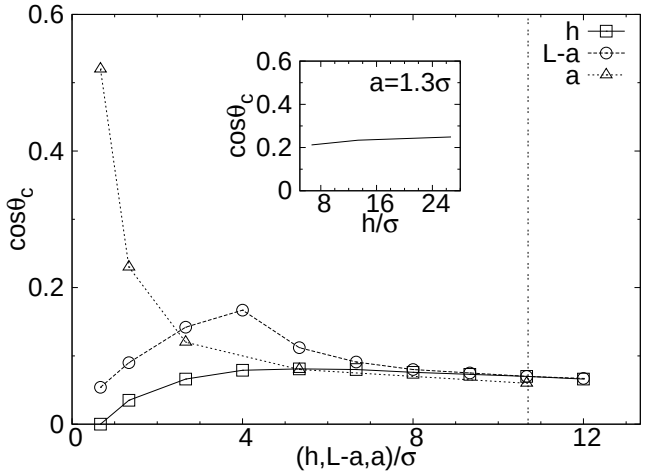


FIGURE 3.18. *Cosine of inversion contact angle* $\cos\theta_c$ *as a function of 1) crenel depth h, 2) crenel width* $L-a$ *and 3) pillar width a. Nanometric pillars can show a large wetting inversion angle. The W wetting inversion effect of narrow crenels is less important (squares:* $L-a=a=10.7\sigma$*, circles:* $h=a=10.7\sigma$*, triangles:* $h=L-a=10.7\sigma$*). The insert shows* $\cos\theta_c$ *as a function of crenel depth h for fixed nanometric pillar width* $a=1.3\sigma$*, where the W wetting inversion angle is only very weakly height-dependent.*

In summary we can consider this as a dewetting needle tip effect which stems from the less attractive potential directly on the top of the pillar (needle). This effect can be quantified by measuring the extra energy from the PF simulations, but since it is strongly a dependent it must be calculated for every a under consideration (see fig. 3.17).

Crenel geometry

Two other parameters are important in the crenel geometry: the crenel width $L-a$ and the pillar height h. The W wetting inversion angles θ_c in fig. 3.18 as a function of a, h and $L-a$ (the other parameters are constant at values where the wetting inversion effect is already leveled) demonstrates that the W inversion angle depends only weakly on the depth h of the crenels since for large depths both corner contributions at the outer and inner corner separates. Thanks to this separation mesoscopic crenels are well described by the CB-W theory plus corner energies. For a very small depth h the corner terms vanish together (see fig. 3.18). The width $L-a$ of the crenel plays only a minor

role to tune the W wetting inversion. Very narrow crenels entail a nearly symmetric wetting diagram but without W states. This confinement prevents the liquid phase to enter the crenel. Only a small number of particles enter and produce an intermediate density with large energy penalties in the bulk and the interface term. In slightly larger crenels the corners are too close to separate the regions connected with the corner-energies. The non-linear character of the corner terms results to a minor increase of the W wetting inversion.

3.4.1. Randomness

fig. 3.10 (Box B) demonstrates a smooth transition from the CB branch to the W branch. This is visible for the S1 geometry but hardly for the more regular S2 geometry. This smoothing stems from the irregular roughness of the S1 geometry. To model this smoothing effect we write the mesoscopic wetting theory of ref. [35] in a stochastic way and assume for simplicity regular pillars with constant depth h and width a but a randomly distributed crenel width $d \equiv L - a$ (see fig. 3.11).

To calculate the effective contact angle θ_{eff} from the intrinsic contact angle θ, we first calculate the energy of the thermodynamic equilibrium state. There is a critical width d_{kr} for the wetting transition from the CB state to the W state. Larger diameters favor filled crenels. We assume that the drop is much larger than the typical L. The overall energy per unit area is

$$E = \int_0^{d_{\text{kr}}} \frac{E_{\text{CB}} + \exp(-\beta\Delta E) E_{\text{W}}}{1 + \exp(-\beta\Delta E)} P(d)\,\mathrm{d}d + \int_{d_{\text{kr}}}^{\infty} \frac{E_{\text{W}} + \exp(-\beta\Delta E) E_{\text{CB}}}{1 + \exp(-\beta\Delta E)} P(d)\,\mathrm{d}d, \quad (3.16)$$

where the crenel width d is randomly distributed with the probability density $P(d)$, $\Delta E = |E_{\text{W}} - E_{\text{CB}}|$ and $\beta = 1/(k_{\text{B}}T)$. In this expression E_{W} and E_{CB} is the average energy in the homogeneous and heterogeneous wetting state per crenel-pillar pairs, resp.:

$$E_{\text{CB}} = -(\gamma_{\text{SV}} - \gamma_{\text{SL}})\frac{a}{L} + \frac{L-a}{L}\gamma \quad (3.17)$$

$$E_{\text{W}} = -(\gamma_{\text{SV}} - \gamma_{\text{SL}})\frac{L+2h}{L}. \quad (3.18)$$

The critical crenel width d_{kr} is given by the equality $E_{\text{W}} = E_{\text{CB}}$, which leads to $d_{\text{kr}} = \frac{-2h\cos\theta}{1.0+\cos\theta}$. Finally the effective wetting angle is defined via an effective Young equation which can be written as $\cos\theta_{\text{eff}} = -\frac{E}{\gamma}$, and $E = \gamma_{\text{SV}}^{\text{eff}} - \gamma_{\text{SL}}^{\text{eff}}$.

So far this model does only describe the macroscopic theory. This is based on the assumption that the excess energy due to wetting or dewetting is proportional to the

wetted/dewetted surface area but not to the curvature. On a mesoscopic scale this need not longer to be true. Line tensions like the corner contributions occur when the liquid interface is curved at the edges of the pillars. Please note that we do not take into account the needle tip effect. Of course these contributions are small for macroscopic structures since they scale with the density of edges. Equation (3.18) turns to be

$$E_{\mathrm{W}} = -(\gamma_{\mathrm{SV}} - \gamma_{\mathrm{SL}})\frac{L+2h}{L} + \frac{\varepsilon}{L} \tag{3.19}$$

This extra term leads to a symmetry breaking of the wetting diagram or more precisely to a displacement of the W wetting state in the origin of the diagram to the right. The amplitude of the displacement depends on the corner-energies ε and also on $P(d)$. With this extra term we get for d_{kr}

$$d_{\mathrm{kr}} = \frac{-2h\cos\theta + \frac{\varepsilon}{\gamma}}{1.0 + \cos\theta}. \tag{3.20}$$

We checked that the model works quite accurately for mesoscopic crenels and reproduces a smoothed CB→W transition that range over an interval of about 0.3 on the $\cos\theta$-axis (see fig. 3.19) for S2 geometries, if the variance of the crenel width distribution is large enough ($\approx$ three times larger than S2 in fig. 3.10). This model does not account for line tensions of the three phase contact line like other authors do [314]. Nevertheless, it is straight forward to add line tensions to the CB energy too.

In RRS S1 geometry it is even possible that the metastable branch follows nearly the stable branch in the wetting diagram. It is thus not possible on such substrates to identify the wetting state only from the wetting diagram. Figure 3.20 shows two possible wetting situation with nearly the same effective wetting angle θ_{eff}. The right situation shows a clearly suspended state, thus we call it a CB state, while the left density profile is partially penetrated. Although this is not a strictly homogeneous wetting regime the shape of the wetting diagram is reminiscent to the W branch, except for the wetting inversion.

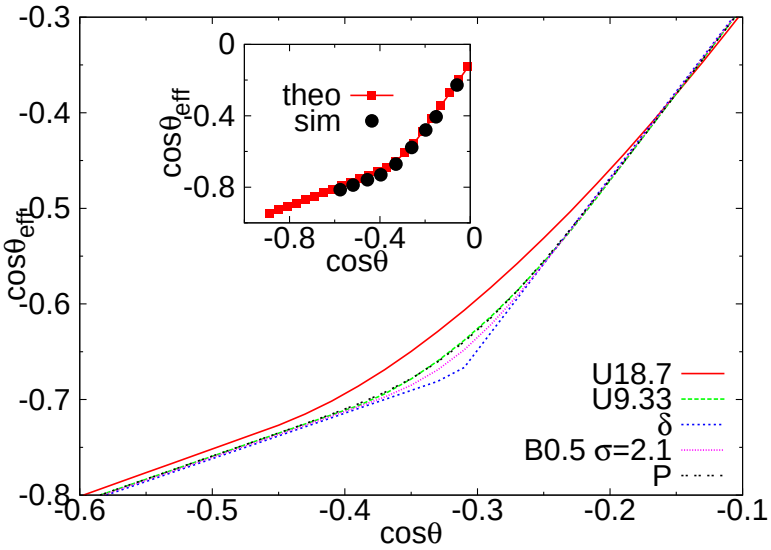


FIGURE 3.19. *The lines are computed with eqs. (3.16) and (3.19) for several distributions of the crenel width (uniform- U(interval half width), binomial- B and Poisson- P, δ-distribution) with equal mean value $< (L-a) >= 10.7\sigma$. The broader the variance of the distribution the smoother the transition. The black dots in the insert are simulation results (crenelated surface with $a = 10.7\sigma$,$h = 13.3\sigma$ and equal distributed crenels with widths $(6.7, 10.7, 14.7)\sigma$) together with the theoretical results for the same geometry.*

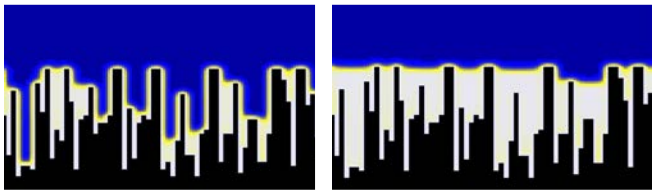


FIGURE 3.20. *Wenzel-like and fakir-like states in the S1 geometry for* $\cos\theta = 0.09$. *The effective wetting angles are* $\cos\theta_{\mathrm{eff,W}} = -0.59$ *and* $\cos\theta^{\mathrm{eff,CB}} = -0.60$. *We observe the same effective contact angle in a quite broad range* ($0.09 \leq \cos\theta \leq 0.25$) *for the CB and the W range although the wetting states are reminiscent to the CB-W transition. Thus this transition can be hardly seen in the wetting diagram of fig. 3.10.*

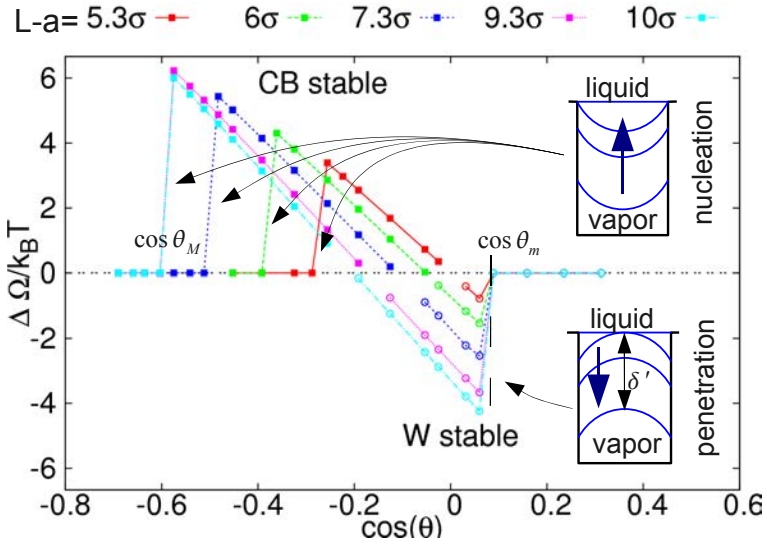


FIGURE 3.21. *Energy gap* $|\Delta\Omega|$*:* $\Delta\Omega := \Omega_{\text{Wenzel}} - \Omega_{\text{Cassie}}$ *as a function of* $\cos\theta$ *for different crenel widths* $(L-a)$*. The Cassie state minimizes the grand potential* Ω *if* $\Delta\Omega > 0$*. The points in this half space rest in the metastable Wenzel state. The energy gap lowers with increasing width* $(L-a)$ *for fixed* $\cos\theta$ *but the* $\cos\theta$*, where the collapse of the metastability increases with d in a way that the maximal* $|\Delta\Omega|$ *also increases with* $(L-a)$*. The bottom half-space* $\Delta\Omega < 0$ *indicates configurations, where the W state minimizes the grand potential* Ω*. The points in this region correspond to metastable CB states, whereas points on the* $\Delta\Omega = 0$ *line indicate that no metastability occurs. It is noteworthy that in the lower half-space the energy gap* $|\Delta\Omega|$ *increases with larger* $(L-a)$ *while there is a critical* $\cos\theta_{\text{m}}$ *where all metastabilities (for a crenel width* $L - a \gtrsim 5\sigma$*) collapse.*

3.5. Metastabilities

Marmur [198] and others [125] pointed out that metastabilities can play an important role gaining omniphobic surfaces. Marmur considered multivalued surfaces where the liquid is pinned at the top of the cavities. Even monovalued nanostructures can exhibit strong metastabilities avoiding the W state due to corner energies/line tensions. The macroscopic CB-W theory does not allow metastable states between the CB and the W state for positive $\cos\theta$ and monovalued surfaces like crenels. The corner energies ε_{U} at the outer edges of the pillars can support a metastable CB state up to a critical intrinsic wetting angle $\cos\theta_{\text{m}} \approx 0.1$.

Fig. 3.21 shows the energy gap $|\Delta\Omega|$ defined as a difference between grand canonical potentials for W and CB state: $\Delta\Omega := \Omega_{\text{Wenzel}} - \Omega_{\text{Cassie}}$ or in other words—the energy difference between the stable and the metastable state. By definition $\Delta\Omega = 0$ indicates that no metastable state exists. For mesoscopic crenels ($\gtrsim 5\sigma$) a critical wetting angle θ_{m} can be found in the simulations that is independent of the crenel width $L - a$ and is a result of the upper corner energy contribution. The same mechanisms as for the wetting inversion can support larger θ_{m} for nanometric pillars with a in the range of a few atomic diameters (see fig. 3.22). Our findings show $\theta_{\text{m}} \approx \theta_{\text{c}}$ for these crenels—reflecting the common origin of the two effects.

On the left side of the wetting diagram the simulations show a crenel width dependent critical dewetting angle θ_{M} for nanometric crenels but a constant θ_{M} for larger crenels. This width sensitive dewetting metastability collapse lead to the rather complex W branch in fig. 3.10 leading to an unique CB state for $\cos\theta \leq -0.4$. Corner contributions on the upper corners increase the energy barrier between the suspended CB state and the penetrated W state. Thus they play a role even on larger scale. Conversely the inverse dewetting transition is not affected by the corner energies, since it is a nucleation process building up a new liquid-vapor interface from the bottom of the crenel.

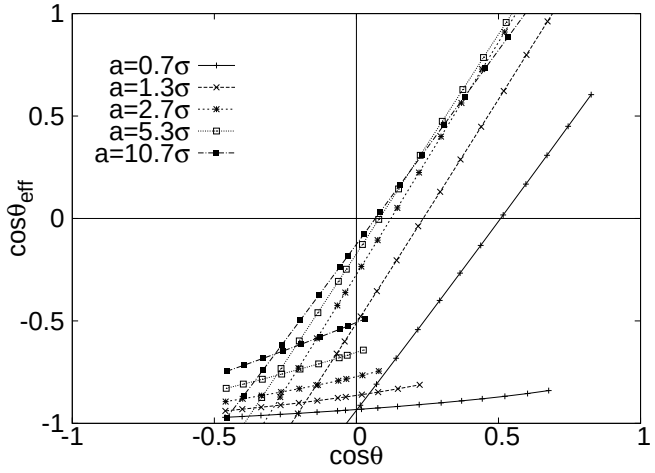


FIGURE 3.22. *Wetting diagram of regular crenel with* $L - a = h = 13.3\sigma$ *and* $a = (0.7, 1.3, 10.7)\sigma$. *The steep W branches show the stable W state at* $\cos\theta_{\text{eff}} = 0$, *the other branches are the CB states (metastable on the right of the crossover) For small pillar widths a existence of metastable CB states is increased to quite high contact angles up to* $\theta \approx 35°$.

3.6. Conclusion

We showed that even monovalued substrates can show omniphobic behavior and studied the dependence of the Wenzel inversion contact angle $\cos\theta_c^W$ on random rough substrates on nanometric scales. The study of the inversion angle guides the focus to thermodynamically stable non-wetting states which is in contrast to most of the studies on omniphobicity. Furthermore in the spirit of roughness induced non-wetting of Herminghaus [125], the inversion angle is the limit to exploit the roughness to gain a stable superhygrophobic/superomniphobic state. It was shown that among several structure parameters small pillar widths a are the most efficient route to increase omniphobicity. In our PF simulations W inversion angles up to $\theta_c \approx 60^\circ$ for monovalued substrates were found. This effect is based on two distinct microscopic energy corrections (line tensions) at the corners and tips of a nanorough substrate. From these findings we conclude that the experiments of Ramos et al. [250] correspond rather to a W wetting inversion than to a metastable wetting inversion of the CB branch. The needle tip effect might be combined with the idea of hierachical roughness proposed by Herminghaus [125] in order to obtain superomniphobicity. While these line tension effects do not contribute to macroscopic roughness (i.e. when the corner and tip density is small) one should not conclude that they are negligible because of the stabilizing effect on metastability. Further we showed that on random-rough surfaces it is not sufficient to study the wetting diagram when searching for a wetting transition from vapor-suspended Cassie-Baxter states to penetrated Wenzel states, since the random-rough substrate can smooth out the transition. Nevertheless a wetting transition still exists. The filling of the crenel goes stepwise when the Young angle is varied. The phase field model used in this study is a versatile method to bridge the gap between microscopic MD and MC simulations and more macroscopic Lattice-Boltzmann techniques.

4. Slip on nanorough substrates

The continuum description of hydrodynamics with the Navier-Stokes equation is often complemented with a no-slip boundary condition (BC). I.e., the hydrodynamic velocity field vanishes in tangential direction at the substrate-liquid interface (which is assumed to be sharp). For long time, there was agreement, that this BC is correct for any hydrodynamic problem, although there is no strict physical argument implying this BC [174]. It turned out in the last years, that in microfluidic devices this assumptions is not necessarily fulfilled in experiments. Thus, recently a lot of studies were performed to investigate the actual BC behavior. Navier already proposed in 1823 [224] the so-called (partial-)slip BC, which turned out to be very useful modeling microfluidics with the Navier-Stokes equation. This BC is based on a friction force between the wall and the fluid proportional to the tangential slip velocity. As a result, this slip velocity is in general proportional to the local shear rate, and we can quantify this effect with the help of a "slip length" b (see fig. 4.1). This condition for the tangential velocity is accompanied by $\mathbf{v}_\perp = 0$ at the boundary, assuming an impermeable solid. One have to distinguish two types of slip. The intrinsic (or molecular) slip describes the possibility of non-vanishing tangential velocities at planar or ideal substrate boundaries. Such slip phenomena are found in molecular simulations, depending on the pressure P [24], the intrinsic contact angle θ [41, 130] and the commensurability of

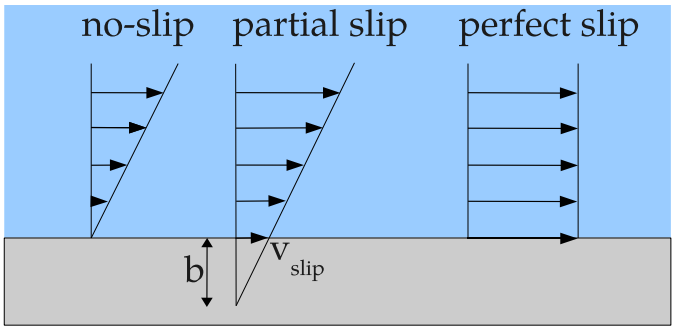


FIGURE 4.1. *Navier partial slip boundary condition, the no-slip limit and perfect slip limit*

liquid molecules and the crystal structure of the substrate [41, 95]. One may think, that slip is also velocity dependent. Many studies showed in a broad range of velocities, that the slip length does not vary with the velocity v [73, 124, 64, 27]. Apparent slip describes the phenomenon, that on a heterogeneous wall (rough or chemically heterogeneous) slip-lengths at different scales can occur. For example, in Cassie-Baxter states a no-slip BC or partial slip BC (b_1) is observed at the direct surface-liquid contact while there is a perfect slip ($b_2 \to \infty$) at the liquid-vapor interface. On length-scales, where the rough wall can be approximated by a flat wall, one may have a slip length B related to the roughness length scale L. B is called the apparent slip length. According to Lauga et al. we denote any slip phenomena which is not related to the intrinsic slip only as effective slip [174].

Assuming a certain velocity $\mathbf{v}_{\text{slip}}$, one expects a friction force acting on the liquid, which is proportional to $\mathbf{v}_{\text{slip}}$ [224]

$$\mathbf{f}_{\text{friction}} = -\lambda \mathbf{v}_{\text{slip}}. \tag{4.1}$$

For simplicity we assume a linear flow profile between two plates in a Couette experiment of an incompressible liquid with bulk viscosity η, one finds the viscous force at the surface z_0

$$\mathbf{f}_{\text{viscous}} = \eta \frac{\partial \mathbf{v}}{\partial z}|_{z_0}. \tag{4.2}$$

In a steady state the force is balanced and yields $\mathbf{v}_{\text{slip}} = \lambda/\eta v'$, where v' is the constant velocity profile slope, i.e. the shear rate at the boundary. From (4.1) we find the dimensions of λ as N/m^3 so that λ/η has dimension $1/m$, which can be interpreted as the inverse slip length $1/b$. From this arguments it becomes clear, that measurements of slip lengths from the velocity profile need a steady state flow. At low Reynolds Re number

$$Re = \rho m \frac{vl}{\eta} \ll 1, \tag{4.3}$$

when the dynamics are dominated by the linear viscous term in the Navier-Stokes equation and the non-linear convective term is negligible, the flow field is laminar (evolving to a steady state). The latter case is described by the Stokes equation

$$\eta \triangle \mathbf{v} = \nabla P \tag{4.4}$$

In the heterogeneous wetting state, where free liquid-vapor interfaces are present, a steady state flow may deform the free interfaces at high velocities. Therefore we work at low capillary number

$$Ca = \frac{\eta v}{\gamma}, \tag{4.5}$$

where v is the typical velocity in the channel.

Apparent slip vs. intrinsic slip Philip [243], Lauga and Stone [175] gave a theory for apparent slip on rough substrates with parallel ridges in the Cassie-Baxter state. The intrinsic slip is assumed to be perfect at the liquid-vapor interface and no-slip at the solid-liquid surface patches. The apparent slip parallel to the ridges $B_\parallel$ is

$$B_\parallel = \frac{L}{\pi} \ln\left(\frac{1}{\cos((1-f)\pi/2)}\right), \tag{4.6}$$

where f is the wetted fraction in the CB theory and L the periodicity of the pattern. Lauga and Stone derived a similar formula for the perpendicular flow

$$B_\perp = \frac{L}{2\pi} \ln\left(\frac{1}{\cos((1-f)\pi/2)}\right). \tag{4.7}$$

Notice the factor 2 between both directions. Indeed, apparent slip is in general a tensorial quantity representing anisotropic behavior, if the substrate roughness exhibits preferred directions [99]. This theory was extended by Cottin-Bizonne and others [73] to partial slip for either of the heterogeneous patches (stripes); in the case $b_1, b_2 > 1/10L$

$$B_\parallel = \frac{1-f}{b_1} + \frac{f}{b_2}, \tag{4.8}$$

where b_1 is the intrinsic slip of the liquid-solid patches which covers the fraction f of the surface.

4.1. Experiments and simulations

For slip-length measurements in experiments and simulations different methods are used. While in simulations the velocity profile is directly accessible, in most experimental setups tracking the velocity is not possible. Thus indirect methods have to be used. These methods are based on the comparison of the actual flow rates Q and the expected no-slip flow rate Q_{NS}. Together with a model for Q as a function of b one can fit the slip length, and this method is used for various geometries: e.g. circular pipes [64, 269]. Variations of this method, using sedimentation velocity instead of Q are also used in the literature [174]. In surface force apparatus (SFA) and atomic force microscopy (AFM) experiments comparison of drainage and viscous force gives estimations of the slip length [305]. In some recent experiments one tries to gain access to the velocity profile with tracker particles [263, 299].

In simulations, when the full velocity profile in a microchannel is known, it is easy to obtain slip. From Stokes equation one knows the profile of either Poiseuille- (POF)

or Couette (COF) flow analytically. Fitting to the profile either a parabolic function or a linear slope respectively and extrapolation to the wall position z_0 gives access to b with the Navier BC for a flat wall

$$b\, \partial_z v_x\,(z)|_{z=z_0} = v_x\,(z)|_{z=z_0}\,. \tag{4.9}$$

For a flat wall there is no ambiguity with the defintion of z_0, but for a rough wall the situation is more complex. Various prescriptions can be chosen: For example (i) the top of the structure ($z_0 = 0$), (ii) the average position of the roughness profile, and less arbitrary, (iii) we can use z_0 as a fitting parameter as well. We shall call the value of b obtained by assuming $z_0 = 0$ "1 parameter fit" and the values obtained by adjusting b and z_0 "2 parameter fit".

Assuming a POF profile $v_x(z) = a_0 z^2 + b_0 z + c_0$ and a COF profile $v_x(z) = a_1 z + b_1$ one obtains for the slip length b

$$b = \frac{\pm\sqrt{a_0^2 b_1^2 - a_0 a_1 b_1 b_0 + a_0 a_1^2 c_0}}{a_0 a_1} \tag{4.10}$$

and for the wall position z_0

$$z_0 = \frac{-a_0 b_1 \pm \sqrt{a_0^2 b_1^2 - a_0 a_1 b_1 b_0 + a_0 a_1^2 c_0}}{a_0 a_1}. \tag{4.11}$$

This method is referred to as 2 parameter fit. Notice the quantity $z_0 - b = -b_1/a_1$ depends on the COF profile only, and equals the 1 parameter fit result for $z_0 = 0$. In certain cases one have to take great care when using the 2 parameter fit to prevent numerical inaccuracy, which stems from numerical errors estimating the second derivatives of the POF profile and the square root term.

4.1.1. Simulations

MD simulations There are two possible ways to obtain slip in molecular simulations. In non-equilibrium MD one can average the velocity profile and apply a fitting method. Unfortunately due to the small sizes and short time scales accessible with nowadays computer power, thermal noise velocity is quite large compared to the pressure driven flow. Therefore unrealistically fast flows are needed to obtain a reliable speed profile in a nanochannel (tens and hundreds of m/s) [40]. Since this is far from experiments and the Reynolds numbers are large, slip lengths in non-equilibrium MD simulations

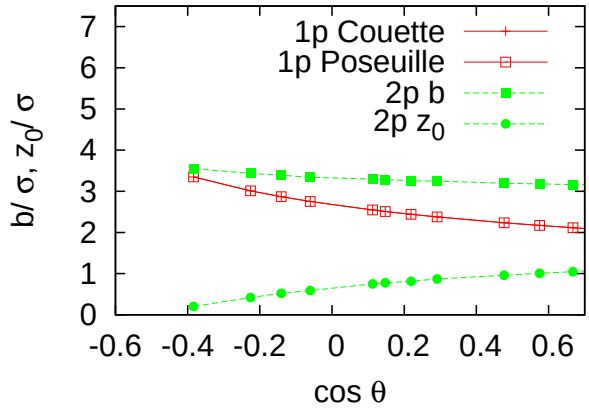


FIGURE 4.2. *Slip length b and wall position z_0 for 1 parameter and two parameter fitting method. Poiseuille and Couette flow give virtually the same result, 2 parameter method (2p) displays wall positions different from 0 and according to this larger slip lengths. Notice for the 2 parameter method: $z_0 - b = -b_1/a_1$.*

are a priori not a good reference. However, Bocquet et al. [41] compared the non-equilibrium MD results of Huang et al. [130] to various experimental results in the literature and found a good agreement on the reported θ-dependence. Barrat and Bocquet demonstrated, that slip is in principle accessible with non-driven equilibrium MD, using a Green-Kubo approach to calculate λ [40]:

$$\lambda = \frac{1}{Ak_BT}\int_0^\infty \mathrm{d}t\langle F_f(t)F_f(0)\rangle, \tag{4.12}$$

where A is the surface area of the substrate in the observation box and $F_f(t)$ is the total microscopic tangential force at the surface. Recalling, that $b = \eta/\lambda$ gives the slip length. However, this method has the disadvantage, that the viscosity at the wall differs in general from the viscosity in the bulk [267]. We used MD simulation findings to adjust the intrinsic slip behavior of the PF model.

LB simulations While most of the LB studies impose no-slip boundary conditions, methods are known to reproduce intrinsic slip [124]. Kunert et al. [162] used these methods to understand the apparent slip in random rough microchannels. They aim to estimate the effective wall position in means of the roughness parameters. Ridges with Gaussian height distribution show that the effective wall position is roughly at the position $h_{\text{eff}} = h_{\text{mean}} + 3.1\sigma_h$, where σ_h is the standard deviation of the Gaussian.

This means in practice the slip is dominated by the largest posts. Sbragaglia et al. [265] report in a study of apparent slip in microchannels with regular and non-regular distributed ridges, that the slip lengths decrease dramatically when the wetting situation is Wenzel-dominated. In the vapor-supported state they report slip lengths of 15nm.

4.1.2. PF simulations

As already discussed in the model section, the PF model has the merit, that no BC has to be defined explicitly. Indeed, the effective BC is obtained from the steady state solution, when working at low Reynolds- and low capillary number. The effective (macroscopic) slip comes from the friction force $\mathbf{f}_{\text{wall}}$, like in eq. (4.1) and (4.2). The intrinsic slip is controlled by $\mathbf{f}_{\text{wall}}$, while the apparent slip depends also on the geometry. Before we can use our model to measure effective slip lengths, the free parameter k of $\mathbf{f}_{\text{wall}}$ has to be adjusted. We recall the definition of the friction force

$$\begin{aligned}\mathbf{f}_{\text{wall}}(\mathbf{r}) = \quad & -k\varepsilon_{\text{LJ}}\rho(\mathbf{r})\left(\mathbf{v}(\mathbf{r}) - \mathbf{v}_{\text{wall}}(\mathbf{r})\right) \times \\ & \int \mathrm{d}\mathbf{r}' \left(\rho_{\text{wall}}(\mathbf{r}')\frac{1}{\sqrt{\pi}^3\sigma^3}\mathrm{e}^{-\frac{(\mathbf{r}'-\mathbf{r})^2}{\sigma^2}}\right) .\end{aligned} \tag{4.13}$$

As friction is an irreversible process, the ansatz is linear to the velocity difference between the fluid and the wall. Further, it is reasonable that the friction increases with higher fluid density at the wall. Barrat et al. confirmed this hypothesis in MD simulations [23, 24]. The left panel of fig. 4.3 shows that the intrinsic slip b increases with the Young's contact angle [130, 306, 307] (diagram from ref [130]). Therefore, the friction force is coupled to the Lennard-Jones parameter ε_{LJ}. Finally, the force is proportional to the wall particle density ρ_{wall}. In (4.13) the wall density is smoothed with a Gaussian, which allows for larger time steps in the numerical schemes than a sharp friction force distribution. Indeed, due to thermal motion and the molecular arragnement of the wall atoms, it is reasonable to model a diffuse friction field with a thickness of approximately 1σ. The right panel of fig. 4.3 displays the slip length as a function of $\cos\theta$, which corresponds quite well to the MD results alongside. (Notice the different scaling θ and $\cos\theta$ in both panels. See a selection of the 1 parameter slip data in the left panel). Low contact angles give no-slip BC as expected. The parameter k is chosen to be $100\tau\sigma$ to give agreement with the microscopic simulations. Higher values of k can be used to model rather θ independent no-slip. The insert shows a Poiseuille- and Couette-flow profile, and the definitions of b and z_0 of the 2 parameters slip measurement described above. The dashed line in the main panel indicates the hydrodynamic wall position z_0. Interestingly it slightly varies with $\cos\theta$ and is about 1σ inside the fluid, which is consistent with the findings of ref. [24].

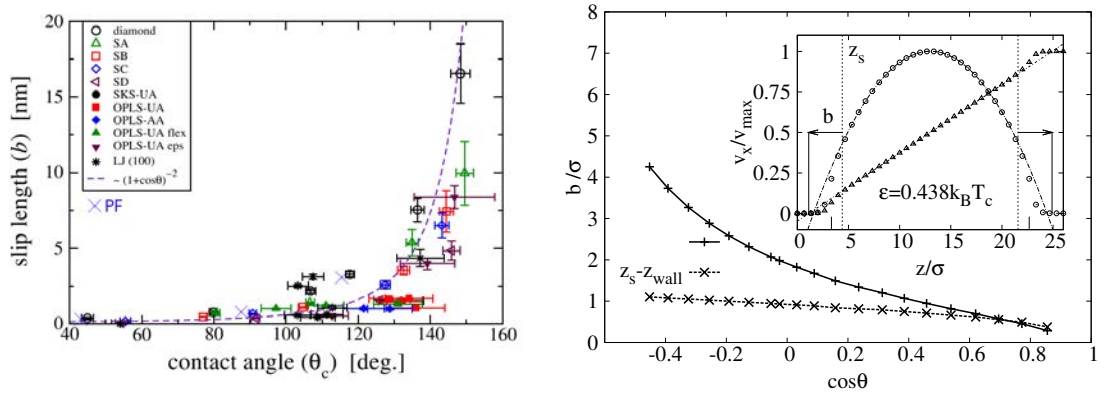


FIGURE 4.3. Left *MD simulation results of Huang et al. for the intrinsic slip length as a function of the wetting angle θ_c. Figure taken from ref. [130]. The crosses mark approximately a selection of the PF results from the right panel.* Right: *Slip length b and position of substrate $z_s - z_{\text{wall}}$ as a function of the intrinsic angle θ in a slit geometry with a friction constant $k = 100\,\tau\sigma$.*
Insert*: Velocity profile parallel to the slit with either flow-profiles. The linear and quadratic fit parameters are used to compute the slip length b and the the position z_s where the slip boundary condition is applied. z_{wall} is indicated by larger tics ($z_{\text{wall}} = 3\frac{1}{3}\,\sigma$ and $22\frac{2}{3}\,\sigma$).*

With this well adjusted model, we now investigate the slip on substrates with nanometric roughness. In particular we are interested if there is a noticeable slip enhancement due to nanometric roughness features like the needle tips. Therefore we performed PF simulations with the same crenels as in chapter 3. Figure 4.4 shows the slip length b (1 parameter fit) for crenels with three different depths ($h = 0.7\sigma - 10.7\sigma$, indicated by colors) and fixed pillar and crenel width $L - a = a = 13.3\sigma$. Simulations were performed either with flow fields perpendicular ($\square$) or parallel to the ridges ($+$). Bifurcation occurs due to coexistence of Wenzel and Cassie-Baxter states. Larger b corresponds to CB configurations. The slip in the Wenzel state is rather negligible ($b < 3\sigma$) and significant apparent slip occurs in the CB state only. One may notice slip anisotropy between perpendicular and parallel flow. Like in the Philip and Lauga-Stone theory both directions exhibit different slip lengths by a factor of roughly 2, when $h > 5.3\sigma$, even in the Wenzel state. Figure 4.5 displays again the slip length b, but this time for different crenel widths $L - a$ and fixed crenel depth h and pillar width a ($a = h = 13.3\sigma$). For very tiny crenel width, where intrusion is hampered, no significant differences from a Wenzel slip behavior is observed. Since the plotted data are the direct measurements, the dependency of b on $L - a$ is due to the larger fraction $1 - f$ of the total area, which is not in contact with the wall. Again, rather small slip

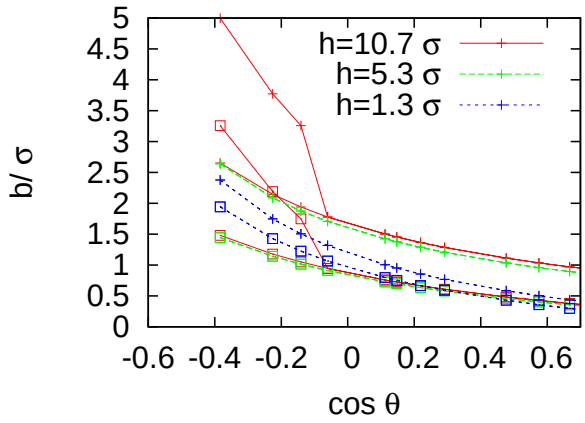


FIGURE 4.4. *Slip length b as a function of* $\cos\theta$ *on crenelated rough surfaces for three values of the crenel depth h (colors). $+$ symbols correspond to parallel slip and $\square$ symbols to perpendicular slip. Bifurcations ($h = 10.7\sigma$) indicate coexisting CB and W states ($T = 0.7T_c$). Branches with larger b are CB states.*

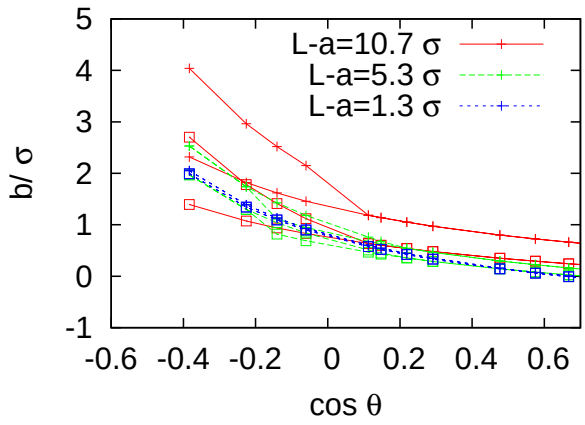


FIGURE 4.5. *Like fig. 4.4 (see also caption there) but for various crenel width d (colors).*

lengths are observed in the W state, noticeably larger in the CB state. Figure 4.6 shows the same diagram for nanometric pillar width a. We recall that nanometric $a < 2\sigma$ exhibit the non-wetting amplifying needle tip effect, which renders the Wenzel contact angle non-wetting even for intrinsic wetting behavior. Interestingly, there is no significant effect on the slip length b due to needle tips in the W state, but enlarged range of CB-supporting Young's angles θ, makes needle decorated substrates good candidates for efficient flow in nano-devices. The viscous dissipation in an incompressible fluid

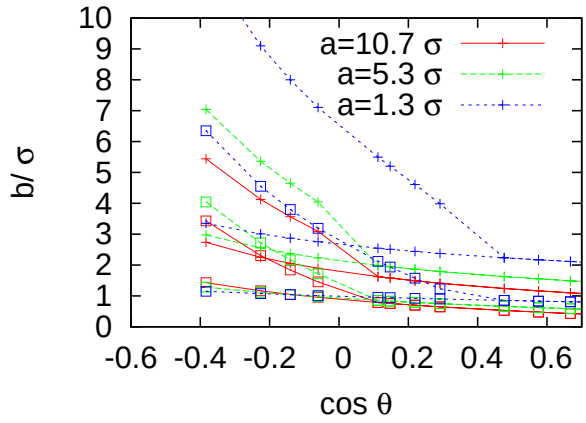


FIGURE 4.6. *Like fig. 4.4 (see also caption there). The pillar width a is varied (colors).*

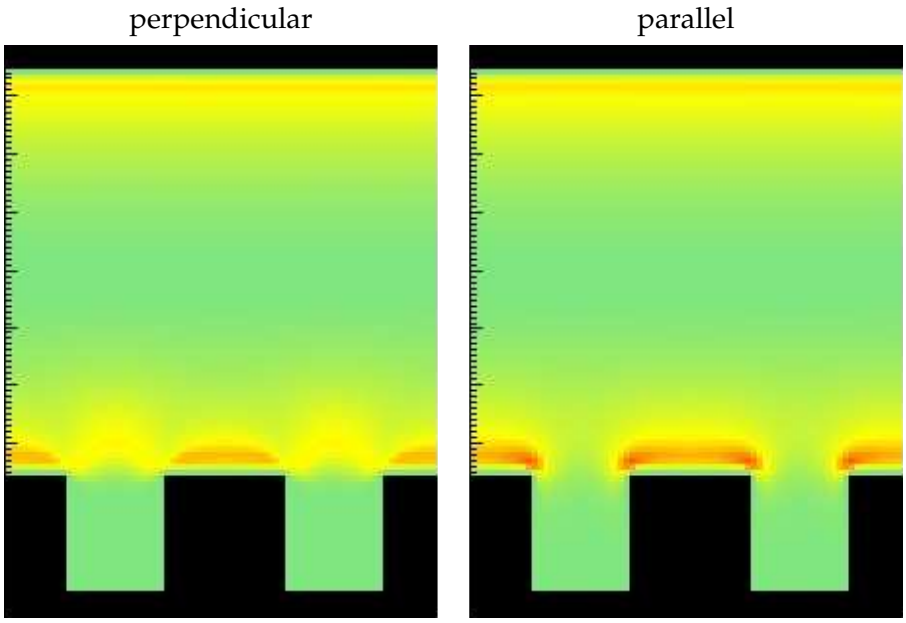


FIGURE 4.7. *Dissipation power density for PF in W wetting state:* left: *perpendicular flow* right: *parallel flow*

is given by

$$P_{\text{viscous}} = \int \mathrm{d}^3 r \frac{1}{2\eta} \Sigma : \Sigma, \tag{4.14}$$

where Σ is the viscous stress tensor and η the shear viscosity [172]. In the Wenzel state

we can use this expression as an approximation to study, where dissipation in the flow occurs. Figure 4.7 shows the dissipation in parallel and perpendicular flow direction. Clearly, the dissipation signature is different. While in the parallel flow, the dissipation is rather homogeneous distributed apart from the walls, in the perpendicular flow profile the corrugations behave like obstacles and lead to extra dissipation between the crenels.

4.2. Apparent slip vs. intrinsic slip

For a crenelated wall as e.g. considered in fig. 4.7 the slip length can be determined as well by using the same prescription: a Couette- and a Poiseuille-flow are applied and extrapolated inside the walls to measure the effective slip length B and Z_s (see eq. 4.8). We use capital letters for B and Z_s here to distinguish between the effective slip length of the textured wall and the intrinsic slip length b of the planar wall with the same chemical nature. The main question for practical applications is to understand which length scale controls the slip length: the intrinsic slip length b or the periodicity of the structure L. Macroscopic calculations based on hydrodynamics have been done in ref. [73] for a simplified geometry: the crenels in the Cassie-Baxter state are represented by an alternation of stripes of two types: stripes with infinite slip length represent the liquid-vapor interfaces sustained between the crenels while the stripes with a slip length b are representing the top of the crenels, where the liquid is in contact with the wall. The surface is planar for these calculations. It has been shown in particular that a flow parallel to the stripes can exhibit quite a large slip length $B_\parallel$ which is proportional to the largest of the two length scales. If $f \equiv a/L$ denotes the fraction of the crenels in contact with the liquid in the Cassie-Baxter state, an approximate relation between $B_\parallel$, b and L can be written as:

$$\frac{B_\parallel}{L} \simeq \frac{1}{f}\frac{b}{L} + c \tag{4.15}$$

where c is a constant close to 0.1 for $\phi_s = 0.5$, and between 0.1 and 0.3 for $\phi_s = 0.25$ ref. [73]. We could check with our model (fig. 4.8) that the slip length measured for the crenelated geometry in the Cassie-Baxter state agrees nicely with this expression. This nice behavior is somehow a crosscheck between the PF model, that contains all the complexity of the dynamically moving interfaces, and the simplified geometry considered in ref. [73]. It is important to mention here that these results have been obtained at low capillary number (*i.e.* the liquid-vapor interface is not affected by the

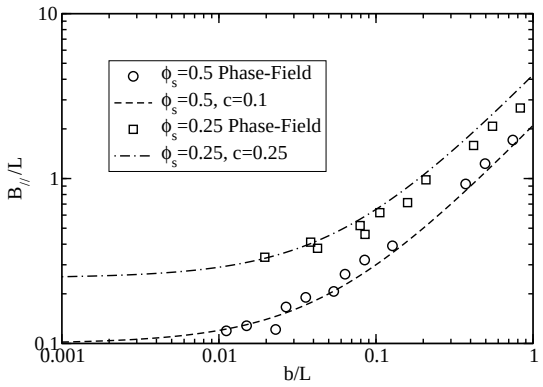


FIGURE 4.8. *Scaling law satisfied by $B_{\|}$ as a function of b and L. the symbols correspond to the values obtained with the PF model for a crenelated surface, the dashed and dot-dashed lines corresponds to the simple approximation (4.15) for $\phi_s = 0.25$ and $\phi_s = 0.5$. It is remarkable that the obtained values of c are in quantitative agreement with fig. 12 of ref. [73], though the geometries are different (see text).*

flow). A deformation of the interface by the flow at large capillary number may change the picture.

4.3. Capillary rise: Lucas-Washburn-law

To test the dynamical behavior of the model the capillarity force is used to pump the liquid phase into a pore with a slit geometry. In 1918 Lucas and independently in 1921 Washburn gave a classical theory of the penetration of liquids into wetting pores [310, 187]. Capillary rise occurs, when a pore with hydrophilic interior is in contact with a fluid reservoir. The local contact angle in the capillary tries to gain its thermodynamic equilibrium state: the Young's angle. To fulfill this criterion the meniscus is concavely curved and the Laplace pressure builds up a driving force, which pumps the fluid inside the pore.

Considering a pore made from a perfectly wetting substrate the transport velocity is proportional to the pressure gradient and to $1/\eta$

$$\mathbf{v} \propto \frac{1}{\eta}\frac{\mathrm{d}p}{\mathrm{d}x}. \tag{4.16}$$

The transport is driven by the Laplace pressure due to curvature $\mathcal{H}$ of the meniscus which is $-\gamma\mathcal{H}$. Assuming the position of the meniscus as l the pressure gradient $\frac{\mathrm{d}p}{\mathrm{d}x} \propto \frac{\gamma\mathcal{H}}{l}$ and noting $\mathbf{v} = \frac{\mathrm{d}l}{\mathrm{d}t}$ we get the well-known Washburn law for a slit geometry:

$$l^2 = \frac{D\gamma\cos\theta}{3\eta}t, \tag{4.17}$$

where D is the distance between the confining planes in the slit geometry. This test is well suited to check the coupling between the thermodynamic description of the model and hydrodynamics. Without any external driving, we can compare the meniscus position l with the theoretical expression (4.17).

With LB methods, the Lucas-Washburn scenario attracted recently interest since of new experiments in microfluidics. Diotallevi et al. [80] derived a generalized version of the Lucas-Washburn law incorporating intrinsic slip and finite viscosity of the supplanted gas and found good agreement with Shan-Chen like multiphase modelling. In ref. [218] Mognetti et al. investigated capillary filling in patterned channels. Obstacles and pinning lines can block the imbition, depending on the intrinsic contact angles and the details of the geometry.

4.3.1. PF model test

To compute this capillary driven motion, we consider a system with a reservoir of liquid connected to the pore, as depicted in fig. 4.9. This figure shows the meniscus

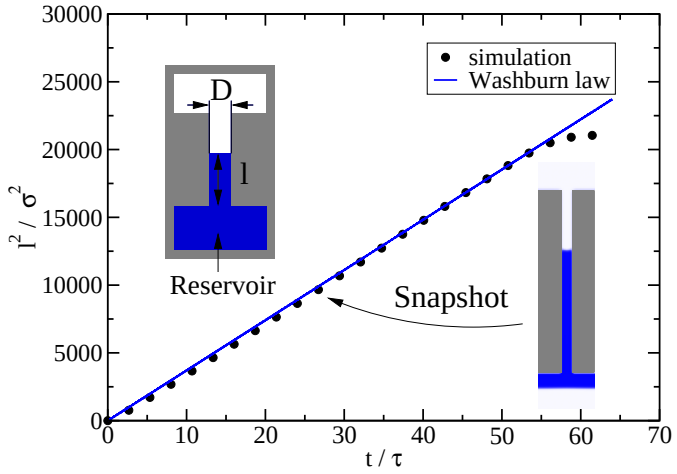


FIGURE 4.9. *Position l of the meniscus in the Washburn capillary over the time. The geometry is indicated schematically on the left of the figure, a reservoir contains the liquid that enters in the pore and climbs until it reaches the top (there is no gravity here). A snapshot of the actual system is shown on the left, it corresponds to the point indicated by the arrow. The simulation shows clearly the square-root relation showed by Washburn in 1921 [310, 187], and the theoretical line is calculated using the Washburn law with no adjustable parameter. l saturates when the meniscus reaches the top of the pore.*

position in the simulation plotted over the time, compared with the theoretical curve. The agreement is quite good; all the parameters entering in the Washburn law have been measured separately and there is no adjustable parameter here. The pore thickness is $D = 9.66\,\sigma$, $\gamma_{LV} = 0.342\,k_B T_c/\sigma^2$, $\cos\theta = 0.6$, and $\eta = 1.78\,10^{-3}\sigma^3/(k_B T_c \tau)$ for this simulation. The friction between the walls and the liquid is large enough to ensure a no-slip boundary condition. This is a strong test of the performance of the model since it couples the static properties of wetting to the dynamical penetration process.

4.4. Contact angle hysteresis

The term contact angle hysteresis describes the effect, that on rough surfaces (chemically or geometrically) the observed apparent wetting angles are history dependent and lie in some interval around the theoretically thermodynamic equilibrium angle. The Young equation assumes a perfect planar and homogeneous surface, which in reality is rarely found. Slight impurities or defects on the substrate might have a large influence on the contact angle due to pinning. Indeed, this is the reason, why up to now—more than one and a half century ago—no experimental verification of the Young equation is reported [307]. Johnson and Dettre [146] were the first reporting pinning at a chemical step from hydrophilic to hydrophobic patches, due to the free energy cost of dewetting the former and wetting the latter. Oliver and others [234] made first experiments with sharp edges, where line pinning occurred. This was already postulated by Gibbs [111] in is nowadays called Gibbs criterion. Figure 4.10 illustrates this criterion (panel b). It states: Assuming a hydrophilic contact angle and increasing the volume of a drop, the contact line keeps pinned at the sharp edge, till the contact angle with the inclined wall equals the Young angle.

Kusumaatmaja et al. [165, 167, 168, 169] studied contact angle hysteresis on chemically and geometrical rough surfaces, symmetric and asymmetric grooves and on square posts. For two dimensional drops on chemically rough surfaces the authors refined a theory of Marmur [197] to describe the stick—slip—jump dynamics, i.e. alternating hydrophilic and hydrophobic stripes (see panel c in fig. 4.10). The idea is to analyze the Gibbs energy of the cylindrical drop when it is quasi statically increased. The surface area of the cross section

$$S = R_0^2 \frac{\theta - \sin\theta_{\text{app}} \cos\theta_{\text{app}}}{\sin^2\theta_{\text{app}}}, \tag{4.18}$$

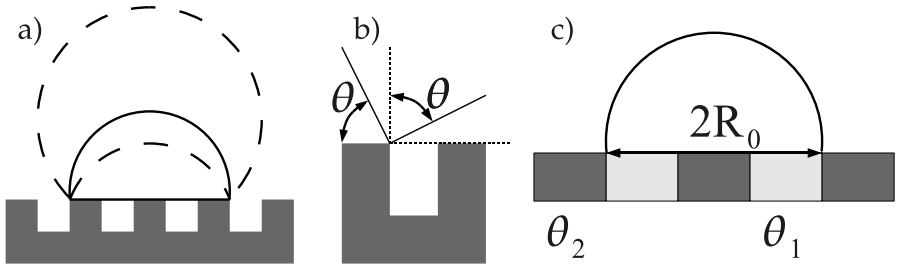


FIGURE 4.10. a) *Contact angle hysteresis during evaporation* b) *Illustration of the Gibbs criterion* c) *Pinning on chemically rough surfaces*

where θ_{app} is the apparent contact angle. The liquid-vapor interface length is $L = 2R_0\theta_{app}/\sin\theta_{app}$, so that the Gibbs energy reads

$$G = \gamma L + \int (\gamma_{SL}(x) - \gamma_{SV}(x))\,\mathrm{d}x, \tag{4.19}$$

where the integral goes over the base line of the drop. For stripes with equal thickness this formula simplifies (using the Young eq.) to

$$G/\gamma = \frac{2R_0\theta_{app}}{\sin\theta_{app}} - (2k+1)\cos\theta_1 - 2k\cos\theta_2 - 2x\cos\theta_2, \tag{4.20}$$

where $0 < x < 1$ and k is the number of covered stripes. The hydrophilic and hydrophobic stripes have intrinsic contact angles θ_1 and θ_2 resp. Analysis of this Gibbs energy equation shows stability at the pinning line: The triple line sticks at the border from the hydrophilic to the hydrophobic stripe, when advancing. At a certain contact angle (given by the Gibbs criterion[1]) it slips over the hydrophobic stripe and when reaching the next hydrophilic stripe, the contact line jumps to the next stripe border. This is qualitatively found also in the 2D LB simulations, too [168]. The authors emphasize, that in 3D the case is far more complicated and due to line pinning no contact angle at the triple line can be defined, a rather heuristic solution is to define an averaged contact angle from fitting the drop profile far away from the triple line. Importantly they state that the precise details of the surface profile/patterning control the contact angle hysteresis, thus strategies including averaging over the roughness can not lead to satisfying results [168]. Recently the same authors reported that asymmetric grooves as found on butterfly wings [169] yield preferred flow directions, due to contact angle hysteresis. Drops in regularly patterned microchannels are studied by Zhang and others [326]. They found on superhydrophobic substrates stick—jump—slip dynamics when driving the drops with a body force through the channel. Surprisingly, they found partial imbition to the grooves, indicating large capillary numbers.

Marmur studied the Gibbs energy systematically with a model similar to that one described above. He reported results as a function of the drop volume and found an oscillatory behavior of the apparent contact angle [199, 201]. The succession of apparent contact angles was connected to a succession of the metastable states. The conclusion of Marmur's analysis is that the receding and advancing contact angles in this scenario are volume dependent and the larger the drop is the closer are both angles to the apparent thermodynamic contact angles from the classical wetting theories. Formally the contact angle hysteresis can be defined as the interval from the lowest to

[1] The Gibbs criterion on chemically heterogeneous substrates allows local contact angles between θ_1 and θ_2, when the triple line is pinned between the stripes

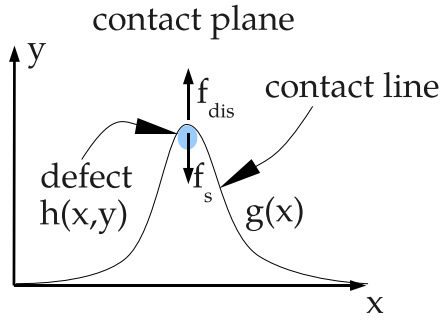


FIGURE 4.11. *Illustration of the contact angle hysteresis model of Joanny and de Gennes [143]. The triple line is distorted due to a pertubation field of the surface tensions $h(x, y)$, which leads to a distortion force f_{dis}. Here, an example of a local defect is sketched. The blue spot marks an area where $h(x, y)$ is non-zero. An elastic force f_{s} acts to straighten the line. Stable contact angles are found when both forces are balanced.*

the highest contact angle in the succession of metastable states, while in experiments only those are probed, for which energy is available to overcome the energy barriers (e.g. vibrational energy).

Joanny et al. [143] proposed a model to described the hysteresis at a pronounced geometrical or chemical defect. Starting from a perturbation field of the surface tensions

$$h(x, y) = \gamma_{\mathrm{SV}}(x, y) - \gamma_{\mathrm{SL}}(x, y) - \gamma \cos\theta, \tag{4.21}$$

where $\gamma \cos\theta$ is the surface averaged wetting energy, one wants to derive the distortion energy of the triple line, which is parametrized path $g(x)$. The authors derive for weak perturbations h, that the distortion energy is

$$F_{\mathrm{dis}} = \int \int_{g(x)}^{\infty} h(x, y) \mathrm{d}y \, \mathrm{d}x \tag{4.22}$$

which is a functional of the triple line path. The local force $f_{\mathrm{dis}}(x)$ is thus a function of the $g(x)$. On the other side an elastic force $f_{\mathrm{s}}(x)$ (modeled with a spring constant) arises from the minimization principle of the liquid-vapor interface. Thus, stable states need a balance of both forces. Figure 4.11 illustrates this. An analysis of several types of pertubations fields $h(x, y)$ shows, that e.g. smooth Gaussian-like pertubations may or may not lead to contact angle hysteresis at a single pronounced defect. Step-like defects always show contact angle hysteresis.

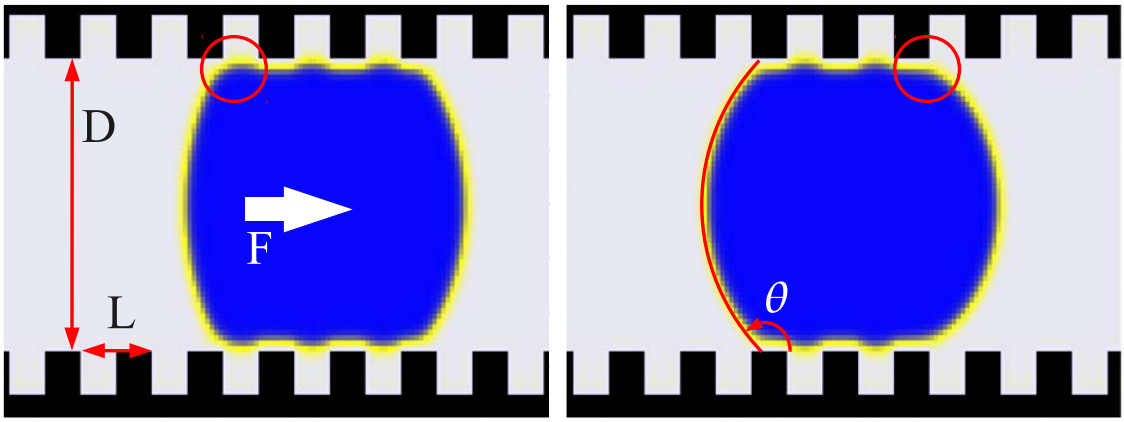


FIGURE 4.12. *Drop in a slit geometry with crenelated walls and a horizontal driving force. The two images correspond to pinning situations: the left drop is pinned at the rear (the pinning point is indicated by a circle), and the right drop at the front. Pinning of an interface results in a deformation of its shape: pinning at the front increases the contact angle at the pinning point, whereas pinning at the rear decreases it. For contact angles between θ_r and θ_a the drop sticks at the pinning point.*

4.4.1. PF simulations

The synchronous solving of the density-evolution equation (2.72) and the transport equation (2.76) enables us also the study of stick-slip transitions of droplets on a rough wall. This paragraph demonstrates the ability of the model to investigate the contact angle hysteresis.

When a sticking drop is spread over an inclined surface with certain spatial heterogeneities several contact angles are observed as a function of the inclination [245] or more generally as a function of the driving force. If the driving force F overcomes a certain threshold F_c the drop starts to move. At the point $F = F_c$ the maximal advancing contact angle θ_a at the front line of the drop and the minimal retarding contact angle θ_r at the rear of the drop define an interval around the equilibrium contact angle θ for which the drop sticks.

For simplicity we consider a setup with regular heterogeneities as shown in fig. 4.12. The force F is applied through an uniform acceleration field a_g similar to a gravity field oriented in the direction of F (see fig. 4.12). Instead of measuring the contact angle directly we used the more robust method of measuring the curvature

radius of the drop around the centerline of the setup. Depending on the details of a direct measurement method both methods differ typically between 5° and 10°. Since the setup is at low capillary number ($Ca \leq 0.1$) we assume a circular shape of the drop in the channel center and fit the curvature radius to points on an isodensity-contour as it is shown in fig. 4.12. For further improvement of the estimation we averaged the curvature radius R over the best fit results of three different isodensity profiles. The contact angle is given by $\theta = \pi/2 + \arcsin(D/2R)$.

When the drop is moving, the rear and the front interfaces oscillate and we can follow the variation of their radii, R_a for the advancing front and R_r for the receding one. The left panel of fig. 4.13 shows the curvature radius of the interfaces over the position of the drop center of mass C for various accelerations a_g. The x-axis is scaled in the length unit of one crenel L, the periodicity of the system. Accelerations larger than $0.67\sigma/\tau^2$ are sufficient to move the drop over the heterogeneities, lower values correspond to a drop trapped by the crenels (sticking drops). The two configurations shown in fig. 4.12 correspond indeed to the sticking case, and two pinning situations are possible in this case: a pinning of the rear line (left image) or a pinning of the front line (right one). The front line pinning corresponds to $a_g = 0.33\sigma/\tau^2$ while the rear line pinning has been obtained for $a_g = 0.47\sigma/\tau^2$. For these two cases the drop sticks to the crenels and its center of mass is thus fixed. After a transient the drop stops and the points corresponding to the steady configurations $a_g = 0.33\sigma/\tau^2$ and $a_g = 0.47\sigma/\tau^2$ are indicated by the two arrows on fig. 4.13 (left). When $a_g \geq 0.67\sigma/\tau^2$ the drop moves and we can follow the variations of the front and rear radius as a function of the position of the center of mass in fig. 4.13 (left). Interestingly, the variations of R_a and R_r are only weakly sensitive to the value of a_g in this regime, we can only note a difference in the relaxation dynamics after overcoming the pinning: The dynamics is slow as long as the meniscus is pinned, and the radius of curvature is thus only fixed by the position of the center of mass of the drop in this regime, while the dynamics is fast after unpinning, and we observe a dependence in a_g in this case. Unpinning occurs when the advancing (front) radius is minimal for a front line pinning, while it occurs when the receding (rear) radius is maximal for a rear line pinning. These extremal values of R_a and R_r can be converted in extremal values of the corresponding contact angles: unpinning occurs when the force is large enough to overcome a critical contact angle. We estimated these critical values by taking the maximal retarding contact angles θ_r and the minimal advancing contact angles θ_a, resp., for the moving drops and extrapolate the values to the zero velocity limit. The results are printed in tab. 4.1. The receding contact angle $\cos\theta_r = -0.51$ we found is around the equilibrium contact angle $\cos\theta = -0.45$. Other groups [219, 168, 326]

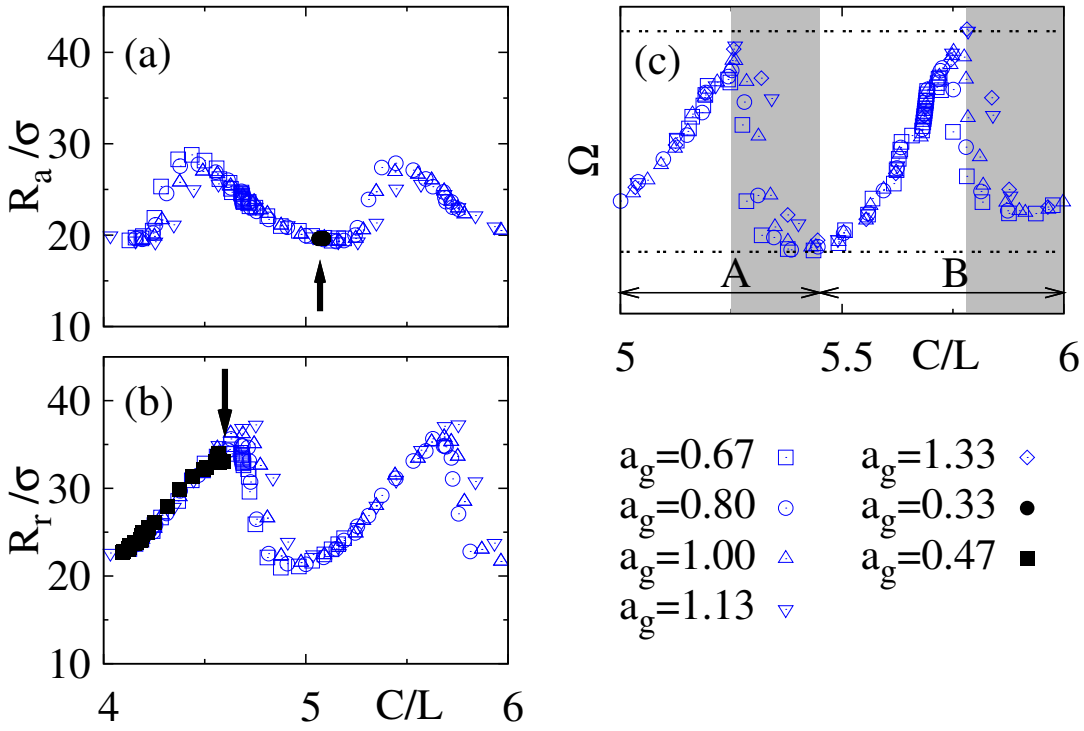


FIGURE 4.13. *(a/b) Advancing radius R_a and retarding radius R_r of the a drop driven along a heterogeneous substrate as shown in fig. 4.12 plotted over the position of the center of mass C for values of a_g ranging from $0.33\sigma/\tau^2$ to $1.33\sigma/\tau^2$. The center of mass is scaled by the period L. After overcoming the pinning point at the front line the interfaces relax rapidly to a larger curvature radius and vice versa for the retarding interface. The sticking drop marked in the bottom panel belongs to the acceleration $a_g = 0.47\sigma/\tau^2$, where the drop is pinned at the rear line. The mark in the top left panel belongs to the acceleration $a_g = 0.33\sigma/\tau^2$. In this case the drop is pinned at the front. This curve is shifted by one period to the right for better clarity.*
(c) Grand canonical potential Ω of the system as a function of the center of mass C. The gray highlighted regions show the jump/relaxation dynamics which can differ slightly with the applied acceleration while the slip-stick dynamics (white regions) are the same for different accelerations a_g.

report that θ_r is equal to θ but the deviation we observe here is a consequence of the microscopic structure we impose by the substrate (repelling corner-energies). The

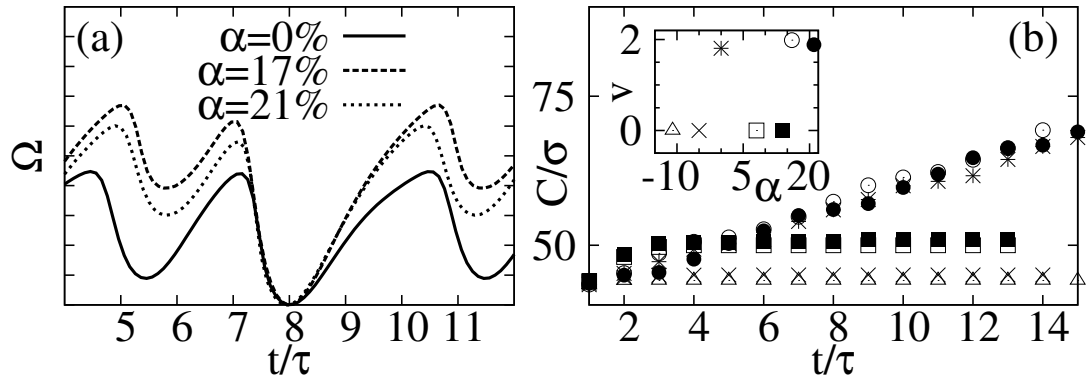


FIGURE 4.14. *(a) Grand canonical potential Ω of drops with different sizes (shifted to be one upon the other) as a function of time t. The $\Delta\Omega$ barrier clearly varies strongly with the size of the drops.*
(b) Center of mass position C as a function of time. Due to the complex variations of $\Delta\Omega$ with the volume one observes moving drop and sticking drops alternating when the volume is increased. The volume ($\alpha = -5\%, 0\%, 8\%, 14\%, 17\%, 21\%$) corresponding to the symbols in the main panel is indicated in the insert plot, which shows the mean velocity over the volume parameter $\alpha = (S - S_0)/S_0$.

advancing contact angle we found is $\cos\theta_a = -0.87$. This is also around the values, the other groups found.

Figure 4.13 (right) shows the grand canonical potential Ω of the system plotted over the center of mass of a drop with constant volume for several forces. If the drop is pinned the system stays in a steady state at a constant potential whereas the moving drops probe the full non-equilibrium profile of Ω. The figure presents a succession of peaks: the grand canonical potential barriers that the drop needs to overcome in order to move. The peaks look similar but are in fact not identical: two adjacent peaks correspond to a successive pinning of the front meniscus and a pinning of the rear meniscus (the difference is better seen if we look at the minima, the difference in the maxima is indeed small in the case we consider in fig. 4.13). An interesting feature is the very weak dependence of the grand canonical potential landscape with respect to the force: for all forces which are sufficient to push the drop the potential is nearly the same; This shows that a model of a drop moving in fixed potential should be sufficient to describe the dynamics in this case.

Of course the pinning situation depends on the drop size. For certain drop sizes

a_g	v	R_a	$\cos\theta_a$	R_r	$\cos\theta_r$	Ca
	$\to 0$	19.5	-0.87	33.6	-0.51	
0.67	1.05	19.4	-0.88	35.0	-0.49	0.02
0.80	1.75	19.3	-0.88	35.7	-0.48	0.03
1.00	2.48	19.3	-0.88	36.7	-0.46	0.05
1.33	3.57	19.1	-0.89	38.9	-0.45	0.07

TABLE 4.1. *Average velocity v, advancing radius R_a, retarding radius R_r and the corresponding contact angles θ_a, θ_r for different accelerations a_g in σ/τ^2 to extrapolate the contact angle hysteresis at $v \to 0$. v is the average velocity in σ/τ. The intrinsic equilibrium contact angle is $\cos\theta = -0.45$ an the effective contact angle is $\cos\theta_{eff} = -0.69$.*

the pinning at the front and at the rear occurs together, whilst in other cases only one interface is pinned at the same time. Therefore the acceleration a_{gc} which is needed to overcome the pinning varies but not the critical contact angle. We consider the influence of the drop size in fig. 4.14. This figure shows the grand canonical potential Ω for drops with different volume but exposed to a constant acceleration to demonstrate the effect of synchronous pinning. To show the sensitivity with respect to the drop size, we introduce the parameter $\alpha = (S - S_0)/S_0$ which indicates the variation of the drop volume S with respect to the reference drop (S_0) of fig. 4.12: *e.g.* $\alpha = 10\%$ means that we increased the drop volume by 10%. First we can see that the peak of the potential which has to be overcome is quite sensitive to the drop size: the different curves in fig. 4.14 (left) are superimposed to illustrate the $\Delta\Omega$ between the minimum and the maximum of the Ω-landscape. We selected the values of α that corresponds to a motion of the droplet in fig. 4.14 (left), but changing the drop size for a given applied force can also result in the sticking of the drop, when rear and front pinning occurs at the same time. This effect is illustrated in fig. 4.14 (right) where we can observe a succession of moving drops (pinning-unpinning motion of the drop) and trapped drops in a steady state.

4.4.2. Conclusion

Nanometric dynamics is an important feature of the PF/DDFT model. We checked with the Washburn cell the correct interplay between the thermodynamic description of the model and the transport equations. We employed the model for testing contact angle hysteresis on nanometric corrugated nanochannels and in agreement with macroscopic LB simulations we find jump—slip—stick dynamics with $\cos\theta_a = -0.81 < \cos\theta_{\text{eff}} = -0.69 < \cos\theta_r = -0.51$.

Since the complex nature of the pinning phenomenon itself, together with the difficult statistics of the spatial pinning point distribution contact angle hysteresis is a challenging problem for experimentalists. Moreover, a consistent theory is still missing. Therefore, reliable simulation methods are needed to clarify the understanding of the contact angle hysteresis.

5. Minkowski functionals and Minkowski tensors

In many disciplines of science careful description of morphology is needed. The morphology of complex spacial patterns can be roughly classified into certain structure types. To cite some examples, foams are considered to be cellular patterns, limestones or sandstones are porous, biopolymers build up network-like structure, surfactants can create bicontinuous intertwined networks or lamellar phases (e.g. eutectic alloys) can exhibit rod-like structures. Other classifications would be ordered—e.g. hexagonal, cubic, icosahedral—or disordered, fractal, percolating etc. Often quantitative descriptors are only relevant to one specific type; e.g. tangent vector distribution estimators in networks or percolation diameters in porous media. Scalar Minkowski functionals (MF) and Minkowski tensors (MT) are a class of morphology descriptors which apply to nearly any kind of patterns in real-space.

In this chapter we will review the theory of Minkowski measures (scalar and tensorial) which are used in the following to describe morphology in: first spinodal decomposition patterns (2D) in section 5.3 of this chapter and second in sphere packings or molecular ensembles (3D) in chapter 6. In this section we will therefore concentrate on the special cases of 2D and 3D systems. With (5.1), (5.25) and (5.27) we define morphological measures, which are employed in the chapters below.

MF are inspired by stochastic and integral geometry as robust and continuous structure descriptors and were introduced to physics to study point patterns [211, 206] and porous media [207]. Nowadays they are established as concise morphology parameter and used to study spinodal decomposition [282] or to expand thermodynamic potentials of confined fluids [170].

Tensor-valued generalizations of the scalar Minkowski functionals have been used to investigate orientation in ice core drills [110], galaxy cluster formations [28], networks of neurons [28] and orientation in F-actin networks [274]. MT have also proven useful to develop free energy functionals (like the DFT-Rosenfeld functional of hard spheres)

for non-spherical shapes [205] and to describe DNA-conformation [123]. MT have been also used to model molecular motors [285].

5.1. Minkowski functionals

There are two possible routes to define Minkowski measures. We will first present an approach which is based on differential geometry. This approach is more popular in physics since it allows for a more intuitional understanding of MF and MT. For the sake of comprehension, an equivalent approach based on fundamental measure theory is briefly discussed in the second part of this section. This latter approach is useful to prove some strong theorems, which make Minkowski measures such powerful shape measures. We focus on these theorems in the last part of this section.

We will denote a compact set (body) P with non-empty interior in Euclidean space $\mathbb{E}^d$, where $d = 2, 3$ is the dimension. Assuming a sufficiently smooth bounding surface ∂P of P, the $d+1$ integrals

$$W_0 = \int_P \mathrm{d}^d r \tag{5.1}$$

$$W_\nu = \frac{1}{3} \int_{\partial P} G_\nu(\kappa_i(\mathrm{r}))\mathrm{d}^{d-1} r \tag{5.2}$$

are the scalar Minkowski functionals W_ν, $0 \leq \nu \leq d$. G_ν is the ν-th symmetrical polynomial of the $d-1$ principal curvatures κ_i of the bounding surface ∂P, i.e. in two dimensions $G_1 = 1$ and the curvature $G_2 = \kappa$. In three dimensions G_ν are: $G_1 = 1$, the mean curvature $G_2 = \frac{1}{2}(\kappa_1 + \kappa_2) = \mathcal{H}$ and the Gaussian curvature $G_3 = \kappa_1\kappa_2 = \mathcal{K}$. $\mathrm{d}^d r$ denotes the volume integration and $\mathrm{d}^{d-1} r$ the scalar surface integration. This definition naturally applies to convex and non-convex bodies whatever their topology are, when the surface is sufficiently smooth. It is noteworthy to mention that in spite of the occurrence of local curvature measures in these integrals, they are well-defined also for polyhedra with sharp edges. This fact is easy to understand in the framework of fundamental measure theory and will be discussed below as a consequence of the Steiner's theorem. The prefactors in eq. (5.1) are chosen in a way that for an unit sphere all MF give the same value $4\pi/3$ in three dimensions and 2π in two dimensions. For the rest of this paragraph, we restrict ourselves for the sake of clarity to $d = 3$. Equation 5.1 is (up to prefactors) equal to the volume, the surface area, the surface-integrated mean curvature $\mathcal{H}$ and the surface-integrated Gaussian curvature $\mathcal{K}$. Therefore MF are motion-invariant. This means that MF are invariant under rotations g_r in the rotation group $SO(3)$ and translations g_t in the translation group $T(3)$.

Before we turn to MT we shall use the integral geometrical approach to demonstrate some useful features of MF in the next paragraph.

5.1.1. Integral geometry of Minkowski tensors

This paragraph gives a brief introduction of the way in which MF are properly defined in mathematics. Minkowski measures have been known in mathematical disciplines for decades, starting mainly with the works of Hadwiger [117] in 1957. Hadwiger already proved the strong completeness theorem for scalar Minkowski measures. For the last 15 years scalar Minkowski measures have also become known in physics [211, 206]. Already Hadwiger [118] and Schneider [119] studied vector-valued Minkowski measures. First ideas on Minkowski tensors were published by Müller [223]. Completeness theorems of tensor-valued Minkowski tensors were published in 1999 by Alesker [4] and linear relationships among the tensors were proven by McMullen [204].

Starting with convex sets K in Euclidean space $\mathbb{R}^d$ with $d = 2, 3$ one defines the convex characteristic function

$$\tilde{\chi}(K) := \begin{cases} 1 & \text{if } K \neq \emptyset \\ 0 & \text{else} \end{cases}, \tag{5.3}$$

where $\emptyset$ is the empty set. A ν dimensional plane in $\mathbb{R}^d$ which contains $\mathbf{r}$ is called $E^{(\nu)}(\mathbf{r})$. The integral over all 0-dimensional planes (points)

$$V(K) = \int \mathrm{d}E^{(0)}\, \tilde{\chi}(E^{(0)}(\mathbf{r}) \cap K) \tag{5.4}$$

is nothing else than the volume of K. This integral can be interpreted as the integration over the entire group of motions $\mathcal{G}$, which rotates and moves the plane $E^{(\nu)}$. Doing so for $d = 3$ and $\nu = 1$ gives the surface area $A(K)$ of the convex set K. The meanings of $\nu = 2, 3$ for $d = 3$ were discussed above, i.e. in the three dimensional case $\nu = 2$ gives the integrated mean curvature and $\nu = 3$ the integrated Gaussian curvature. To overcome the restrictions of convex sets, which is indeed a far too strong restriction for practical use in physics, the definition range for integrals of the type, mentioned above, the concept of additivity is used: A functional ϕ is called additive, when

$$\phi(K_1 \cup K_2) = \phi(K_1) + \phi(K_2) - \phi(K_1 \cap K_2), \tag{5.5}$$

for two convex sets K_1 and K_2. The class $\mathcal{P}$ of sets P which can be decomposed in a countable set of convex sets is called polyconvex ring. For polyconvex sets $P = \bigcup_i K_i$

(K_i convex) in $\mathcal{P}$ we define the Euler characteristic

$$\chi(P) = \sum_i \widehat{\chi}(K_i) - \sum_{i,j,i>j} \widehat{\chi}(K_i \cap K_j) + \ldots, \tag{5.6}$$

where $\ldots$ are three and more body intersecions. Indeed this functional equals the well-known topological quantity with the same name [211, 57]. It is easy to see, that χ is an additive functional.

Following the definition of Hadwiger [117] the Minkowski functionals are defined as

$$\begin{aligned} W_\nu(P) &:= c_{d\nu} \int \chi(P \cap E^{(\nu)}) \, \mathrm{d}E^{(\nu)} \qquad \nu = 0, \ldots, d-1 \\ W_d(P) &:= c_{dd} \, \chi(P), \end{aligned} \tag{5.7}$$

with some prefactors $c_{d\nu}$, $\nu = 1, \ldots, d$. $dE^{(\nu)}$ denotes the integration over the group of motion for the ν-dimensional planes $E^{(\nu)}$ in Euclidean space $\mathbb{R}^d$. For the rest of this paragraph, we restrict ourselves to $d = 3$; the extension of the concepts to arbitrary dimension is straightforward [131].

Continuity: A functional ϕ is called continuous when for an arbitrary sequence of sets A_n with $A_n \to A$ [1] the sequence $\phi(A_n)$ converge: $\phi(A_n) \to \phi(A)$.

Motion invariance: A functional ϕ is called motion invariant, when it is translation invariant $\phi(A) = \phi(tA)$ and rotation-invariant $\phi(A) = \phi(rA)$ for all rotations in the group $SO(3)$ and all translations in $T(3)$. We also call a motion invariant functional $\mathcal{G}$-invariant, where $\mathcal{G}$ is the direct sum of $SO(3)$ and $T(3)$.

When ϕ is $\mathcal{G}$-invariant, the integral

$$I_\phi(A, B) = \int_{\mathcal{G}} \phi(A \cap B) \mathrm{d}A = \int_{\mathcal{G}} \phi(A \cap B) \mathrm{d}B, \tag{5.8}$$

where $A, B \in \mathcal{P}$ and $\mathrm{d}A, \mathrm{d}B$ denotes the integration w.r.t. the Haar measure (which is up to prefactors the only $\mathcal{G}$-invariant measure [268]), then $I_\phi(A, B)$ is $\mathcal{G}$-invariant.

It is easy to see that $\tilde{\chi}$ is motion-invariant. χ is a countable sum of the motion-invariant $\tilde{\chi}$, thus χ is motion-invariant. Finally all MF as an integral of motion-invariant χ-functional are $\mathcal{G}$-invariant. The Minkowski measures $W_\nu(A)$ read (expressed with the Lebesgue-measure)

$$W_\nu(A) = c_{d\nu} \int_3 \mathrm{d}\mathbf{t} \int_0^\pi \sin\theta \mathrm{d}\theta \int_0^{2\pi} \mathrm{d}\varphi \chi(A \cap E^{(\nu)}). \tag{5.9}$$

[1] w.r.t. the Hausdorff metric

Since integration is additive, MF are additive.

Theorem of completeness: Hadwiger proved a strong theorem for the class of *(i)* motion-invariant *(ii)* continuous and *(iii)* additive functionals. Such functionals ϕ can be decomposed into the four MF with scalars c_ν, $\nu \leq 0 \leq 3$, which are independent of the convex argument A:

$$\phi(A) = \sum_{\nu=0} c_\nu W_\nu(A). \tag{5.10}$$

Thus the MF are a basis of the space $\mathcal{M}$ of the $\mathcal{G}$-invariant, continuous and additive functionals. This theorem could be extended without any restrictions to the full polyconvex ring $\mathcal{P}$. A prove of this theorem can be found in ref. [117, 262].

Steiner's formula: The calculation of MF as defined in integral geometry is rather complicated, since an integration over motions $g \in \mathcal{G}$ is needed. A theorem which is useful to compute MF for arbitrary sets $P \in \mathcal{P}$ is the Steiner's formula, which connects the MF of a parallel set P_ε and P.

The Minkowski-sum $A \uplus B$ is defined as $A \uplus B := \{x + y | x \in A, y \in B\}$. The parallel set P_ε of a set P is the Minkowski-sum of P with a ε-sphere B_ε centered at the origin: $P_\varepsilon := P \uplus B_\varepsilon$. Following the notation of Santalo [262] the Steiner's formula reads for convex sets K and $\varepsilon > 0$:

$$W_0(K) = \sum_{i=1}^{3} \binom{d}{i} W_i(K)\varepsilon^i \tag{5.11}$$

$$W_\nu(K) = \sum_{i=0}^{3-\nu} \binom{3-\nu}{i} W_{\nu+i}(K)\varepsilon^i, \quad \nu = 1, ..., 3. \tag{5.12}$$

The Steiner's formula is a particular case of the kinematic formula. This theorem can be proven with the completeness theorem. Writing the integral

$$I(A, B) := \int_{\mathcal{G}} W_\nu(A \cap gB) \mathrm{d}g \tag{5.13}$$

we know, that it fulfills the requirements of the completeness theorem and is an functional of A and B. Thus it can be decomposed into a linear combination of

$$I(A, B) = \sum_{i,j} c^\nu_{i,j} W_i(A) W_j(B). \tag{5.14}$$

The prefactors $c^\nu_{i,j}$ are determined by homogeneity-relations and can be calculated using arbitrary convex sets A and B. Thus we obtained the kinematic formula

$$\int_{\mathcal{G}} W_\nu(A \cap gB) \mathrm{d}g = \sum_{i,j} c^\nu_{i,j} W_i(A) W_j(B). \tag{5.15}$$

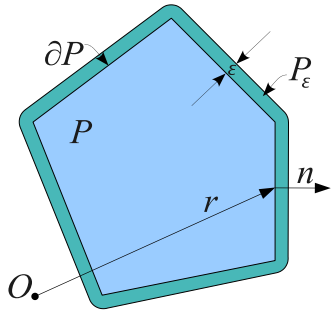


FIGURE 5.1.

Using $B \equiv B_\varepsilon$ the kinematic formula turns into Steiner's formula.

5.1.2. Computation of Minkowski functionals

Coming back to the differential geometric approach, we can now use Steiner's theorem to compute the MF for arbitrary polyhedra $Q \in \mathcal{P}$. The idea is simple. We decompose Q into convex polyhedra K_i. Since the MF W_ν are continuous we take the parallel bodies $K_{i,\varepsilon}$ to compute with eq. (5.1) the MF and take the limit $\varepsilon \to 0$.

$$W_\nu(K_i) = \lim_{\varepsilon \searrow 0} W_\nu(K_{i,\epsilon}) \tag{5.16}$$

Using additivity one obtains $W_\nu(Q)$.

5.2. Minkowski tensors

The concepts of the sections above can be generalized to tensor-valued quantities of arbitrary rank. Here we will rather concentrate on rank-2. Rank-4 tensors are considered in chapter 6.

The Minkowski tensors (MT) of a convex body K with the boundary ∂K are defined as:

$$\begin{aligned} W_0^{r,0}(K) &:= c_0 \int_K \mathbf{r}^r \, \mathrm{d}^3 r \\ W_\nu^{r,s}(K) &:= c_\nu \int_{\partial K} \mathbf{r}^r \mathbf{n}^s G_\nu(\kappa(\mathbf{r})) \, \mathrm{d}^2 r, \end{aligned} \tag{5.17}$$

where $\mathbf{n}$ are the outer bound normal vectors and $\mathbf{r}$ the location vectors on the boundary. In 3D the prefactors are $1/3$ for $\nu > 0$ and 1 for $\nu = 0$. The abbreviated form $\mathbf{r}^r\mathbf{n}^s$ denotes the power taken to be symmetric dyadic tensor product

$$\mathbf{r}^r\mathbf{n}^s := \underbrace{\mathbf{r}\odot\ldots\odot\mathbf{r}}_{r \text{ times}}\odot\underbrace{\mathbf{n}\odot\ldots\odot\mathbf{n}}_{s \text{ times}} \tag{5.18}$$

$$(\mathbf{r}^r\mathbf{n}^s)_{i_1\ldots i_{r+s}} = \frac{1}{(r+s)!}\sum_{\sigma\in S_{r+s}}\mathbf{r}_{\sigma(i_1)}\ldots\mathbf{r}_{\sigma(i_r)}\mathbf{n}_{\sigma(i_{r+1})}\ldots\mathbf{n}_{\sigma(i_{r+s})}, \tag{5.19}$$

where S_{r+s} is the $(s+r)$-permutation group. This gives for the case of rank-2 tensors

$$(\mathbf{a}\odot\mathbf{b})_{ij} := \frac{1}{2}(a_ib_j + a_jb_i) \tag{5.20}$$

MF are a powerful tool because of their robustness, stemming from the continuity and additivity. These features of the MF hold for the MT too.

Table 5.1 lists the Minkowski tensors of rank 2 in three dimensions and table 5.2 in 2D. In three dimensions, equation (5.17) gives 10 MT, another 4 trivial tensors can be defined by the product of the scalar MF with an unit tensor. In 2 dimensions one obtains from (5.17) 7 MT and 3 trivial tensors. The set of Minkowski tensors (defined by eq. (5.17)) and the trivial tensors obtained from the Minkowski functionals is called set of basic tensor valuations.

Clearly, MT are not motion-invariant, but motion-covariant (isometry covariant). This means, that $W_\nu^{r,s}$ of rank n transform under translation $P \to P \uplus \mathbf{t}$ with the translation vector $\mathbf{t}$ and under rotation $P \to \hat{U}_1P = \{\hat{U}_1x | x \in P\}$, $\hat{U}_1 \in SO(d)$ with the rotation operator $\hat{U}_1$ for vectors

$$W_\nu^{r,s}(K\uplus\mathbf{t}) = \sum_{p=0}^{r}\binom{r}{p}\mathbf{t}^pW_\nu^{r-p,s}(K) \tag{5.21}$$

$$W_\nu^{r,s}(\hat{U}_1K) = \hat{U}_{r+s}W_\nu^{r,s}(K).. \tag{5.22}$$

U_{r+s} is a short version, which is defined by $(U_nT_n)_{i_1,\ldots,i_n} = \sum_{j_1,\ldots,j_n}U_{i_1j_1}\ldots U_{i_1j_n}T_{j_1,\ldots,j_n}$ for the rotation of the rank-n tensor T_n with the rotation matrix U_{ij}.

For tensors which only depend on $\mathbf{n}$, the transform under translations reduces to

$$W_\nu^{0,s}(K\uplus\mathbf{t}) = W_\nu^{0,s}(K), \tag{5.23}$$

i.e. they are translation invariant. We shall see that also some tensors of the form $W_\nu^{1,1}$ are *translation invariant*. We use the term *genuinely translation covariant* for those tensors which are translation covariant but do not obey (5.23). For simplicity we use also

Homogeneity [unit]	rank 0	rank 2	translation behavior
λ^5 $[m^5]$	–	$W_0^{2,0}$	genuinely t. cov.
λ^4 $[m^4]$	–	$W_1^{2,0}$	genuinely t. cov.
λ^3 $[m^3]$	W_0	$W_2^{2,0}$	genuinely t. cov.
	–	$W_0\, E_3$	t. invariant
λ^2 $[m^2]$	W_1	$W_3^{2,0}$	genuinely t. cov.
	–	$W_1\, E_3$	t. invariant
	–	$W_1^{0,2}$	t. invariant
λ^1 $[m^1]$	W_2	$W_2^{0,2}$	t. invariant
	–	$W_2\, E_3$	t. invariant
λ^0 $[1]$	W_3	$W_3\, E_3$	t. invariant

TABLE 5.1. *Basic tensor valuations in 3D. The scalar Minkowski functionals are motion invariant and for the tensors or rank two the behavior under translation is specified in the last column. The space of tensors of rank two decomposes in two complementary subspaces of genuinely translation covariant and translation invariant tensors. The latter include tensors obtained by multiplying the scalar Minkowski functionals W_ν with the unit tensor $E_3 := \mathbf{e}_1^2 + \mathbf{e}_2^2 + \mathbf{e}_3^2$ of rank two, where $\mathbf{e}_1, \mathbf{e}_2, \mathbf{e}_3$ is an orthonormal basis of $\mathbb{E}^3$.*

abbreviated version *translation covariant*. To study intrinsic shape characteristics with translation-covariant tensors a specific choice of the origin is needed. Müller proved the so-called envelope theorem. This states that rank-1 tensors (Minkowski vectors) of the form $W_\nu^{0,1}$ vanish for all polyconvex sets [223]. Since only these Minkowski vectors appear in the expansion of $W_\nu^{1,1}$ according to (5.21), these tensors are also translation-invariant.

Similar to the Hadwiger's theorem for MF, Alesker has proven [4] that for a given rank the MT span a vector space of additive, continuous and isometry-covariant tensors. But not all of the tensors in tables 5.1 and 5.2 are independent. McMullen found some linear relationships among them [204]. The relationships in two and three dimensions read

$$E_d W_\nu = \nu W_\nu^{0,2} + (d-\nu) W_{\nu+1}^{1,1}, \tag{5.24}$$

for $\nu = 0, \ldots, d$ and $W_\nu^{r,s} = 0$ for $\nu > d$ or $\nu = 0, s > 0$. The particular relationship $E_d W_0 = d W_1^{1,1}$ is simply the Gauss' theorem $\int_P \operatorname{div} \mathbf{f}(x)\, \mathrm{d}^d r = \oint_{\partial P} \mathbf{f} \cdot \mathbf{n}\, \mathrm{d}^{d-1} r$, where $\operatorname{div} \mathbf{f} = 1$. With the McMullen theorem and Alesker theorem we could reduce the 14 MT in 3D and the 10 MT in 2D independent 10 MT in 3D and 7 independent MT in 2D resp. A basis for either case is given in tables 5.1 and 5.2.

5.2.1. Algorithm

This brief paragraph introduces some basic ideas of how MT are computed numerically. For detailed descriptions of the algorithm in 3D it is referred to ref. [274] and the 2D version is discussed in ref. [110]. The computation in 3D can be done for two types of datasets, first voxalized data or second polyhedral meshes. How to approximate a smooth boundary surface out of voxalized data is an active topic of mathematical research [157]. One algorithm which transforms voxelized date into triangulated meshes is the so-called marching cubes algorithm [182].

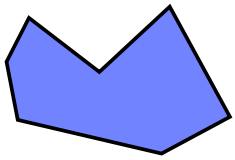
Homogeneity [unit]	rank 0	rank 2	translation behavior
λ^4 $[m^4]$	–	$W_0^{2,0}$	genuinely t. cov.
λ^3 $[m^3]$	–	$W_1^{2,0}$	genuinely t. cov.
λ^2 $[m^2]$	W_0	$W_2^{2,0}$	genuinely t. cov.
	–	$W_0\, E_3$	t. invariant
λ^1 $[m^1]$	W_1	$W_1\, E_3$	t. invariant
	–	$W_1^{0,2}$	t. invariant
λ^0 $[m^0]$	W_2	$W_2\, E_3$	t. invariant

TABLE 5.2. *Basic tensor valuations in 2D. The scalar Minkowski functionals are motion invariant and for the tensors or rank two the behavior under translation is specified in the last column. The space of tensors of rank two decomposes in two complementary subspaces of genuinely translation covariant and translation invariant tensors. The latter include tensors obtained by multiplying the scalar Minkowski functionals W_ν with the unit tensor $E_2 := \mathbf{e}_1^2 + \mathbf{e}_2^2$ of rank two, where $\mathbf{e}_1, \mathbf{e}_2$ is an orthonormal basis of $\mathbb{E}_2$.*

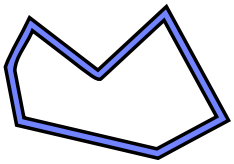
In 2D pixelized data or polytope contours can be used as input, while pixel data are transformed to polytopes by a marching squares algorithm [110].

In 3D a polyhedra mesh structure consists of three types of surface elements: facets (2 dim.), edges (1 dim.) and vertices (0 dim.). On the facets, mean curvature $G_2 = H = 0$ and Gaussian $G_3 = \mathcal{K} = 0$ vanish trivially. As it has been discussed above, that the differential geometric representation is also valid for polyhedra with sharp edges. We recall the Steiner's formula, which connects the MF of a convex set to MF of its parallel surface. Thus, one can derive analytic formulas from Steiner's formula to compute the MF of polyhedra. On edges, one can show with local versions of the Steiner's formula that the Gaussian curvature $\mathcal{K} = 0$ vanishes and the surface area on a zero set is trivially zero. At vertices Steiner's formula shows that only the Gaussian curvature $\mathcal{K}$ is non-zero. Furthermore the contributions of each element depend only on its location (center of area or center of a line), its orientation expressed by a normal vector and the angles to the adjoint elements. Thus the computation for $\nu = 1$ is simply a sum over all facets, $\nu = 2$ runs over all edges and $\nu = 3$ over vertices only. The volume integrals $\nu = 0$ can be evaluated with an adapted version of Gauss' integral theorem. Hence the computation is linear in the number of surface elements. By analogy in 2D the sums run over edges and vertices only. Some selected details on this algorithms in 3D can be found in the appendix C.

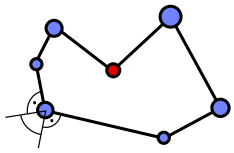
A: Two-dimensional bodies



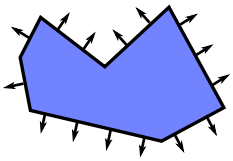
$W_0^{2,0}$ – moment tensor solid



$W_1^{2,0}$ – moment tensor hollow

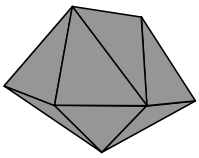


$W_2^{2,0}$ – moment tensor wire frame

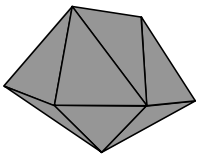


$W_1^{0,2}$ – normal distribution

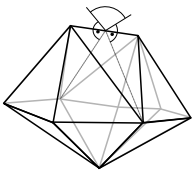
B: Three-dimensional bodies



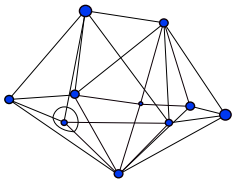
$W_0^{2,0}$ – moment tensor solid



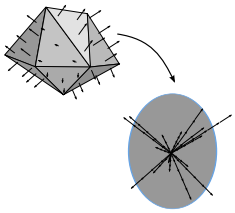
$W_1^{2,0}$ – moment tensor hollow



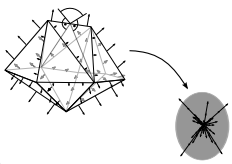
$W_2^{2,0}$ – moment tensor wire frame



$W_3^{2,0}$ – moment tensor vertices



$W_1^{0,2}$ – normal distribution



$W_2^{0,2}$ – curvature distribution

FIGURE 5.2. *Different MT capture different morphological information*

5.2.2. Invariants and shape descriptors

Looking at orientation dependent quantities, the natural physical representation is tensorial. It is convenient to reduce this tensorial information to a single scalar in order to obtain a comparable descriptor. Furthermore these scalars should not dependent on the choice of the coordinate system, thus functions of the rotation invariants are a good choice for simple scalar shape descriptors. Rank-2 Minkowski tensors can be used to quantify anisotropy of a spatial structure in a concise way. $(\mu_\nu^{r,s})_\alpha$ and $\alpha = 1, \ldots, d$ denote the eigenvalues of $W_\nu^{r,s}$ in descending order (by their absolute values). A succinct descriptor of anisotropy is defined by

$$\beta_\nu^{r,s} := \frac{|(\mu_\nu^{r,s})_d|}{|(\mu_\nu^{r,s})_1|} \in [0,1], \tag{5.25}$$

where $|(\mu_\nu^{r,s})_d|$ is the eigenvalue with the smallest absolute value and $|(\mu_\nu^{r,s})_1|$ with the largest absolute value. Please note, that for non-convex planar bodies $W_2^{2,0}$ may have negative eigenvalues. Clearly, $\beta_\nu^{r,s} = 1$ for sets, where all eigenvalues are identical, and thus these tensors are called isotropic. Deviations from 1 indicate shape anisotropy. This might appear qualitatively equivalent to the asphericity measure a_S, which is sometimes used in the literature [288]. Other measures are also imaginable to measure asphericity, for example the isoperimetric ratio V^2/A^3, where $V = W_1$ is the volume and $A \propto W_1$ is the surface area. But asphericity quantifies deviations of the shape from a *sphere* (at the same volume). Anisotropy rather quantifies orientation differences in a tensorial sense, i.e. if the body appears identical w.r.t. a particular property from any two planar or three spatial orthogonal directions, it is isotropic. Cubes, tetrahedra, spheres, some regular polyhedra, etc. are isotropic w.r.t. rank-2 Minkowski tensors.

The fact that the set of anisotropy indices which can be derived from the Minkowski tensors $W_\nu^{r,s}$ might be interpreted as some ambiguity of the anisotropy analysis. This interpretation overlooks the merit of completeness theorem for Minkowski tensors. Since the set of MT contain all relevant morphlogical information one can easily check whether anisotropy is generic or subject to subset of morphological informations. Different MT measure different quantities, e.g. the distribution of surface normals or the mass distribution. Figure 5.2 illustrates this fact. For example, the location vector weight tensors measure in 3D the second moments of (1) mass distibution ($W_0^{2,0}$), the boundary surface distibution ($W_1^{2,0}$) the wire frame distribution ($W_2^{2,0}$) and the vertex distibution ($W_3^{2,0}$). The normal weighted tensors are the second moments of the normal distribution ($W_1^{0,2}$) and the mean curvature distibution ($W_2^{0,2}$) on an unit sphere. On the other hand, analyzing the anisotropy with all MT in the basis, the analysis is not restricted to any specific morphometric feature. If all anisotropy indices indicate

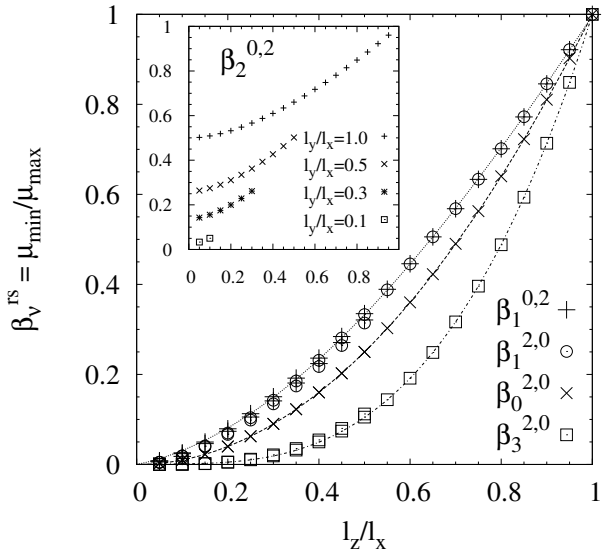


FIGURE 5.3. *Eigenvalue ratio of the smallest and largest eigenvalues $\mu_{\min} = \mu_3$ and $\mu_{\max} = \mu_1$ of the Minkowski tensors $W_\nu^{r,s}$ of an ellipsoid with radii $l_x = 1$ and $l_x = 1 \geq l_y \geq l_z$ as function of $r = l_z/l_x$. Each symbol in the main plot represents data (hardly distinguishable) for three different intermediate radii $l_y = 0.1, 0.5, 0.9$ indicating that for these four tensors the minimal to maximal eigenvalue ratio is approximately the same for all values of the intermediate radius.*

the same dependence, it clearly demonstrates that the anisotropy is generic and not depending on the choice of the morphological quantities [276].

An 3D example of the anisotropy indices is shown in fig. 5.3 for ellipsoids given by the three principle radii $(x/l_x)^2 + (y/l_y)^2 + (z/l_z)^2 = 1$. All surface integrals result in elliptic integrals and cannot be expressed in closed form. However, the scalar Minkowski functional $W_0 = \frac{\pi}{6} l_x l_y l_z$ and the tensor $W_0^{2,0}$ is diagonal with

$$(W_0^{2,0})_{ii} = \frac{\pi}{120} l_i^3 l_j l_k, \tag{5.26}$$

where $\{i, j, k\}$ is $\{x, y, z\}$ and cyclic permutations thereof. The integration of all other tensors is easily obtained numerically by use of the ellipsoid parametrization $\vec{r}(u, v) = \{l_x \cos(u) \sin(v), l_y \sin(u) \sin(v), l_z \cos(v)\}$ which yields explicit expressions for the metric tensor of the ellipsoidal surface, the normal vector, and the mean and Gaussian curvatures. These are readily integrated numerically. Figure 5.3 shows the minimal to maximal eigenvalue ratio of the Minkowski tensors of rank two of el-

lipsoids with $l_x = 1$ and $1 \geq l_y \geq l_z$ as function of $r = l_z/l_x$. Each symbol in the main plot represents data (hardly distinguishable) for three different intermediate radii $l_y = 0.1, 0.5, 0.9$ indicating that for these four tensors the minimal to maximal eigenvalue ratio is approximately the same for all values of the intermediate radius. The solid curves are fits to the data giving $\beta_3^{2,0} \approx 1.210r^3 - 0.235r^2 + 0.024$, $\beta_0^{2,0} = r^2$, $\beta_1^{2,0} \approx \beta_1^{0,2} \approx -0.366r^3 + 1.222r^2 + 0.139r$. The insert shows the eigenvalue ratio of the tensor $W_2^{0,2}$ as function of l_z/l_x. In contrast to the above four tensors, this ratio depends strongly on the value of the intermediate radius l_y. In particular, for $l_z = 0$ the eigenvalue ratio only becomes zero if the intermediate radius is also $l_y = 0$. For the maximal $l_y = 1$ the eigenvalue ratio converges to 0.5 for $l_z/l_x \to 0$. Functions of eigenvalues are not the only way to obtain invariants of a tensor. Other methods will be part of chapters 6 and 7.

A second kind of anisotropy indices is obtained by projecting a rank-2 tensor onto preferential directions, e.g. the unit vectors $\mathbf{e}_\alpha$ and $\alpha = x, y, z$. As an example we define the $x-y$-projector index

$$\beta_\nu^{*r,s} := \frac{|\mathbf{e}_x W_\nu^{r,s} \mathbf{e}_x| - |\mathbf{e}_y W_\nu^{r,s} \mathbf{e}_y|}{|\mathbf{e}_x W_\nu^{r,s} \mathbf{e}_x| + |\mathbf{e}_y W_\nu^{r,s} \mathbf{e}_y|}. \tag{5.27}$$

This kind of anisotropy descriptors converges to 0 in a truly isotropic distributed system. In case of a preferred orientation $\beta_\nu^{*r,s}$ along one of the axes x or y $\beta_\nu^{*r,s}$ tends to 1 or -1 resp.

The Minkowski analysis with scalar and tensorial descriptors is a versatile method to quantify morphological properties. Strong theorems underline the signfication of this method, i.e. (1) Minkowski functionals and Minkowski tensors are robust against noise from a numerical and experimental point of view. (2) Due to the completeness theorems of Hadwiger and Alesker it follows, that the set Minkowski functionals/tensors capture all relevant morphological information for a given tensor rank. The latter point is of great importance in the structure analysis, as we shall this see in chapter 6. For example, with the set of $\beta_\nu^{r,s}$ one could check whether order or disorder in a system is a generic feature or subject to one morphological quantity only, e.g. the curvatures.

5.3. Spinodal decomposition

To make an example of applications of MF and MT, in this section we shall study the morphology of spinodal decomposition patterns which emerge from the van der Waals phase fluid in the PF model. Spinodal decomposition occurs, when an over-critical ($T > T_c$) vdW-fluid is quenched to temperatures below the critical point and the average density is between the spinodal lines in the phase diagram. This means, that the low temperature state with homogeneous density is neither globally nor locally stable. The homogeneous mixture separates therefore to a liquid and a vapor phase (see the phase diagram in fig. 5.4) [47]. The phase separation process is driven by local instabilities, this results in complex pattern formation. After an early stage decomposition, where the homogeneous fluid separates in adjacent liquid/vapor domains with a typical length scale there is a crossover to a domain growth regime, where the small patches of either phase accumulate. The latter process is described by the Lifschitz-Slyuzov-Wagner (LSW) theory [47]. In systems with an excess of vapor domains the growth from small droplets to larger droplets is called the Ostwald ripening, where small drops shrink and large drops grow. It will be demonstrated that the PF model captures the correct time behavior of the pattern evolution. In particular we investigate the influence of gravity onto the pattern formation. In real systems, spinodal decomposition processes are exposed to gravity and confined by a small container to provide good isothermal conditions after the quench. This container walls exhibit a large impact to the local pattern formation. We shall show, that among the controlling parameters the contact angle and the average density play a crucial role. Layering processes in the vicinity of a substrate is observed. The results of this section are still preliminary.

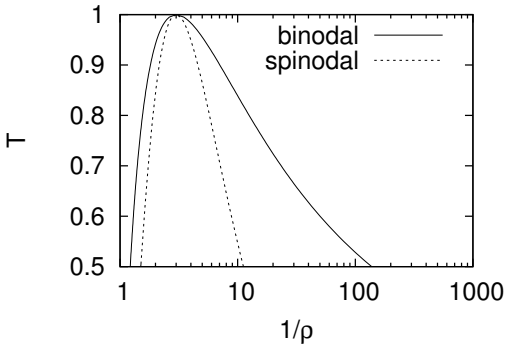


FIGURE 5.4. *Phase diagram of a van der Waals fluid*

5.3.1. Introduction to spinodal decomposition

As mentioned above, at short times the spinodal decomposition process is governed by the local instability when the fluid is quenched below the spinodal line. As we work in our simulations at fixed volume and temperature we regard the free energy

$$F[\rho] = \int f_{\text{bulk}} + \frac{w^2}{2}|\nabla\rho|^2 \mathrm{d}^3 r. \tag{5.28}$$

We want to check the stability of the free energy of the system against tiny perturbation $\delta\rho$ after a quench from a homogeneous density ρ_0 above the critical point; $\rho = \rho_0 + \delta\rho$ [91]. Assuming for simplicity a plain wave perturbation field $\delta\rho = A\cos(qx)$, which vanishes at the boundaries, we can write the free energy

$$F[\rho] = \int f_{\text{bulk}}(\rho) + \frac{\mathrm{d}f_{\text{bulk}}}{\mathrm{d}\rho}\delta\rho + \frac{1}{2}\frac{\mathrm{d}^2 f_{\text{bulk}}}{\mathrm{d}\rho^2}\delta\rho^2 + \frac{w^2}{2}|\nabla\delta\rho|^2 \mathrm{d}^3 r. \tag{5.29}$$

Note, that only $\delta\rho$ depends on the location, thus we obtain

$$F[\rho] = F_0 + \frac{1}{2}\frac{\mathrm{d}^2 f_{\text{bulk}}}{\mathrm{d}\rho^2}\int \delta\rho^2 \,\mathrm{d}^3 r + \frac{w^2}{2}\int |\nabla\delta\rho|^2 \mathrm{d}^3 r. \tag{5.30}$$

We use the plain wave, so that the first integral reads $VA^2/2$ and the second reads $VA^2q^2/2$. The state is unstable, if the perturbation reduces the free energy:

$$\frac{1}{2}f''_{\text{bulk}} + \frac{w^2}{2}q^2 < 0, \tag{5.31}$$

where f''_{bulk} is the second derivative of f_{bulk} w.r.t. the density. For positive f''_{bulk} this criterion is always invalidated, but negative f''_{bulk} yields the critical wave number q_{c}

$$\sqrt{-\frac{1}{w^2}f''_{\text{bulk}}} > q_{\text{c}}. \tag{5.32}$$

For wave numbers larger than q_{c} the system gains energy and the decomposition is triggered, if $f''_{\text{bulk}} < 0$. The dynamics of spinodal decomposition of binary mixtures can be described with the Cahn-Hilliard theory [53, 52, 51, 129].

5.3.2. Morphology

Below, we discuss the morphology of the liquid vapor phase separation in spinodal decomposition processes with the PF model. First, to test our model, we want to check

the time dependence of our model. The typical size of the liquid/vapor domains L scales with an universal power law

$$L \propto t^{\alpha}, \tag{5.33}$$

where α is the growth exponent [75]. This exponent depends on the mechanism which is dominant in the system, e.g. purely diffusive growth, viscous regimes or inertia driven regimes. In our case after the initial phase separation, it is expected that $\alpha = \alpha_{\text{viscous}} = 1$ for the symmetric liquid-vapor system. This value was found in the LB simulations of Cristea [75] and describes a viscous growth regime. The LSW theory for high viscosity gives an exponent $\alpha = 1/3$, for intermediate viscosity $\alpha = 1/2$ and low viscosity $\alpha = 2/3$ [282]. An inertial regime is expected to have an exponent $\alpha = 2/3$ [75].

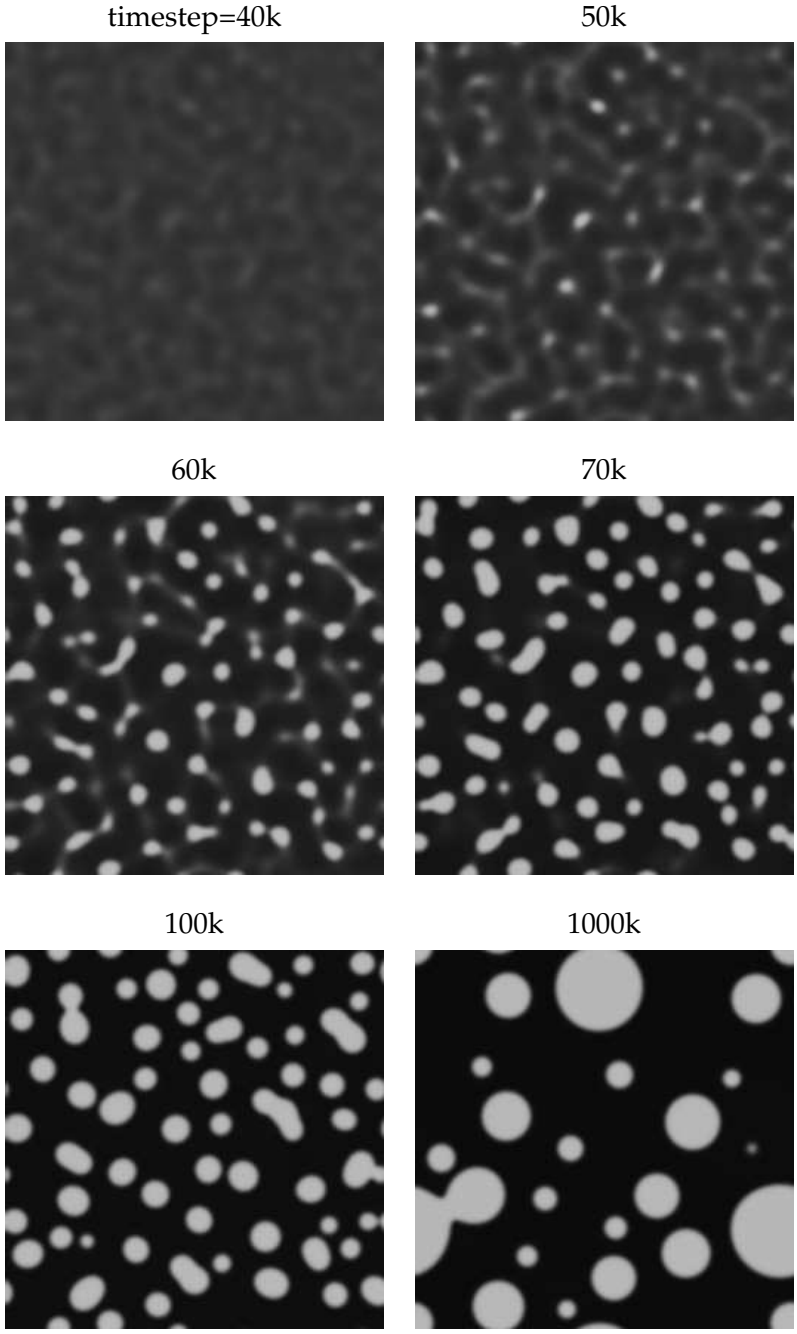


FIGURE 5.5. *Spinodal decomposition and Ostwald ripening in a liquid vapor mixture of a van der Waals fluid after a temperature quench to $T = 0.7T_c$ (without walls and gravity). The average density is off-symmetric with $< \rho >= \frac{3}{4}\rho_v + \frac{1}{4}\rho_l$.*

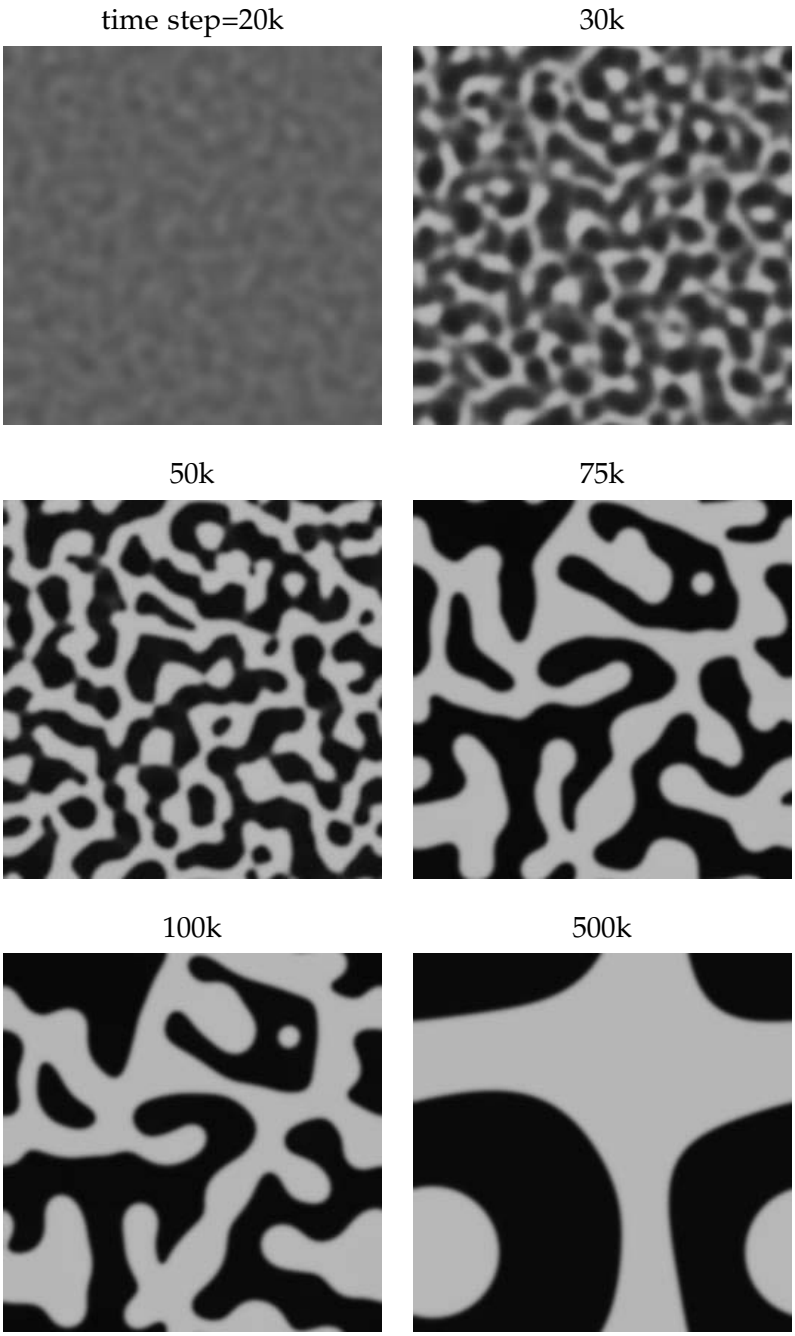


FIGURE 5.6. *Spinodal decomposition and domain growth in a liquid vapor mixture of a van der Waals fluid after a temperature quench to $T = 0.7T_c$ (without walls and gravity). The average density is symmetric with $< \rho >= \frac{1}{2}\rho_v + \frac{1}{2}\rho_l$.*

Typical patterns from vapor-dominated (off-symmetric) and symmetric liquid-vapor systems are illustrated in fig. 5.5 and fig. 5.6 resp. Simulations were run in a box with 256×256 lattice sites, with $w = 2h$, without an external potential and periodic boundary conditions at $T = 0.7T_c$. We see, that in the off-symmetric case, the initial phase separation is significantly slower. The patterns from the symmetric and the off-symmetric simulations are quite different. While the former show immediately an interconnected network of liquid (gray) domains with similar thickness everywhere the latter leads to droplets of similar diameter. For either situations it starts a growth process of the typical thickness. To measure this characteristic domain length scale several methods are proposed in the literature. Widely used is the density correlation function or the structure factor [5]. This measures does not offer access to the morphology, therefore Sofonea et al. [282, 210] proposed length-scale characterizations based on Minkowsi-functionals: The density is transformed to a binary image of white and black pixels and the morphology of the white phase is analyzed with the volume $F = W_0$, the perimeter $U \propto W_1$ and the Euler number $\chi \propto W_2$ (in 2 dimensions). A dimension argument connects these numbers naturally to an intrinsic length-scale L of the pattern

$$F \sim 1 \qquad U \sim L^{-1} \qquad \chi \sim L^{-2}\,. \tag{5.34}$$

We used this method to check our simulations against the lattice Boltzmann (LB) findings of ref. [75]. Similarly, in ref. [75] the spinodal decomposition of a van der Waals fluid is studied under the influence of gravity, where a scaling of $\alpha = 1$ has been found. Figure 5.7 evince the Minkowski functionals as a function of the simulation time steps. After the early stage spinodal decomposition process the crossover to the growth regime is clearly indicated by the maximum/minimum of the Minkowski functionals W_1 and W_2. Although these maxima do not indicate exactly the same crossover time, the difference is quantitatively not significant [282]. The volume of the liquid domain F reaches around these times its long time average of $F \to \frac{\rho-\rho_v}{\rho_l-\rho_v}$. The maximum in the perimeter W_1 comes from the large number of tiny droplets which emerge from the early stage process, while in the domain growth regime small drops accumulate to larger patterns, reducing the boundary. The Euler number ($\sim W_2$), counting the number of separated domains minus the number of holes is in the off-symmetric system reaching a maximum, counting all the separated droplets and reduces with the agglomeration process. In symmetric systems, where the liquid phase builds up an interconnected network from merging droplets, this first maximum is followed by a minimum, where the number of holes in the patterns exceed the number of separated domains. Afterwards, the number of holes reduces, since they get blurred by the surrounding liquid. Thus the Euler number increases, towards the value of only one remaining drop or stripe.

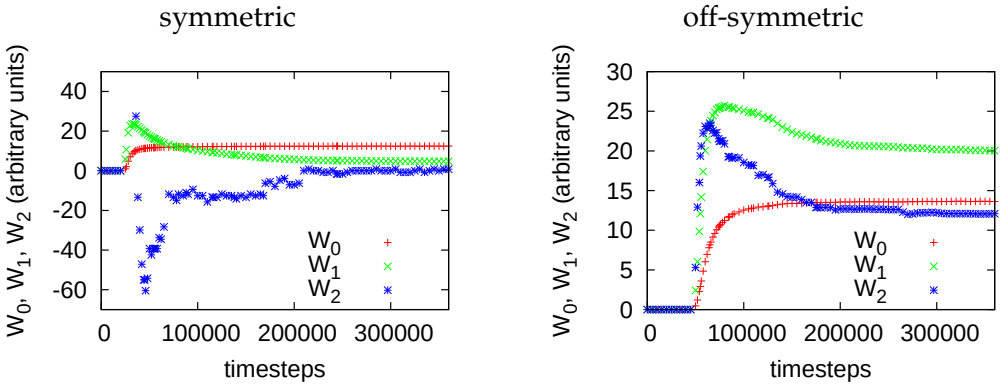


FIGURE 5.7. *Time-evolution of the morphological measures W_1, W_2 and W_3. See also fig. 5.5 and 5.6.*

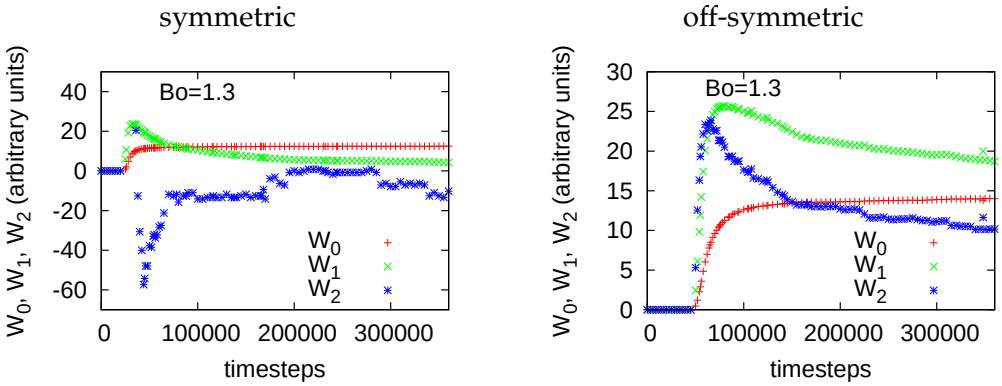


FIGURE 5.8. *Time-evolution of the morphological measures W_1, W_2 and W_3 with gravity.*

The time-scaling of the growth regime in the symmetric liquid-vapor system is in good agreement with the results from ref. [75]. This can be seen in the figure 5.9 (left panel). L is measured here by the inverse perimeter W_1^{-1} (L_U). The red points indicate the length scale in the symmetric system and the green line is a reference line with the scaling exponent $\alpha = 1$. Interestingly, for the off-symmetric system we find an other time scaling. The pink line represents a scaling of $1/3$ which is clearly a too large exponent. Fitting yields a scaling exponent of 0.1559. We are not aware of such a scaling in the literature. This case is particularly interesting. So far we only investigated the length scale L defined by the perimeter. Using the Euler number $\sim W_2$ to define the length scale L (L_χ) we find a scaling law of $\alpha = 1$ in the first

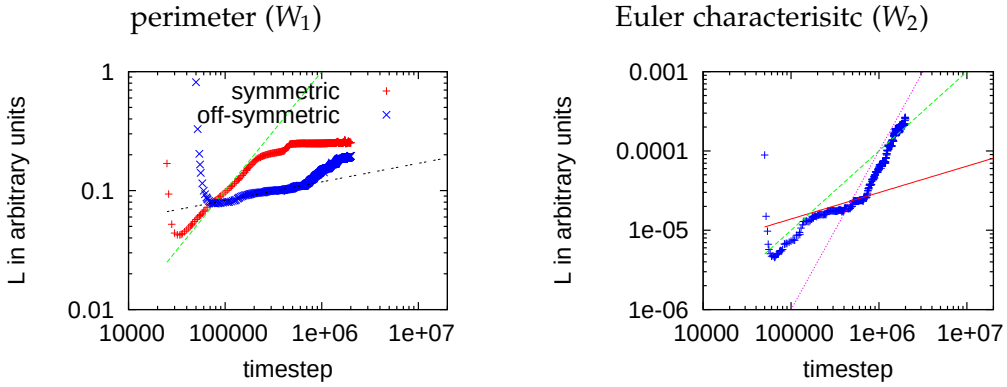


FIGURE 5.9. Left: *Time scaling of the* perimeter *based length scale in symmetric and off-symmetric liquid-vapor systems. Black line: best fit in the timestep range* $[70k : 700k]$ *with* $\alpha = 0.1559 \approx 1/6$. *green line:* $\alpha = 1$ Right: *Time scaling of the off-symmetric system with the* Euler-number *based length scale. A scaling with* $\alpha = 1$ *(green line) is found in the first growth regime, followed by a* $\alpha = 1/3$ *(red line) regime in later stages. The late stage appears to grow with* $\alpha = 2$ *(pink line).*

regime (right panel of fig. 5.9 followed by a regime with $\alpha = 1/3$. Comparing fig. 5.5 we see that the typical drop shape is not spherical for less than 10^6 timesteps. Thus shape rearrangements due to surface fluxes also play a role in the time scaling L_U. This surface mechansim is not captured by L_χ. The connectivity scales as expect in the early stage followed by a $\alpha = 1/3$-regime. The late stage appears to grow with $\alpha = 2$. We are not aware that such a value has been reported in the literature. The data for the symmetric case are extremly noisy in W_2. Larger systems are needed to obtain reliable data. Therefore the data are omitted in the right panel of fig. 5.9. However, we have first indications, that the L_χ scales with $\alpha = 1$.

The results for the same initial conditions with gravity (see figures 5.7 and 5.8) shows nearly the same curves, indicating that the time-evolution is independent of the gravity in the early regime and the beginning of the growth stage. Gravity without walls is modeled by a body force, which is balanced by a volume force. In the early regime, the impact of gravity is expected to be negligible, since in the nearly homogeneous system a body force does not affect the particle distribution. Only when the system clearly separats in two distinct phases with different mass densities gravity plays a role. Thus, the time-evolution is affected in the late stage. While the scalar measures indicate only a tiny difference in the cases with and without gravity, the projection index $\beta_1^{*0,2}$ derived form the MT $W_1^{0,2}$ distinguishes quite early between a final stripe state or

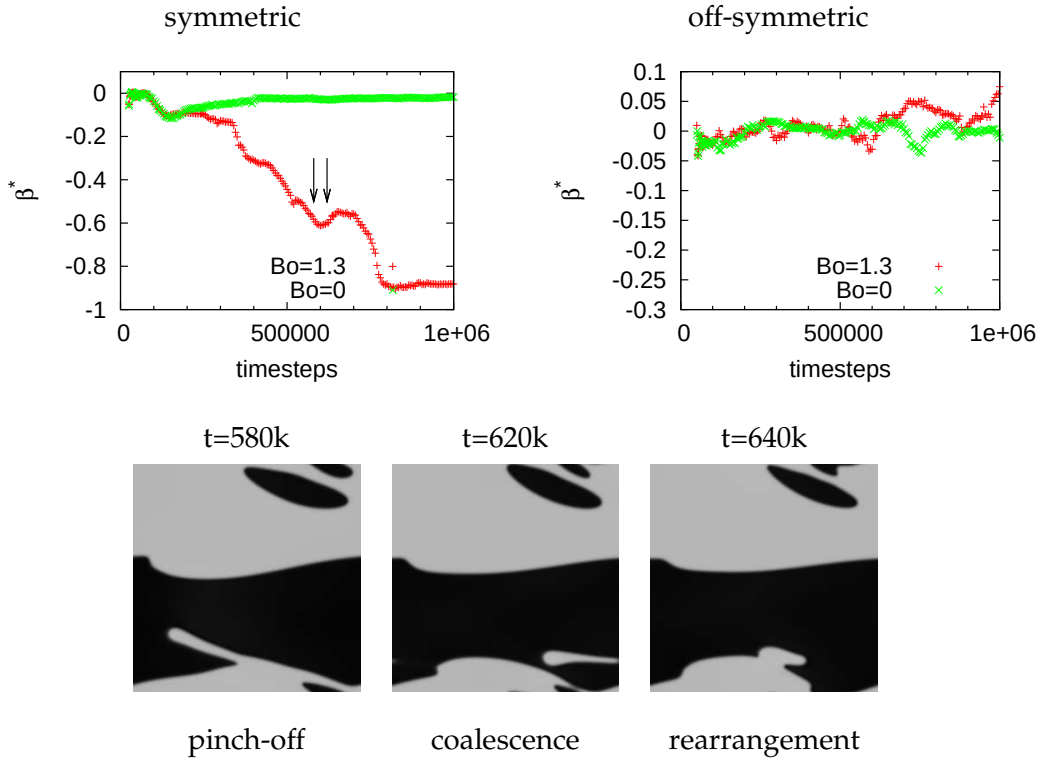


FIGURE 5.10. *Time evolution $x-y$-projector index $\beta_1^{*,0,2}$. $\beta_1^{*,0,2}=0$ indicates an isotropic system, -1 an alignment of the boundary normals parallel to the y-axis. The projection index $\beta_1^{*,0,2}=0$ indicates in the late stage even small rearrangements like (just before) the pinch-off and (just before) coalescence of the droplet in lower part of the snapshots. In the top left panel, the snapshots are marked with arrows. After coalescence the drop shape becomes first spherical before the surface smooths out. This causes the increase of $\beta_1^{*,0,2}$ after coalescence.*

bubble/drop (see fig. 5.10). At this preliminary level of the analysis, we speculate, that the different final situation (spherical or striped) depend on the initial state *and* on gravity.

After we checked, that the model works correctly to capture the time behavior we focus on the interplay of walls. Indeed in realistic systems, gravity and walls occur always together, and in binary fluid mixture experiments layering effects at the substrate are already reported [292]. We want to emphasize, that in contrast to ref. [75] our walls are modeled as an attractive wall potential inside the cavity and repulsive at the borders. Therefore, we expect to capture the layering effect. The wall potential

controls the wetting in the late stage, when drops emerge. In the early stage, where the interface term does not play an important role, particles are accumulated close to the substrate. Therefore, even a partially non-wetting substrate can build up liquid layering, at least in a transient time frame. Interestingly, if such a liquid layer is build in the early stage, particles near the wall are moved closer, forcing a depletion layer above the liquid layer. This depletion yields in turn a vapor phase. The phenomenology is displayed in fig. 5.11 (page 127) and 5.12 (page 128). The former figure are results from symmetric densities, the latter from off-symmetric ones. The left column are snapshots at large contact angles and on the right the substrate is partially wetting. The early occurrence of the accumulation layer is observed in fig. 5.11 in both wetting situations (first row), even before the pattern in the channel center are formed. It depends crucially on the wetting, whether the liquid layer sticks to the wall or is repelled from the substrate. At symmetric densities, the first case occurs, when the potential is strongly attractive, so that it is strong enough to compete with the emerging interface energy. Else, the interface terms keeps the accumulated phase together, and produces a depletion layer close to the wall. Indeed, this can only occur, if enough particles are close to the wall to build up a strong liquid layer in sufficiently short time. Otherwise (compare the off-symmetric case) a dense layer is formed directly at the substrate, which is followed by a depletion layer. The thickness of the depletion layer can be seen in fig. 5.13, where we plotted the volume $W_0|_y$ per line of the lattice (parallel to the x-axis). The depletion layer in the symmetric simulations are monotonuously growing in time for wetting and non-wetting substrates. We do not expect this layers to be long time stable, since noise, gravity or film rupture can drive drop building or film coalesence. In the off-symmetric case after the creation of the depletion layer, drops are attracted by the walls. Thus the depletion layer thickness decreases in time. The time scale for the vanishing of the depletion layer depends on the contact angles.

Whether the first liquid layer is long-time stable or not, can not be answered in general by deterministic simulations. Thermal noise driven dewetting mechanisms has been reported in the literature [208]. For instance, we observe in the non-wetting regime and off-symmetric density, that the potential is too weak to build up a homogeneous layer in at the upper wall. Film rupture can occur, even in our deterministic model. In binary mixtures it is reported that layering effects only occur at transient regimes [292].

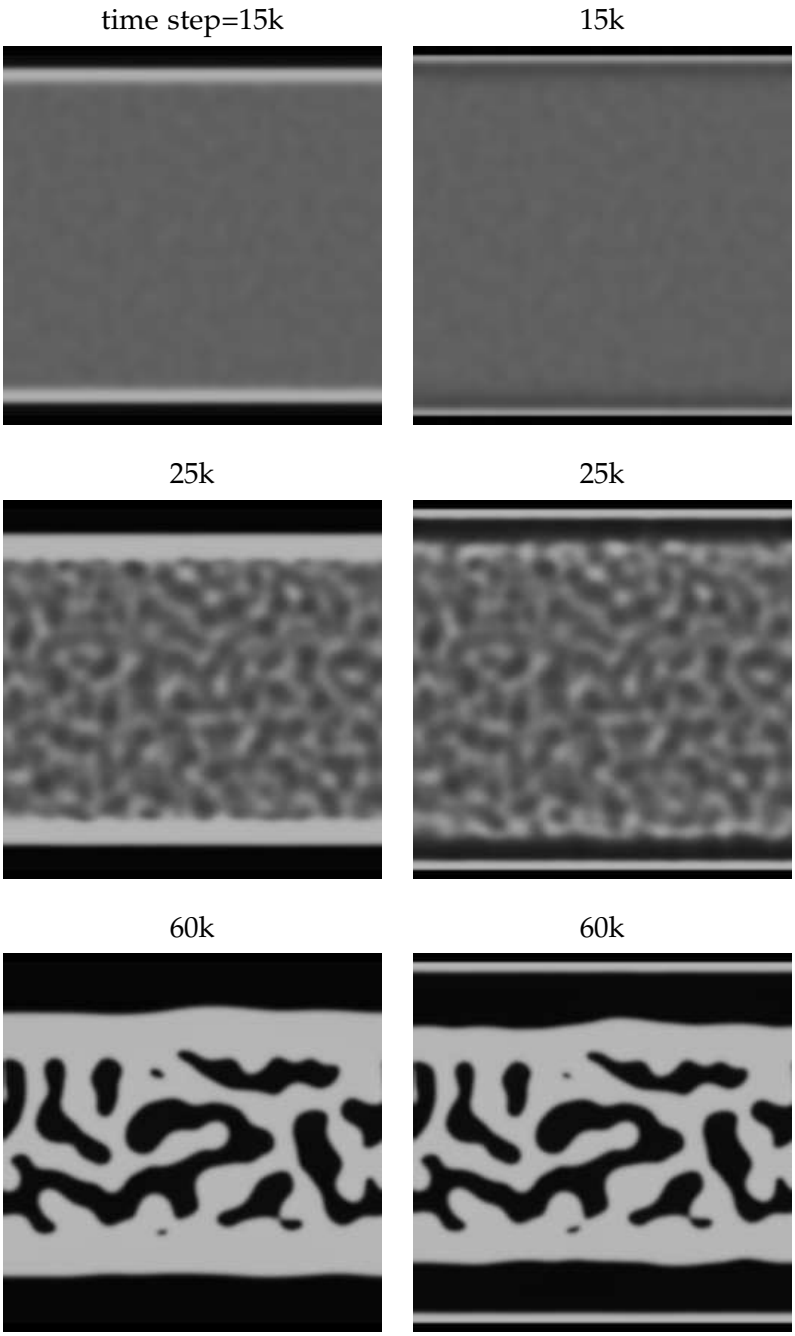


FIGURE 5.11. *Spinodal decomposition* with walls *in a liquid vapor mixture of a van der Waals fluid after a temperature quench to* $T = 0.7T_c$*: left column* $\cos\theta \approx -0.5$ *tight column* $\cos\theta \approx 0.6$*. The average density is symmetric with* $< \rho >= \frac{1}{2}\rho_v + \frac{1}{2}\rho_l$.

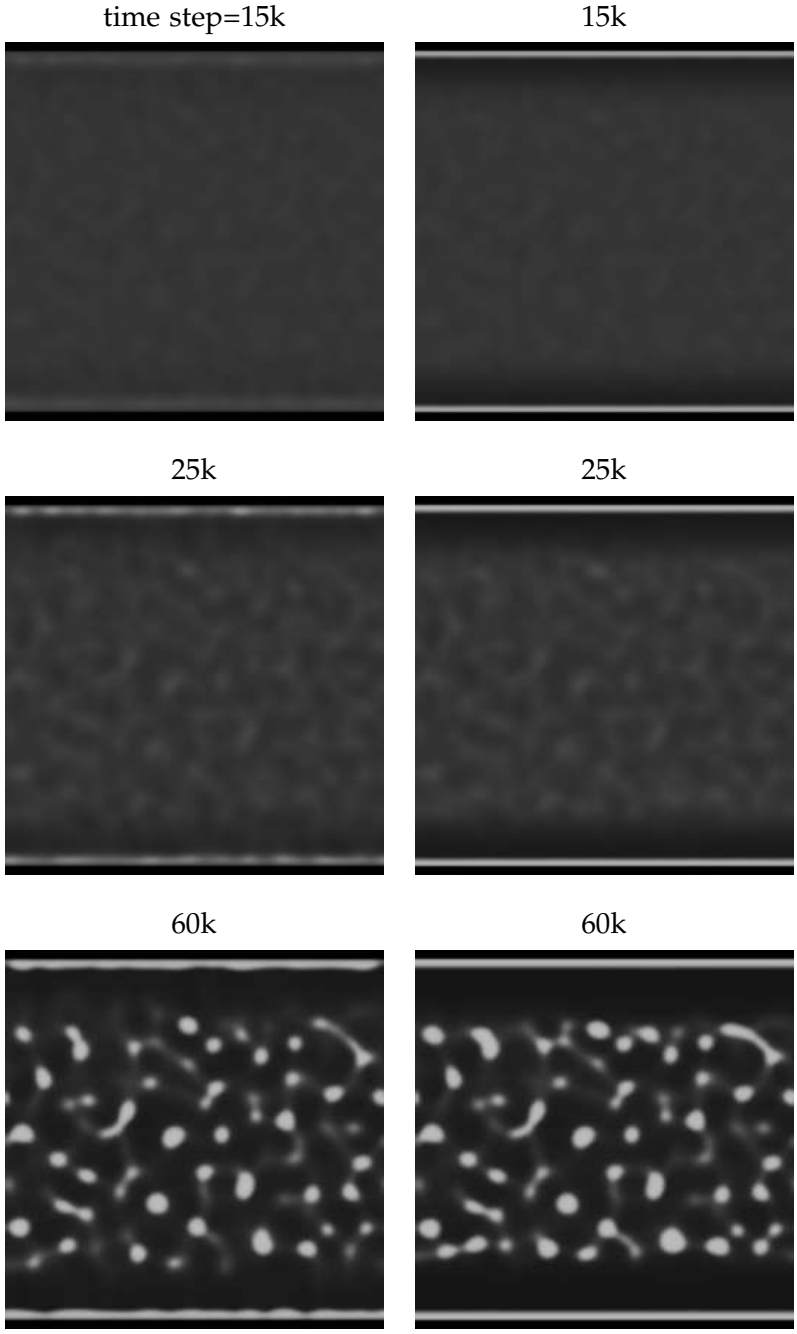


FIGURE 5.12. *Spinodal decomposition* with walls *in a liquid vapor mixture of a van der Waals fluid after a temperature quench to* $T = 0.7T_c$ *with walls: left column* $\cos\theta \approx -0.5$ *tight column* $\cos\theta \approx 0.6$. *The average density is off-symmetric with* $< \rho >= \frac{3}{4}\rho_v + \frac{1}{4}\rho_l$. *Wall position:* $y_{wall} = 167\sigma$

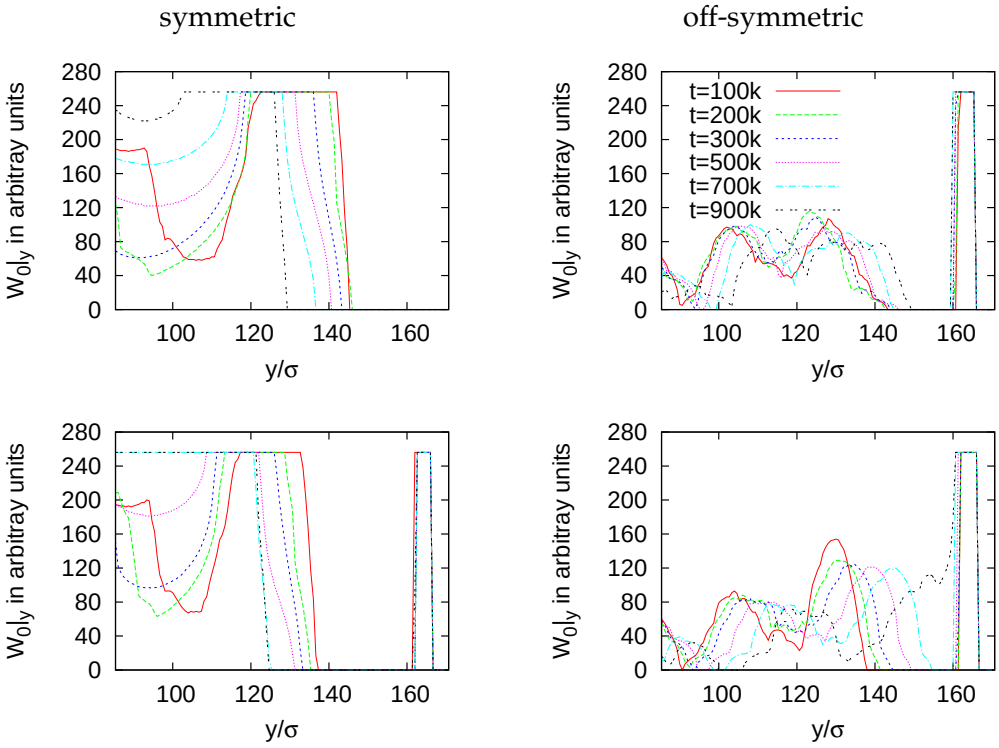


FIGURE 5.13. *Time-evolution of the layering, in particular the depletion layer. $W_1|_y$ is the volume W_1 restricted to one line parallel to the x-axis at position y. The line thickness is constantly one lattice spacing. The depletion layer corresponds to the low $W_1|_y$ values around the position $x = 150 \sim 160\sigma$.*

regime	scaling exponent	reference	
diffusive	1/3	[47, 75]	
viscous	1, 1/2	[75, and references therein]	1/2 in some 2D systems
intertial	2/3	[75]	

TABLE 5.3. *Growth exponents α for vapor-liquid systems.*

5.3.3. Discussion

Spinodal decomposition is an important mechanism in nanotechnology to exploit self-organization to create spatial patterns [91]. Since at these scales the attractive part of these potentials is of great importance, simulation techniques are needed which account for all the mechanism at play: early stage decomposition, viscous and inertial driven hydrodynamics and proper substrate coupling. We suggest therefore the PF model, as convenient tool to study spinodal decomposition and domain growth for liquid-vapor systems. Although studied for long times a fully understanding of these phase-separation processes is still lacking [75], e.g. the crucial role of layering effects at the boundaries [292]. Substrate walls break translation symmetry, and thus motion-dependent morphological measures are needed to describe the morphology sufficiently. The study of the substrate impact is still an open project, where descriptor development and dynamical description are going hand in hand.

We found in the late stage of off-symmetric systems an exponent $\alpha = 2$ which is so far not connected to a dynamic mechanism. Also surface effects seem to lead to formerly unknown growth exponents when perimeter based lengthscales are measured. Investigations of these regimes should be addressed in the futur.

In detail, it remains unclear, whether there is a sharp transition for the occurrence of a transient liquid wetting layer or its production is history dependent. Empirically, this can be studied with more simulations and a large variety of initial noise. Since, the preliminary results indicate a strong dependence on the average density, this problem becomes heavy with respect to the computational costs. A reliable non-wetting layer (depletion in contact with the wall) in liquid-vapor systems might be of great importance in microfluidic transport problems e.g. to clean microchannels with a heat—cool—pumping cycle. Therefore, the time-evolution and the θ-dependence vapor layer at the wall is of great interest too.

We would like to investigate the question, whether and how the time-evolution exponents are affected by the broken symmetry of an attractive wall potential. This question is strongly connected with finite size effects in the simulations. While we believe, that the phenomenology is already correctly captured in our simulation box, a systematical check about finite size effects in systems with walls is still open.

Last but not least, wetting layers are known to be unstable under certain circumstances [208], due to thermal motion. Therefore, a PF model with thermal motion, i.e. the thermostatting is done by a stochastic stress tensor instead of the DDFT or

Cahn-Hilliard thermostat term. Numerical stability together with the wall-coupling in our PF appeared to be a great challenge, which still remains unsolved.

6. Local structure analysis and anisotropy in particulate matter

In the former chapters we investigated the impact of the confining geometry onto the phase behavior of liquid-vapor system with a mean-field description. Here we use a microscopic perspective to study geometrical effects in the local arrangements of fluid particles or grains onto the phase behavior.

Many studies in condensed matter science involve a careful local structure characterization for crystal cluster characterization [133, 266, 294], precursor identification of Lennard-Jones fluid crystallization [294, 266], order description in supercooled liquids [293, 155], melting [241] or the emergence of order in glassy systems [220]. For instance, Speedy et al. [284] connected the free volume and cavity volume in hard sphere systems to the thermodynamical quantaties pressure and chemical potential. Sastry et al. [264] proposed an algorithm based on Speedy's formula to obtain these quantaties from Monte-Carlo simulations in hard spheres. In the literature many fruitful concepts are available to describe local structure. Nevertheless some often used descriptors lack robustness in its defintion, which may lead to misinterpretations and artefacts under certain circumstances. Therefore, routine methods are needed which are robust and easily evaluated.

In this chapter we shall use the tensorial Minkowski analysis to study the local order of hard sphere (HS) systems with and without friction. Frictionless hard spheres are the focus of many investigations to model simple liquids, colloidal suspensions or jammed systems. With the Rosenfeld-functional a very accurate free energy functional is known for equilibrium DFT calculations and thermalized HS ensembles are often created with event driven molecular (EDMD) dynamics or Monte-Carlo (MC) simulations [257, 161, 5]. It is well-known, that at low packing fractions ϕ (percentage of the volume occupied by spheres) thermal[1] hard spheres ensembles are amorphous and disordered, whereas at high packing fractions a fcc-like (face centered cubic) phase is entropically favored [315, 316, 43, 106]. In 3 dimensions a first order phase transition

[1] i.e. typical equilibrium configurations

between the amorphous liquid and the crystalline solid phase is observed. Compressing hard sphere fluids sufficiently fast one obtains a so-called supercooled liquid, which exhibits slow relaxation times [122].

In the thermal and supercooled regime, the collisions of hard particles are assumed to be infinitely short in time. Dissipative dynamics, as it is experienced for example in powders or sand, lead to jammed packings, where all the degrees of freedom (DOF) of momenta are dissipated and the system gets compactified till the number of constraints (contacts of spheres) exceeds the number of DOF. These systems are found in experiments and simulations for packing fractions larger than a certain packing fraction, widely referred to as *random loose packing* (RLP). But its precise definition and value is still under debate [10]. In experiments there is also an upper limit for packing fractions of jammed beads[2] packs, which is called *random close packing* (RCP). Its precise definition and value is under debate too [247, 297]. Up to now, only simulations are known that produce (quasi) jammed sphere packs beyond the RCP packing fraction [144, 8, 186], without initial crystallization germs. Geometric studies reported quasi jammed crystalline packings for low packing fractions too [100]. Figure 6.1 summarizes HS systems which are mentioned above. In this chapter HS ensembles over the full range of packing fractions are studied with Minkowski tensors, and the results are compared to other local order measurements.

[2]The term *bead* is here used for spheres with dissipative dynamics

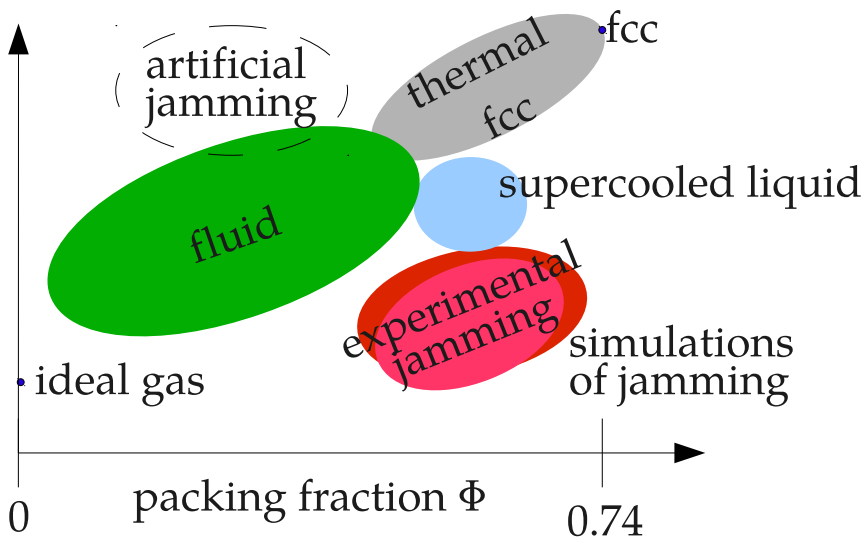


FIGURE 6.1. *Thermal HS systems range from the disordered ideal gas to the closed packed fcc crystal. Non-thermal HS packings exhibit different configurations, from supercooled liquids to jammed. The vertical axis is not precised and can be considered as an order parameter.*

This chapter is organized as followed: In section 6.1 the application of Minkowski tensors as local order parameters is discussed and compared to other common order parameters in section 6.2. Afterwards the local structure of jammed states is analyzed in detail (sec. 6.3), this leads to an investigation of the RCP point in section 6.4 and the development of new techniques which are based on rank-4 Minkowski tensors.

6.1. $\beta_\nu^{r,s}$ as local order parameter

In this section shall discuss, that local order measures, based on the anisotropy measure $\beta_\nu^{r,s}$ are suitable in hard sphere (HS) systems, i.e. thermal equilibrium HS systems. In next sections we shall employ this technique to study also jammed bead packs and supercooled fluids.

In order to develop local order parameters based on the Minkowski functionals and tensors for sphere packings we start with the Voronoi graph [233, 287] of a seed point pattern, e.g. the set of sphere centers. The Voronoi tessellation is a subdivison

of space into convex tiles (Voronoi cells) without overlap and every sphere k is entirely embedded in its Voronoi cell V_k. Every point $\mathbf{r}$ of the Euclidean space $\mathbb{E}^3$ is assigned to the nearest seed $\mathbf{s}_k$ (assuming pairwise disjoint seeds) of the point pattern $\mathcal{P} = \{\mathrm{s}_k | k = 1, \ldots, N\}$. The set of points $\mathbf{r}$ with more than one nearest neighbor seed generate Voronoi cell structure (points on Voronoi facets have two nearest neighbors, points on edges of Voronoi cells have three nearest neighbors,...). The Voronoi cells are therefore convex and each cell contains exactly one seed. Taking the centers of the spheres as seeds, the Voronoi graph represents thus a fair partition of space. Indeed, the Voronoi graph construction is just the simplest representation of a class of tessellations, the so-called Laguerre- or power-tessellations, which can be used for non-monodisperse systems [176]. Figure 6.2 shows an illustration of a Voronoi graph (tessellation) in 2 dimensions. It is noteworthy to mention, that for any countable seed pattern, with pairwise different seeds, Voronoi cells have a non-vanishing volume, but Voronoi facets can exhibit zero surface area, thus we shall see below that the number of Voronoi facets is not robust. Figure 6.3 shows typical hard disc sets at different packing fractions and their inscribed Voronoi graphs.

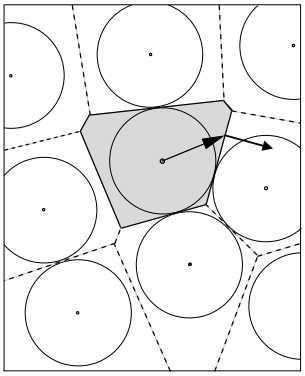


FIGURE 6.2. *2D Voronoi graph of monodisperse hard discs. The seeds are the disc centers. Each Voronoi cell V contains its seed and is convex.*

The key idea of a local order parameter is to describe the shape of the Voronoi cells with robust measures. Such shape descriptors can be for example the volume or the surface area. Indeed local structure analysis based on this two measures have been used often before [17, 181, 248, 287] and these correspond to the simplest Minkowski functionals (up to prefactors).

For instance, Rahman has used Voronoi tessellations to study the self diffusion beyond Brownian theory and harmonic crystals in Lennard-Jones fluids [248]. He has demonstrated that with the Voronoi graph it is possible to decompose the pair-correlation function into a set of pair-correlation functions w.r.t. the number of coordination shells lying between the particles. The Voronoi graph has been used in several papers to compute the so-called free volume and the cavity volume [264, 72, 284]. The cavity volume is connected to the chemical potential of the hard sphere fluid [284]. In recent studies the Voronoi volume has been connected to the thermodynamic molar volume [132]. Furthermore the Voronoi graph is often used to define nearest neighbors [319, 238, 317, 279, 181].

Going beyond the scalar measures, the rank-2 tensors explore the elongation of the cells with the anisotropy measures $\beta_\nu^{r,s}$ as defined in (5.25). This is a precise definition of best fitting of an ellipsoid to a Voronoi cell w.r.t. a certain morphological feature, which is expressed by a MT. To make an example we present in fig. 6.4 the mean (left) and the standard deviation (right) of thermal hard sphere systems obtained from MC and MD simulations [3]. We shall compare the anisotropy of equilibrium HS systems with those of supercooled liquids and jammed states in sec. 6.2 and 6.3. All 6 anisotropy measures capture the first order phase transition and follow qualitatively the same trend, showing that the local anisotropy of thermal HS systems is not subject to special characteristics of the morphology. For the details of the diagram, see the caption.

In fig. 6.4 the ideal gas limit $\phi \to 0$ (solid bullet), which is generated as a Poisson point process is the limiting value for thermal systems. On the other side of the diagram the fcc (face centered cubic) closed packed system ($\phi \approx 0.74048$) is an isotropic system. Note, that the hcp (hexagonal closed packed) system, which is equally favored

[3] MC simulations by M. Spanner, MD simulations by T. Nogawa, see ref. [151]

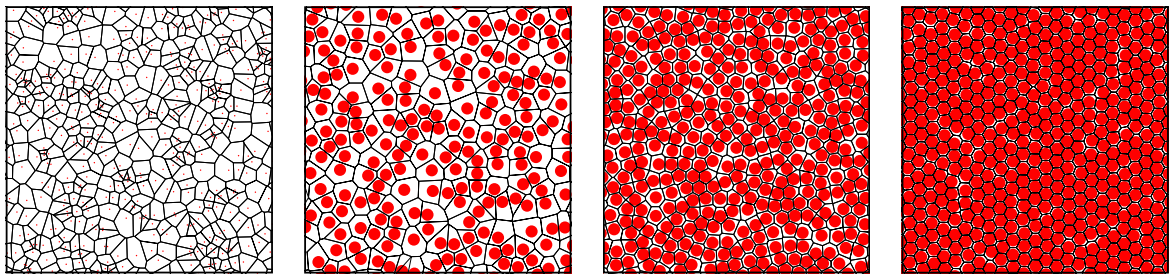


FIGURE 6.3. *Voronoi cells in a Poisson point pattern, a dilute hard disks fluid ($\phi = 32\%$), and hard disks configurations below and above the phase transition ($\phi = 61\%, 76\%$).*

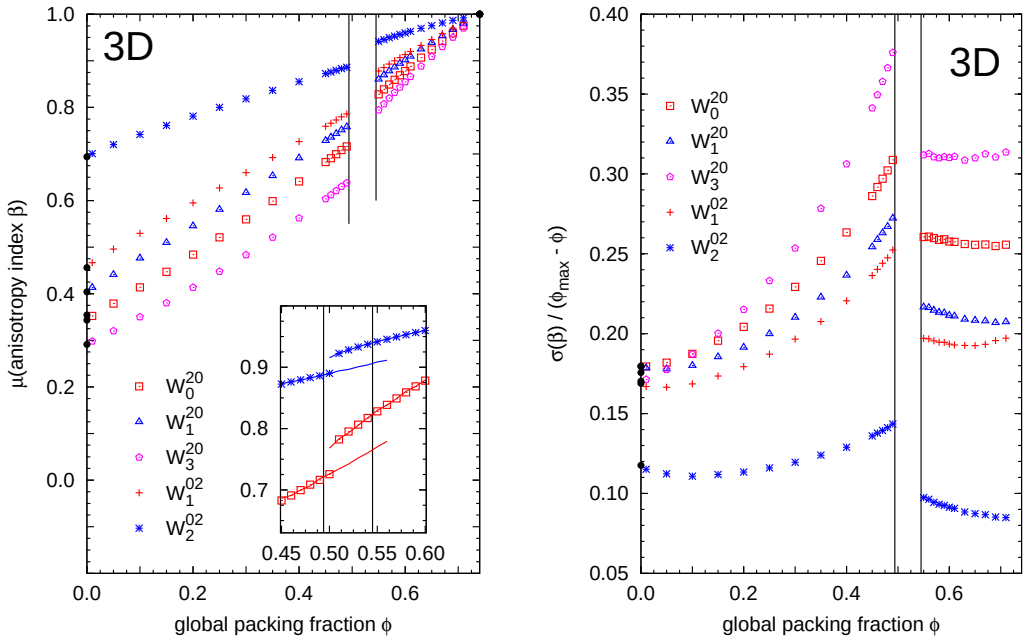


FIGURE 6.4. Left: *Average anisotropy indices* $\langle \beta_\nu^{r,s} \rangle$ *for equilibrium ensembles of hard spheres vs. packing fraction* ϕ. *In the limit* $\phi \to 0$, *the hard spheres anisotropy approaches those of the Poisson process (solid bullets). All average* $\langle \beta_\nu^{r,s} \rangle$ *display a discontinuity at the first-order phase transition at* $\phi \approx 0.49$ *[253]. The inset shows metastable states in or close to the coexistence region; symbols are MC results, lines are MD simulations (see appendix B).* Right: *Standard deviations of the* β *distribution for equilibrium hard spheres. A linear decrease as* $\phi \to \phi_{\text{fcc}}$ *as been divided out. All data points are calculated from MC simulations. Data close to the phase transition might not be fully equilibrated, therefore the standard deviations are omitted in these range. The values of* $\beta_2^{2,0}$ *are very close to those of* $\beta_0^{2,0}$ *and have been omitted for the sake of clarity.*

from a geometric point of view—but dynamically not stable [315, 316, 43, 106]—results in the same values $\beta_\nu^{r,s}$. The mean values $\langle \beta_\nu^{r,s} \rangle$ show a discontinuity at the first order phase transition point $\phi \approx= 0.49$ [253]. The standard deviation $\sigma(\beta_\nu^{r,s})$ goes almost linearly to zero: $\sigma(\beta_\nu^{r,s}) \propto \phi - \phi_{\text{fcc}}$, where ϕ_{fcc} is the packing fraction of the fcc packing ($\phi_{\text{fcc}} = 0.74048$).

To further investigate the morphological information carried by the anisotropy indices, figure 6.5 displays the correlation coefficients of $\text{corr}(X, Y)$ of $X = \beta_\nu^{r,s}$ with *(a)* $Y = \beta_{\nu'}^{r',s'}$, *(b)* $Y = \gamma_\nu^{r,s}$ and *(c)* the isoperimetric ratio (also called "shape index") $\zeta = W_1^3/W_0^2 \propto A^3/V^2$. The correlation coefficient of two random variates is defined

$\mathrm{corr}(X,Y) = \langle (X - \langle X \rangle)(Y - \langle Y \rangle) \rangle / \sigma(X)\sigma(Y) \in [-1,1]$, where $\sigma(\,.\,)$ is the standard deviation. The $\beta_\nu^{r,s} - \beta_{\nu'}^{r',s'}$ correlations in panel *(a)* for all combinations of ν, r, s and ν', r', s' shows quite large positive values. Values close to one indicate strong positive correlation, this means $\beta_\nu^{r,s}$ and $\beta_{\nu'}^{r',s'}$ depent similarily on shape variations of the Voronoi cells. These large values of the correlation coefficient verify that the anisotropy signatures in the thermal system are generic and not subject to a specific property of the morphology. Panel *(b)* shows the correlations of $X = \beta_\nu r, s$ with $Y = \gamma_\nu^{r,s}$ (ratio of the intermediate eigenvalue and the maximal eigenvalue). We find moderate positive values for all MT. The anisotropy measure $\beta_\nu^{r,s}$ does not carry the full anisotropy information, but captures already significant shape information. The correlations in panel *(c)* of $\beta_\nu^{r,s}$ with the isoperimetric ratio ζ [221, 287] are rather poor (values close to zero), especially close to the phase transition. Low correlations between ζ and $\beta_\nu^{r,s}$ underlines the signification of the rank-2 tensors as shape descriptors beyond the scalar MF, i.e. different charateristics are captured. ζ for example differs for a cube and a sphere and can be interpreted as an asphericity index, $\beta_\nu^{r,s}$ captures e.g. elongations (depending on the choice of ν, r and s).

Conclusion We used the hard sphere model to validate rank-2 Minkowski tensors as order parameters. Thanks to the completeness theorem for Minkowski tensors, we can conclude that the local anisotropy of the Voronoi cells in equilibrium hard sphere packings is generic. This means anisotropy is not dependent on a special choice of the morphological characteristics under consideration. Furthermore, we demonstrated that MT capture different information compared to the scalar MF.

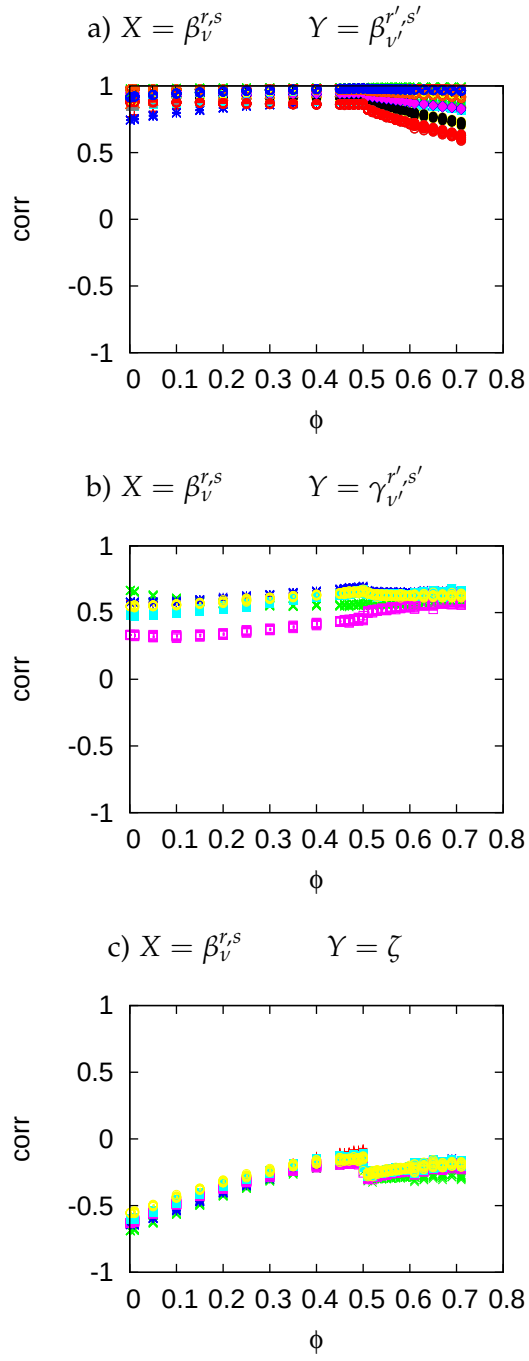


FIGURE 6.5. *Correlations* corr $:= \frac{\langle (X-\langle Y\rangle)(Y-\langle Y\rangle)\rangle}{\sigma(X)\sigma(Y)} \in [-1,1]$. a) $X = \beta_\nu^{r,s}$ *and* $Y = \beta_{\nu'}^{r',s'}$ *for all combinations of anisotropy indices: All anisotropy measures a quite strongly correlated.* b) $X = \beta_\nu^{r,s}$ *and* $Y = \gamma_\nu^{r,s}$ *for all* ν *and* $r+s=2$*, where* $\gamma_\nu^{r,s} := \frac{|(\mu_\nu^{r,s})_2|}{|(\mu_\nu^{r,s})_1|} \in [0, \beta_\nu^{r,s}]$*: Both measures of eigenvalue ratios have only an intermediate correlation.* b) $X = \beta_\nu^{r,s}$ *and* $Y = \zeta$ *for all* ν *and* $r+s=2$*, where* $\zeta = W_0^2/W_1^3$ *is the isoperimetric ratio: In the vicinity of the phase transitions both measures are quite poorly correlated. Because of the similarity of all curves, the legend is suppressed.*

6.2. Alternative commonly used local order parameters

Structure descriptors for particle systems are already widely used in the literature. Most of these measures depend crucially on how the set of nearest-neighbors is defined. The most famous order-parameter family are the so-called bond orientation order parameter (BOO) [217, 297, 177, 289]. Further measures are e.g. tensorial measures such as Edwards' configurational tensor [88], quadrons [39] and fabric/texture tensors [87]. While these structure indices are undoubtfully valuable, their application need great care in the choice of a suitable neighborhood definition. Often, these neighbors are referred by bonds, and clearly the number of neighbors is discontinuous over the changes of the seed pattern. In crystallography the number of nearest neighbors (also called coordination number) z_{NN} is used directly or combined with other parameters to localize crystal defects [156, 2, 94].

In this section we shall study BOO in the light of the neighborhood definition. As a further example of nearest neighbor definition dependent structure parameters, we shall disscus the Edwards tensor. We show, that the lack of continuity in the coordination number may lead to artefacts which adulterate the structure analysis.

Steinhardt bond orientation order parameters In the following the Steinhardt bond orientation order parameter (BOO) [289] and the Edwards tensors [88] are defined and compared to the Minkowski approach. In order to define the bond orientation order parameter in a system of particles, a suitable set of n_k nearest neighbors for each particle k has to be chosen. Let θ_j and φ_j denote the spherical coordinate angles of the vector connecting the center of k to the centers of its jth nearest neighbor. Then, the bond orientation order parameter $q_l(k)$ of particle k is defined as

$$q_l(k) = \sqrt{\frac{4\pi}{2l+1} \sum_{m=-l}^{l} \left| \left\langle \sum_{j=1}^{n_k} Y_m^l\left(\theta_j, \varphi_j\right) \right\rangle \right|^2}, \tag{6.1}$$

where Y_m^l are spherical harmonics. The squared norm ensures that q_l is rotationally invariant. Third-order invariants can be constructed

$$w_l(k) = \sum_{\substack{m_1, m_2, m_3 \\ m_1+m_2+m_3=0}} \begin{pmatrix} l & l & l \\ m_1 & m_2 & m_3 \end{pmatrix} \overline{Y_{m_1}^l}\, \overline{Y_{m_2}^l}\, \overline{Y_{m_3}^l}, \tag{6.2}$$

where $\overline{Y_m^l} = \sum_{j=1}^{n_k} Y_m^l(\theta_j, \varphi_j)$ and $\begin{pmatrix} l & l & l \\ m_1 & m_2 & m_3 \end{pmatrix}$ is the Wigner 3j-symbol [289]. Although we will not use the global bond order parameter Q_l we define it for completeness as

$$Q_l = \sqrt{\frac{4\pi}{2l+1} \sum_{m=-l}^{l} \left| \left\langle \sum_{k=1}^{N} \sum_{j=1}^{n_k} Y_m^l(\theta_j, \varphi_j) \right\rangle \right|^2}, \tag{6.3}$$

where N is the number of particles. The average over all bonds is taken inside the norm, and for disordered systems the sum over the Y_m^l vanishes as $1/\sqrt{\sum_{k=1}^{N} n_k}$, while it remains finite for common crystalline structures [289, 256] Usually, the case $l = 6$ is considered, which is sensitive to fcc, hcp and icosahedral bond orientation. In equlibrium hard sphere systems hcp and fcc nuclei are found [43, 106].

Bond definition As noted above, the bond or neighborhood definition lies at the heart of the definition of the local bond order. Some different definitions are illustrated in fig. 6.6. Steinhardt proposed any suitable definition of nearest neighbor bonds for q_l and he used in his original work a cutoff radius of 1.2σ with the particle diameter σ [289]. Widely used definitions of the coordination (bonds) are fixed cutoff radii e.g. $(1.2, 1.4)\sigma$, used e.g. in refs. [220, 231, 202, 85, 158] or cutoff radii based on the first minimum of the two-point correlation function $g(r)$, as in [163, 54, 127, 1, 308]. This most common definition in the literature assigns a bond between sphere k and sphere j if the distance between the sphere centers is less or equal r_c.

Alternatively, the Delaunay graph construction on the particle centers [20] is used to define nearest neighbors [319, 238, 317, 279, 181]. Every sphere center connected to k by a Delaunay edge is a neighbor of k. This parameter-free definition, solely based on locations of particle centers, is equivalent to the definition of Voronoi neighbors.

A less commonly used definition is to assign a fixed number n of nearest neighbors per seed k [78, 320]. We shall use the more precise symbols like $q_6^{r_c}$, q_6^{D} or q_6^{n} to specify the definition of nearest neighbors.

Figure 6.6 summarizes these commonly used definitions in 2D. Panels *a)* and *b)* show the relationship of the Voronoi graph and the Delaunay graph. The Voronoi graph is plotted red and the Voronoi neighbors are indicated with blue bonds. Please note, spheres share a bond, whenever there exists a shared facet in the Voronoi graph (no matter the area of the facet). The diagram of these bonds is called Delaunay graph. Panel *c)* is an example of a cutoff-radius coordination and depends on the arbitrary choice of r_c. The definition of a fixed number of nearest neighbors (panel *d*) follows the

fact, that if a certain cluster configuration is searched for, the ideal cluster configuration number is known. While usually no physical rule for bond coordination exists each of these definitions cover (slightly) different aspects and is subject to artefacts.

The remainder of this section illustrates how sensitively q_6 depends on the nearest neighbor, by analysis of hard sphere systems and solid models. In figure 6.7 *a)* we present the average local bond parameter $\langle q_6^D \rangle$ as function of the packing fraction ϕ for several hard sphere systems. The Delaunay definition is used for the simple fact that it is well defined for all packing fractions ϕ. The blue squares represent Monte-Carlo (MC) simulations from above [151]. The snapshots (point pattern of sphere centers) are taken in thermodynamical equilibrium in the fluid phase and the solid fcc phase. One can clearly see a qualitative change from the fluid to the crystal at $\phi \approx 0.53$. The black crosses are Lubachevsky-Stillinger (LS) simulations [186, 281] (see also app. B.4 for details of the simulations). These simulations generate jammed states between packing fractions $0.55 > \phi > 0.65$. The orange bullets presents (MD) simulation snapshots of supercooled liquid like states. The supercooled liquids are prepared by a compression technique specified in app. B.3. Although it is numerically demanding to

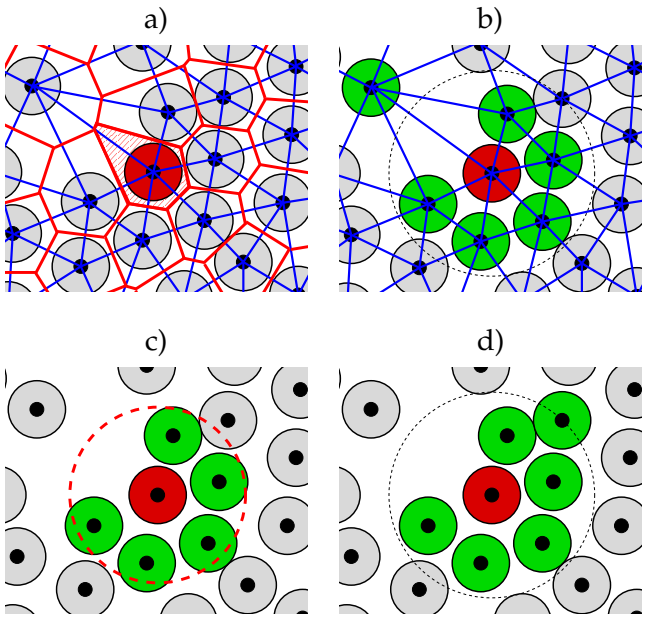


FIGURE 6.6. *Widely used neighborhood definitions: a) Voronoi graph (red) and its dual Delaunay graph (blue) b) Delaunay bonds c) bonds via cutoff radius r_c d) $n = 6$ nearest neighbors bonds*

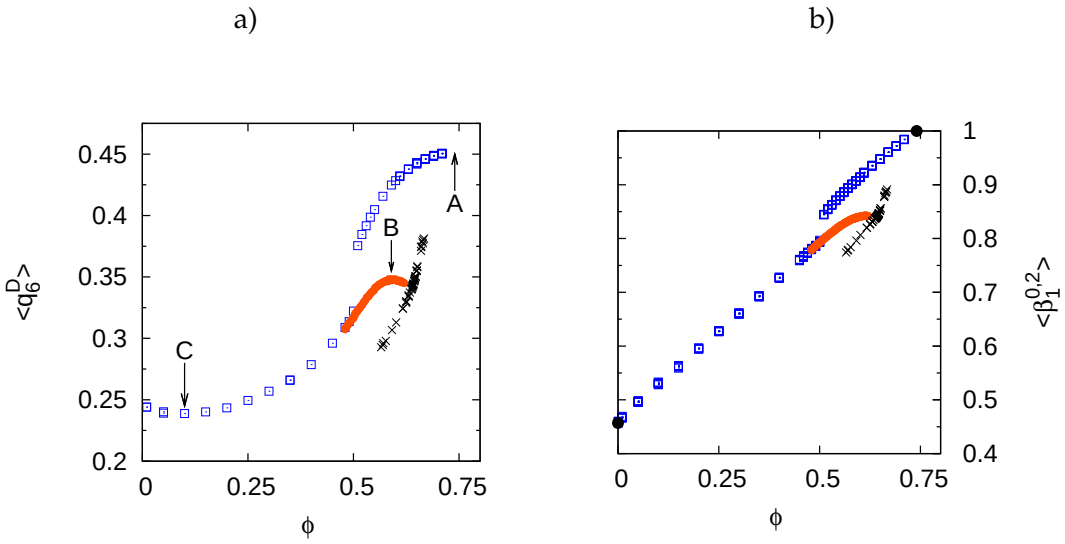


FIGURE 6.7. *a) Local order of spherical particles, measured by q_6^{D}. Blue squares: Monte Carlo simulations, orange squares: MD supercooled fluid, black crosses: Lubachevsky-Stillinger final (jammed) states. b) Local order of spherical particles, measured with $\beta_1^{0,2}$. Symbols and colors match those of a)*

drive the supercooled fluid towards packing fractions of RCP ($\phi_{\mathrm{RCP}} \approx 0.64$) it appears that the continuation of this branch reaches nearly the jammed states at RCP.

Figure 6.7 *b)* shows the same simulations as *a)* but with the anisotropy measure $\beta_1^{0,2}$. One can clearly see a qualitative matching between the local order diagram with q_6. This coincidence underlines the interpretation of β as a local order parameter. The jammed LS (black crosses) structures between packing fractions $0.55 > \phi > 0.65$ fall on a line for $\beta(\phi)$. In sec. 6.3 we shall show that this universal behavior is also valid for other jamming protocols (simulations and experiments). The dense-LS (DLS) packings beyond RCP do not continue the universal line of the jammed states $\phi < 0.65$ and rather exhibit a kink at that point. These observations will be the subject of the section 6.4.

A careful look at the q_6 diagram *a)* exhibits two flaws of this measure that becomes evident for the MC (blue squares) equilibrium simulations. The first but avoidable defective appearance is the fcc limit which does not lead to the q_6 value of an ideal fcc crystal (*A* in fig. 6.7 b). Indeed in an ordered phase small perturbations of the seed points end up in a quite large impact to the number of Voronoi facets (equivalent to the

Delaunay neighbors) and thus q_6 is calculated in general with more than the 12 nearest neighbors in the fcc or hcp lattice [298, 255], while the ideal fcc and hcp configurations have exactly 12 nearest neighbors at the same distance (See also the 2D example in fig. 6.11) Some authors use additional criteria in order to refine the Delaunay bond definition, e.g. a cutoff radius [319]. In a disordered phase no systematical degeneracy in the Delaunay graph appears. In amorphous systems the Delaunay definition suits therefore better. Furthermore this parameterless definition is rather independent from the packing fraction (see below).

The second flaw can be found in the region of very diluted fluids (*C* in fig. 6.7 b). The Poisson point process (ideal gas), which clearly is the least ordered state, nevertheless has a higher q_6^{D} than the HS equilibrium at $\phi \approx 0.1$. As these low packing fractions are barely studied in the literature using local order parameters this flaw is not practically relevant but conceptually interesting. In contrast β shows a well defined signature in either case. In the zero packing fraction limit $\phi \to 0$ the local structure of the hard sphere gas approaches in a monotonic behavior the one of an uncorrelated Poisson point process marked with a black bullets.

In the other limit $\phi \to \phi_{\mathrm{fcc}}$ the hard sphere crystal structure unambiguously leads to that of an ideal fcc crystal (black bullet) with $\beta_{\nu'}^{r,s} = \beta_1^{0,2} = 1$. The supercooled branch (orange bullets) of $q_6(\phi)$ follows a non-monotonic curve. We shall discuss in the next paragraph that q_6 leads to misinterpretation in this regime.

q_6^{D} exhibits a local maximum (*B* in fig. 6.7 b) in the supercooled liquid branch, which does not necessarily correspond to increased ordering. Instead, abnormal behavior of q_6 in this regime is due to the interplay between two competing effects. Such local order anomalies are the focus of several studies [78, 90, 320]. First the number of nearest neighbors is ϕ-dependent and second the ordering of the spheres around a center sphere is also ϕ-dependent, since compressing the fluid changes the local neighborhood. In a totally uncorrelated system q_6 will scale with $1/\sqrt{n_k}$ [256]. In a supercooled fluid this effect is less strong in the first coordination shell up to $n_k \approx 12$ and stronger when the second shell is included (fig. 6.8).

Figure 6.9 (left panel) show the supercooled branch of Figure 6.7 with four different definitions of coordination and the right panel the mean coordination number in this samples. This example of a disordered system shows that a coordination number dependent order/disorder parameter can give conflicting results depending on the choice of coordination or bonds. Since the q_6 order parameter is subject to artefacts in this regime, it is not clear whether q_6 correctly represents the physics of the system, whether physical effects are obscured or whether observed anomalies are due

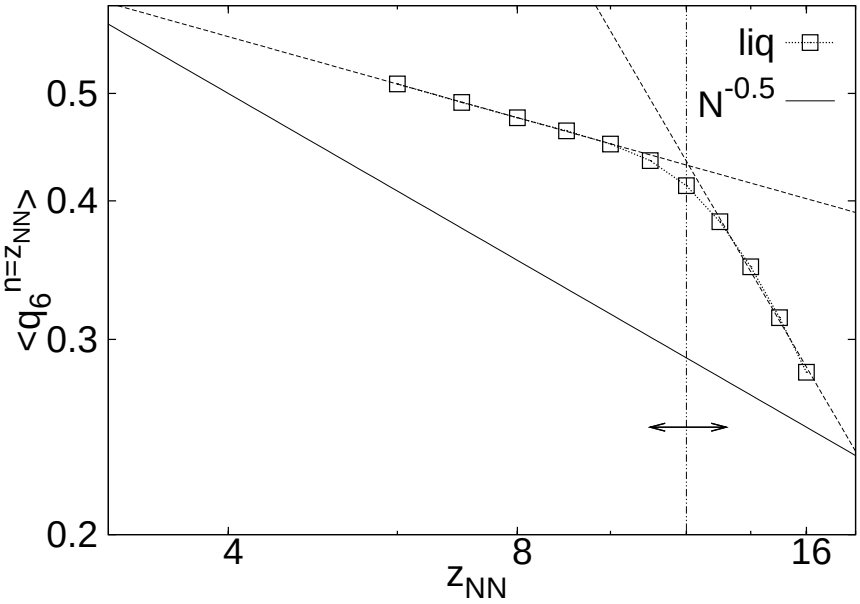


FIGURE 6.8. *Mean $< q_6^n >$ as function of $n = z_{\mathrm{NN}}$, i.e. the nearest neighbor definition detects the set of z_{NN} nearest spheres as bonds. The squares are MD simulations of the supercooled fluid branch with $\phi = 0.6$. The solid lines correspond to the perfectly uncorrelated case ($\langle q_6^n \rangle \propto 1/\sqrt{n}$, see ref. [256]). The dotted lines are fits for the first coordination shell for $n < 12$ and first and second shell $n > 12$. The first shell exponent is -0.24 and the second shell exponent is -1.48.*

to the definition of the order parameter. Since the discrete nature of the coordination number leads to undesirable jumps some authors use weight functions to smooth the parameters [323, 246]. The choice of weight functions is discussed in chapter 7.

Einstein solid A simple model of ordered structures is the so-called Einstein solid. It is used here to generate point patterns continuously between a certain ordered crystal structure and a fully disordered pattern. Placeing seeds on the ideal sites $\mathbf{r}_i$ of a crystal (fcc, hcp, ...) with lattice spacing $\mathbf{a}$ and displacing each seed by a random vector $\vec{\varepsilon}_i = (\varepsilon_x, \varepsilon_y, \varepsilon_z)$, where ε_i, $i = x, y, z$ are independent random variates of a distribution P. A common choice for P is a Gaussian distribution with zero mean. The root mean square displacement (RMSD) is therefore $\varepsilon = \sqrt{< |\vec{\varepsilon}|^2 >}$. Tuning the noise amplitude ε from zero to infinity destroys the lattice order and changes continuously to an ideal gas process (Poisson point process). While real solids exhibit strong correlations in the particle positions and fluctuations around the average lattice sites, the simple Einstein

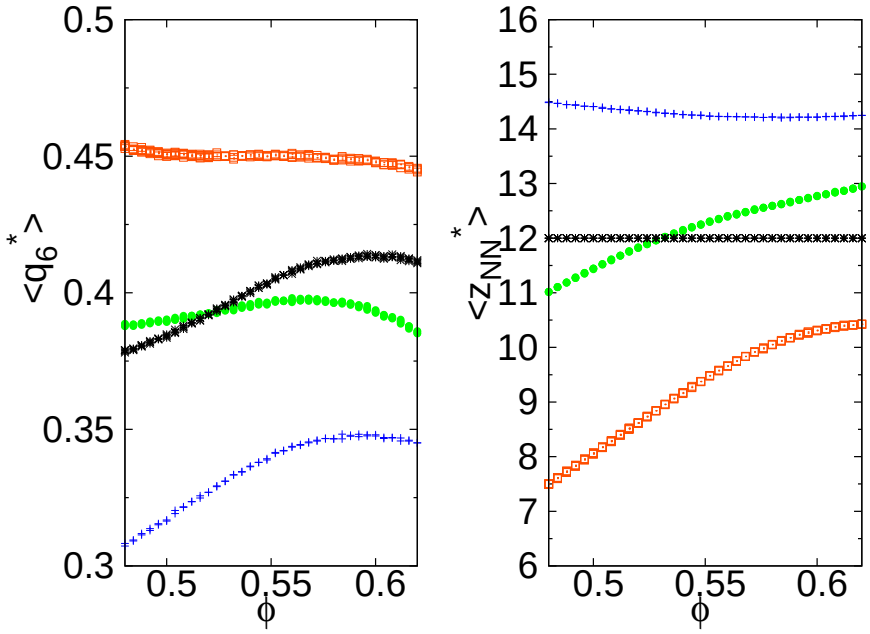


FIGURE 6.9. *Left panel: Local bond order parameter $< q_6 >$ in the supercooled fluid with several definitions of the coordination neighbors: orange squares: $r_c = 1.2\sigma$, green bullets: $r_c = 1.4\sigma$ blue crosses: Delaunay-definition and black stars: $n = 12$. Depending on the definition, q_6 shows an overall rising or falling trend with or without extrema. Right panel: Corresponding number of nearest neighbors. While the Delaunay-neighbor definition stays rather constant, a fixed cutoff-radius results to a strong increase.*

model shows decreasing correlations of the positions with an increase of ε and no correlations in the fluctuations around the ideal seed points. An arbitrarily large overlap for finite-sized particles is therefore allowed. The left panel of fig. 6.10 presents the local bond order parameter q_6^* with different definitions of the neighborhood $*$. The corresponding mean coordination number is shown in the right panel. While in the ordered systems the definition is not very important (except for the Delaunay definition, as discussed above) with increasing disorder the details of the definition of z_{NN} become more important. The use of neighborhood-dependent order parameter in amorphous particulate media needs great care for the details of the bond definition.

Edwards tensor Edwards and others proposed a tensor construct for granular matter which we shall call Edwards tensor C [88, 39]. They make use of C to investigate stress transmission in grain packings and it is used e.g. to characterize isotropy of the

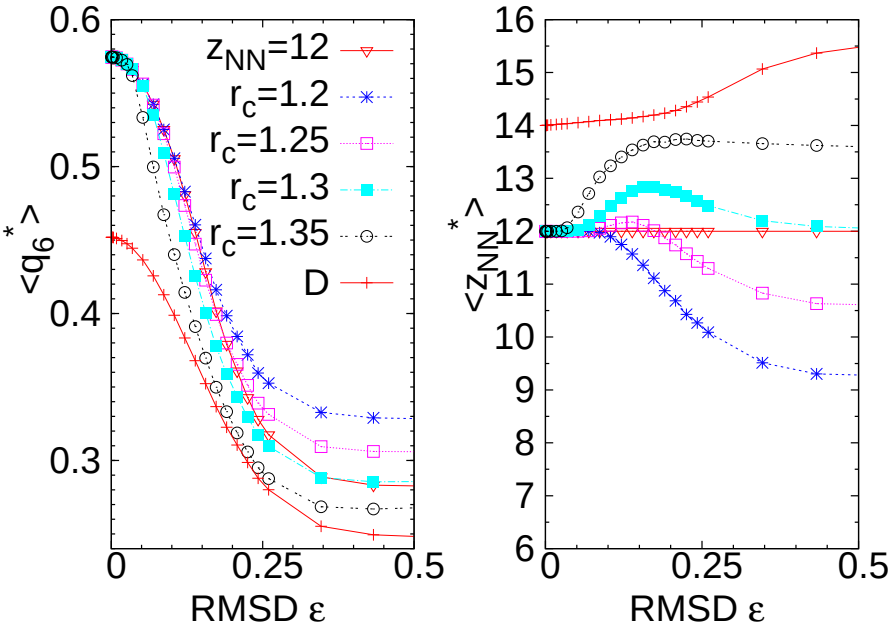


FIGURE 6.10. Left: *Local bond order parameter over the RMSD ε of an uncorrelated fcc Einstein solid with 6 different definitions of bonds.* Right: *Corresponding coordination numbers* z_{NN}. *The dimensionless RMSD is normalized with the lattice spacing* **a**.

packing. As we will see, this tensorial measure is quite similar to one of the MT, but lacks continuity. Let us denote the n_k neighbors of sphere k (which is located at r_k) with $1 \leq j \leq n_k$ and their position vectors with r_j. The bond vectors are $\mathbf{b}_{kj} = \mathbf{r}_j - \mathbf{r}_k$. The Edwards tensor is

$$C = \sum_{j=1}^{n_k} \mathbf{b}_{jk} \otimes \mathbf{b}_{jk}. \tag{6.4}$$

Similar to the MT, one can define an anisotropy measure β_{C} by the ratio of the minimal and the maximal eigenvalues $(\mu_{\mathrm{C}})_d$ and $(\mu_{\mathrm{C}})_1$. In fig. 6.11 the average anisotropy measures $< \beta_1^{0,2} >$ and $< \beta_{\mathrm{C}} >$ for fcc-Einstein solids are compared, and three different bond-definitions are used for the latter tensor ($\langle . \rangle$ denotes the average over all seed points). While the continuous defined MT varies monotonic with RMSD and meets the correct fcc limit of 1, the Edwards tensor has some defective behavior, especially close to degenerated configurations, i.e. close to the ideal fcc configuration. First we shall concentrate on the Delaunay bonds, or equivalent the Voronoi facets: In perfect hcp or fcc configurations, the second nearest neighbors create Voronoi facets with zero surface area, and the Delaunay tetrahedra of four adjoint spheres, are not uniquely defined. In 2D this degeneracy is the same for Delaunay triangles, as sketched be-

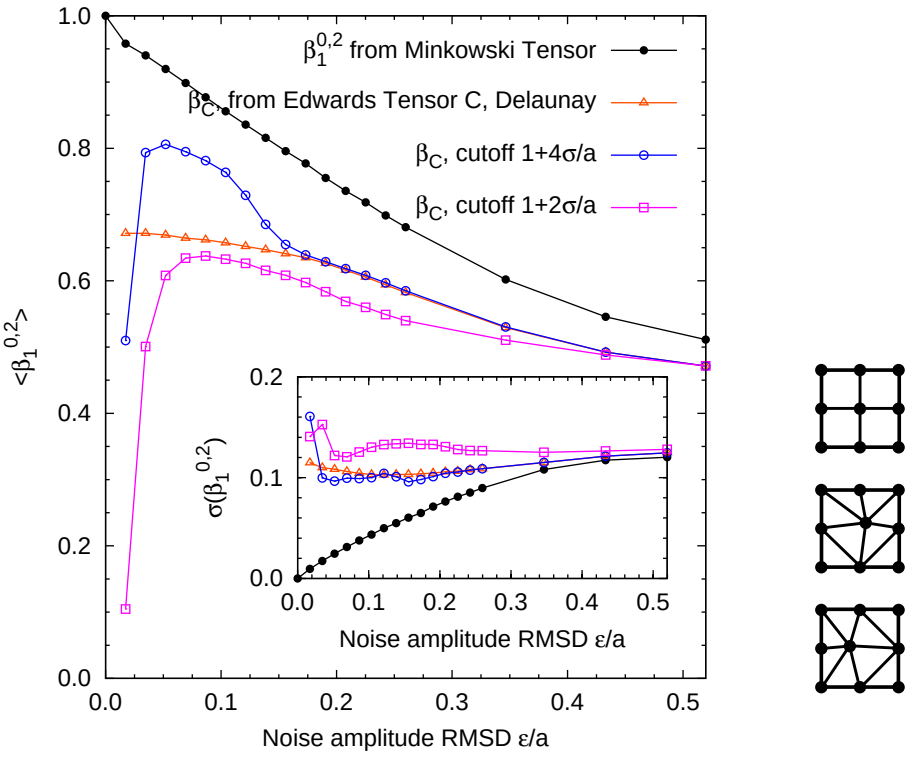


FIGURE 6.11. Left: *Anisotropy index for $W_1^{0,2}(I)$ and Edwards' configurational tensor $C^{(i)}$, applied to a fcc Einstein solid. The noise amplitude is quantified by the root mean square displacement* RMSD *of the germs from their ideal lattice sites. The Minkowski tensor $W_1^{0,2}(I)$ is computed from the Voronoi tessellation of the lattice, $C^{(i)}$ is computed with the Delaunay neighborhood and distance cutoff neighborhoods of the order of the noise amplitude. It is seen that, even for vanishingly small levels of noise, $C^{(i)}$ of a single lattice site is not an isotropic tensor, while $W_1^{0,2}(I)$ is. Tensor isotropy is defined via the ratio of eigenvalues, as in eq.* (5.25)*. The x axis and cutoffs are in units of the fcc nearest neighbor distance a.* Right: *Illustration of point configuration with a degenerate Delaunay triangulation. A small perturbation (not drawn to scale) lifts the degeneracy and breaks the isotropic 4-simplices into anisotropic triangles.*

side the main panel of fig. 6.11. In the degenerated case it is therefore not possible to choose one of either diagonal bonds. For any tiny distortion of the seed points, the degeneracy is broken, and of course this is extremely sensitive to noise [255, 298]. Furthermore, since these additional bonds are the longest bonds of the center-sphere the quadratic weight in C spoil the correct close-crystal behavior. This arguments ap-

ply also to cutoff radius definitions of nearest neighbor sets. We find therefore equal deficiencies (both, in the mean of β_C and its fluctuations, see insert). Actually, the discontinuous Edwards tensor with Delaunay bonds is similar to the MT $W_1^{0,2}$, which is the normal weighted surface area tensor. But in contrast to the Edwards tensor only the direction $\mathbf{n}_{jk}$ is taken, which is $\mathbf{b}_{jk}/|\mathbf{b}_{jk}|$, and this contribution is weighted with the surface area of the Voronoi facet. While the number of Voronoi facets is discontinuous the surface area of the Voronoi cells is continuous. An infinitesimal seed-points displacement might create a new facet, but it initially has infinitesimally small surface area. The MT $W_1^{0,2}$ is therefore robust against noise of the seed point pattern, although it is similarly defined via the Voronoi graph. The mean anisotropy index $\langle \beta_1^{r,s} \rangle$ in fig. 6.11 and the HS fcc crystal (fig. 6.7) look very similar (the former as a function of RMSD, the latter as a function of ϕ).

However, the two systems are clearly quite different. The HS crystal involves high correlations of the local arrangements and individual spheres, which are not covered

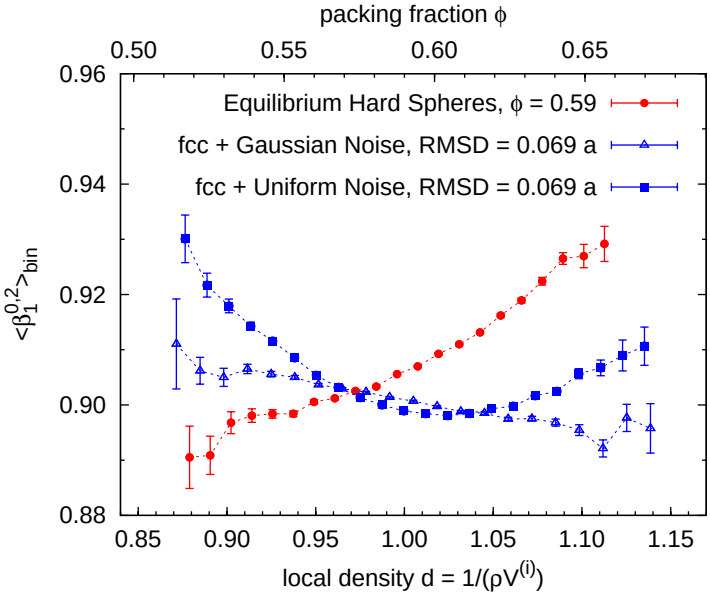


FIGURE 6.12. *Comparison of average anisotropy index $\beta_1^{0,2}$ as a function of local normalized densities d. The Voronoi cells are binned in density bins, and an average of their anisotropy indices is computed separately for each bin. The plot shows that the correlation of anisotropy index and cell volume distinguishes between the Einstein solid and the equilibrium hard spheres structure (in the solid phase), even though parameters are chosen such that the global averages $\langle \beta_1^{0,2} \rangle$ are equal.*

by the simple Einstein solid model. This structural differences are displayed by the correlations of the local normalized density $d = 1/(\rho V)$ and the local anisotropy $\beta_\nu^{r,s}$. A positive correlation for d and β is found for the HS crystal, while the Gaussian Einstein model shows a negative correlation (see fig. 6.12). Also, the correlations are sensitive to subtle changes of the random process in the Einstein model. Using uniform random variates for the displacements $\vec{\varepsilon}$ lead to rather uncorrelated behavior, displayed by the U-shape of the correlation curve. Positive correlations indicate repulsive interactions. It was also found for jammed bead packs and will be discussed in section 6.4, and negative correlations has been found in foams [151]. In repulsive systems, such as HS, high pressure (or high packing fractions) drive the system to local structure close to the particle shape itself, and minimizing the void space. Thus a positive correlation is expected. In the Einstein solid, no minimal distance is imposed, and high densities stem from intrusion of seeds to the void space of an adjacent seed. This displacement results in two oblate cells. In ref. [151] it was demonstrated, that the Minkowski analysis is also useful for other systems, like Lennard-Jones fluids in 3D and hard discs in 2D.

Conclusion Many common local structure parameters rely on a definition how the set of nearest neighbors is chosen. The number of nearest neighbors is an integer and thus not continuous. This can yield artefacts in the local structure analysis. We demonstrated this for example in a system of amorphous HS fluids for the BOO and in the so-called Einstein solid for the Edwards tensor. Conversely, MT of Voronoi cells are continuous order parameters of the local arrangement and therefore robust against noise in the seed point pattern.

6.3. Jamming in athermal dissipative HS systems

In this section we shall discuss the local structure of jammed spheres. As a first working definition for jamming, we shall call a bead pack jammed when every (or at least most) beads are confined by their neighbors so that no motion is possible. This is called mechanically stable. Clearly, jammed states emerge from metastable states and non-equilibrium processes. A priori one has to expect that the features of jamming are history-dependent, i.e. the packing characteristics differ for each protocol and initial configurations [239]. Often, jamming is regarded as an infinite pressure limit of glasses [239, 296, 14, 149], Figure 6.13 presents a schematic hard sphere (HS) phase diagram (fig. taken from ref. [239]). Upon slow compression hard spheres the ensemble follows the solid line. Faster compression leads to metastable states, where the dynamics slow down. An ideal glass transition in 3 (or in general in finite) dimension is subject of an intense debate [239, and references therein]. A glassy state has an infinite relaxation time and vanishing diffusivity.

Among several definitions of jamming, Donev and Torquato proposed a hierarchy of jamming definitions, which is widely adopted for ideal packings [83]. Before quoting the jamming conditions, one should note that experimental or simulated packings are never ideal, e.g. often so-called rattlers can be found. Rattlers are sole spheres,

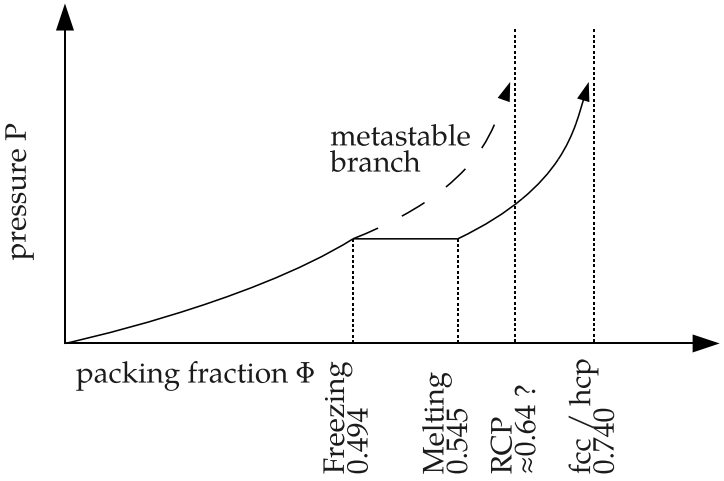


FIGURE 6.13. *Schematic phase diagram of hard spheres as described by Parisi [239]. Compressing hard spheres slowly, the ensemble will follow the solid line. However, fast compression leads to metastable states, which, arguably, cannot be compressed beyond a maximal packing fraction (ϕ_{RCP}) as the pressure converges.*

trapped in a cage of jammed spheres, but free to move inside the cage. A sphere is called *locally jammed* when it is fixed by its neighbors, i.e. 4 appropriate distributed contacts in 3D. A packing is locally jammed, if each sphere is locally jammed. A stricter condition is *collectively jammed*, this means that the packing is locally jammed and no subset of spheres can be moved simultaneously so that any sphere lose contacts. Finally, a packing is called strictly jammed, if the packing is collectively jammed and a volume-conserving deformation of the boundary is not possible [296]. While this formal definitions are hardly verifiable in experiments, jamming is often considered as the state where the packing got stuck after a compactification process, e.g. sedimentation. Packing hard spheres densely is a purely geometrical problem. The local structure analysis in jammed bead packs is a long-standing research subject. In 1960 Bernal [32] published his study of structure in liquids and discussed in another paper in the same year the coordination in jammed bead packs [33]. In this study he proposed the existence of random close packing (RCP). Since than, many studies have focused on the preparation and structure analysis of jammed packings [144, 150, 281, 275, 140, 181, 228, 163, 153, 238, 12].

Often, the structure analysis has focused onto Voronoi graph constructions and the volumes of the Voronoi cells. Aste et al. [16] found a rescaled k-gamma distribution for the Voronoi and Delaunay volumes in experimental packings. Further, the authors showed, that the emergence of this distribution can be derived from minimal ingredients, namely, the assumption, that in any meaningful tiling of space a theoretical lower limit exists for the cell volume. The k-gamma distribution reads

$$P(V) = P(V, V_{\min}, k) = \frac{k^k}{(k-1)!} \frac{(V - V_{\min})^{k-1}}{(\langle V \rangle - V_{\min})^k} \exp\left(-k \frac{V - V_{\min}}{\langle V \rangle - V_{\min}}\right), \tag{6.5}$$

where $P(V)$ is the probability of a Voronoi cell with volume V, $\langle V \rangle$ is the average volume and $V_{\min} = V_{\text{sphere}}/0.7546$ is the Voronoi volume of an icosahedron center sphere, which is the most compact configuration [18]. k is a free parameter of the distribution, which was found to be 12 reflecting the fact, that in a dense packing the number of neighbor spheres is approx. 12.

One of the experiments, which were used to verify the k-gamma-distribution theory of Aste, are fluidized bed experiments of refs. [139, 140]. Beads settle under gravity against a liquid flow and build a jammed packing in the bottom of the container. One advantage of this experimental technique is, that the sedimentation time can be varied in a very broad range, so that the slow sedimentation limit can be checked. For frictional spheres this study gave empirical evidence of the existence of the random loose packing RLP packing limit around $\phi \approx 0.55$. Song et al. [283] tried to clarify this point

theoretically and proposed a theory of jamming. They have argued, that in the large friction limit ($\mu_f \to \infty$) 4 contact points are sufficient to fix beads in a packing, while frictionless spheres ($\mu_f \to 0$) need 6 contact points. It is argued, that disordered packings of frictional spheres show mean contact numbers between 4 and 6. The number Z of mechanical contacts can be thus interpolated from both extreme values. The theory from the Song paper is based on some fundamental considerations by Edwards and Oakeshott [89]. In 1989 they proposed a statistical mechanics approach to powders and grain packings, which follows some analogy to classical thermodynamics. They argue that the system is governed by its overall volume V instead of a free energy in standard thermodynamics, since the thermal motion vanishes in dissipative grain ensembles. Further a function W is considered, which connects the volume to the grain positions. Therefore, it takes a role of a Hamiltonian function in classical mechanics. In a microcanonic systems all possible states are chosen by the conservation of energy condition. An equivalent role takes a filter operator in the Edwards-Oakeshott theory, which formally filters all the mechanically stable packings. This condition function gives access to the entropy $S(V, X, N)$, where X is the so-called compactivity $X = \partial V / \partial S$ and plays a role comparable to temperature in thermodynamics. Based on this formalism, Song et al. [283] derived a formula for RLP

$$\phi_{\mathrm{RLP}} \approx \frac{Z}{Z + 3.46} \quad , \tag{6.6}$$

which leads to $\phi_{\mathrm{RLP}} = \phi_{\mathrm{RCP}}$ for frictionless spheres, which makes this packing fraction unique and it is also referred as to point-J ϕ_J. Chaudhuri et al. [61] showed in a simulation study of 50 : 50 binary sphere mixtures (radius ratio = 1.4), that frictionless hard spheres can produce a continuous range of volume fractions for jamming. A consistent theory of jamming is still lacking.

6.3.1. Anisotropy of jammed bead packs

In fig. 6.14 we present the mean anisotropy indices $\beta_\nu^{r,s}$ of the Voronoi cells in jammed bead packs of a number of different protocols. The solid squares indicate "dry acrylic" (DA) experiments [13, 12, 17] of dry acrylic beads in a cylinder geometry. The "fluidized bed" (FB) experiments are point patterns obtained from glass beads in a vertical cylinder [16, 275]. The discrete element method (DEM) simulations are relaxed packing of the original DA experiments, to remove small degrees of polydispersity [273]. Finally event-driven MD simulations with the Lubachevsky-Stillinger (LS) algorithm were performed [273]. This algorithm allows to create quasi-jammed bead packs of frictionless spheres, by continuous compression. Details of the experiments and the

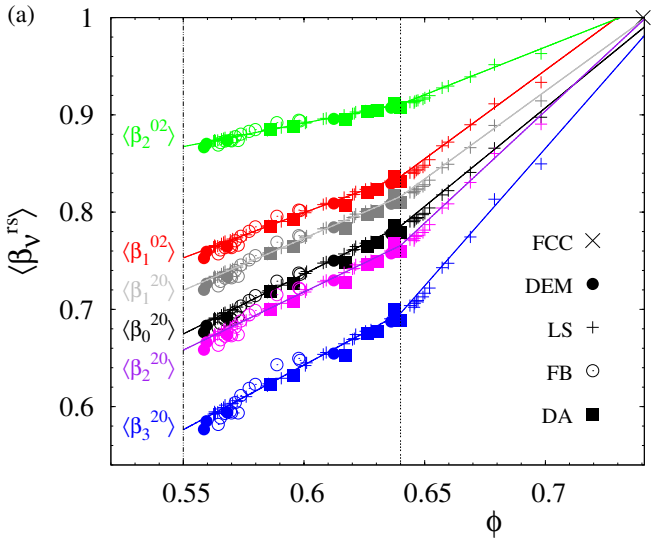


FIGURE 6.14. *Average anisotropy of the Voronoi cells, measured by averaged eigenvalue ratios* $\langle \beta_\nu^{rs} \rangle$ *of Minkowski tensors* $\mathbf{W}_\nu^{rs}$*, as function of packing fraction* ϕ *for* jammed *bead configurations. Isotropic cells have* $\beta_\nu^{rs} = 1$ *and deviations from 1 measure the degree of anisotropy. The straight lines are linear fits for* $\phi < 0.64$ *and* $\phi > 0.64$*.*

simulations can be found in the appendix B. The two vertical lines mark the jamming limits RLP and RCP (values taken from the literature: $\phi_{\mathrm{RLP}} = 0.55$ [139] and $\phi_{\mathrm{RCP}} = 0.64$ [33]). Significant deviations of all $\langle \beta_\nu^{r,s} \rangle$ from 1 for all jammed bead packs below RCP indicate a considerable typical anisotropy. Independent of the choice of the MT, bead packs with packing fractions ϕ between RLP and RCP show a nearly linear trend over ϕ and no significant differences between the several protocols can be observed. For monodisperse bead packs this effect can be—at least on basis of these experimental data—interpreted as an universal behavior for jamming. Please note, that this holds for both, frictional beads in the experiments (DA, FB) and DEM simulations and frictionless spheres in simulations (LS). With the DEM-relaxation (see app. B.6) polydispersity is removed from the dry acrylic beads without substantially modifying the packing configuration. The difference between the anisotropy in the DA data and the DEM data is negligible. This demonstrates the robustness of our analysis to small degrees of polydispersity. In the interval between RLP and RCP we observe a nearly linear relationship between the mean anisotropy $\langle \beta_\nu^{r,s} \rangle$ and the packing fraction ϕ for all protocols. The independence of the protocols is remarkable, since a priori (non-equilibrium) realizations of jammed packings strongly depend on their

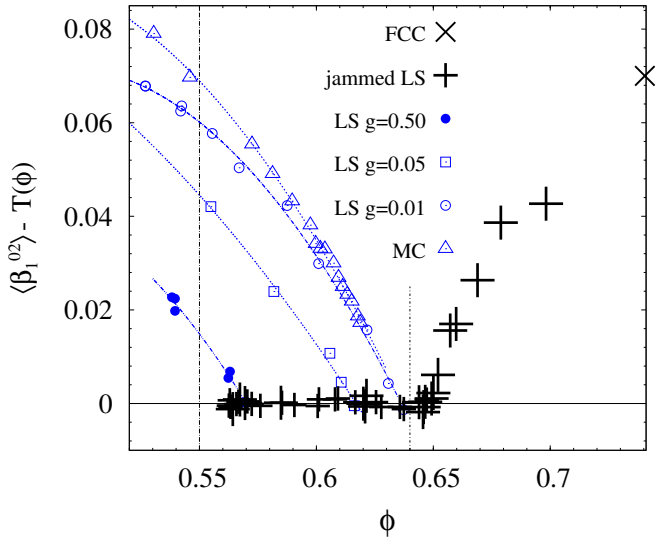


FIGURE 6.15. *Anisotropy index* $\langle\beta_1^{02}\rangle$*, as representative of the six* $\langle\beta_\nu^{r,s}\rangle$*, for jammed and unjammed configurations generated by the LS algorithm, after subtraction of the linear trend* T*. The symbols (+) correspond to jammed LS configurations, the same as in fig. 6.14 minus the linear fit* $T(\phi)$ *to all data points of* $\langle\beta_1^{02}\rangle$ *with* $0.55 \leq \phi \leq 0.64$*. A distinct change of the slope* $d\langle\beta_1^{02}\rangle/d\phi$ *is evident at RCP* $\phi \approx 0.64$*. The squares and circles correspond to* unjammed *configurations for different growth rates* g *of the LS algorithm. MC simulations are displayed with* $\triangle$*-symbols. The data for all other* $\langle\beta_\nu^{rs}\rangle$*, not shown for the sake of clarity, are qualitatively similar.*

history and each protocol follows a different class of paths into the jammed packing. For instance LS uses non-equilibrium collisions with Newtonian dynamics. FB experiments are sedimentation processes with hydrodynamic interactions and friction. DA experiments dynamics involve dissipation via visco-elastic dissipation and friction of dry acrylic beads in air.

The LS algorithm allows also to create sphere packings beyond RCP. The data in fig. 6.14 clearly show a change in the slope in $< \beta >$ as a function of ϕ close to RCP. This change of the local structure will be discussed below in detail. This kink is even more visible in fig. 6.15. The symbols $+$ represent $\beta_1^{0,2}$ for the jammed LS packings in fig. 6.14, where the linear trend $T(\phi)$ is subtracted. The other symbols are for unjammed LS and MC simulations. Unjammed LS packings are generated by a standard LS compression, but the process is stopped before the packing jams.

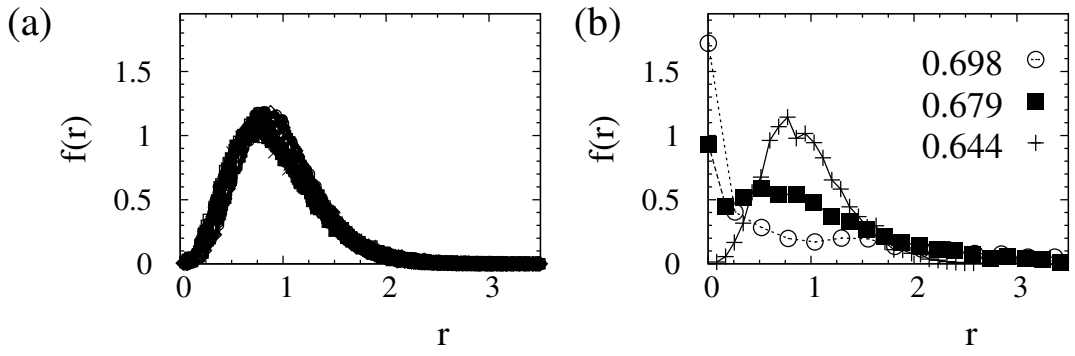


FIGURE 6.16. *(a) Rescaled distribution of all six anisotropy indices β_ν^{rs} for all experimental and simulated bead packs with $0.55 < \phi < 0.64$, with $r = (1/\beta_\nu^{rs} - 1)/(1/\langle\beta_\nu^{rs}\rangle - 1)$, showing a vanishing probability for isotropic cells ($r = 0$). (b) The same distribution (with identical axes) for β_0^{20} of the Lubachevsky-Stillinger configurations only with packing fractions $\phi = 0.644, 0.679, 0.698$. The finite probability for isotropic cells is an indication of the presence of semi-crystalline regions.*

The MC simulation is a decompressing routine. Initializing a jammed bead pack close to RCP, decreasing gradually the bead radius and jiggling around with MC moves reduces the packing fraction ϕ. With both protocols unjammed configurations show a significantly lower anisotropy, than the jammed bead packs. And the universal curve consists of all jamming points (one for each respective jamming process). One can conclude, that for this class of jamming protocols, the jammed states maximizes the anisotropy for a given packing fraction ϕ. Thermal HS systems and supercooled liquids are more isotropic (compare fig. 6.7).

In fig. 6.16 probability distributions $f(r)$ of all experimental and simulation results are presented in the left panel, where r is the rescaled anisotropy measure

$$r = \frac{(\beta_\nu^{r,s})^{-1} - 1}{\langle\beta_\nu^{r,s}\rangle^{-1} - 1}. \tag{6.7}$$

$r = 0$ presents the isotropic case. This rescaling leads to universal (at least very similar) anisotropy distribution for all MT and all protocols with $\phi < 0.64$. This distribution is similar to a gamma distribution. Similar scaling was found for the volume of Voronoi cells in jammed packings [16]. Looking at LS simulations above $\phi = 0.64$ shows qualitatively different distributions. Very close to $\phi = 0.64$ the distribution still looks the same as for lower packing fractions, but packings with $\phi = 0.679, 0.698$ have finite probability for isotropic cells (see right panel in fig. 6.14). This is an onset of

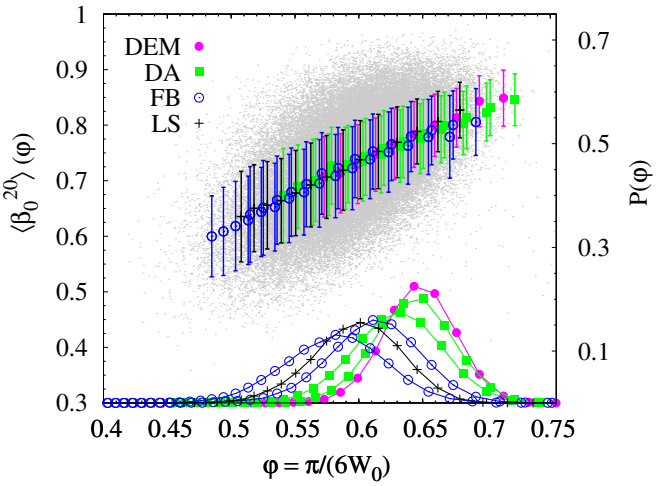


FIGURE 6.17. *Relationship between local packing fraction* $\varphi = (\pi/6)/W_0$ *and anisotropy index* β_0^{20}. *At the bottom (and using the right-hand scale) the distributions* $P(\varphi)$ *of the local packing fractions are plotted. At the top, the gray scattered points are coordinate pairs* $\left(\varphi(K), \beta_0^{20}(K)\right)$ *plotted individually,* i.e. *without any averaging, for each Voronoi cell* K *in the six samples. The top data points with errorbars represent the averages* $\langle \beta_0^{20} \rangle_\varphi$, *computed individually for each of the six data sets with a binning of* $\Delta\varphi \approx 0.01$. *The error bars represent the standard deviations,* i.e. *the width of the distributions of* β_0^{20}, *and not the negligible small error of the average. The six datasets shown here have global packing fractions* $\phi = 0.567$ *(FB),* 0.598 *(FB),* 0.636 *(DEM),* 0.630 *(DA),* 0.617 *(DA) and* 0.585 *(LS). Note that the global packing fraction* ϕ *is given as the average* $\langle(\pi/6)/W_0\rangle$ *over all Voronoi cells.*

crystallization and will be demonstrated below.

Before we turn to this transition point, the correlations of the jammed configurations below RCP is discussed. Figure 6.17 shows the correlations of β and the local packing fraction $\varphi = V_{\text{sphere}}/W_0 = \pi/(6W_0)$, where W_0 is the Voronoi cell volume and V_{sphere} the sphere volume. The gray dots in the background correspond to each Voronoi cell in all jammed point patterns with global packing fraction $\phi < 0.64$. The symbols (for 6 different packings and different global packing ϕ) in the foreground are averages of $< \beta_0^{0,2} >_\varphi$ in the interval $[\varphi, \varphi + \Delta\varphi]$ (bin) as a function φ. $\Delta\varphi \approx 0.01$. A positive slope corresponds to positive correlations of the anisotropy and the local packing fraction as expected for repulsive interactions. The errorbars indicate the standard deviation in each bin. The curves on the bottom of the plot display the distributions of the

local packing fraction φ of the 6 datasets. All datasets (FB, DA, DEM, LS) fall onto a common nearly linear correlation curve. This underlines the universal structure of jammed bead packs. The linear trend does neither extrapolate to the isotropic fcc point $\varphi_{\mathrm{fcc}} = 0.7405$ nor to the isotropic icosahedral configuration at $\varphi_{\mathrm{ico}} = 0.7546$. Higher anisotropy in globally less denser systems stems thus from more larger Voronoi cells with higher anisotropy.

6.3.2. Random ellipsoid packings

It was found that non-spherical particles such as ellipsoids (e.g. M&M candies) have higher packing fraction than random packings of their spherical counterparts [82]. For beads at $\phi = 0.64$ the typical $\beta_0^{2,0} \approx 0.78$, which gives a length ratio of $\lambda \approx 0.89$ (see fig. 6.18). This observed anisotropy of the void space suggests that commensurable anisotropic particles can pack closer. A hypothetical substitution of spheres at ϕ in a packing near RCP with ellipsoids filling more void space (see fig. 6.18) leads to global packing fractions of $\phi_{\text{ellipsoids}} \approx 0.72$, which is consistent with the experiments and the simulations of ref. [82, 192].

6.3.3. Conclusion

In this section we demonstrate that the local arrangements of isotropic spheres in a jammed packing is substantially anisotropic. This anisotropy is shown to be universal.

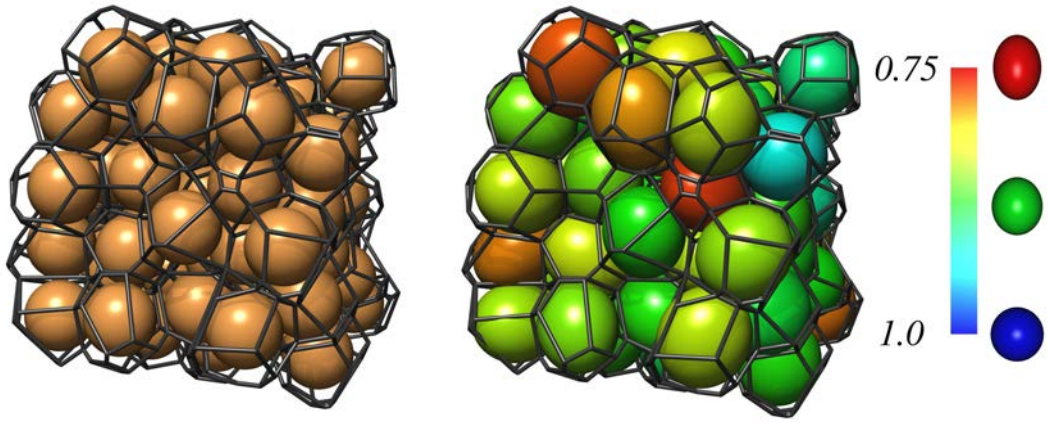


FIGURE 6.18. Left *A subset of a jammed disordered packing of beads in 3D with the corresponding Voronoi graph. The Voronoi cell is the region of space around a bead that is closer to this bead than to any other in the packing. The configuration is a subset of the DA dataset with packing fraction* $\phi = 0.586$. Right *The same subset of the Voronoi graph, however with the beads replaced by ellipsoids that match the anisotropy and orientation of the Voronoi cells. The anisotropy is quantified by the eigenvalue ratios* β_0^{20} *of* $\mathbf{W}_0^{20}$ *of the Voronoi cells. Colors represent the ratio of the shortest and longest axis of the ellipsoid. An isotropic cell has* $\beta_0^{20} = 1$ *and deviations from 1 quantify anisotropy. An ellipsoid with axes* (a, a, c) *with shortest-to-longest axis ratio* $a/c = 0.8$ *corresponds to* $\beta_0^{20} \approx 0.65$.

More precise, all employed jamming protocols—experiments and simulations—lead to the same rescaled anisotropy distribution and the same (within small statistical errors) mean local anisotropy as a function of the packing fraction in the packing fraction interval from RLP to RCP. In jammed bead packs for packing fraction below RCP, the probability to find isotropic cells vanishes. Beyond RCP however, we find a finite probability for such cells. This effect is investigated in greater detail in the next section. Furthermore, local anisotropy is maximal compared to thermal hard sphere systems, metastable systems and compressed hard sphere ensembles with the same packing fraction.

Substantial anisotropy in jammed bead packs may explain, why disordered packings of ellipsoids pack denser than their spherical counterparts. The virtual replacement of isotropic beads by anisotropic ellipsoids occupies the anisotropic void space more efficiently.

6.4. Crystallization onset at RCP

The results of this section are joint work with S. Kapfer from the University Erlangen-Nürnberg.

In section 6.3 (see also fig.6.16 therein) it is discussed that at a certain packing fraction roughly around $\phi \approx 0.64$ the distribution of anisotropy changes qualitatively: from the universal jammed distribution with vanishing probability for isotropic cells to a bimodal distribution with finite probability for isotropic cells. In this section we shall demonstrate, that this change stems from a distinct structure transition, from totally disordered to partially ordered. The partial order is connected to a minimization of the volume. We shall analyse the packings for the occurence of hcp and fcc and icosahedral Voronoi cells. In order to distinguish between these structures we shall extend the MT method to tensors of rank 4, in particular to $W_1^{0,4}$. Beyond RCP the emergence of hcp and fcc order is found, icosahedral structures are not observed.

In the non-ergodic jamming problem, three ordered configurations are of special interest—structures that maximize the packing fraction. The fcc and hcp crystals structures are known [120] to fill space globally most efficiently with a packing fraction of $\phi \approx 0.7405$ (see fig. 6.19). The fcc crystal is obtained as stacking of hexagonal ordered layers with three ($A-B-C-A-B-C$) alternating displacements between sequent layers. The hcp crystal consist equally of hexagonal ordered planes in a $A-B-A-B$ stacking. Between this both crystals with highest symmetry an infinite number of closed packings can be generated by an arbitrary succession of the layers A, B, C where no two equal layers are adjacent (see fig.6.19).

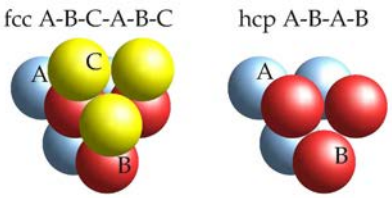


FIGURE 6.19. *Stacking of globally closed packed spheres*

In three dimensions these globally densest packings are not the locally optimal packing. It is believed, while not yet proven, that the icosahedral structure (ico) is the limit for local dense packing with a local packing fraction of $\varphi_{\text{ico}} \approx 0.7546$ [18]. With the

term icosahedral a sphere configuration is meant, that consist of one sphere in the center of gravity of an icosahedron and at every edge of this regular polyhedron a satellite sphere is located. Figure 6.20 illustrates this most compact sphere packing.

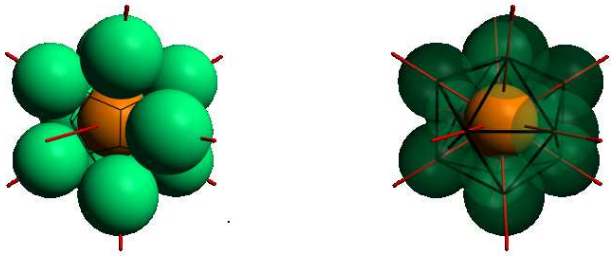


FIGURE 6.20. *Locally most dense packed sphere (orange) in icosahedral configuration. The corresponding Voronoi cell is a dodecahedron (right panel)*

The Voronoi cells of the sphere in hcp or fcc packing are isotropic. The same holds for the center sphere in the icosahedral configuration. For the latter, the Voronoi cell is the dual body of the icosahedron: the dodecahedron.

As discussed above, the RCP point was proposed by Bernal [32] as the largest packing fraction that one can obtain by jamming spheres randomly. Indeed this or similar definitions are rather fuzzy, and Torquato et al. [297] raised the question, whether RCP is ill-defined, or rather not definable. According to his argumentation, in several experiments different limits were found [278, 228] furthermore computer simulations [144] studies report different values as maximal packing fraction. Torquato argued that this is not consistent with the definition from above. Therefore the authors recommended to use a more mathematical definition—the so-called maximally random jammed (MRJ) packing fraction ϕ_{MRJ}. This packing fraction "minimizes ψ among all statistically homogeneous and isotropic jammed structures" [297], where ψ is any order parameter with a minimum. The authors argue that every order parameter ψ_k, which exhibit a minimum is sensitive to ψ_{MRJ}. Though, this definition is not less fuzzy than that one formerly given for RCP this paper released a broad discussion, whether MRJ or RCP is the right definition [8, 149, 232, 318, 247].

Radin revisited the definition of RCP and proposed a non-thermodynamic first order phase transition [247]. This transition has to be understood in the framework of

Edwards, and can be understood as analogy to the freezing transition in HS fluids. Up to a certain packing fraction ϕ_{RCP} the Edwards entropy S is higher in the disordered phase avoiding any crystallization, compareable to thermal HS fluids below $\phi < 0.49$. Above that point a coexistence of ordered and disordered phase domains is expected. This corresponds to the $0.49 < \phi < 0.54$ interval in the freezing/melting picture [247]. The question of a phase transition in the classical thermodynamic picture assums history independent systems. As we saw from the previous section—at least for the disordered jamming—packings of several protocols show an universal structure in all anisotropy measures. This is in agreement with earlier findings based on volume distribution [16] and volume fluctuation and reversibility analysis [230, 244, 254, 275].

Anikeenko and Medvedev [8] investigated the structural order of LS and Jodrey-Torey simulations. They looked for so-called polytetrahedral order, i.e. aggregates of tetrahedral simplices, which are generalizations of a regular tetrahedra. The Delaunay cell shape is analyzed w.r.t. the longest edge. Comparison with a regular tetrahedron gives a quality factor for polyhedra. At a packing fraction of $\phi \approx 0.646$ it is reported, that nearly every sphere participate in at least one tetrahedron simplice, which qualifies for icosahedra, fcc or hcp. Approaching this point from lower packing fractions shows a monotonic increase in the frequency of in tetrahedral structure involved spheres. Further densification would need other mechanisms. The volume fraction of the polytetrahedra aggregates takes a maximum at $\phi = 0.646$. This studies shows nicely, a structural change of simulated HS systems at a point, which we shall refer to as RCP. This findings support the proposal of Radin [247], but do not clarify whether crystallization occurs.

In a recent study Xu et al. [319] investigated the local structure of LS simulations below and above RCP. They used the local and global bond orientation order parameters q_6 and Q_6 to find clusters in the system and found evidence of fcc and hcp. Furthermore, it is demonstrated that the compression parameter γ in the LS algorithm determines the final packing fraction (within typical errors). The inverse parameter γ^{-1} and the packing fraction ϕ display a structural transition.

While the Xu study [319] demonstrates clearly, that crystalline fcc and hcp structures are created beyond a certain ϕ several questions remain, e.g.: Is there a critical packing fraction below which crystalites are not found and above which crystalites must exist? Are there icosahedral structures in the system? Does non-ergodicity allow even small crystallites? Although fcc and hcp are equally favored in terms of packing efficiency is there one type favored? At which precise value of ϕ does crystallization occur?

Indeed, for the latter question the term crystallization need to be specified: In equi-

librium systems, where particles are thermally excited, crystallization is considered as a persistent order which is not sharp but follows a clearly peaked distribution. For example, this can be measured in a scattering experiment as Bragg peaks. Thus a sufficiently large crystal cluster is needed to be identified. In the athermal packing problem, crystallization is rather a state of local order. Only those symmetries in 3D will be found, which maximizes the packing fraction. With local is meant, that even a single sphere with minimal void space is ordered. Thus the methods to identify sufficiently large crystalline clusters known from thermal systems are not necessarily applicable to dissipative systems.

6.4.1. Crystallization identification with Minkowski tensors

We shall address the above questions in the following. Therefore the Minkowski analysis method is extended to a method capable of identifying or discerning different crystal- or ordered[4] structures. All rank-two MT become isotropic (proportional to the unit tensor) for cubic-symmetry cells (fcc, bcc) and hexagonally close-packed (hcp) cells. Consequently the ratio of eigenvalues $\beta_\nu^{r,s}$ equals unity for all crystalline nuclei in monodisperse hard-sphere configurations, and even though detection of nucleation clusters is noise-background-free, the distinction of different types is not possible [34, 274]. But in the framework of the Minkowski analysis crystal structure identification can be done in two ways. The direct extension to what was beforehand shown (based on MT of rank 2) is extended to higher ranks, especially rank 4. A more sophisticated and systematical way is, to make use of spherical and irreducible tensor representations and derive invariants from these measures. This shall be discussed in chapter 7.

Cartesian rank 4 normal Minkowski tensors Equation (5.17) defines the so-called Cartesian Minkowski tensors, since their representation is directly given in the canonical representation. Reliable distinction of crystalline cells is not possible using Cartesian MT of rank two, since all cubic or hcp crystals have isotropic rank-2 MT. Robust crystal identification can be made by extending the framework of Minkowski tensors to rank-four tensors. The symmetry of lattice cells can be characterized without methods that rely on somewhat arbitrary definitions of nearest neighbors. Here, we shall restrict the discussion to the simplest rank-four Minkowski tensor

$$S_{ijkl} = \frac{1}{A}(W_1^{r,s})_{ijkl} = \tfrac{1}{3A} \cdot \int_{\partial K} n_i n_j n_k n_l \mathrm{d}^2 r, \tag{6.8}$$

[4] in particular the icosahedral structure

where A is the surface area of the Voronoi cell K. Like the rank-two Minkowski tensors, $S_1^{0,4}$ is a continuous function of the particle positions. Due to its symmetry under permutation of indices, the 81 components of this tensor can be represented by a 6×6 matrix, analogous to the theory of the elastic tensor [212, 173]. The $S_1^{0,4}$ tensor is even symmetric under permutation of *all* the indices, whereas the elastic tensor is symmetric under exchange of the first two indices, and the first and second index pair [173, 134]. The higher degree of symmetry leads to further restrictions on the eigenvalues. In the case that $\beta_1^{0,2} = 1$, such as for the symmetric cells in table 6.1, one can show that this restriction fixes one of the eigenvalues to $1/3$ and the sum of the remaining eigenvalues to $2/3$.

$$M\left(S_1^{0,4}\right) = \begin{pmatrix} S_{xxxx} & S_{xxyy} & S_{xxzz} & \sqrt{2}S_{xxyz} & \sqrt{2}S_{xxxz} & \sqrt{2}S_{xxxy} \\ S_{xxyy} & S_{yyyy} & S_{yyzz} & \sqrt{2}S_{yyyz} & \sqrt{2}S_{yyxz} & \sqrt{2}S_{yyxy} \\ S_{xxzz} & S_{yyzz} & S_{zzzz} & \sqrt{2}S_{zzyz} & \sqrt{2}S_{zzxz} & \sqrt{2}S_{zzxy} \\ \sqrt{2}S_{xxyz} & \sqrt{2}S_{yyyz} & \sqrt{2}S_{zzyz} & 2S_{yzyz} & 2S_{yzxz} & 2S_{yzxy} \\ \sqrt{2}S_{xxxz} & \sqrt{2}S_{yyxz} & \sqrt{2}S_{zzxz} & 2S_{yzxz} & 2S_{xzxz} & 2S_{xzxy} \\ \sqrt{2}S_{xxxy} & \sqrt{2}S_{yyxy} & \sqrt{2}S_{zzxy} & 2S_{yzxy} & 2S_{xyxz} & 2S_{xyxy} \end{pmatrix} \tag{6.9}$$

The eigenvalues of this matrix are invariants of the tensor $S_1^{0,4}$, denoted ς_i with $i = 1, \ldots, 6$ and robustly characterize the shape of the Voronoi cell.

For symmetric Voronoi cells, some of the eigenvalues are degenerate. The six-tuple of eigenvalues, ordered descendingly (by the absolute value), $(\varsigma_1 \geq \cdots \geq \varsigma_6)$ reflects the symmetry of the Voronoi cell and is called *symmetry fingerprint*. Isotropic tensors have a 1-fold non-degenerate eigenvalue ς_1 and a 5-fold degenerate eigenvalue ς_2. We shall refer to this case as type $(5, 1)$. A cubic tensor has three independent eigenvalues with degeneracies 1, 2, and 3, referred to as $(3, 2, 1)$. Hexagonal tensors are of type $(2, 2, 1, 1)$ [212]. Analytical values for the eigenvalues of ideal lattice Voronoi cells are given in table 6.1.

The rotation and scale invariant symmetry fingerprint can be used to define a symmetry index for any type of crystalline nucleus in a straightforward way. Let $\varsigma_1^{\mathrm{fcc}}, \ldots, \varsigma_6^{\mathrm{fcc}}$ denote the symmetry fingerprint of an ideal fcc Voronoi cell. The scalar fcc symmetry index

$$\Delta_{\mathrm{fcc}} := \sqrt{\sum_{i=1}^{6} (\varsigma_i - \varsigma_i^{\mathrm{fcc}})^2} \tag{6.10}$$

vanishes if the Voronoi cell characterized by ς_i is perfect fcc. Unfortunately, the converse of this statement is false, i. e. there are non-fcc cells with $\Delta_{\mathrm{fcc}} = 0$ (In mathematical terms, Δ_{fcc} is not related to a distance, but merely a pseudo-distance, thus

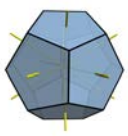
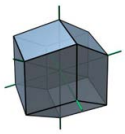
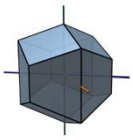
structure	ico	fcc	hcp	bcc	sc
symmetry					
type	(5,1)	(3,2,1)	(2,2,1,1)	(3,2,1)	(3,2,1)
ς_1	$\frac{1}{3}$	$\frac{1}{3}$	$\frac{1}{3}$	$\frac{1}{3}$	$\frac{1}{3}$
ς_2	$\frac{2}{15}$	$\frac{1}{6}$	$\frac{1}{6}$	$\frac{8-4/\sqrt{3}}{33}$	$\frac{1}{3}$
ς_3	$\frac{2}{15}$	$\frac{1}{6}$	$\frac{2}{15}$	$\frac{8-4/\sqrt{3}}{33}$	$\frac{1}{3}$
ς_4	$\frac{2}{15}$	$\frac{1}{6}$	$\frac{2}{15}$	$\frac{8-4/\sqrt{3}}{33}$	0
ς_5	$\frac{2}{15}$	$\frac{1}{12}$	$\frac{1}{9}$	$\frac{-1+2\sqrt{3}}{33}$	0
ς_6	$\frac{2}{15}$	$\frac{1}{12}$	$\frac{1}{9}$	$\frac{-1+2\sqrt{3}}{33}$	0
q_6	0.66333	0.57452	0.48476	0.62854	0.35355
	$(z = 12)$	$(z = 12)$	$(z = 12)$	$(z = 8)$	$(z = 6)$
				0.51069	
				$(z = 14)$	
					

TABLE 6.1. *Ideal values of q_6 (based on the set of z nearest neighbors) and analytic eigenvalues of the normalized $W_1^{0,4}$ rank-four Minkowski tensor and illustrations of fcc, hcp Voronoi cells and the dodecahedron.* Abbreviations *ico: icosahedral configuration, fcc: face centered cubic, hcp: hexagonal close packed, bcc: body centered cubic and sc: simple cubic.*

we shall call it a pseudo-metric). Such non-fcc cells with $\Delta_{\text{fcc}} = 0$ can be constructed by deformation of the fcc-Voronoi cell facets, in a way, that the new body obeys the same symmetries as the fcc Voronoi cell. These bodies do not occur as cells in Voronoi graphs. Pseudo-metrics were used before for bond orientational order parameters too [133].

Non-fcc cells with $\Delta_{\text{fcc}} = 0$ were not found to occur in practice. This makes Δ_{fcc} useful for the background-free detection of crystalline nuclei. We checked this with

several methods. Figure 6.22 (left panel) shows the scatter plot of $|q_6^{n=12} - q_6^{\mathrm{fcc}}|$ and Δ_{fcc}, where q_6^{fcc} is the reference value for ideal fcc configuration. The choice of the 12 nearest neighbors ensures, that q_6 counts exactly all relevant neighbors when near the ideal fcc configuration. By definition, both measures vanish when the cell is fcc-like. Cells with low values in Δ_{fcc} have also low values in $|q_6^{n=12} - q_6^{\mathrm{fcc}}|$. The inverse statement is false, as shown in the diagram. Another method to test the robustness of the pseudo-metric is the analysis of Voronoi cells in fcc-Einstein solids. Small RMSD ε values lead to slightly distorted cells. Thus the average value of Δ_{fcc} increases (linear) in ε. The data are presented in figure 6.24 on page 171. The error bars represent the standard deviation. In the double logarithmic scale, the errorbars (which indicate the standard deviation) keep roughly constant. This indicates, the also the Δ_{fcc} of the cells with the highest fcc-indication grows linear with ε (for small RMSD). Further we tested Δ_{fcc} with a vertex distortion model, i.e. starting from an ideal fcc Voronoi cell, we add a random displacement vector to each vertex of the cell. The wire frame of the distorted cells have the same topology. We define RMSD in this model with the random displacement vectors. Again, for small values of RMSD the mean of Δ_{fcc}

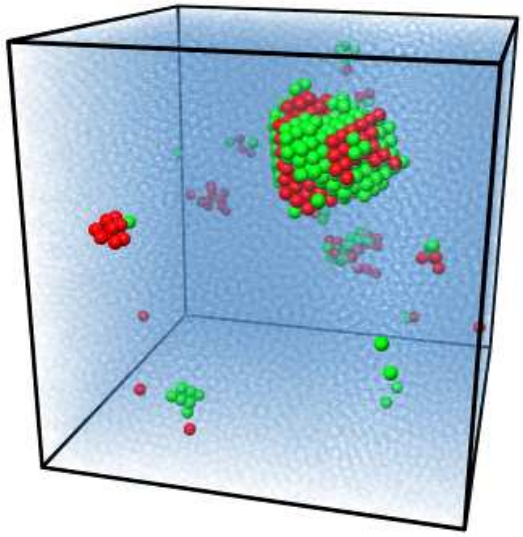


FIGURE 6.21. *Three-dimensional jammed packing of $N = 4 \times 10^4$ beads with $\phi = 0.656$. Crystalline local environments are marked by green (hcp, $\Delta_{\mathrm{hcp}} < 0.005$) and red (fcc, $\Delta_{\mathrm{fcc}} < 0.005$) spheres; all other spheres are translucent.*

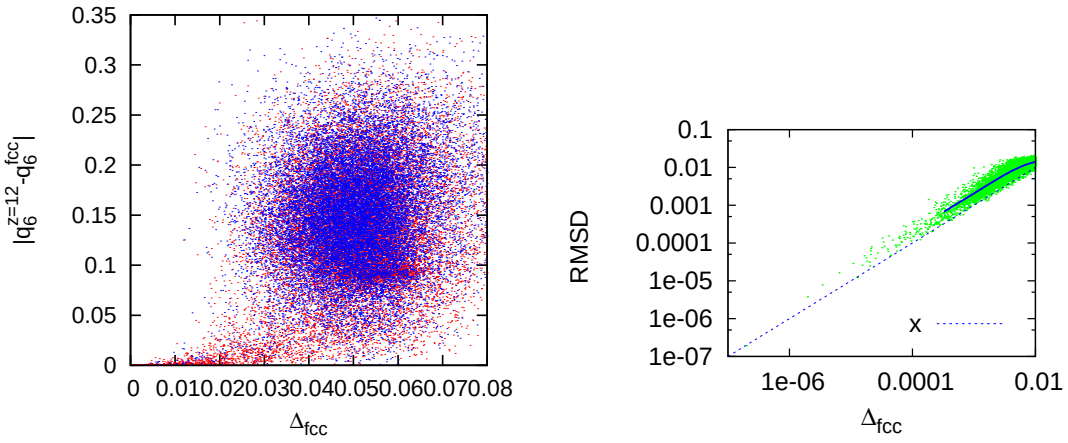


FIGURE 6.22. left $|q_6^{n=12} - q_6^{\text{fcc}}|$ *vs.* Δ_{fcc} *in LS simulations with* $\gamma = 0.0001$ *(red) and* $\gamma = 0.0003$ *(blue).* right *RMSD of vertex displacements of fcc Voronoi cell vs.* Δ_{fcc}. *The solid line represents the sliding mean and the dashed line is the reference with slope 1.*

grows linear with RMSD. The mean value minus standard deviation also grows linear with RMSD (see right panel of figure 6.22).

Symmetry indices are defined in an analogous way for other types of nucleation clusters (icosahedral-, bcc-, simple cubic- or hcp-symmetry), and for icosahedral bond order (with the dodecahedron as the Voronoi cell), using the reference fingerprints in tab. 6.1. Single beads embedded into an ordered environment can be marked using the symmetry finger print in a robust manner with thresholding of the symmetry index. Figure 6.21 illustrates a jammed LS packing where spheres in fcc (red) and hcp (green) configuration are marked. Other spheres are translucent. We can see from this picture that ordered spheres appear either in clusters (fcc, hcp or mixed) and as single ordered beads. In arrested systems even a single bead can be found in locally/globally packing-optimized structure.

Since S is a tensor and 6 of its invariants are used in the symmetry indices much more shape information is taken into account than by the single scalar shape measure q_6. Steinhardt [289] discussed the fcc identification and used two independend invariants. Icovella et al. [133] used e.g. q_4 and q_6 to construct a pseudo-metric, for reliable structure detection. The need of more than one member in the orientational order parameter in order to identify doubtledd fcc or hcp is often neglected in the literature [216], e.g. in [319, 150]. To demonstrate the insufficiency of q_6, when used as a

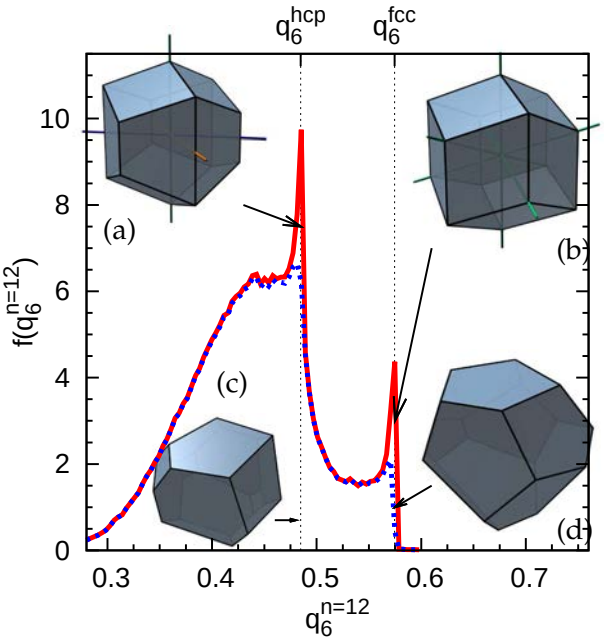


FIGURE 6.23. *Frequency distribution* $f(q_6^{n=12})$ *of* all *cells (red) and of the subset (blue) of cells that are identified as neither hcp nor fcc using Minkowski tensor analysis (i. e.* $\Delta_{\mathrm{fcc}} > 0.015$ *and* $\Delta_{\mathrm{hcp}} > 0.015$*) The cells depicted represent (a) an ideal hcp cell, (b) an ideal fcc cell, and cells identified by* $q_6^{n=12}$*, but not by Minkowski tensors, as (c) hcp and (d) fcc. The data is taken from ten configurations with* $\gamma = 0.0001$ *combined, each consisting of* $N = 40000$ *spherical particles, with* ϕ *between 0.656 and 0.660.*

single scalar shape index, fig. 6.23 shows the distribution of $q_6^{n_k=12}$ for 10 independent LS simulation ($N = 40000$ for each simulation) with $\gamma = 0.0001$. With Δ_{hcp} and Δ_{fcc} it is now possible to separate the amorphous component of the q_6 distribution from the contribution of the crystalline nuclei by dropping all cells with small values of Δ_{fcc} or Δ_{hcp} (dashed line), that is those cells that are actually hcp or fcc. This shows conclusively that, using Minkowski tensor analysis, is a more robust description of the geometry is achieved than by q_6 only, which is a scalar quantity. Combining q_6 with other members of the BOO family may also remove the background in practice. Searching for ordered clusters, the bond definition can be adjusted with ad-hoc methods; a proper adjustment in disordered systems is more challenging. Using a scalar measure such as the $l = 6$ member of the BOO family is not sufficient to distinguish more than one crystal type, since one have to deal with the noisy background. In fact,

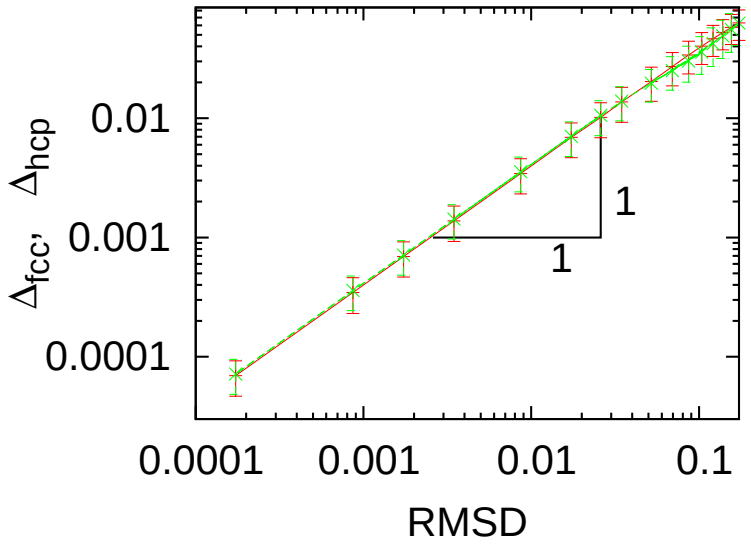


FIGURE 6.24. *Average Δ_{fcc} as a function of the RMSD ε in an fcc Einstein solid in units of the lattice spacing. The errorbars indicate the standard deviation at constant RMSD.*

the highest q_6 value for 12 neighbors is the icosahedral structure. A noisy realization of an icosahedra can reduce q_6 to values which are identical to q_6^{fcc}. Also noisy realizations of fcc or the icosahedra may look like hcp in the q_6 analysis. Clearly, distributions of order parameters, which do not display ordered structures as peaks in regions with vanishing background are prone to create type-II errors, i.e. structures that are not ordered but are accepted to identify order (also called: false-positive). Figure 6.16 shows, that the identification of structures with β works robustly, since all kinds of crystalline structures are found at one end of the distribution. Again, either more invariants of the BOO family or tensorial shape-measures are needed to reduce the false-positives.

We want to answer the following question: How many of the cells in the LS samples are (almost) hcp and fcc cells, in particular for packing fractions beyond RCP. Therefore a method is needed, which counts hcp and fcc cells with equal sensitivity. A calibration of the suitable acceptance thresholds is done, by using the Einstein solid model again (see sec. 6.2). A priori, the measures Δ_{fcc} and Δ_{hcp} can have different sensitivity, requiering two different thersholds δ_{fcc} and δ_{hcp}. Figure 6.24 displays the mean Δ_{fcc} and Δ_{hcp} for an fcc resp. an hcp Einstein solid. The errorbars indicate the standard deviations. In the log-log plot, the slope equal 1 proves the linear correlation of RMSD and the symmetry indices. The fact that the offset between both symmetry

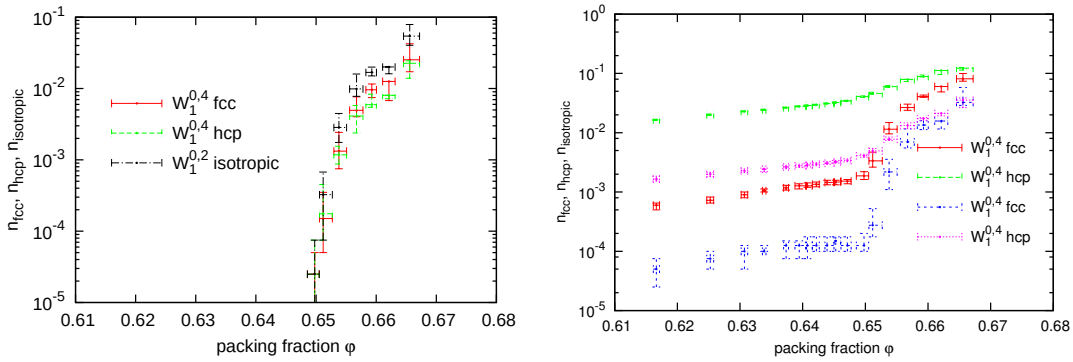


FIGURE 6.25. *Occurrence frequency of isotropic, fcc-like, and hcp-like cells in the final states of LS simulations. Frequencies are calculated as* $n_{\mathrm{fcc}} = N_{\mathrm{fcc}}/N$, *where* N_{fcc} *is the number of cells with* $\Delta_{\mathrm{fcc}} < 0.005$, N_{fcc} *is* $\Delta_{\mathrm{hcp}} < 0.005$, *and* N_{iso} *is* $\beta_1^{0,2} > 0.99$. *The occurrence frequency of crystalline cells in loose packings is very small, and rises several orders of magnitude at* $\phi \approx 0.65$.

indices in fig. 6.24 is very small, shows that either indices are equally sensitive in this model. The choice of the same threshold value δ_{fcc} and δ_{hcp} is hence justified. We assume the same behavior in the LS simulations.

An operative definition for ϕ_{RCP} now is *the packing fraction, above which any infinite jammed configuration necessarily includes a finite fraction of crystalline nuclei.*

Figure 6.25 shows the fcc occurrence frequency $n_{\mathrm{fcc}} = N_{\mathrm{fcc}}/N$ and hcp occurrence frequency $n_{\mathrm{hcp}} = N_{\mathrm{hcp}}/N$ in LS final configurations as a function of the packing fraction ϕ, where N_{fcc} denotes the number of Voronoi cells in the configuration with $\Delta_{\mathrm{fcc}} < 0.005$, N_{hcp} those with $\Delta_{\mathrm{hcp}} < 0.005$, and N is the total number of particles; the threshold values are empirical. It will be shown later that results are to a large extent independent of the thresholds. Configurations are binned on the ϕ axis, with the packing fraction range indicated by the horizontal error bars. The data point represents the median of n, and the vertical error bars show the upper and lower quartiles. We use the median and the quartiles instead of the mean and the standard deviation since these measures are more robust against outliers. This is of particular importance when the number of sampled isotropic cells is very small.

In fig. 6.25, at a packing fraction of $\phi \approx 0.65$, n_{fcc} and n_{hcp} rise several orders of magnitude, indicating the onset of crystallization. We simulated 3365 packings each with $N = 40000$ in a packing fraction range of $0.5647 \leq \phi \leq 0.66721$. We found 3019 packing configurations with less than 3 crystalline cells in a packing fraction range $0.5647 \leq \phi \leq 0.65142$ and 346 packing configuration with more than 2 crystalline

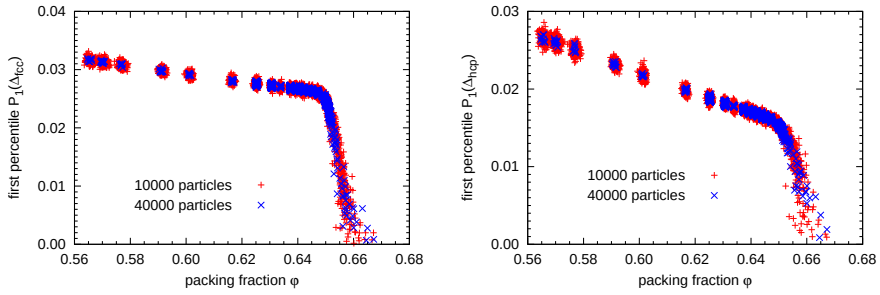


FIGURE 6.26. *Scatterplot showing the first percentile of the Δ_{fcc} distribution in the final states of LS simulations as a function of the final packing fraction φ. Each data point represents a single configuration of 40.000 or 10.000 particles. A qualitative change of the distribution is observed at $\varphi \approx 0.65$, where the first percentile drops considerably, marking the onset of crystallization.*

germs in a packing fraction range $0.64062 \leq \phi \leq 0.66721$. Some overlap of both intervals can be understood from the pressure-determined jamming condition in the LS algorithm, i.e. the system can be considered as jammed when the pressure exceeds a certain threshold [319, 281]. That means, slight rearrangements might be still possible, if the pressure threshold is increased even further.

The signature of crystallization is also visible using the $q_6^{n=12}$ BOO parameter, although a background of false positives is observed. It is invisible using e.g. q_6^{D}.

Figure 6.25 may suggest that the use of a fitting routine fix ϕ_{RCP}. But fitting these data is a notoriously hard job and the errors are quite large, because of the logarithmic singularity. To find the onset of closed packed crystallization, we search for the structural change in the distributions of Δ_{fcc} and Δ_{fcc}. From the paragraph above, it appears that for small $\Delta_{\mathrm{fcc/hcp}}$ the probability jumps to finite values. This feature is captured, when one looks to the small percentiles of this distributions. Since for fully random jammed systems, the most ordered cells (order is measured quantitatively by $\Delta_{\mathrm{fcc/hcp}}$) are not very crystalline. At a certain point—the crystallization onset—when tiny fractions of crystallites are created, the small percentile jumps to smaller values. We show in fig. 6.26 that this method works robustly. Each point in this plot represents one LS simulation of either $N = 10000$ and $N = 40000$. We define the quantile P_f of the distibution of $\Delta_{\mathrm{fcc/hcp}}$, which is defined as

$$P_f := \Delta_{\mathrm{fcc}} \text{ with } P(X < \Delta_{\mathrm{fcc}}) = f. \tag{6.11}$$

The 1% quantile is the first percentile $P_{1\%}$. The left panel presents data for the first

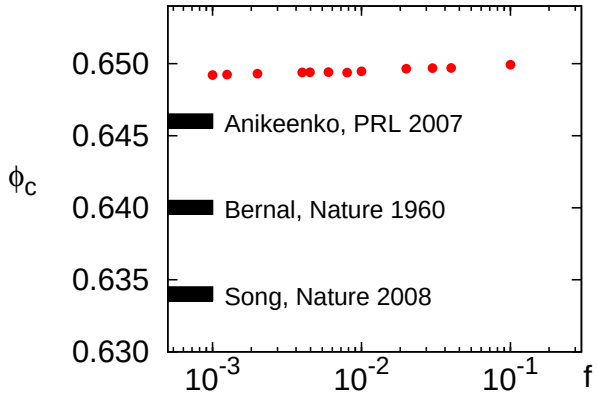


FIGURE 6.27. *Values for ϕ^c as an estimate for RCP obtained from fits of the kink in fig. 6.26 for different quantiles P_f. The black bars indicate values from refs. [8, 33, 283].*

percentile $P_{1\%}$ over the global packing fraction ϕ and the right panel the same data for hcp. While both plots look qualitatively equal and indicating the same ϕ for the kink, the slope for small packing fractions look different. Although both measures are roughly equally sensitive in the ordered phase the symmetry indices have no particular meaning in the disordered phase (they measure rather the absence of order than the degree of disorder) and thus the slope is not necessarily the same. According to Xu [319] finite size effects are small for LS packings with these sizes. This is consistent with our data, as we do not observe differences for $N = 10k$ and $N = 40k$. RCP can be estimated as the kink in the $P_{1\%} - \phi$ planes. Other percentiles than 1%, namely $0.1\%, 2\%, 3\%$ where analyzed as well, yielding about the same values for the kink (see figure 6.27).

RCP for $f = 1\%$ is estimated with $\phi^c = 0.649$. This is rather a high value compared to values in the literature. Anikeenko reports 0.646 for RCP in LS and Jodrey-Torey simulations [8], based on the simplicies method. From experiments values in the range of 0.63 to 0.64 are reported [33, 259]. The Minkowski-method value is rather an upper limit estimation, because of the limited statistics in the LS samples (parallel computer code would be needed to perform larger samples in acceptable time). The value reported here seems to be consistent with the kink in the $\gamma^{-1} - \phi$ plane, reported by Xu (see fig. 2 in ref. [319]).

6.4.2. Conclusion

This analysis shows the occurrence of locally crystalline environments in Lubachevsky-Stillinger hard sphere simulations. The fraction of cells with fcc and hcp order increases by several orderes of magnitude at a critical packing fraction. We interprete this packing fraction where the structural change occurs as the point of random close packing (RCP). This findings support the conjecture of Radin [247] that RCP is the point where phase coexistence of crystalline structure and the disordered phase occurs. On the other hand Radin proposed to search for this transition by some response functions rather than by structural analysis tools. We have shown how useful the Minkowski tensor analysis is in order to identify the crystallization. It would be interesting, to study the response function of packings with ordered and disordered domains in comparison to jammed packings below RCP.

As shown above, this oberservations need new structure measures such as $W_1^{0,4}$ and the symmetry indices. Alternatively, one could use a set of independent invariants in the BOO family, if suitable nearest neighbor definitions are available. Indeed, MT can be interpreted as a special bond definition of BOO, which overcomes the robustness deficiencies. This is discussed in the next chapter.

7. Spherical normal Minkowski tensors and bond order parameters

The results of this chapter are joint work with S. Kapfer from the University Erlangen-Nürnberg.

Normal density, Gauss map and multipole expansion In this section we demonstrate that the bond orientation order parameters (BOO) are closely related to Minkowski tensors. To this end proper weight-functions are introduced, which render the classical BOO continuous. We shall briefly sketch the idea here and the full formalism is explained below. Let us denote a Voronoi cell in the Voronoi graph with K. Further this Voronoi cell has n facets with the surface area A_i and outer normal vectors $\mathbf{n}_i$, $i = 1, \ldots, n$. The Gauss map yields a normal density distribution $\varrho(\theta, \varphi)$ on the unit sphere $\mathbb{S}^2$

$$\varrho(\theta, \varphi) = \frac{1}{A} \sum_{i=1}^{n} A_i \delta(\mathbf{n}_i - \mathbf{n}(\theta, \varphi)), \tag{7.1}$$

where A is the total surface area of K and δ the Dirac delta function. From this representation of K one can derive the multipole expansion of the boundary surface normal density

$$\varrho(\theta, \varphi) = \sum_{l=0}^{\infty} \sum_{m=-l}^{l} \alpha_m^l Y_m^l(\theta, \varphi) \tag{7.2}$$

where Y_m^l are the spherical harmonics and α_m^l are constant weights which only depends on K. For convex K the monopole moment is 1 regardless of the shape of K. Due to the envelope theorems (for MT in reads $W_\nu^{0,1} = 0$) the dipole moment vanishes [223]. Thus the first non-trivial multipole moment is of order $l = 2$. Eq. (7.2) is reminiscent to eq. (6.1), which indicates the close relation between both approaches. Already Steinhardt [289] recognized, that the BOO are exactly a multipole expansion of bond densities.

In this chapter we demonstrate, that the family of $W_1^{0,r}$ of (normal vector weighted rank-r) Minkowski tensors are equivalent to a multipole expansion of the normal den-

sity. The mathematical details are part of the following two sections. The results are summarized in section 7.4.

7.1. Irreducible tensors

Tensorial methods combined with symmetry considerations are widely used in solid state-, atomic- and molecular physics. Depending on the symmetry of the system and the symmetry of the quantity of interest, one can find the non-vanishing parts of the tensor [34]. But these methods leave the difficulty of choosing the reference frame aligned to certain crystallographic axes [141]. It would be more convenient to extract elements, which are rotation independent. Therefore the concept of irreducible tensors was introduced by Racah [141]. A tensor T of rank $r \geq 2$ is an element of a r-dimensional product representation of special orthogonal group $SO(3)$. This product representation has an orthogonal basis. Thus, T can be decomposed in irreducible tensors, which transform as the basis elements [71, 70, 141, 44]. For example, the spherical harmonics Y_m^l are the matrix elements of the irreducible representation of the group $SO(3)$, and build an orthognal basis of the irreducible representation.

First we want to find an irreducible decomposition of T in cartesian representation. Indeed there are several ways to find such a decomposition. Coope et al. [71, 70] gave an explicit reduction scheme to derive irreducible tensors $T^{(q,l)}$ directly from the cartesian representation $T_{i_1 i_2 \ldots i_r}$ of the rank r tensor T. q is called the seniority and l the weight. Andrews and others [7] derived the decomposition explicit for rank 4 tensors in the Euclidean space $\mathbb{E}^3_{\mathbb{R}}$ over $\mathbb{R}$. While this reduction scheme is rather cumbersome calculus, one can use another way by converting it the cartesian tensor into a spherical tensor first. A spherical tensor $T_{m_1 m_2 \ldots m_r}$ is the representation of the rank-r tensor T in the spherical coordinate frame. The decomposition into irreducible parts T_m^l (in the spherical representation) can be worked out with the Clebsch-Gordan coefficients $CB^{l;1\ldots1}_{m;m_1 m_2 \ldots m_r}$—well-known from the angular momentum algebra in quantum mechanics [313, 261]. Figure 7.1 illustrates the relationship among these representations. We follow two distinct ways to obtain irreducible parts. From the spherical irreducible parts of the normal Minkowski tensors $W_1^{0,r}$ we derive a particular form of Steinhardt bond orientation order parameters. The cartesian tensors are used to discuss the invariants ς_i mentioned in chapter 6.

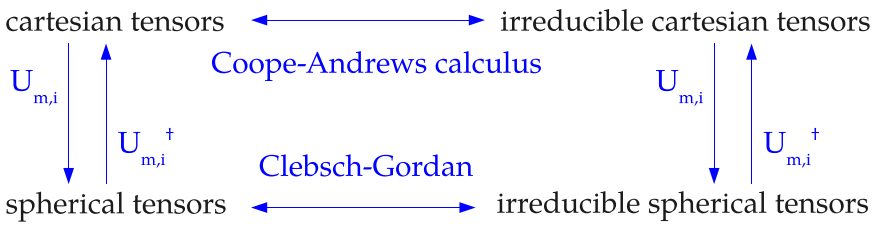


FIGURE 7.1. *Cartesian tensors, spherical tensors and the irreducible elements*

7.2. Cartesian irreducible tensors

Any cartesian rank-r tensor $T_{i_1 \dots i_r}$ can be decomposed into a direct sum of irreducible tensors $T^{(q,l)}$ with weights $0 \leq l \leq r$ and seniority $1 \leq q \leq Q_r^l$,

$$Q_r^l = \sum_{k=0}^{\lfloor (n-j)/3 \rfloor} (-1)^k \binom{r}{k} \binom{2r-3k-l-2}{n-2}. \tag{7.3}$$

Q_r^l is called the multiplicity of l and $\lfloor . \rfloor$ is the Gaussian floor function. The seniority distinguishes between several irreducible tensors of the same weight. Each irreducible tensor $T^{(q,l)}$ has $2l+1$ independent entries. While tensors in general do not obey symmetries w.r.t. index permutation, many tensors in physics obey such symmetries. The rank-4 elastic tensor e.g. is invariant under permutations of the first two indices or the change of the first pair of indices with the second pair:

$$T_{i_1 i_2 i_3 i_4} = T_{i_2 i_1 i_3 i_4} = T_{i_3 i_4 i_1 i_2}. \tag{7.4}$$

Minkowski tensors such as $W_1^{0,r}$ are fully index symmetric. For $r = 4$ this reads

$$T_{i_1 i_2 i_3 i_4} = T_{i_2 i_1 i_3 i_4} = T_{i_3 i_4 i_1 i_2} = T_{i_1 i_3 i_2 i_4} \tag{7.5}$$

Index permutation symmetry simplifies the decomposition: some $T^{(q,l)}$ may degenerate or vanish. For fully symmetric tensors, only the irreducible tensors with seniority $q = 1$ do not vanish.

By definition, all $T^{(q,l)}$ transform under rotations of the reference frame as a basis set of irreducible representations of $SO(3)$. All rank-r tensors ($r \geq 2$) are elements of the product representation $\underbrace{1 \otimes 1 \otimes \cdots \otimes 1}_{r \text{ times}}$ of $SO(3)$. From a quantum mechanical point of view, the tensor product space can be interpreted as a coupling of r spin 1 bosons [313].

We concentrate here on the special case $W_1^{0,4}$ or more precisely on fully symmetric rank-4 tensors. The algebra for higher ranks are quite lengthy, but straightforward. Therefore $r \geq 5$ is omitted here. The reduction scheme for generic tensors of arbitrary rank is given by Coope [71, 70], and explicitly for rank $r \leq 4$ given in ref. [7] and the results for $r \leq 4$ are stated below. In the following we use the Einstein summation rule, i.e. it is summed over all indices that appears two times or more often in a product term. Further we define the fully symmetric tensor product

$$a_{i_1 \ldots i_r} \odot b_{i_{r+1} \ldots i_{r+s}} = s_{r+s}\left(a_{i_1 \ldots i_r} b_{i_{r+1} \ldots i_{r+s}}\right) = \frac{1}{(r+s)!} \sum_{\sigma \in S_{r+s}} a_{\sigma(i_1) \ldots \sigma(i_r)} b_{\sigma(i_{r+1}) \ldots \sigma(i_{r+s})}, \quad (7.6)$$

where $s_{r+s}(.)$ is the full symmetrizer w.r.t. to the rank $r+s$ and S_{r+s} is the permutation group of $r+s$ elements.

Rank 0 and rank 1: The reduction of W_1 and $W_1^{0,1}$ is trivial. We denote the tensors in cartesian irreducible decomposition of $W_1^{r,s}$ as $[W_1^{r,s}]^{q,l}$ with seniority q and the weight l.

$$[W_1]^{1,0} = W_1 \quad (7.7)$$

and with the envelope theorem

$$\left[W_1^{0,1}\right]^{1,1} = 0. \quad (7.8)$$

Rank 2: A fully symmetric tensor T with even weight l decomposes in irreducible tensors with even weight $j \leq l$. All irreducible tensors with $q > 1$ vanish. Thus, the rank-2 $W_1^{0,2}$ tensor decomposes into the subspaces $(l = 0) \otimes (l = 2)$.

$$\begin{aligned} \left[W_1^{0,2}\right]^{1,0} &= \frac{1}{3} W_1 \, \delta \\ \left[W_1^{0,2}\right]^{1,0} &= I_1^{0,2}, \end{aligned} \quad (7.9)$$

where $I_1^{0,2}$ is the traceless interface tensor [81]. $\left(I_1^{0,2}\right)_{ij} = \left(W_1^{0,2}\right)_{ij} - \frac{1}{3} W_1 \delta_{ij}$.

Rank 3 For fully symmetric rank-3 tensors there is only one component of weight $l = 1$ and one component of $l = 3$. Note that the $l = 1$ components vanish for Minkowski tensors due to the envelope theorem.

$$\begin{aligned} \left[W_1^{0,3}\right]^{1,1} &= 0 \\ \left[W_1^{0,3}\right]^{1,3} &= W_1^{0,3}. \end{aligned} \quad (7.10)$$

Rank 4 According to Andrews [7], fully symmetric tensors can be decomposed in $(l=0)\otimes(l=2)\otimes(l=4)$

$$\begin{aligned}\left[W_1^{0,4}\right]^{1,0} &= \frac{1}{5}\delta\odot\delta\, W_1\\ \left[W_1^{0,4}\right]^{1,2} &= \frac{6}{7}\delta\odot\, I_1^{0,2}\\ \left[W_1^{0,4}\right]^{1,4} &= W_1^{0,4}-\frac{6}{7}\delta\odot\, I_1^{0,2}-\frac{1}{5}\delta\odot\delta\, W_1. \end{aligned} \tag{7.11}$$

For the rank-4 tensors we deduce some invariants from the decomposition above. A first invariant λ_0 is obtained from $l=0$, which is proportional to W_1. Another 2 invariants are found for $l=2$, since we have $2l+1=5$ degrees of freedom (DOF). Three DOF are Euler angles $\theta_1,\theta_2,\theta_3$ and hence not of particular interest. The two remaining ones are equivalent to $\beta_1^{0,2}$ and $\gamma_1^{0,2}$, i.e. the ratios of the eigenvalues of $W_1^{0,2}$. Explicitly, these 2 invariants can be obtained from the three eigenvalues $\lambda_1,\lambda_2,\lambda_3$ of $I_1^{0,2}$ and the relationship $\lambda_1+\lambda_2+\lambda_3=0=\mu_1+\mu_2+\mu_3-W_1$, where μ_i are the eigenvalues of $W_1^{0,2}$. From eq. (7.11) is easy to see, that $\left[W_1^{0,4}\right]^{(1,2)}$ vanishes when $\beta_1^{0,2}=1$.

Similarily one can obtain invariants from $\left[W_1^{0,4}\right]^{(1,4)}$, when writing the tensor in the 6×6-matrix notation (analogous to the elastic tensor in continuum mechanics, see also eq. (6.9)) and calculating the eigenvalues. This tensor ($l=4$) has $2l+1=9$ independent entries. The subspace $(l=4)$ is orthogonal to $(l=2)$, consequently it rotates independently with three Euler angles $(\theta_4,\theta_5,\theta_6)$ and thus 6 DOF remain. $\left[W_1^{0,4}\right]^{(1,4)}$ is traceless and therefore the sum of eigenvalues $\sum_{i=4}^{10}\lambda_i=0$ vanishes. Furthermore one eigenvalue (λ_4) is trivially 0 (with the eigenvector $(1,1,1,0,0,0,)$), and hence diagonalization gives up to 4 independent invariants. The deduction of the remaining eigenvalues remains unfortunately unclear in this presentation. In the case of genuine fcc, hcp or icosahedral cells, the eigenvalues ς_i, which were used to define $\Delta_{\mathrm{fcc/hcp}}$ are identical to $\lambda_5,\ldots\lambda_{10}$ and λ_1, up to the normalization (see chapter 6).

7.3. Spherical Minkowski tensors

Up to now we always used the indices i_s for cartesian elements of the tensor T, where $i_s\in\{x,y,z\}$ or $i_s\in\{1,2,3\}$. Spherical representations of tensors are often more convenient when considering T under rotations. A cartesian representation $T_{i_1 i_2\ldots i_r}$ of

the rank-r tensor T is transformed to its spherical representation (representation in spherical harmonics) with the transformation matrix U_{mi} (see fig. 7.1)

$$T_{m_1 m_2 \ldots m_r} = U_{m_1 i_1} U_{m_2 i_2} \cdots U_{m_r i_r} T_{i_1 i_2 \ldots i_r} \tag{7.12}$$

with the spherical indices $m \in \{-1, 0, 1\}$. U_{mi} is defined as [141]

$$U_{mi} = \frac{1}{\sqrt{2}} \overbrace{\begin{pmatrix} -1 & -i & 0 \\ 0 & 0 & \sqrt{2} \\ 1 & -i & 0 \end{pmatrix}}^{x \quad y \quad z} \left.\begin{matrix} \\ \\ \\ \end{matrix}\right\} \begin{matrix} m = +1 \\ m = 0 \\ m = -1 \end{matrix} . \tag{7.13}$$

For example, a vector $(T_i) = \left(T_x, T_y, T_z\right)^t$ reads in spherical components $(T_m) = (T_1, T_0, T_{-1})$

$$\begin{aligned} T_{\pm 1} &= \frac{1}{\sqrt{2}} \left(\mp T_x - i T_y\right) \\ T_0 &= T_z \end{aligned} \tag{7.14}$$

It is important to emphasize that reference frame transformations of cartesian tensors are orthogonal transformations O and thus represented by orthogonal maatrices ($O^{-1} = O^t$) with real entries. This makes their properties independent of the reference frame of their definition. Spherical tensors, in contrary, are embedded in $\mathbb{C}^3 = \mathbb{E}^3_{\mathbb{C}}$ and the transformations U of the reference frame are unitary , $U^{-1} = U^\dagger$, i.e. for example, that the ordinary scalar product of two vectors $\mathbf{v} \cdot \mathbf{u}$ writes in cartesian form $v_i u_i$ but in spherical representation it is a hermitian product $(-1)^m u_m v_{-m} = u_m v_m^\dagger = u_m^\dagger v_m$. This means the indices of $\mathbf{v}$ and $\mathbf{u}$ appears in different positions [141]. This appears e.g. in all kinds of contractions of tensors. The inverse transformation matrix U^{-1}_{im} is

$$\begin{aligned} U^{-1}_{im} &= \frac{1}{\sqrt{2}} \overbrace{\begin{pmatrix} -1 & 0 & 1 \\ i & 0 & i \\ 0 & \sqrt{2} & 0 \end{pmatrix}}^{+1 \quad 0 \quad -1} \left.\begin{matrix} \\ \\ \\ \end{matrix}\right\} \begin{matrix} x \\ i = y \\ z \end{matrix} \\ &= U^*_{mi} = U^{*t}_{im} , \end{aligned} \tag{7.15}$$

i.e., $U^{-1} = U^\dagger$, so that we recover cartesian components by

$$\begin{aligned} T_{i_1 \ldots i_r} &= U^{-1}_{i_1 m_1} \cdots U^{-1}_{i_r m_r} T_{m_1 \ldots m_r} \\ &= (-1)^{m_1 + \cdots + m_r} U_{-m_1 i_1} \cdots U_{-m_r i_r} T_{m_1 \ldots m_r} . \end{aligned} \tag{7.16}$$

The merit of the spherical tensors is that they can be easily decomposed into their irreducible components with the Clebsch-Gordan coefficients $CG^{j;11}_{m;m_1m_2}$—well-known from angular momentum algebra in quantum mechanics—for rank $r \geq 2$, which reads

$$T_{m_1m_2\cdots m_r} = \sum_{l,m} CG^{l;1\cdots 1}_{m;m_1\cdots m_r} T^l_m, \tag{7.17}$$

where T^l_m are the spherical irreducible tensors of a tensor T. For rank 0 and rank 1 one finds special cases, where the Clebsch-Gordan coefficients are simply 1: scalar $T = T^0_0$ and vector $T_m = T^1_m$.

The Clebsch-Gordan coefficients perform orthogonal transformations, so that the inversion of eq. (7.17) is

$$\begin{aligned} T^j_m &= \sum_{m_1\ldots m_r} CG^{j;1\ldots 1}_{m;m_1\ldots m_r} T_{m_1\ldots m_r} \\ &= \sum_{m_1\ldots m_r} CG^{l;1\ldots 1}_{m;m_1\ldots m_r} U_{m_1i_1}\ldots U_{m_ri_r} T_{i_1\ldots i_r} \\ &= (C^l_m)_{i_1\ldots i_r} T_{i_1\ldots i_r} \end{aligned} \tag{7.18}$$

for a given weight j. $(C^l_m)_{i_1i_2}$ are the Clebsch-Gordan transformation matrices

$$(C^l_m)_{i_1i_2} = \sum_{m_1\ldots m_r} CG^{l;1\ldots 1}_{m;m_1\ldots m_r} U_{m_1i_1}\ldots U_{m_ri_r}\,. \tag{7.19}$$

The inversion of eq. (7.18) reads

$$T_{i_1\cdots i_r} = U^{-1}_{i_1m_1}\cdots U^{-1}_{i_rm_r} T_{m_1m_2\cdots m_r} = \sum_{l,m} T^l_m\ (C^l_m)^\dagger_{i_1\cdots i_r} \tag{7.20}$$

with

$$\begin{aligned} (C^l_m)^{-1}_{i_1\cdots i_r} &= \left(CG^{l;1\cdots 1}_{m;m_1\cdots m_r}\right)^\dagger U^{-1}_{i_1m_1}\cdots U^{-1}_{i_rm_r} \\ &= (C^l_m)^\dagger_{i_1\cdots i_r}\,. \end{aligned} \tag{7.21}$$

The Clebsch-Gordan coefficients for fully symmetric tensors up to rank 4 can be found in the appendix C.2.

Spherical and irreducible normal Minkowski tensors The paragraphs above are generic calculus for arbitrary tensors. We restrict ourselves to derive spherical irreducible Minkowski tensors. We define the normal rank-r tensor $N^{(r)}$ as the tensor product of normal unit vectors $\mathbf{n}$. We use this tensors below the boundary surface integral of the normal weighted Minkowski tensors $W^{0,r}_1$.

Its cartesian representation reads

$$N_{i_1 i_2 \ldots i_r} = n_{i_1} n_{i_2} \cdots n_{i_r}, \tag{7.22}$$

where $\mathbf{n} = \left(n_x, n_y, n_z\right)^t = \left(\sin\left(\theta\right)\cos\left(\phi\right), \sin(\theta)\sin(\phi), \cos(\theta)\right)^t$, with $\theta \in [0, \pi]$ and $\phi \in [0, 2\pi]$. This definition is used to write normal tensors as

$$N_{i_1 \cdots i_r} = \sin^{f_x + f_y}(\theta)\cos^{f_z}(\theta)\sin^{f_y}(\phi)\cos^{f_x}(\phi), \tag{7.23}$$

where f_x is the number of times that index x occurs in the set $i_1 \cdots i_r$ (analogously for f_y and f_z). The spherical components are

$$N_{m_1 m_2 \cdots m_r} = (-1)^{(M+|M|)/2} 2^{-|M|/2} \sin^{|M|/2}(\theta)\ \cos^{r-|M|/2}(\theta)\ e^{iM\phi}, \tag{7.24}$$

where $|M| = \sum_{s=1}^{r} |m_s|$ and $M = \sum_{s=1}^{r} m_s$. For example, N_m reads

$$\left(N_m\right) = \begin{pmatrix} -\frac{1}{\sqrt{2}}\sin(\theta)e^{i\phi} \\ \cos(\theta) \\ \frac{1}{\sqrt{2}}\sin(\theta)e^{-i\phi} \end{pmatrix} = \begin{pmatrix} \sqrt{\frac{4\pi}{3}}Y_1^1 \\ \sqrt{\frac{4\pi}{3}}Y_0^1 \\ \sqrt{\frac{4\pi}{3}}Y_{-1}^1 \end{pmatrix}, \tag{7.25}$$

with the spherical harmonics Y_m^l. Notice the convention of the spherical harmonics with the helicity as lower index. As an example the spherical components of rank 0 and rank 1 are listed below (see also app. C for rank-2)

$$\begin{aligned} N^{(0)}\Big|_0^0 &= 1 &&= \sqrt{4\pi}Y_0^0 \\ N^{(1)}\Big|_0^1 &= N_0 &&= N_z = \sqrt{\frac{4\pi}{3}}Y_0^1 \\ N^{(1)}\Big|_{\pm 1}^1 &= N_{\pm 1} &&= \frac{1}{\sqrt{2}}(\mp N_x - iN_y) = \sqrt{\frac{4\pi}{3}}Y_{\pm 1}^1 \end{aligned} \tag{7.26}$$

It is convenient to use Racah's definition of reduced spherical harmonics (called C_m^l in ref. [44]). In order to avoid confusion with the Clebsch-Gordan transformation matrices we denote the reduced spherical harmonics N_m^l, which are defined as

$$N_m^l = \sqrt{\frac{4\pi}{2l+1}}Y_m^l, \tag{7.27}$$

so that $\sum_{l=-m}^{m}\left(N_m^l\right)^* N_m^l = 1$ with $\left(N_m^l\right)^*$ the complex conjucgation of $\left(N_m^l\right)$ and

$$\begin{aligned} N^{(0)}\Big|_0^0 &= N_0^0 \\ N^{(1)}\Big|_m^1 &= N_m^1 \end{aligned} \tag{7.28}$$

Since Y_m^l is an irreducible basis in the spherical tensor representation, the N_m^l are also a spherical irreducible basis.

7.4. Spherical Minkowski tensors and normal orientation order parameters (NOO)

In this section the main result of this chapter is discussed, namely the relationship between the bond orientational order parameters of Steinhardt and the normal Minkowski tensors $W_1^{0,r}$.

Normal tensors are a particular case of Minkowski tensors $W_1^{0,r}$ which can be written with the definitions from above as a decomposition of spherical irreducible tensors $W_1|_m^l$

$$W_1|_m^l(K) := \int_{\partial K} d^2r \;\; N_m^l(\theta(\mathbf{r}), \phi(\mathbf{r})) = \sqrt{\frac{4\pi}{(2l+1)}} \int_{\partial K} d^2r \;\; Y_m^l(\theta(\mathbf{r}), \phi(\mathbf{r})), \tag{7.29}$$

where $\theta(\mathbf{r}), \phi(\mathbf{r})$ are the spherical representation of the normal vector $\mathbf{n}(\mathbf{r})$ at the point $\mathbf{r}$ on the surface ∂K of the body K. $W_1|_m^l(K)$ is thus the multipole expansion component for weight l and helicity m of the normal vector density of boundary surface of K. N_m^l are reduced spherical harmonics defined in eq. (7.27). A rank-r tensor $W_1^{0,r}$ decomposes in spherical representation into irreducible parts $W_1|_m^l$ up to $l = r$ and $-l \leq m \leq l$.

Voronoi cells—or convex polyhedra in general—with n_k facets of area A_j one obtains from eq. (7.29)

$$W_1|_m^l = \sum_{j=1}^{n_k} A_j N_m^l(\theta_j, \phi_j) = \sqrt{\frac{4\pi}{2l+1}} \sum_{j=1}^{n_k} A_j Y_m^l(\theta_j, \phi_j) \; . \tag{7.30}$$

Normalizing the area weights A_j with the total area $A = \sum_{i=1}^{n_k} A_j$ and using the Steinhardt bilinear order parameter definition one gets

$$\begin{aligned} q_l^V &= \sqrt{\sum_{m=-l}^{l} \left| \sum_{j=1}^{n_k} \alpha_j \, N_m^l(\theta_j, \phi_j) \right|^2} \\ &= \sqrt{\frac{4\pi}{2l+1} \sum_{m=-l}^{l} \left| \sum_{j=1}^{n_k} \alpha_j \, Y_m^l(\theta_j, \phi_j) \right|^2} \; , \end{aligned} \tag{7.31}$$

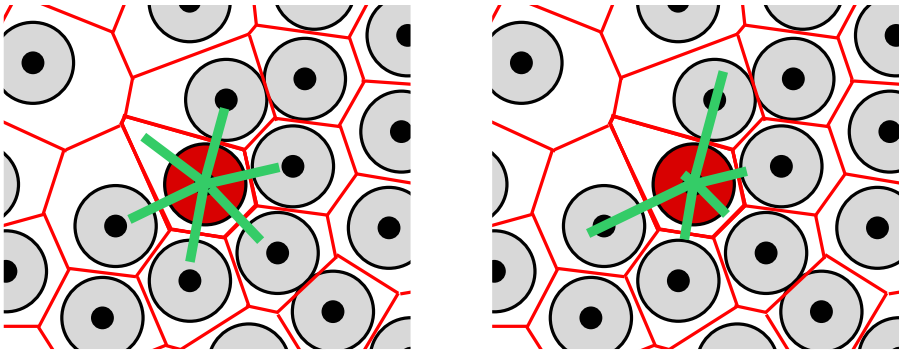


FIGURE 7.2. *Comparison of bond and normal based order parameters.* Left: *Bonds are defined by Vornoi facets and equally weighted* Right: *Bonds are defined by Voronoi facets but weighted with the surface area (length in 2D).*

where $\alpha_j = A_j/A$. The superscript ^{V} denotes the Voronoi-facet weights of the normal directions (bonds). We have derived with the calculus of spherical tensors a bond orientation order parameter, which obeys the same robustness as known from cartesian Minkowski tensors. In analogy, one could decompose other Minkowski tensors to capture different aspects of the morphology. Because of additivity and continuity of Minkowski tensors it is clear, that one could use the NOO also for other attempts to quantify symmetry.

q_l^V are bilinear invariants. According to the Steinhardt formalism, one can also write down the multilinear invariants (such as w_l^V). This higher order invariants (3-forms) can be derived from the eq. (7.30), as it is shown in the Steinhardt paper [289]. n-forms in general are accessible, but the calculus becomes more and more cumbersome. The spherical tensor representations give direct acces to high order invariants q_l^V and w_l^V (bi- and trilinear forms), while the computation of n-linear forms with $n \geq 3$ is cumbersome. Eigenvalues of irreducible cartesian tensors are simpler to evaluate, at least up to $l \leq 4$.

Figure 7.2 shows schematically the difference in the attempt of BOO and NOO. In the left panel the neighbor hood is defined solely by the number of Voronoi facets. The bond weight is represented by the length of the green lines. Misleadingly the regarded sphere appears in a quite symmetric environment. Unlike, in the area weighted bonds in the right panel clearly represents the asymmetric Voronoi cell. A asymmetric appearence seems to be more suitable for the considered sphere. Thus, we emphasize the importance of using robust bond weights for BOO: An obvious method is to use NOO which are based on Voronoi facet surface area.

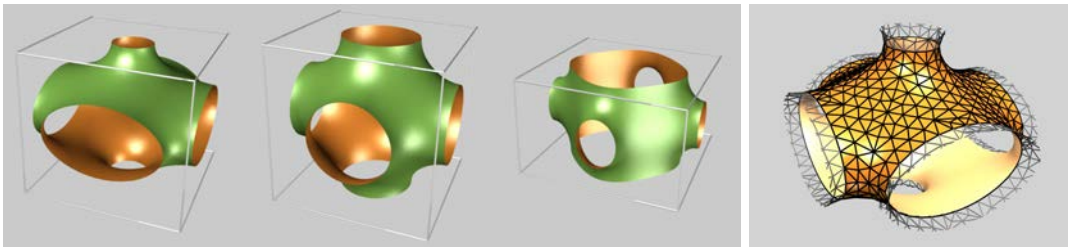


FIGURE 7.3. Left: *Three members of the tP family:* $r_0 = 0.25$, $r_0 = 0.5$ *and* $r_0 = 0.75$. Right: *translation unit cell of tP surface with triangulated mesh*

7.5. NOO of triply periodic minimal surfaces

As an example, fig. 7.4 shows the first even invariants of some triply periodic minimal surfaces (TPMS). Omitting the mathematical details, we note, that these surfaces build up three dimensional periodic interwoven networks of two disjoint domains [270, 103, 272]. As TPMS are minimal surfaces, their mean curvature vanishes everywhere. They are found in nature, e.g. in the structure of butterfly wings, which gives them their colors [271, 260]. An interesting feature of TPMS is that they occur in families with one free parameter [101, 102]. Figure 7.3 shows three members of the tP family. Each member of this family has tetragonal symmetry (P4/mmm in Hermann-Mauguin notation). Some families have distinguished members, e.g. tG and rG contain the cubic gyroid. Indeed, an analysis of the H surface (see fig. 7.4) with the irreducible interface tensor $I_1^{0,2}$ (q_2^V is its bilinear invariant) showed, that the H surface contains a special member ($r_0 = 0.678$) that is likely to be realized in nature but due to similarities in scattering experiments to cubic surfaces it may be overlooked in former investigations [277]. Vanishing of the q_2^V marks the primitive surface (P) and the diamant surface (D) in the tP and tD families, resp. The rPD familiy contains both the P and the D surface.

Higher orders invariants mark special members in other families too, e.g. in the tG q_4 vanishes around 0.37. Unfortunately, no physical interpretation can yet be associated to these mathematically special cases. However, derivates of the surfaces lead to structures with isotropic elasticity tensors [152], and might be successfully characterized by irreducible Minkowski tensors. The NOO were calculated from triangular meshes using eq. (7.31) (see fig. 7.3).

We want to stress the point that when q_l^{V} vanishes this also implies that $W_1|_m^l$ vanishes for all m. Thus the irreducible tensor with weight l vanishes. This indicates

isotropy w.r.t. the weight l. For example the normal density of all Voronoi facets together in a Poisson process is isotropic. Thus, q_l^V vanishes for every l in the large system limit ($N \to \infty$), when q_l^V is used as a global order parameter (analogous to Q_l in chapter 6). But one could also find patterns of high symmetry, where some l vanish and others do not [289]. E.g. the icosahedron is isotropic w.r.t. $l = 2$, $l = 4$ and $l = 8$ but anisotropic $l = 6$ and $l = 10$. Therefore isotropy can be considered as a concept of vanishing of certain invariants. It is plausible, though speculative, that each symmetry class obeys some isotropy, which uniquely determines its transformation group members. Such invariants need not be of bilinear form, but may also be multilinear forms and a mixture of certain weights [289, 216]. Finding appropriate invariants is a hard job, therefore ad-hoc methods, e.g. pseudo-metrics of invariants have to fill the gap to determine structures of surface patterns.

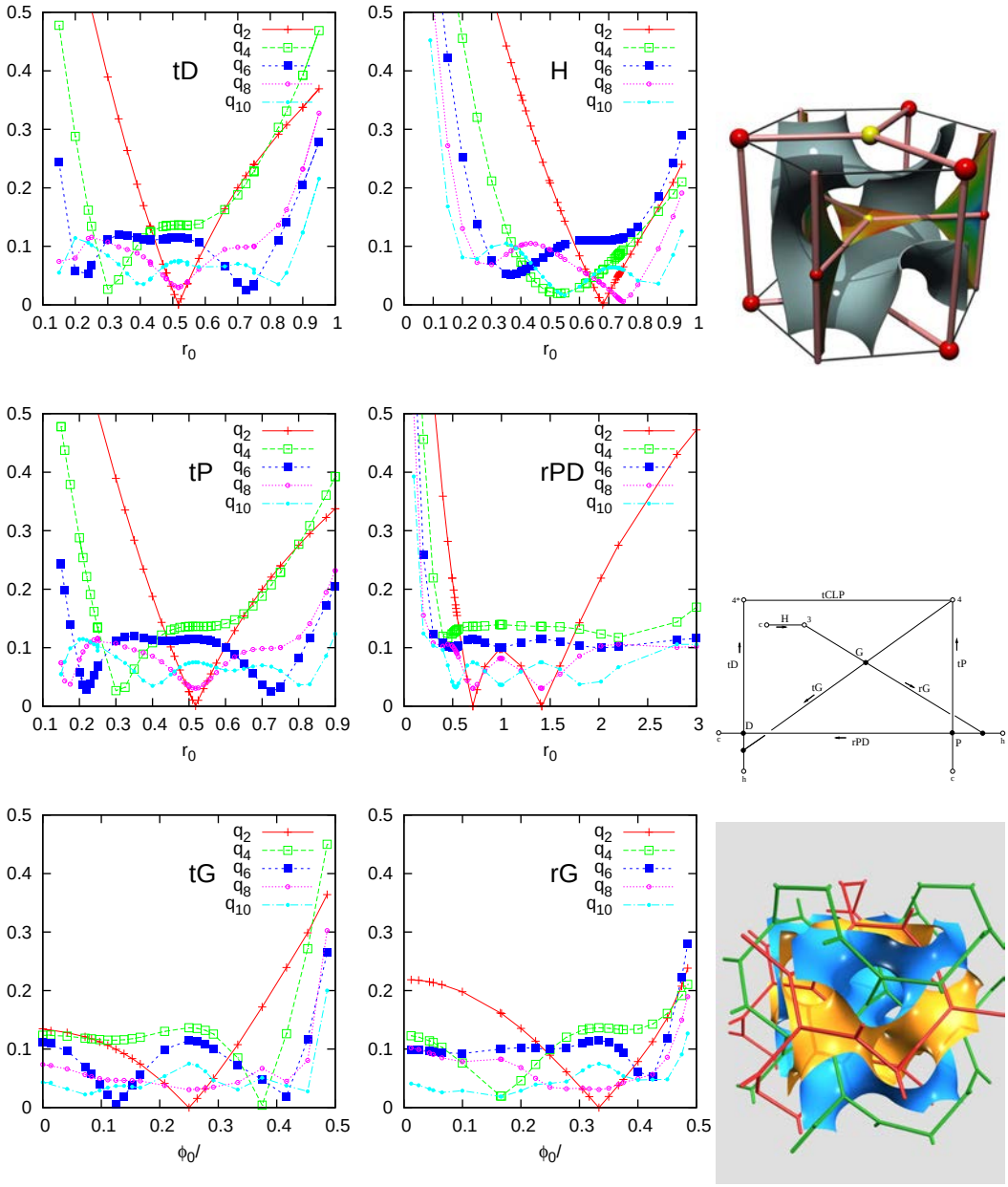


FIGURE 7.4. *q_l^V as a function of the free surface parameter for six families of TPMS. $q_2^V = 0$ indicates the cubic gyroid (G) (right column bottom, from ref. [272]) in the tG and rG family. Right column top shows the H surface with $q_2^V = 0$ (from ref [277]). The schematic diagram at the right, shows the interconnections between the TPMS families (from ref. [103])*

7.6. Discussion

The analysis of the irreducible tensors, either in cartesian or in spherical representation, offers new insights into the inherent structure of the Minkowski analysis and shows the natural connection between BOO and NOO. While the algebra in spherical coordinates leads to the direct decomposition in irreducible parts, and thus to the n-linear invariants, the calculations in the spherical tensors might be tedious. Often, the cartesian counterparts are easier to interpret, e.g. the interface tensor is the irreducible element of $W_1^{0,2}$ or the tensor of inertia is the irreducible element of $W_0^{2,0}$. This dual picture completes the power of the systematic Minkowski framework. In many cases, it seems sufficient to work with either eigenvalue invariants from the cartesian representation or the bilinear form of the spherical irreducibles, and transformations among them are not necessary. Indeed, Jerphagon [141] also gave formulas to derive q_l^V from the irreducible cartesian tensors. The total contraction tensor norm

$$\begin{aligned} T : T = \|T\|^2 &= \sum_J \left\| T^{(J)} \right\|^2 = \sum_{i_1,\ldots,i_r} T_{i_1,\ldots,i_r} T_{i_1,\ldots,i_r} \\ &= \sum_{i_1,\ldots,i_r,J} T^{(J)}_{i_1,\ldots,i_r} T^{(J)}_{i_1,\ldots,i_r} \\ &= \sum_{m,J} (-1)^{r+J+m} T^J_m \, T^J_{-m}, \end{aligned} \tag{7.32}$$

where r is the rank of the fully symmetric T and $T^J_{i_1,\ldots,i_r}$ the cartesian irreducible elements of T. T^J denotes the spherical irreducibles with the entries T^J_m. The last two lines, can be recasted as

$$\left\| T^J \right\|^2 = \sum_m (-1)^m T^J_m \, T^J_{-m}. \tag{7.33}$$

Recalling that $T^J_m = \left\| T^J \right\| N^l_m$ in the case of $W_1^{0,r}$, one gets a relation for the bilinear invariants from the cartesian representation.

We want to emphasize the significantion of the weight $l = 2$ ($\beta_\nu^{r,s}$ or q_2) for local order description in disordered materials. This weight is the lowest weight, where the irreducible normal Minkwoski tensors are not trivial (when normalized with W_1). By Steinhardt this weight was omitted, since the corresponding invariants vanish all together for any crystal order of monodisperse spheres. Indeed, this latter fact makes this weight especially interesting to study disordered packings, so that all ordered (crystalline) structures are at the border of the random distribution and not mixed up with the random background. A clear separation of ordered and disordered domains is therefore with only one scalar measure possible. We made use of this fact, when

studying the crystallisation onset at RCP. Furthermore, the merit of a low weight l measure like $\beta_V^{r,s}$ or q_2 is, that (negative) interference of the normal vectors in the multipole expansion is less likely.

Last but not least NOO are robust due to the area weights. The NOO order parameters preserve all the merits of the spherical harmonics approach originally proposed by Steinhardt [289]. This makes them a superior local order descriptor than the Steinhardt BOO with the bond definitions based on discrete sets of nearest neighbors. NOO combined with power tessellations (Laguerre-tessellations) or medial surfaces tessellations are a straight forward generalization of the BOO in order to study polydisperse sphere packings and non-spherical particle ensembles.

8. Summary

In this work we investigated the geometry controlled phase behavior in the vicinity of nanorough substrates and in jammed bead packs. With a phase field (PF) model we are able to study the generic behavior of a vapor-liquid system down to sizes of a few molecular diameters. Non-wetting, i.e. vapor suspended Cassie-Baxter drops are favored over Wenzel drops due to geometrical corrugation at nanoscale. Geometrical effects are also found in the simple hard sphere fluid model, in particular when dissipative processes lead to jamming. A purely geometrical driven phase transition of jammed sphere packings is found at the so-called random close packing point, which marks the onset of crystallization.

8.1. Nanowetting, nanoslip

In the first chapters of this work we focus on the geometrical effects in wetting problems on nanometric length scales—or more precisely the wetting of macroscopic drops on substrates with roughness length scales of a few nanometers. This gap between length scales is a notoriously difficult problem in numerical simulations. Therefore, we employed, refined and thoroughly tested a phase field model for nanowetting, which allows for simulations of such systems. This model is designed to provide an insight into the generic wetting behavior of a fluid in the vicinity of a corrugated substrate. This model finds its place between the commonly used lattice Boltzmann (LB) simulations and molecular dynamics simulations (MD). LB is used in many microfluidic studies, where large system sizes (compared to the particle diameter) and large time scales are needed. MD simulations are very powerful when small system sizes are under investigation and dynamical effects occur on short time scales (up to nanoseconds).

With the PF model we studied the contact angles of macroscopic drops on nanometric corrugated monovalued surfaces made of chemically homogeneous materials. We demonstrated that nanofeatures are of great importance to enhance non-wetting and

hence allow for omniphobicity—i.e. the repellency of liquids, no matter the chemical pairing—even on corrugations without overhangs. This effect is mainly driven by line tensions at needle (or blade) shaped surface structures. These line tensions lead to a thermodynamically stable wetting inversion in a homogeneous wetting regime, which can not be explained with the classical Wenzel law. Generalizing the Wenzel formula with a line tension contribution closes this deficiency in the classical theory. These findings from simulations are in agreement with experiments of Ramos et al. [250]. Molecular simulations with water molecules [76, 180] find similar results for particular systems. Our results reveal rather the generic geometrical features that are at play.

Further we regarded the impact of random-rough surfaces, which are a toy model for fractal surfaces. We find qualitative agreement with the experimental results of ref. [250], when considering the wetting transition from the Cassie-Baxter wetting branch to the Wenzel-like wetting regime. The transition between both regimes is smoothed out on such structures and can be modeled with a stochastic model. With this model we can calculate the apparent wetting angle of the thermodynamically stable wetting state. In our examples, we found that the Cassie-Baxter regime and the Wenzel regime show remarkable similarities in the wetting diagram, though the interface contact profiles with the wall are quite distinct.

To understand this complex transition a detailed understanding of the metastabilites is needed. The PF model gives access to the free energy landscape and thus to the energy barriers between homogeneous and heterogeneous states. The transition process from one state to another depends on the initial state. Dewetting a crenel from a cylindric Wenzel drop to the Cassie-Baxter state needs a nucleation process of a bubble at the bottom of the crenel, while the Cassie-Baxter to Wenzel transition is an intrusion process. Line tensions along needle or blade shaped obstacles increase the energy barrier between both states, so that the Cassie-Baxter state can be metastable up to wetting angles of $\approx 60^\circ$.

From intrinsic slip length studies, one may expect that large contact angles imply large slip lengths. We showed with PF simulations that on nanocorrugated substrates, even large apparent contact angles may have very small slip lengths when the crenels are filled with liquid, i.e. in the Wenzel state. Large slip is found in the Cassie-Baxter state. Therefore, the needle tip driven Wenzel-wetting inversion does not allow for large flow enhancement. However, in the Cassie-Baxter state we showed that significant slip can occur at intrinsic contact angles less than 90°. This effect is based on the stabilization of the Cassie-Baxter state due to the needle tips. This might be a practical

route to increase flow rates.

With the PF model we also studied contact angle hysteresis of driven drops in a nanochannel. Contact angle hysteresis stems from pinning at heterogeneous substrates. We found slip—stick—jump dynamics of the drop front line, i.e. the triple line slips over the top layer of the pillar, till it sticks at the outer edge of the pillar. Liquid of the drop is redistributed under the influence of the driving force (e.g. gravity) to increase the wetting angle. If the force is large enough, jump dynamics of the front line are observed, i.e. the drop crosses the crenel until it continues the cycle at the next pillar. This is in agreement with findings from LB simulations. What is new is, that the critical driving force does not affect the critical contact angle for depinning. In our simulations we made use of synchronous/asynchronous rear and front line pinning to vary the critical driving force. Synchronous or asynchronous depinning may explain volume dependency for sticking drops. Free energy landscaping lead to the simple picture that a drop on a heterogeneous substrate can be considered as a drop that is driven in an external potential with fast motion in the potential valleys and slow motion at the peaks.

As mentioned above, the dynamics of the 3D dewetting transition of crenels might be different. In the same manner contact angle hysteresis and pinning becomes more complex in three dimensions. Therefore, it would be fruitful to develop efficient algorithms for the PF model in that case, i.e. parallelization and probably adaptive mesh methods are needed in order to study sufficiently large 3D systems. Further conceptional work can tackle the question how to model non-isothermal problems including heat transfer or to study stochastic problems including thermal motion. PF models are known as versatile simulation techniques, which are capable of solving these problems in general.

We hope that experimentalists may access these nanoscopic length scales in wetting experiments and test the hypothesis of the needle tip effect and its practical relevance in the future. One may think about flat substrate decorated with carbon nano tubes or well controlled etching processes. In the meantime one may test the needle tip hypothesis with molecular simulations, e.g. with phantom wall method that has been recently developed in the Müller-Plathe group.

A consistent theory for contact angle hysteresis is still lacking. The PF model may help to clarify the picture of the contact angle hysteresis, since the free energy landscape is directly accessible. For instance the question, whether there is a substantial difference in dynamics of the front/rear line of driven drops in contrast to evaporating or inflating drops should be addressed in future work. We currently run simulations to

clarify this point. Furthermore, 3D PF simulations may be used to test the Joanny–de Gennes theory of pinning.

8.2. Jamming, RCP, defects

In the latter chapters we employed the Minkowski analysis to gain structural information about sphere packings of frictionless and frictional spheres. We used rank-2 Minkowski tensors to quantify local anisotropy in sphere packs and showed that local mean anisotropy is a phase indicator in thermal fluids and also in metastable states and jammed bead packs. The Minkowski analysis of sphere packs is the shape analysis of the tessellation cells—Laguerre tessellations in general and Voronoi tessellations in the special case which we used in this work. Many widely used order parameters depend crucially on the arbitrary choice of a set of nearest neighbors. Commonly used definitions for nearest neighbors are not robust against noise. Minkowski tensors in turn are robust against noise by their definition. In particular, when investigating disordered systems of particulate matter robustness is an important issue. For instance the common local order parameter q_6 was found to lead to conflicting results, when the set of nearest neighbors is redefined according to commonly used definitions.

We used the hard sphere model to validate rank-2 Minkowski tensors as order parameters and compared the results to commonly used order parameters, i.e. the Steinhardt bond orientational order parameter family and the Edwards tensor. Thanks to the completeness theorem for Minkowski tensors, we found that the local anisotropy of the Voronoi cells in equilibrium hard sphere packings is generic. This means anisotropy is not dependent on a special choice of the morphological characteristics under consideration.

The rank-2 Minkowski tensor analysis was also used to investigate the local structure in jammed bead packs from experiments and simulations in a packing fraction interval between ≈ 0.55 and ≈ 0.64. In the literature the former is called random loose packing and the latter random close packing. We found substantial local anisotropy, which is maximal compared to thermal hard sphere systems, metastable systems and compressed hard sphere ensembles with the same packing fraction. Furthermore, anisotropy is universal in jammed packings. More precise, all employed jamming protocols—experiments and simulations—lead to the same rescaled anisotropy distribution and the same (within small statistical errors) mean local anisotropy as a function of the packing fraction. Also, the correlations between anisotropy and local

packing fraction is universal. Universal behavior is astonishing, since the jamming protocols are non-ergodic and thus, a priori, the final state is history dependent. Conversely, universal structure of jammed bead packs implies history-independence of the arrested state. This is in agreement with findings of *volume* based structure analysis, e.g. in ref. [16, 15].

Substantial anisotropy in jammed bead packs may explain, why disordered packings of ellipsoids pack denser than their spherical counterparts. The virtual replacement of isotropic beads by anisotropic ellipsoids occupies the anisotropic void space more efficiently. We think the structural analysis of ellipsoidal packings can verify this hypothesis in the future.

With the Lubachevsky-Stillinger (LS) algorithm arrested sphere packs with a large range of packing fractions were created, especially below and above the so-called random close packing point. The rank-2 Minkowski tensor analysis revealed a structural change around this point: The universal distribution with vanishing probability for isotropic cells breaks down for high packing fractions, including finite probability for isotropic cells. This is a precursor of crystallization which was analyzed in great detail with the $W_1^{0,4}$ rank-4 Minkowski tensor. We developed pseudo-metrical symmetry indices from $W_1^{0,4}$ invariants to distinguish between several ordered phases. With this method we clearly identified an onset of crystallization at a packing fraction around 0.649 in LS simulations and interpret this as the random close packing (RCP) point. Crystallization is meant to be local ordering to hexagonal close packed (hcp) and face centered cubic (fcc) clusters of different sizes. No icosahedral structures are found, although the local packing fraction of the center sphere in such configurations is higher than in hcp and fcc clusters. This is in agreement with findings in recent publications from the Medvedev group [8, 181].

While we chose for this analysis the rank-4 Minkowski tensor $W_1^{0,4}$, which is represented in cartesian coordinates, the analysis can be done also with spherical Minkowski tensors. Cartesian tensors have the merit that they are more intuitional while the latter allows for easier systematic derivation of their invariants for abitrary rank. Therefore, we made a comparison of cartesian and spherical representations of normal Minkowski tensors and linked them to the Steinhardt bond orientational order parameter family (BOO). Indeed, the Minkowski and the Steinhardt approaches are quite similar. However the latter lacks robustness. Thus, the Minkowski approach is a method to enhance the BOO tool. Our analysis of disordered structures shows the merit of descriptors with $l = 2$, e.g. q_2 (which is virtually equivalent to the anisotropy measure $\beta_\nu^{r,s}$) to study disorder. While higher even values of l, e.g. q_4 and q_6 are sensi-

tive to several ordered configurations, some of these configurations suffer from a large random background of disordered configurations. $l = 2$ leads to the first non-trivial invariants, and all crystal symmetries found in monodisperse sphere packings yield vanishing q_2.

To avoid confusion we call the spherical Minkowski tensor method normal orientation order parameter (NOO). This reinterpretation of the BOO allows also to enrich the field of applications. NOO can also be applied to investigate the structure of almost arbitrary boundary surfaces.

A closed theory to identify the set of independent invariants of irreducible Minkowski tensors is still lacking and has to be worked out in the future. Nevertheless, in order to exploit this robust order measurement tool, a family of invariants has to be identified, which allows for concise and reliable cluster identification. This might follow two different routes. First, from the independent Minkowski tensors on could derive a linear combination of tensors which vanishes exclusively for a certain symmetry configuration. Due to the continuity of Minkowski tensors, such an approach offers a systematic way for robust cluster identification. A second route might be the definition of proper pseudo metrics based on NOO as we did for the symmetry indices in the jamming regime. We assume this approach to be numerically cheaper. Such a pseudo metric has been worked out here for fcc, bcc, hcp, sc and icosahedral order.

The calculus of spherical Minkowski tensors might be also useful to connect structure properties to physical properties, e.g. elastic moduli of bicontinuous networks or optical properties of optical crystals.

Last but not least, NOO combined with power tessellations (Laguerre-tessellations) or medial surfaces tessellations are a straight forward generalization of the BOO in order to study polydisperse sphere packings and non-spherical particle ensembles.

A. Details on the Parameters of the PF Model

Some details on the wall parameters

As discussed in chapter 2 the wetting angle is a function of ε_{LJ}. Other parameters which may change the wetting angle are kept constant. Fig. A.1 shows the $\cos\theta$ as a function of ε_{LJ} for different resolutions and ratios w/σ. A $w/\sigma = 4/3$ appears convenient to tune the full wetting range for $\varepsilon_{LJ} \in [0, 4]$.

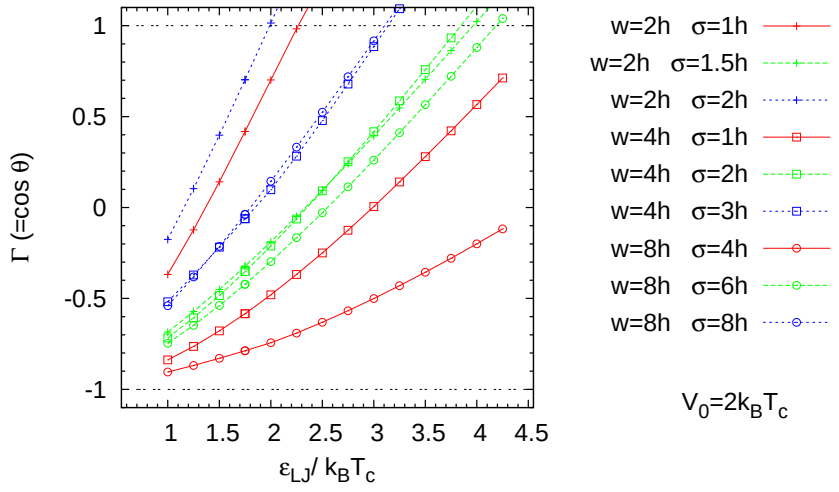


FIGURE A.1.

Parameters

We listed the parameters which are used in tables A.1 to A.3. The kinematic and dynamical viscosity is roughly that of water at standard conditions. There are basically to time-scales involved. Firstly the time-scale of the PF diffusion and secondly the time-scale of the hydrodynamic equations determined by the viscosity. We chose the smaller time-scale, the diffusion time-scale, to define the intrinsic unit-system.

Parameter	Symbol	Value
Cahn-Hilliard constant	G^{CH}	$2.0 \cdot 10^{-9}\mathrm{m}^2/\mathrm{s}$
Allen-Cahn constant	G^{AC}	$2.0 \cdot 10^{9}\mathrm{s}^{-1}$
particle diameter	σ	$1.0 \cdot 10^{-9}\mathrm{m}$
interfacial thickness	w	$1.33 \cdot 10^{-9}\mathrm{m}$
kinematic viscosity	ν	$1 \cdot 10^{-6}\mathrm{m}^2/\mathrm{s}$
mass per particle	m	$3.0 \cdot 10^{-26}\mathrm{kg}$
critical temperature	T_c	500K
Boltzmann constant	k_B	$1.38065 \cdot 10^{-23}\mathrm{J/K}$
Lennard-Jones prefactor	ε	$[1.72, 6.9] \cdot 10^{-21}\mathrm{J}$

TABLE A.1. *Model parameter in real units.*

Scaling-parameter	Symbol	Value
length-scale	σ	$1.0 \cdot 10^{-9}\mathrm{m}$
time-scale	$\tau = \sigma^2/G^{CH}$	$5.0 \cdot 10^{-10}\mathrm{s}$
energy-scale	$k_B T_c$	$6.9035 \cdot 10^{-21}\mathrm{J}$

TABLE A.2. *Scaling parameters of the lattice model*

Parameter	Symbol	Value in $(\sigma, \tau, k_B T_c)$
Cahn_Hilliard constant	G^{CH*}	1
Allen-Cahn constant	G^{AC*}	1
particle diameter	σ^*	1
interfacial thickness	w^*	4/3
kinematic viscosity	ν^*	500
dynamic viscosity	η^*	$6.67\,10^{-3}$
mass per particle	m^*	$1.7382 \cdot 10^{-5}$
Lennard-Jones prefactor	ε^*	$[0.3, 1.00]$
friction parameter	k^*	100
temperature	T^*	$0.6^{\#}, 0.7$
liquid denisty	ρ_L^*	0.77
liquid denisty	ρ_V^*	0.02

TABLE A.3. *Dimensionless parameters in the $(\sigma, \tau, k_B T_c)$-unit-system, # default parameter*

Nanorough wall parameters

Since we consider a geometry which is translation invariant in the direction of the ridges, we can reduce the numerical solution to the x and y direction. The external potential is integrated in z-direction. The bottom substrate is corrugated and the top substrate is a planar reference surface. Figure 3.10 (top panel) on page 67 shows an example of a wetting configuration on the random rough substrates (RRS).

The S1 geometry is defined as follows: A slab geometry is taken and at the bottom we grow independently pillars on each lattice block (2x2 lattice sites). If the lattice block below is already marked as wall, there is a 95% probability that the next block belongs to the wall too. We use a cutoff for the maximal height of 30 lattice block and the lattice block spacing is 1.33σ.

The more regular S2 geometry consists of pillars with constant width $a = 1.33\sigma$ while the crenel width is randomly distributed. $L - a$ follows a binomial distribution $B(N, p)$: $L - a = \alpha X; X \sim B(30, 0.3)$ with $\alpha = 0.67\sigma$, the number of repetitions N and the a priori probability p. The pillar height $h = 13.3\sigma$ is constant. The internal unit of length is one lattice site which is 0.67σ. All lengths under consideration are

integer-valued lattice spacings [214]. The liquid density $\rho_{\mathrm{L}} = 0.77\sigma^{-3}$ and the vapor density $\rho_{\mathrm{L}} = 0.02\sigma^{-3}$ at a temperature $T = 0.6T_{\mathrm{c}}$, where T_c is the critical temperature of the van der Waals fluid ($T_c = 500K$).

B. Experiments and simulations of particulate matter

In this chapter we list protocols and details of the point-pattern generation in chapter 6.

B.1. Monte-Carlo simulations

The MC of equilibrium hard spheres simulations were performed by Spanner according to a local Metropolis move and cluster flip algorithm [161, 84, 151]. This means that the algorithm performs alternating single sphere move followed by a cluster flip move. The clusters are identified by an inversion at a random pivot point. One advantage of this method is, that it works well around the liquid-solid transition point. [84]. 16000 hard spheres are used in the MC simulations (4000 for densities $\phi > 0.6$ in 3D) in a cubic simulation box with periodic BC (NV-ensemble). The equilibration is checked the pair correlation function, which is in agreement with the Percus-Yevick approximation and with the mean square displacement is analyzed [151].

B.2. Molecular dynamics simulations

Event-driven MD simulations of hard spheres were performed by Nogawa [251, 137, 151]. The number of spheres in the cubic simulation box is up to 256000 with periodic BC (NV-ensemble). The same tests whether the system is equilibrated or not were performed as for the MC simulations in the section above. Well equilibrate systems were produced for small and large densities. In the region of the phase transition, the ensemble lacks perfect equilibration (see marked interval for in fig. 6.4).

B.3. Supercooled liquids-MD simulations

The super-cooled HS liquid simulations were done in the group of Ito at the university of Tokyo and performed by Nogawa [229]. A novel algorithm has been used, similar to the LS algorithm (see also following section). A random point pattern is initialized and decorated with spheres $R = 0$. This step is followed by a Voronoi graph computation. Spheres are expanded up to the smallest distance between the center point and the corresponding Voronoi facets or a certain final radius. This results into a polydisperse packing. With event driven MD moves the system is relaxed for short time intervals alternated with the radius expansion step till one ends up in a monodisperse system, where all spheres have the final radius. This algorithm preserves the random character of the initial state better than e.g. the LS algorithm (see description below), however it becomes inefficient when approaching the RCP point. The simulations were run with 160000 spheres in a periodic and cubic box. This algorithm is intended to avoid crystallization and allows for efficient computation.

B.4. Lubachevsky-Stillinger

The LS simulations presented in Figs. 6.15, 6.14, 6.16 and 6.17 are done by Aste [273] and the LS simulations presented in Figs. 6.4, 6.21, 6.22, 6.23, 6.25 and 6.26 are performed by Kapfer.

The Lubachevsky-Stillinger algorithm [185] is an out-of-equilibrium event driven molecular dynamics simulation. Packings with 10000 and 40000 hard spheres have been simulated in a periodic cubic box. The system is initialized with a random point pattern decorated with spheres which have radius $R(t = 0) = 0$. The radius is time dependent and increased linear in time with the expansion rate γ. The system is simulated with Newtonian dynamics and an extra force acting at contact ensures that spheres depart after the collision. The simulation is either terminated when a pressure threshold is reached (jammed packing) or when a certain packing fraction threshold is obtained (non-jammed/supercooled systems). The expansion rate γ controls roughly the packing fraction at jamming. Jammed packings are found in an interval of roughly $0.55 \leq \phi \leq 0.70$. Large γ yields low packing fraction.

B.5. Monte-Carlo simulations of nearly jammed

The decompression MC jammed beads were performed by Schröder-Turk [273]. Starting from a jammed bead pack (experimental packing A were used, see B.7), the radius of the spheres is reduced in order to obtain a certain packing fraction. Thus the systems become unjammed. Then, canonical MC moves are applied (random direction and random length between 0 and 20% of the sphere diameter). One million MC moves are performed in our examples for each different packing fraction.

B.6. DEM-simulations

The discrete element method (DEM) simulations were performed by Delaney [273, 79]. DEM results are bead packs with almost monodisperse spheres, which are obtained from numerically relaxation of experimental bead packs with some degree of polydispersity. DEM integrates Newton's equation including translational and rotational degrees of freedom. Elasto-frictional behavior of spheres and gravity are also included. In this study packings from the DA experiments were used as initial packing (see section below).

Model The normal interaction force is modeled as a repulsive contact force (i.e. when overlapping): $F_\mathrm{n} = k_\mathrm{n}\xi^{3/2}$, where ξ is the overlap, i.e. $\xi = d - |\mathbf{r}_i - \mathbf{r}_j|$. $\mathbf{r}_i$ and $\mathbf{r}_j$ are the actual particle centers and d the ideal diameter of the spherical particle. The tangential interaction force describes friction and reads $F_\mathrm{t} = -\min(|k_\mathrm{t}\xi_\mathrm{n}^{1/2}\xi_\mathrm{t}|, |\mu F_\mathrm{n}|)\mathrm{sign}(v_\mathrm{t})$, where v_t is the tangential velocity and ξ_t is the tangential displacement $\xi_\mathrm{t} := \int_{t_0}^{t} v_\mathrm{t}(t')\mathrm{d}t'$. t_0 is the time where the contact occurred. The displacement is thus the velocity integrated over the lifetime of the contact. To fulfill the Coulomb friction criteria $F_\mathrm{t} \leq \mu F_\mathrm{n}$ with the friction coefficient μ, the tangential force is truncated as written above.

Dissipative terms are also included, i.e. in order to account for visco-elastic dissipation the dissipative normal force reads $F_\mathrm{n}^\mathrm{d} = -\gamma_\mathrm{n}\xi_\mathrm{n}^{1/2}\dot{\xi}_\mathrm{n}$ and in tangential direction the friction force is $F_\mathrm{t}^\mathrm{d} = -\gamma_\mathrm{t}v_\mathrm{t}$.

Parameter Realistic input parameters were used, i.e. for the acrylic beads the Young modulus is $E = 3.2\ GPa$, the Poisson ratio $\nu = 0.3$ the static grain friction coefficient

is $\mu = 0.28$ and the density 1150 kg/m^3. $d = 0.5mm$ in samples A and C and the samples B,D,E and F have $d = 0.795mm$. For the glass beads the parameter are Young modulus $E = 70\ GPa$, a Poisson ratio $\nu = 0.2$, density of 2500 kg/m^3 grain static friction coefficient $\mu = 0.9$ and radius $0.125mm$. [273].

The input parameter are connected to k_n and k_t by

$$k_n = \frac{d^{1/2}E}{3(1-\nu^2)} \tag{B.1}$$

$$k_t = \frac{2}{7}k_n. \tag{B.2}$$

For further details of the DEM simulation see ref. [79].

B.7. Dry acrylic experiments

The experiments and point-pattern extraction of the dry acrylic (DA) beads were done by Aste, Senden and Saadatfar [17, 12, 13]. The experimental DA data consist of 6 individual realizations of dry acrylic beads in air, confined by a cylindrical container ($= 55mm$). The filling height is around $75mm$. Intermediate packing fractions were obtained by slow pouring (C) of the beads into the container. Low packing fractions (A,B) were obtained by placing a stick inside the container and removing the stick slowly after the beads are poured into the cylinder. Higher packing fractions are obtained by faster pouring (D), gently tapping the walls (E) and by a combination of tapping and compressing from above (F). The compression piston was removed before the structure were analyzed with computed tomography methods. Table B.1 list the 6 analyzed bead packs.

B.8. Fluidized bed experiments

The experiments and point-pattern extraction of the fluidized bed (FB) setups were performed by Schröter et al. [16, 275]. Beads settle under gravity against a pulsed liquid flow and build a jammed packing in the bottom of the container by sedimentation. The flow rate controls the packing fraction. The container is cylindrical shaped with a diameter of $12.8mm$ and a length of $230mm$. The bead diameter is around $0.25mm$ with a polydispersity of 3%. A list of individual realizations can be found in table B.2

name	sample N_g	minus sampling N_a	ϕ	diameter	polydispersity
DA A	102897	40000	0.586	1.00	0.05mm
DA B	34016	14986	0.596	1.59	0.05mm
DA C	142918	40000	0.619	1.00	0.05mm
DA D	35510	15699	0.626	1.59	0.05mm
DA E	35880	15825	0.630	1.59	0.05mm
DA F	36460	16223	0.640	1.59	0.05mm

TABLE B.1. *Dry acrylic realizations from refs. [17, 12, 13]*

name	sample N_g	minus sampling N_a	ϕ
FB 14	145719	40000	0.568
FB 15	146382	40000	0.571
FB 16	146615	40000	0.572
FB 17	145293	40000	0.567
FB 18	145180	40000	0.566
FB 19	147294	40000	0.575
FB 20	146100	40000	0.571
FB 21	147750	40000	0.579
FB 22	148106	40000	0.582
FB 23	150120	40000	0.591
FB 24	152843	40000	0.600
FB 27	153009	40000	0.600

TABLE B.2. *Fluidized bed realizations from refs. [16, 275]*

C. Minkowski tensors

C.1. MT algorithm

In this paragraph the algorithm for MT of rank-2 is summarized for polyhedral meshes, i.e. triangulated surfaces. The notation of the polyhedral surface is defined in fig. C.1 and the sum-rules for the MT are listed in Tab. C.1.

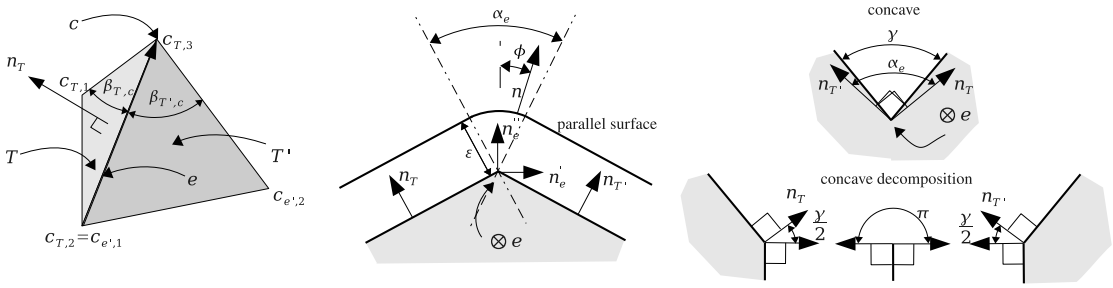


FIGURE C.1. *(Left) Definition of geometric properties of a triangulated surface $\mathcal{F}_2$. For a triangle T, $\mathbf{n}_T$ is the normal vector of T, A_T its area, and $\mathbf{c}_{T,1}$ to $\mathbf{c}_{T,3}$ its corners. An edge $\mathbf{e}$ is defined by its vertices $\mathbf{c}_{\mathbf{e},1}$ and $\mathbf{c}_{\mathbf{e},2}$. The angle $\beta_{T,\mathbf{c}}$ is the angle between the two edges of the triangle T at the vertex $\mathbf{c}$ (Middle) Cross-sectional view along a directed edge $\mathbf{e}$. The normal vectors $\mathbf{n}_T$ and $\mathbf{n}_{T'}$ of the triangle T (that contains $\mathbf{e}$) and T' (that is adjacent to T along edge $\mathbf{e}$) span the angle $\alpha_\mathbf{e} \in]-\pi, \pi[$. More precisely, a rotation by $\alpha_\mathbf{e}$ around $\mathbf{e}$ in counter-clockwise direction maps the triangle normal $\mathbf{n}_T$ of the triangle containing $\mathbf{e}$ onto the $\mathbf{n}_{T'}$. A concave edge has a negative angle $\alpha_\mathbf{e}$. The figure also shows the definition of the local coordinate system used for the computation of $W_2^{0,2}$. The basis vectors $\mathbf{n}'_\mathbf{e}, \mathbf{n}''_\mathbf{e}$ and $\hat{\mathbf{e}}$ are defined as $\hat{\mathbf{e}} = \mathbf{e}/|\mathbf{e}|$, $\mathbf{n}''_\mathbf{e} = (\mathbf{n}_{e,1} + \mathbf{n}_{e,2})/|\mathbf{n}_{\mathbf{e},1} + \mathbf{n}_{\mathbf{e},2}|$ and $\mathbf{n}'_\mathbf{e} = \hat{\mathbf{e}} \times \mathbf{n}''_\mathbf{e}$. (Right) Subdivision of a body K along a concave edge $\mathbf{e}$.*

	scalar measures	
W_0	$\int_K \mathrm{d}V$	$\frac{1}{3}\sum_{T\in\mathcal{F}_2}\langle \mathbf{C}_T, \mathbf{n}_T\rangle A_T$
W_1	$\frac{1}{3}\int_{\partial K}\mathrm{d}\mathcal{O}$	$\frac{1}{3}\sum_{T\in\mathcal{F}_2} A_T$
W_2	$\frac{1}{3}\int_{\partial K} G_2\,\mathrm{d}\mathcal{O}$	$\frac{1}{6}\sum_{\mathbf{e}\in\mathcal{F}_1}\lvert\mathbf{e}\rvert\,\alpha_{\mathbf{e}}$
W_3	$\frac{1}{3}\int_{\partial K} G_3\,\mathrm{d}\mathcal{O}$	$\frac{1}{3}\sum_{\mathbf{c}\in\mathcal{F}_0}(2\pi-\sum_{T\in\mathcal{F}_2(\mathbf{c})}\beta_{T,\mathbf{c}})$
	tensorial measures	
$(W_0^{2,0})_{ij}$	$\int_K \mathbf{r}_i\mathbf{r}_j\,\mathrm{d}V$	$\sum_{T\in\mathcal{F}_2} 2A_T\,J_{T,i,j,k}n_{T,k}$
$(W_1^{2,0})_{ij}$	$\frac{1}{3}\int_{\partial K}\mathbf{r}_i\mathbf{r}_j\,\mathrm{d}\mathcal{O}$	$\frac{1}{18}\sum_{T\in\mathcal{F}_2}\sum_{m=1}^{3}\sum_{l\le m}\left(\mathbf{c}_{T,l,i}\mathbf{c}_{T,m,j}+\mathbf{c}_{T,m,i}\mathbf{c}_{T,l,j}\right)A_T$
$(W_2^{2,0})_{ij}$	$\frac{1}{3}\int_{\partial K} G_2\,\mathbf{r}_i\mathbf{r}_j\,\mathrm{d}\mathcal{O}$	$\frac{1}{18}\sum_{\mathbf{e}\in\mathcal{F}_1}\alpha_{\mathbf{e}}\lvert\mathbf{e}\rvert\times$ $\left(\mathbf{c}_{\mathbf{e},1,i}\mathbf{c}_{\mathbf{e},1,j}+\mathbf{c}_{\mathbf{e},1,i}\mathbf{c}_{\mathbf{e},2,j}+\mathbf{c}_{\mathbf{e},2,i}\mathbf{c}_{\mathbf{e},2,j}\right)$
$(W_3^{2,0})_{ij}$	$\frac{1}{3}\int_{\partial K} G_3\,\mathbf{r}_i\mathbf{r}_j\,\mathrm{d}\mathcal{O}$	$\frac{1}{3}\sum_{\mathbf{c}\in\mathcal{F}_0}\left(2\pi-\sum_{T\in\mathcal{F}_2(\mathbf{c})}\beta_{T,\mathbf{c}}\right)\mathbf{c}_i\mathbf{c}_j$
$(W_1^{0,2})_{ij}$	$\frac{1}{3}\int_{\partial K}\mathbf{n}_i\mathbf{n}_j\,\mathrm{d}\mathcal{O}$	$\frac{1}{3}\sum_{T\in\mathcal{F}_2} A_T\,\mathbf{n}_{T,i}\mathbf{n}_{T,j}$
$(W_2^{0,2})_{ij}$	$\frac{1}{3}\int_{\partial K} G_2\,\mathbf{n}_i\mathbf{n}_j\,\mathrm{d}\mathcal{O}$	$\frac{1}{12}\sum_{\mathbf{e}\in\mathcal{F}_1}\lvert\mathbf{e}\rvert\left((\alpha_{\mathbf{e}}+\sin\alpha_{\mathbf{e}})\mathbf{n}''_{\mathbf{e},i}\mathbf{n}''_{\mathbf{e},j}+\right.$ $\left.(\alpha_{\mathbf{e}}-\sin\alpha_{\mathbf{e}})\mathbf{n}'_{\mathbf{e},i}\mathbf{n}'_{\mathbf{e},j}\right)$

TABLE C.1. *Minkowski tensors in 3 dimensions of a body K with the triangulated surface ∂K. The mean and Gaussian curvature are G_2 and G_3, respectively. The set of facets of the triangulation of ∂K is $\mathcal{F}_2$, the set of edges is $\mathcal{F}_1$ and the set of vertices $\mathcal{F}_0$. The subset of triangles that contain the vertex c is denoted by $\mathcal{F}_2(c)$. The nomenclature for triangulated surfaces is defined in fig. C.1 on the left side. A_T is the area, $\mathbf{C}_T := \sum_{i=0}^{3}\mathbf{c}_i/3$ its center of mass and J_T is given in Tab. C.2, see also [48].*

The volume integral $W_0^{2,0}(K)$ can be computed using

$$
\begin{aligned}
J_{T,i,j,k} = \int_0^1 \mathrm{d}a \int_0^{1-a} \mathrm{d}b \\
&[\mathbf{c}_{T,1} + a(\mathbf{c}_{T,2}-\mathbf{c}_{T,1}) + b(\mathbf{c}_{T,3}-\mathbf{c}_{T,1})]_i \times \\
&[\mathbf{c}_{T,1} + a(\mathbf{c}_{T,2}-\mathbf{c}_{T,1}) + b(\mathbf{c}_{T,3}-\mathbf{c}_{T,1})]_j \times \\
&[\mathbf{c}_{T,1} + a(\mathbf{c}_{T,2}-\mathbf{c}_{T,1}) + b(\mathbf{c}_{T,3}-\mathbf{c}_{T,1})]_k\,, \qquad \text{(C.1)}
\end{aligned}
$$

i, j	$\vec{f}_{i,j}$	$J_{i,j,k}$	n_k
x, x	$(0, 0, xxz)^t$	$J_{x,x,z}$	n_z
y, y	$(0, 0, yyz)^t$	$J_{y,y,z}$	n_z
z, z	$(0, zzy, 0)^t$	$J_{z,z,y}$	n_y
x, y	$(0, 0, xyz)^t$	$J_{x,y,z}$	n_z
x, z	$(0, xyz, 0)^t$	$J_{x,y,z}$	n_y
y, z	$(xyz, 0, 0)^t$	$J_{x,y,z}$	n_x

TABLE C.2. *Utility functions for computing the $\nu = 0$ Minkowski tensors.*

finally the tensor may be expressed as

$$W_0^{2,0}(K) = \sum_{T \in \mathcal{F}_2} 2A_T \cdot J_{T,i,j,k} \cdot \mathbf{n}_{T,k}. \tag{C.2}$$

C.2. Clebsch-Gordan transformation matrices for $W_1^{0,r}$

In this section we list the Clebsch-Gordan transformation matrices for normal Minkowski tensors up to rank $r \leq 4$ [141] Using the Clebsch-Gordan coefficients and the transformation matrices U_{mi} one obtains for scalar Minkowski functionals, $r = 0$:

$$C_0^0 = 1 \tag{C.3}$$

for vectorial Minkowski functionals, $r = 1$:

$$\begin{aligned} (C_0^1)_i &= (0,\ 0,\ 1) \\ (C_{\pm 1}^1)_i &= \frac{1}{\sqrt{2}}(\mp 1,\ -i,\ 0) \end{aligned} \tag{C.4}$$

$$\tag{C.5}$$

for tensorial Minkowski functionals of rank $r = 2$:

$$\begin{aligned} (C_0^0)_{i_1 i_2} &= -\frac{1}{\sqrt{3}}\,\delta_{i_1 i_2} \\ (C_0^2)_{i_1 i_2} &= -\frac{1}{\sqrt{6}} \begin{pmatrix} 1 & 0 & 0 \\ 0 & 1 & 0 \\ 0 & 0 & -2 \end{pmatrix} \\ (C_{\pm 1}^2)_{i_1 i_2} &= -1 \begin{pmatrix} 0 & 0 & \pm 1 \\ 0 & 0 & i \\ \pm 1 & i & 0 \end{pmatrix} \\ (C_{\pm 2}^2)_{i_1 i_2} &= \frac{1}{2} \begin{pmatrix} 1 & \pm i & 0 \\ \pm i & -1 & 0 \\ 0 & 0 & 0 \end{pmatrix} \end{aligned} \tag{C.6}$$

and for tensorial Minkowski functionals of rank $r = 4$:

$$
\begin{aligned}
(C_0^0)_{i_1i_2i_3i_4} &= \frac{1}{\sqrt{5}}\delta_{i_1i_2}\delta_{i_3i_4}\delta_{i_1i_3} + \frac{2}{\sqrt{5}}\delta_{i_1i_2}\delta_{i_3i_4} \\
(C_0^2)_{i_1i_2i_3i_4} &= \frac{1}{\sqrt{7}}C_{xxxx} + \frac{1}{\sqrt{7}}C_{yyyy} - \frac{2}{\sqrt{7}}C_{zzzz} \\
&\quad + \frac{2}{\sqrt{7}}C_{xxyy} - \frac{1}{\sqrt{7}}C_{yyzz} - \frac{1}{\sqrt{7}}C_{zzxx} \\
(C_{\pm1}^2)_{i_1i_2i_3i_4} &= \pm\sqrt{\frac{6}{7}}C_{xxxz} + i\sqrt{\frac{6}{7}}C_{yyyz} \pm \sqrt{\frac{6}{7}}C_{zzzx} \\
&\quad + i\sqrt{\frac{6}{7}}C_{zzzy} + i\sqrt{\frac{6}{7}}C_{xxyz} \pm \sqrt{\frac{6}{7}}C_{yyzx} \\
(C_{\pm2}^2)_{i_1i_2i_3i_4} &= -\sqrt{\frac{3}{14}}C_{xxxx} + \sqrt{\frac{3}{14}}C_{yyyy} \mp i2\sqrt{\frac{3}{13}}C_{xxxy} \\
&\quad \mp i2\sqrt{\frac{3}{14}}C_{yyyx} + \sqrt{\frac{3}{14}}C_{yyzz} - \sqrt{\frac{3}{14}}C_{zzxx} \mp i2\sqrt{\frac{3}{14}}C_{zzxy} \\
(C_0^4)_{i_1i_2i_3i_4} &= \frac{3}{2\sqrt{70}}C_{xxxx} + \frac{3}{2\sqrt{70}}C_{yyyy} + \frac{3}{2\sqrt{70}}C_{zzzz} \\
&\quad + \frac{3}{\sqrt{70}}C_{xxyy} - \frac{12}{\sqrt{70}}C_{yyzz} - \frac{12}{\sqrt{70}}C_{zzxx} \\
(C_{\pm1}^4)_{i_1i_2i_3i_4} &= \pm\frac{3}{\sqrt{14}}C_{xxxz} + i\frac{3}{\sqrt{14}}C_{yyyz} \mp \frac{4}{\sqrt{14}}C_{zzzx} \\
&\quad - i\frac{4}{\sqrt{14}}C_{zzzy} + 3i\frac{3}{\sqrt{14}}C_{xxyz} \pm \frac{3}{\sqrt{14}}C_{yyzx} \\
(C_{\pm2}^4)_{i_1i_2i_3i_4} &= -\sqrt{\frac{1}{28}}C_{xxxx} + \sqrt{\frac{1}{28}}C_{yyyy} \mp i\sqrt{\frac{4}{28}}C_{xxxy} \\
&\quad \mp i\sqrt{\frac{4}{28}}C_{yyyx} - \frac{6}{\sqrt{28}}C_{yyzz} + \frac{6}{\sqrt{28}}C_{zzxx} \pm i\frac{12}{\sqrt{28}}C_{zzxy} \\
(C_{\pm3}^4)_{i_1i_2i_3i_4} &= \mp i\frac{1}{\sqrt{2}}C_{xxxz} + i\frac{1}{\sqrt{2}}C_{yyyz} - i\frac{3}{\sqrt{2}}C_{xxyz} \pm i\frac{3}{\sqrt{2}}C_{yyzx} \\
(C_{\pm4}^4)_{i_1i_2i_3i_4} &= \frac{1}{4}C_{xxxx} + \frac{1}{4}C_{yyyy} \pm iC_{xxxy} \\
&\quad \mp iC_{yyyx} - \frac{3}{2}C_{xxyy}
\end{aligned}
\tag{C.7}
$$

C.3. Normal vectors

With the definitions of 7 one obtains for the normal tensors of weight $l = 2$.

$$
\begin{aligned}
N^{(2)}\Big|_0^0 &= -\sqrt{\frac{1}{3}}N_0^0 \\
N^{(2)}\Big|_m^1 &= 0 \\
N^{(2)}\Big|_0^2 &= \sqrt{\frac{2}{3}}N_0^2 \\
N^{(2)}\Big|_{\pm 1}^2 &= \sqrt{\frac{2}{3}}N_{\pm 1}^2 \\
N^{(2)}\Big|_{\pm 2}^2 &= \sqrt{\frac{2}{3}}N_{\pm 2}^2 \\
N^{(2)}\Big|_0^0 &= = -\frac{1}{\sqrt{3}}\left(N_{xx}+N_{yy}+N_{zz}\right) - \frac{1}{\sqrt{3}} \quad = -\sqrt{\frac{4\pi}{3}}Y_0^0 \\
N^{(2)}\Big|_0^1 &= \frac{i}{\sqrt{2}}\left(N_{xy}-N_{yx}\right) = 0 \\
N^{(2)}\Big|_{\pm 1}^1 &= -\frac{1}{2}\left(N_{xz}-N_{zx}\right) \pm \frac{i}{2}\left(N_{zy}-N_{yz}\right) = 0 \\
N^{(2)}\Big|_0^2 &= -\frac{1}{\sqrt{6}}\left(N_{xx}+N_{yy}-2N_{zz}\right) \\
&= -\frac{1}{\sqrt{6}}\left(3\sin^2(\theta)-2\right) \\
&= \sqrt{\frac{4\pi}{5}}\sqrt{\frac{2}{3}}Y_0^2 \\
N^{(2)}\Big|_{\pm 1}^2 &= \mp\frac{1}{2}\left(N_{xz}+N_{zx}\right) - \frac{i}{2}\left(N_{yz}+N_{zy}\right) \\
&= \mp\sin(\theta)\cos(\theta)(\cos(\phi) \pm i\sin(\phi)) \\
&= \pm\sqrt{\frac{8\pi}{15}}Y_{\pm 1}^2 \\
N^{(2)}\Big|_{\pm 2}^2 &= \frac{1}{2}\left(N_{xx}-N_{yy}\right) \pm \frac{i}{2}\left(N_{xy}+N_{yx}\right) \\
&= \frac{1}{2}\sin^2(\theta)(\cos(\phi) \pm i\sin(\phi)) \\
&= \sqrt{\frac{8\pi}{15}}Y_{\pm 2}^2
\end{aligned}
$$

Bibliography

[1] Sneha Abraham and Biman Bagchi. Suppression of the rate of growth of dynamic heterogeneities and its relation to the local structure in a supercooled polydisperse liquid. *Physical Review E*, 78(5), 2008.

[2] G. J. Ackland and A. P. Jones. Applications of local crystal structure measures in experiment and simulation. *Phys. Rev. B*, 73(5):054104, 2006.

[3] A Ahuja, J A Taylor, V Lifton, A A Sidorenko, T R Salamon, E J Lobaton, P Kolodner, and T N Krupenkin. Nanonails: a simple geometrical approach to electrically tunable superlyophobic surfaces. *Langmuir*, 24(1):9–14, 2008.

[4] S. Alesker. Description of continuous isometry covariant valuations on convex sets. *Geom. Dedicata*, 74:241–248, 1999.

[5] M. P. Allen and D. J. Tildesley. *Computer simulation of liquids*. Clarendon Press, New York, NY, USA, 1989.

[6] D. M. Anderson, G. B. McFadden, and A. A. Wheeler. Diffuse-interface methods in fluid mechanics. *Annual Review of Fluid Mechanics*, 30(1):139–165, 1998.

[7] D. Andrews and W. Ghoul. Irreducible fourth-rank cartesian tensors. *Physical Review A*, 25(5):2647, 1982.

[8] A. Anikeenko and N. Medvedev. Polytetrahedral nature of the dense disordered packings of hard spheres. *Physical Review Letters*, 98(23), 2007.

[9] A J Archer. Dynamical density functional theory for molecular and colloidal fluids: a microscopic approach to fluid mechanics. *J Chem Phys*, 130(1):014509, 2009.

[10] David Aristoff and Charles Radin. Random loose packing in granular matter. *Journal of Statistical Physics*, 135(1):1, 2009.

[11] David Aristoff and Charles Radin. Random close packing in a granular model. *Journal of Mathematical Physics*, 51(11):113302, 2010.

[12] T Aste. Investigating the geometrical structure of disordered sphere packings. *Physica A: Statistical Mechanics and its Applications*, 339(1-2):16, 2004.

[13] T Aste. Variations around disordered close packing. *Journal of Physics: Condensed Matter*, 17(24):S2361, 2005.

[14] T Aste and A Coniglio. Cell theory for liquid solids and glasses: From local packing configurations to global complex behaviors. *Europhysics Letters (EPL)*, 67(2):165, 2004.

[15] T Aste and T Di Matteo. Correlations and aggregate statistics in granular packs. *Eur Phys J E Soft Matter*, 22(3):235–40, 2007.

[16] T Aste, T. Di Matteo, M Saadatfar, T. J Senden, Matthias Schröter, and Harry L Swinney. An invariant distribution in static granular media. *Europhysics Letters (EPL)*, 79(2):24003, 2007.

[17] T. Aste, M. Saadatfar, and T. Senden. Geometrical structure of disordered sphere packings. *Physical Review E*, 71(6):061302, 2005.

[18] T. Aste and D. Weaire. *The persuit of perfect packing*. Institute of Physics Publishing, 150 South Independence Mall West, Philadelphia, USA, 2000.

[19] Christian Aulin, Sang Ho Yun, Lars Wågberg, and Tom Lindström. Design of highly oleophobic cellulose surfaces from structured silicon templates. *ACS Appl Mater Interfaces*, 1(11):2443–52, 2009.

[20] C.B. Barber, D.P. Dobkin, and H. Huhdanpaa. The Quickhull algorithm for convex hull. 22(4):469–483, 1996.

[21] Laura Barbieri, Estelle Wagner, and Patrik Hoffmann. Water wetting transition parameters of perfluorinated substrates with periodically distributed flat-top microscale obstacles. *Langmuir*, 23(4):1723–34, 2007.

[22] J. L. Barrat and J. P. Hansen. *Basic concepts for simple and complex liquids*. Cambridge University Press, 2003.

[23] Jean-Louis Barrat and Lyde*ric Bocquet. Influence of wetting properties on hydrodynamic boundary conditions at a fluid/solid interface. *Faraday Discussions*, 112:119, 1999.

[24] Jean-Louis Barrat and Lydéric Bocquet. Large slip effect at a nonwetting fluid-solid interface. *Phys. Rev. Lett.*, 82(23):4671–4674, Jun 1999.

[25] W. Barthlott and Ehler N. Raster-elektronenmikroskopie der epidermisoberflächen von spermatophyten. *Trop.subtrop. Pflanzenwelt*, 19, 1977.

[26] W. Barthlott and C. Neinhuis. Purity of the sacred lotus, or escape from contamination in biological surfaces. *Planta*, 202:1–8, 1997.

[27] J. Baudry, E. Charlaix, A. Tonck, and D. Mazuyer. Experimental evidence for a large slip effect at a nonwetting fluid−solid interface. *Langmuir*, 17(17):5232, 2001.

[28] Claus Beisbart, Robert Dahlke, Klaus Mecke, and Herbert Wagner. Vector- and tensor-valued descriptors for spatial patterns, 2002.

[29] R Benzi, L Biferale, M Sbragaglia, S Succi, and F Toschi. Mesoscopic two-phase model for describing apparent slip in micro-channel flows. *Europhysics Letters (EPL)*, 74(4):651, 2007.

[30] R. Benzi, S. Succi, and M. Vergassola. The lattice boltzmann equation: theory and applications. *Physics Reports*, 222(3):145–197, 1992.

[31] Gersh O Berim and Eli Ruckenstein. Nanodrop on a nanorough solid surface: density functional theory considerations. *J Chem Phys*, 129(1):014708, 2008.

[32] J. D. Bernal. Geometry of the structure of monatomic liquids. *Nature*, 185(4706):68, 1960.

[33] J. D. Bernal and J. Mason. Packing of spheres: Co-ordination of randomly packed spheres. *Nature*, 188(4754):910, 1960.

[34] S. Bhagavantam and D. Suryanarayana. Crystal symmetry and physical properties: application of group theory. *Acta Crystallographica*, 2(1):21, 1949.

[35] T. Biben and L. Joly. Wetting on nanorough surfaces. *Physical Review Letters*, 100(18):186103, 2008.

[36] Thierry Biben. Phase-field models for free-boundary problems. *European Journal of Physics*, 26(5):S47, 2005.

[37] Thierry Biben, Klaus Kassner, and Chaouqi Misbah. Phase-field approach to three-dimensional vesicle dynamics. *Physical Review E*, 72(4), 2005.

[38] J Bico, C Marzolin, and D Quéré. Pearl drops. *Europhysics Letters (EPL)*, 47(2):220, 2007.

[39] Raphael Blumenfeld and Sam Edwards. Granular entropy: Explicit calculations for planar assemblies. *Physical Review Letters*, 90(11), 2003.

[40] Lydéric Bocquet and Jean-Louis Barrat. Flow boundary conditions from nano- to micro-scales. *Soft Matter*, 3(6):685, 2007.

[41] Lyderic Bocquet and Elisabeth Charlaix. Nanofluidics, from bulk to interfaces. *Chem. Soc. Rev.*, 39(3):1073–1095, 2010.

[42] W. J. Boettinger, J. A. Warren, C. Beckermann, and A. Karma. Phase-field simulation of solidification 1. *Annual Review of Materials Research*, 32(1):163, 2002.

[43] P. G. Bolhuis, D. Frenkel, Siun-Choun Mau, and David A. Huse. Entropy difference between crystal phases. *Nature*, 388:235, 1997.

[44] R Bonneville. Local field in liquid dielectrics: A two-parameter mean field approach. *Physica A: Statistical and Theoretical Physics*, 102(1):49, 1980.

[45] Rodica Borcia and Michael Bestehorn. Phase-field model for marangoni convection in liquid-gas systems with a deformable interface. *Physical Review E*, 67(6):066307, 2003.

[46] J.M. Brader and Matthias Krüger. Density profiles of a colloidal liquid at a wall under shear flow. *Molecular Physics*, 109(7-10):1029, 2011.

[47] A. J. Bray. Theory of phase ordering kinetics. *Advances in Physics*, 43:357, 1994.

[48] B. Breidenbach. *Scalar and tensor-valued Minkowski functionals of spatially complex structures*. PhD thesis, Friedrich-Alexander Universitaet Erlangen-Nuernberg, 2007.

[49] A. J. Briant, A. J. Wagner, and J. M. Yeomans. Lattice boltzmann simulations of contact line motion. i. liquid-gas systems. *Phys. Rev. E*, 69(3):031602, Mar 2004.

[50] A. J. Briant and J. M. Yeomans. Lattice boltzmann simulations of contact line motion. ii. binary fluids. *Phys. Rev. E*, 69(3):031603, Mar 2004.

[51] John W. Cahn. Free energy of a nonuniform system. ii. thermodynamic basis. *The Journal of Chemical Physics*, 30(5):1121, 1959.

[52] John W. Cahn and John E. Hilliard. Free energy of a nonuniform system. i. interfacial free energy. *The Journal of Chemical Physics*, 28(2):258, 1958.

[53] John W. Cahn and John E. Hilliard. Free energy of a nonuniform system. iii. nucleation in a two-component incompressible fluid. *The Journal of Chemical Physics*, 31(3):688, 1959.

[54] F Calvo and D J Wales. Stepwise melting of a model glass former under confinement. *J Chem Phys*, 131(13):134504, 2009.

[55] Liangliang Cao, Hsin-Hua Hu, and Di Gao. Design and fabrication of micro-textures for inducing a superhydrophobic behavior on hydrophilic materials. *Langmuir*, 23(8):4310–4, 2007.

[56] Liangliang Cao, Tyler P Price, Michael Weiss, and Di Gao. Super water- and oil-repellent surfaces on intrinsically hydrophilic and oleophilic porous silicon films. *Langmuir*, 24(5):1640–3, 2008.

[57] Manfredo Do Carmo. *Differential Geometry of Curves and Surfaces*. Prentice Hall, 1976.

[58] A. B. D. Cassie and S. Baxter. Wettability of porous surfaces. *Transactions of the Faraday Society*, 40:546, 1944.

[59] Charusita Chakravarty, Pablo G Debenedetti, and Frank H Stillinger. Lindemann measures for the solid-liquid phase transition. *J Chem Phys*, 126(20):204508, 2007.

[60] Elisabeth Charlaix and Matteo Ciccotti. Capillary condensation in confined media. In Klaus Sattler, editor, *Handbook of Nanophysics - Vol 1*. CRC Press, 2010. arXiv:0910.4626v1.

[61] Pinaki Chaudhuri, Ludovic Berthier, and Srikanth Sastry. Jamming transitions in amorphous packings of frictionless spheres occur over a continuous range of volume fractions. *Physical Review Letters*, 104(16), 2010.

[62] S. Chen, S. P. Dawson, G. D. Doolen, D. R. Janecky, and A. Lawniczak. Lattice methods and their applications to reacting systems. *Computers & Chemical Engineering*, 19(6-7):617–646, 1995. Applications of Parallel Computing.

[63] Shiyi Chen and Gary D. Doolen. Lattice boltzmann method for fluid flows. *Annual Review of Fluid Mechanics*, 30:329–364, 1998.

[64] J.-T. Cheng and N. Giordano. Fluid flow through nanometer-scale channels. *Physical Review E*, 65(3), 2002.

[65] Shreerang S Chhatre, Wonjae Choi, Anish Tuteja, Kyoo-Chul Kenneth Park, Joseph M Mabry, Gareth H McKinley, and Robert E Cohen. Scale dependence of omniphobic mesh surfaces. *Langmuir*, 26(6):4027–35, 2010.

[66] Shreerang S Chhatre, Anish Tuteja, Wonjae Choi, Amélie Revaux, Derek Smith, Joseph M Mabry, Gareth H McKinley, and Robert E Cohen. Thermal annealing treatment to achieve switchable and reversible oleophobicity on fabrics. *Langmuir*, 25(23):13625–32, 2009.

[67] Chang-Hwan Choi and Chang-Jin Kim. Large slip of aqueous liquid flow over a nanoengineered superhydrophobic surface. *Phys. Rev. Lett.*, 96(6):066001, Feb 2006.

[68] T S Chow. Wetting of rough surfaces. *Journal of Physics: Condensed Matter*, 10(27):L445, 1999.

[69] Joseph Collins and Herbert Levine. Diffuse interface model of diffusion-limited crystal growth. *Physical Review B*, 31(9):6119, 1985.

[70] J. A. R. Coope. Irreducible cartesian tensors. ii. general formulation. *Journal of Mathematical Physics*, 11(3):1003, 1970.

[71] J. A. R. Coope, R. F. Snider, and F. R. McCourt. Irreducible cartesian tensors. *The Journal of Chemical Physics*, 43(7):2269, 1965.

[72] D. Corti and R. Bowles. Statistical geometry of hard sphere systems: exact relations for additive and non-additive mixtures. *Molecular Physics*, 96(11):1623, 1999.

[73] C Cottin-Bizonne, C Barentin, E Charlaix, L Bocquet, and J-L Barrat. Dynamics of simple liquids at heterogeneous surfaces: molecular-dynamics simulations and hydrodynamic description. *Eur Phys J E Soft Matter*, 15(4):427–38, 2004.

[74] Cécile Cottin-Bizonne, Jean-Louis Barrat, Lydéric Bocquet, and Elisabeth Charlaix. Low-friction flows of liquid at nanopatterned interfaces. *Nat Mater*, 2(4):237–40, 2003.

[75] Artur Cristea, Giuseppe Gonnella, Antonio Lamura, and Victor Sofonea. A lattice boltzmann study of phase separation in liquid-vapor systems with gravity. *Communications in Computational Physics*, 2009.

[76] Christopher D. Daub, Jihang Wang, Shobhit Kudesia, Dusan Bratko, and Alenka

Luzar. The influence of molecular-scale roughness on the surface spreading of an aqueous nanodrop. *Faraday Discussions*, 146:67, 2010.

[77] P.-G. de Gennes, F. Brochard-Wyart, and D. Quéré. *Gouttes, bulles, perles et ondes*. Belin, Paris, 8 rue Férou, 75278 Paris cedex, 2005.

[78] Alan Barros de Oliveira, Paulo A Netz, Thiago Colla, and Marcia C Barbosa. Structural anomalies for a three dimensional isotropic core-softened potential. *J Chem Phys*, 125(12):124503, 2006.

[79] Gary W. Delaney, T. Di Matteo, and Tomaso Aste. Combining tomographic imaging and dem simulations to investigate the structure of experimental sphere packings. *Soft Matter*, 6(13):2992, 2010.

[80] F. Diotallevi, L. Biferale, S. Chibbaro, A. Lamura, G. Pontrelli, M. Sbragaglia, S. Succi, and F. Toschi. Capillary filling using lattice boltzmann equations: The case of multi-phase flows. *The European Physical Journal Special Topics*, 166(1):111, 2009.

[81] M. Doi and T. Ohta. Dynamics and rheology of complex interfaces. I. *J. Chem. Phys.*, 95(2):1242–1248, 1991.

[82] A. Donev, I. Cisse, D. Sachs, E. Variano, F.H. Stillinger, R. Connelly, S. Torquato, and P.M. Chaikin. Improving the density of jammed disordered packings using ellipsoids. *Science*, 303:990–993, 2004.

[83] Aleksandar Donev. Jamming in hard sphere and disk packings. *Journal of Applied Physics*, 95(3):989, 2004.

[84] C Dress and W Krauth. Cluster algorithm for hard spheres and related systems. *Journal of Physics A: Mathematical and General*, 28(23):L597, 1995.

[85] Nathan Duff and Daniel Lacks. Shear-induced crystallization in jammed systems. *Physical Review E*, 75(3), 2007.

[86] G Durand, F Graner, and J Weiss. Deformation of grain boundaries in polar ice. *Europhysics Letters (EPL)*, 67(6):1038, 2004.

[87] G. Durand, F. Graner, and J. Weiss. Deformation of grain boundaries in polar ice. 67:1038–1044, 2004.

[88] S Edwards and D Grinev. Transmission of stress in granular materials as a problem of statistical mechanics. *Physica A: Statistical Mechanics and its Applications*, 302(1-4):162, 2001.

[89] S Edwards and R Oakeshott. Theory of powders. *Physica A: Statistical and Theoretical Physics*, 157(3):1080, 1989.

[90] J R Errington and P G Debenedetti. Relationship between structural order and the anomalies of liquid water. *Nature*, 409(6818):318–21, 2001.

[91] Serge Etienne and Laurent David. *Introduction à la science physique des polymères : Cours et exercices corrigés*. Dunod, 2002.

[92] R. Evans. The nature of the liquid-vapour interface and other topics in the statistical mechanics of non-uniform, classical fluids. *Advances in Physics*, 28(2):143, 1979.

[93] C. W. Extrand. Contact angles and hysteresis on surfaces with chemically heterogeneous islands. *Langmuir*, 19(9):3793, 2003.

[94] D. Faken and H. Jónsson. Systematic analysis of local atomic structure combined with 3D computer graphics. *Comp. Mater. Sci.*, 2(2):279 – 286, 1994.

[95] Kerstin Falk, Felix Sedlmeier, Laurent Joly, Roland R Netz, and Lydéric Bocquet. Molecular origin of fast water transport in carbon nanotube membranes: superlubricity versus curvature dependent friction. *Nano Lett.*, 10(10):4067–73, 2010.

[96] L. Feng, S. Li, Y. Li, H. Li, L. Zhang, J. Zhai, Y. Song, B. Liu, L. Jiang, and D. Zhu. Super-hydrophobic surfaces: From natural to artificial. *Advanced Materials*, 14(24):1857, 2002.

[97] Lin Feng, Yanan Zhang, Jinming Xi, Ying Zhu, Nü Wang, Fan Xia, and Lei Jiang. Petal effect: a superhydrophobic state with high adhesive force. *Langmuir*, 24(8):4114–9, 2008.

[98] Xi-Qiao Feng, Xuefeng Gao, Ziniu Wu, Lei Jiang, and Quan-Shui Zheng. Superior water repellency of water strider legs with hierarchical structures: experiments and analysis. *Langmuir*, 23(9):4892–6, 2007.

[99] François Feuillebois, Martin Bazant, and Olga Vinogradova. Effective slip over superhydrophobic surfaces in thin channels. *Physical Review Letters*, 102(2), 2009.

[100] Werner Fischer. On sphere packings of arbitrarily low density. *Zeitschrift für Kristallographie*, 220(7-2005):657, 2005.

[101] Andrew Fogden and Stephen T. Hyde. Parametrization of triply periodic minimal surfaces. I. mathematical basis of the construction algorithm for the regular class. A48:442–451, 1992.

[102] Andrew Fogden and Stephen T. Hyde. Parametrization of triply periodic minimal surfaces. II. regular class solutions. A48:575–591, 1992.

[103] Andrew Fogden and Stephen T Hyde. Continuous transformations of cubic minimal surfaces. 7:91–104, 1999.

[104] R. Folch, J. Casademunt, A. Hernández-Machado, and L. Ramírez-Piscina. Phase-field model for hele-shaw flows with arbitrary viscosity contrast. i. theoretical approach. *Phys. Rev. E*, 60(2):1724–1733, Aug 1999.

[105] R. Folch, J. Casademunt, A. Hernández-Machado, and L. Ramírez-Piscina. Phase-field model for hele-shaw flows with arbitrary viscosity contrast. ii. numerical study. *Phys. Rev. E*, 60(2):1734–1740, Aug 1999.

[106] Daan Frenkel and Anthony J. C. Ladd. New monte carlo method to compute the free energy of arbitrary solids. application to the fcc and hcp phases of hard spheres. *The Journal of Chemical Physics*, 81(7):3188, 1984.

[107] Daan Frenkel and Berend Smit. *Understanding Molecular Simulation, Second Edition: From Algorithms to Applications (Computational Science Series, Vol 1)*. Academic Press, 2nd ed. edition, 2001.

[108] Gao and Thomas J. McCarthy. Reply to "comment on how wenzel and cassie were wrong by gao and mccarthy". *Langmuir*, 23(26):13243, 2007.

[109] Lichao Gao and Thomas J McCarthy. How wenzel and cassie were wrong. *Langmuir*, 23(7):3762–5, 2007.

[110] E. Schröder-Turk Gerd Sebastian Kapfer, Boris Breidenbach, Claus Beisbart, and Klaus Mecke. Tensorial minkowski functionals and anisotropy measures for planar patterns. *Journal of Microscopy*, 238(1):57–74, 2010.

[111] Josiah Willard Gibbs. *Scientific Papers of J. Willard Gibbs*. Longmans, Green and co, 1906.

[112] Roy J. Glauber. Time-dependent statistics of the ising model. *Journal of Mathematical Physics*, 4(2):294, 1963.

[113] R. Gonzalez-Cinca, R. Folch, R. Benitez, L. Ramirez-Piscina, J. Casademunt, and A. Hernandez-Machado. Phase-field models in interfacial pattern formation out of equilibrium, 2004. arXiv:cond-mat/0305058v1.

[114] Markus Gross, Fathollah Varnik, Dierk Raabe, and Ingo Steinbach. Small droplets on superhydrophobic substrates. *Physical Review E*, 81(5), 2010.

[115] Eric M Grzelak and Jeffrey R Errington. Nanoscale limit to the applicability of wenzel's equation. *Langmuir*, 26(16):13297–304, 2010.

[116] M Gurtin. Generalized ginzburg-landau and cahn-hilliard equations based on a microforce balance. *Physica D: Nonlinear Phenomena*, 92(3-4):178, 1996.

[117] H. Hadwiger. *Vorlesungen über Inhalt, Oberfläche und Isoperimetrie*. Springer, Berlin, 1957.

[118] H. Hadwiger and C. Meier. Studien zur vektoriellen integralgeometrie. *Math. Nachr.*, 26:49, 1974.

[119] H. Hadwiger and R. Schneider. Vektorielle Integralgeometrie. *Elemente der Mathematik*, 26:49–72, 1971.

[120] Thomas C. Hales. A proof of the kepler conjecture. *Annals of Mathematics*, 162(3):1063–1185, 2005.

[121] Daewoo Han and Andrew J Steckl. Superhydrophobic and oleophobic fibers by coaxial electrospinning. *Langmuir*, 25(16):9454–62, 2009.

[122] Jean-Pierre Hansen and I. R. McDonald. *Theory of Simple Liquids, Third Edition*. Academic Press, 3rd edition, 2006.

[123] Hendrik Hansen-Goos, Roland Roth, Klaus Mecke, and S. Dietrich. Solvation of proteins: Linking thermodynamics to geometry. *Physical Review Letters*, 99(12), 2007.

[124] J Harting, C Kunert, and H. J Herrmann. Lattice boltzmann simulations of apparent slip in hydrophobic microchannels. *Europhysics Letters (EPL)*, 75(2):328, 2007.

[125] S Herminghaus. Roughness-induced non-wetting. *Europhysics Letters (EPL)*, 52(2):165, 2000.

[126] S Herminghaus. Roughness-induced non-wetting. *Europhysics Letters (EPL)*, 79(5):59901, 2007.

[127] Jessica Hernández-Guzmán and Eric R Weeks. The equilibrium intrinsic crystal-liquid interface of colloids. *Proc. Natl. Acad. Sci. U.S.A.*, 106(36):15198–202, 2009.

[128] Janne T Hirvi and Tapani A Pakkanen. Wetting of nanogrooved polymer surfaces. *Langmuir*, 23(14):7724–9, 2007.

[129] P. Hohenberg and B. Halperin. Theory of dynamic critical phenomena. *Reviews of Modern Physics*, 49(3):435, 1977.

[130] D. M. Huang, C. Sendner, D. Horinek, R. R. Netz, and L. Bocquet. Water slippage versus contact angle: A quasiuniversal relationship. *Phys. Rev. Lett.*, 101(22):226101, 2008.

[131] D. Hug, R. Schneider, and R. Schuster. The space of isometry covariant tensor valuations. *St. Petersburg Math. J.*, 19:137–158, 2008.

[132] Jagtar Singh Hunjan and Byung Chan Eu. The voronoi volume and molecular representation of molar volume: equilibrium simple fluids. *J Chem Phys*, 132(13):134510, 2010.

[133] Christopher Iacovella, Aaron Keys, Mark Horsch, and Sharon Glotzer. Icosahedral packing of polymer-tethered nanospheres and stabilization of the gyroid phase. *Physical Review E*, 75(4), 2007.

[134] H. Ibach and H. Lüth. Festkörperphysik. eine einführung in die grundlagen. zweite, überarb. u. erw. auflage. berlin etc., springer-verlag 1988. xii, 344 s., 230 abb., 16 tabellen, dm 59,—. isbn 3-540-19087-2 (springer-lehrbuch). *ZAMM - Journal of Applied Mathematics and Mechanics / Zeitschrift für Angewandte Mathematik und Mechanik*, 70(3):209, 1990.

[135] Atsushi Ikeda and Kunimasa Miyazaki. Glass transition of the monodisperse gaussian core model. *Physical Review Letters*, 106(1), 2011.

[136] T. Ingebrigtsen and S. Toxvaerd. Contact angles of lennard-jones liquids and droplets on planar surfaces. *Journal of Physical Chemistry C*, 111(24):8518, 2007.

[137] Masaharu Isobe. Simple and efficient algorithm for large scale molecular dynamics simulation in hard disk system. *International Journal of Modern Physics C [Computational Physics and Physical Computation]*, 10(7):1281, 1999.

[138] Jacob N. Israelachvili. *Intermolecular and Surface Forces, Second Edition: With Applications to Colloidal and Biological Systems (Colloid Science)*. Academic Press, 2nd edition, 1992.

[139] Melissa Jerkins, Matthias Schröter, Harry Swinney, Tim Senden, Mohammad Saadatfar, and Tomaso Aste. Onset of mechanical stability in random packings of frictional spheres. *Physical Review Letters*, 101(1):018301, 2008.

[140] Melissa Jerkins, Matthias Schroter, Harry L. Swinney, Tim J. Senden, Mohammad Saadatfar, and Tomaso Aste. Onset of mechanical stability in random packings of frictional spheres. *Physical Review Letters*, 101:018301, 2008. arXiv:0710.5160.

[141] J. Jerphagnon, D. Chemla, and R. Bonneville. The description of the physical properties of condensed matter using irreducible tensors. *Advances in Physics*, 27(4):609, 1978.

[142] Hua Jin, Marjo Kettunen, Ari Laiho, Hanna Pynnönen, Jouni Paltakari, Abraham Marmur, Olli Ikkala, and Robin H A Ras. Superhydrophobic and superoleophobic nanocellulose aerogel membranes as bioinspired cargo carriers on water and oil. *Langmuir*, 27(5):1930–4, 2011.

[143] J. F. Joanny and P. G. de Gennes. A model for contact angle hysteresis. *The Journal of Chemical Physics*, 81(1):552–562, 1984.

[144] W. Jodrey and E. Tory. Computer simulation of close random packing of equal spheres. *Physical Review A*, 32(4):2347, 1985.

[145] W. Jodrey and E. Tory. Erratum: Computer simulation of close random packing of equal spheres. *Physical Review A*, 34(1):675, 1986.

[146] Rulon E. Johnson and Robert H. Dettre. Contact angle hysteresis. iii. study of an idealized heterogeneous surface. *Journal of Physical Chemistry*, 68(7):1744, 1964.

[147] Laurent Joly and Thierry Biben. Wetting and friction on superoleophobic surfaces. *Soft Matter*, 2009.

[148] P. Joseph, C. Cottin-Bizonne, J. M. Benoit, C. Ybert, C. Journet, P. Tabeling, and L. Bocquet. Slippage of water past superhydrophobic carbon nanotube forests in microchannels. *Phys. Rev. Lett.*, 97(15):156104, oct 2006.

[149] Randall Kamien and Andrea Liu. Why is random close packing reproducible? *Physical Review Letters*, 99(15), 2007.

[150] Anuraag Kansal, Salvatore Torquato, and Frank Stillinger. Diversity of order and densities in jammed hard-particle packings. *Physical Review E*, 66(4), 2002.

[151] S. C. Kapfer, W. Mickel, F. M. Schaller, M. Spanner, C. Goll, T. Nogawa, N. Ito, K. Mecke, and G. E. Schröder-Turk. Local anisotropy of fluids using minkowski tensors. *Journal of Statistical Mechanics: Theory and Experiment*, 2010(11):P11010, 2010. arXiv:1005.4295v1.

[152] S.C. Kapfer, S.T. Hyde, K. Mecke, C.H. Arns, and G.E. Schröder-Turk. Minimal surface scaffold designs for tissue engineering. *Biomaterials*, to appear, 2011.

[153] Nikos Karayiannis, Katerina Foteinopoulou, and Manuel Laso. Contact network in nearly jammed disordered packings of hard-sphere chains. *Physical Review E*, 80(1), 2009.

[154] Mikael Karlsson, Pontus Forsberg, and Fredrik Nikolajeff. From hydrophilic to superhydrophobic: fabrication of micrometer-sized nail-head-shaped pillars in diamond. *Langmuir*, 26(2):889–93, 2010.

[155] Takeshi Kawasaki and Hajime Tanaka. Structural origin of dynamic heterogeneity in three-dimensional colloidal glass formers and its link to crystal nucleation. *Journal of Physics: Condensed Matter*, 22(23):232102, 2010.

[156] C.L. Kelchner, S.J. Plimpton, and J.C. Hamilton. Dislocation nucleation and defect structure during surface indentation. *Phys. Rev. B*, 58(17):11085–11088, 1998.

[157] Y. Kenmochi and R. Klette. Surface area estimation for digitized regular solids. In L. J. Latecki, D. M. Mount, and A. Y. Wu, editors, *Proc. Vision Geometry IX*, volume 4117, pages 100–111. SPIE, Oct. 2000.

[158] Aaron Keys and Sharon Glotzer. How do quasicrystals grow? *Physical Review Letters*, 99(23), 2007.

[159] Walter Kob and Kurt Binder. *Glassy Materials and Disordered Solids: An Introduction to Their Statistical Mechanics*. World Scientific Pub Co.

[160] Takahiro Koishi, Kenji Yasuoka, Shigenori Fujikawa, Toshikazu Ebisuzaki, and Xiao Cheng Zeng. Coexistence and transition between cassie and wenzel state on pillared hydrophobic surface. *Proc. Natl. Acad. Sci. U.S.A.*, 106(21):8435–40, 2009.

[161] Werner Krauth. *Statistical Mechanics: Algorithms and Computations (Oxford Master Series in Statistical, Computational, and Theoretical Physics)*. Oxford University Press, USA, 2006.

[162] Christian Kunert and Jens Harting. Simulation of fluid flow in hydrophobic rough microchannels. *International Journal of Computational Fluid Dynamics*, 22(7):475, 2008.

[163] Rei Kurita and Eric Weeks. Experimental study of random-close-packed colloidal particles. *Physical Review E*, 82(1), 2010.

[164] H. Kusumaatmaja, M. L. Blow, A. Dupuis, and J. M. Yeomans. The collapse transition on superhydrophobic surfaces. *EPL (Europhysics Letters)*, 81(3):36003, 2008.

[165] H Kusumaatmaja, J Léopoldès, A Dupuis, and J. M Yeomans. Drop dynamics on chemically patterned surfaces. *Europhysics Letters (EPL)*, 73(5):740, 2007.

[166] H. Kusumaatmaja, C. M. Pooley, S. Girardo, D. Pisignano, and J. M. Yeomans. Capillary filling in patterned channels. *Physical Review E*, 77(6), 2008.

[167] H Kusumaatmaja, R J Vrancken, C W M Bastiaansen, and J M Yeomans. Anisotropic drop morphologies on corrugated surfaces. *Langmuir*, 24(14):7299–308, 2008.

[168] H Kusumaatmaja and J M Yeomans. Modeling contact angle hysteresis on chemically patterned and superhydrophobic surfaces. *Langmuir*, 23(11):6019–32, 2007.

[169] H. Kusumaatmaja and J. M. Yeomans. Anisotropic hysteresis on ratcheted superhydrophobic surfaces. *Soft Matter*, 5(14):2704, 2009.

[170] K. König, R. Roth, and K. Mecke. Morphological thermodynamics of fluids: shape dependence of free energies. *Physical Review Letters*, 93, 2004.

[171] Aurélie Lafuma and David Quéré. Superhydrophobic states. *Nat Mater*, 2(7):457–60, 2003.

[172] L. D. Landau and E. M. Lifschitz. *Lehrbuch der theoretischen Physik - Hydrodynamik*, volume 56. Verlag Harri Deutsch, Frankfurt, 1990.

[173] L.D. Landau and E.M. Lifschitz. *Lehrbuch der theoretischen Physik - Elsatizitätstheorie*, volume 7. Verlag Harri Deutsch, Frankfurt, 1991.

[174] E. Lauga, M.P. Brenner, and H.A. Stone. Microfluidcs: The no-slip boundary condition. In C. Tropea, A. Yarin, and J.F. Foss, editors, *Hanndbook of Experimental Fluid Mechanics*. Springer New York, 2007.

[175] E. Lauga and H. A. Stone. Effective slip in pressure-driven stokes flow. *Journal of Fluid Mechanics*, 489:55, 2003.

[176] Claudia Lautensack and Sergei Zuyev. Random laguerre tessellations. *Advances in Applied Probability*, 40(3):630, 2008.

[177] Wolfgang Lechner and Christoph Dellago. Accurate determination of crystal structures based on averaged local bond order parameters. *J Chem Phys*, 129(11):114707, 2008.

[178] Frédéric Leroy, Daniel J. V. A. dos Santos, and Florian Müller-Plathe. Interfacial excess free energies of solid-liquid interfaces by molecular dynamics simulation and thermodynamic integration. *Macromolecular Rapid Communications*, 30(9-10):864, 2009.

[179] Frédéric Leroy and Florian Müller-Plathe. Solid-liquid surface free energy of lennard-jones liquid on smooth and rough surfaces computed by molecular dynamics using the phantom-wall method. *J Chem Phys*, 133(4):044110, 2010.

[180] Frédéric Leroy and Florian Mu*ller-Plathe. Rationalization of the behavior of solid-liquid surface free energy of water in cassie and wenzel wetting states on rugged solid surfaces at the nanometer scale. *Langmuir : the ACS journal of surfaces and colloids*, 27(2):637–645, 2011.

[181] K. Lochmann, A. Anikeenko, A. Elsner, N. Medvedev, and D. Stoyan. Statistical verification of crystallization in hard sphere packings under densification. *The European Physical Journal B*, 53(1):67, 2006.

[182] E.L., Lorensen and H.E. Cline. Marching cubes: A high resolution 3d surface construction algorithm. *Computer Graphics*, 21(4), 1987.

[183] H. Löwen. Lecture notes: Density functional theory for inhomogeneous fluids ii. 3rd Warsaw School of Statistical Physics, July 2009. http://www2.thphy.uni-duesseldorf.de/ hlowen/doc/ra/ra0025.pdf.

[184] Hartmut Löwen. A phase-field-crystal model for liquid crystals. *J Phys Condens Matter*, 22(36):364105, 2010.

[185] Boris D. Lubachevsky and Frank H. Stillinger. Geometric properties of random disk packings. *Journal of Statistical Physics*, 60(5-6):561, 1990.

[186] Boris D. Lubachevsky, Frank H. Stillinger, and Elliot N. Pinson. Disks vs.

spheres: Contrasting properties of random packings. *Journal of Statistical Physics*, 64(3-4):501, 1991.

[187] Richard Lucas. Ueber das zeitgesetz des kapillaren aufstiegs von flüssigkeiten. *Kolloid-Zeitschrift*, 23(1):15, 1918.

[188] Mathias Lundgren, Neil L Allan, and Terence Cosgrove. Modeling of wetting: a study of nanowetting at rough and heterogeneous surfaces. *Langmuir*, 23(3):1187–94, 2007.

[189] Mathias Lundgren, Neil L. Allan, Terence Cosgrove, and Neil George. Wetting of water and water/ethanol droplets on a non-polar surface: a molecular dynamics study. *Langmuir*, 18(26):10462, 2002.

[190] Mathias Lundgren, Neil L. Allan, Terence Cosgrove, and Neil George. Molecular dynamics study of wetting of a pillar surface. *Langmuir*, 19(17):7127, 2003.

[191] James Lutsko. Ginzburg-landau theory of the liquid-solid interface and nucleation for hard spheres. *Physical Review E*, 74(2), 2006.

[192] W. Man, A. Donev, F.H. Stillinger, M.T Sullivan, W.B. Russel, D. Heeger, S. Inati, S. Torquato, and P.M. Chaikin. Experiments on random packings of ellipsoids. *Phys. Rev. Lett.*, 94(19):198001, 2005.

[193] Umberto Marini Bettolo Marconi and Simone Melchionna. Dynamic density functional theory versus kinetic theory of simple fluids. *Journal of Physics: Condensed Matter*, 22(36):364110, 2010.

[194] Umberto Marini Bettolo Marconi and Pedro Tarazona. Dynamic density functional theory of fluids. *The Journal of Chemical Physics*, 110(16):8032, 1999.

[195] Umberto Marini Bettolo Marconi and Pedro Tarazona. Dynamic density functional theory of fluids. *Journal of Physics: Condensed Matter*, 12(A):413, 2000.

[196] Umberto Marini Bettolo Marconi and Pedro Tarazona. Nonequilibrium inertial dynamics of colloidal systems. *J Chem Phys*, 124(16):164901, 2006.

[197] A Marmur. Contact angle hysteresis on heterogeneous smooth surfaces. *Journal of Colloid and Interface Science*, 168(1):40, 1994.

[198] A. Marmur. From hygrophilic to superhygrophobic: Theoretical conditions for making high-contact-angle surfaces from low-contact-angle materials. *Langmuir*, 24(14):7573–7579, jul 2008.

[199] Abraham Marmur. Contact angles in constrained wetting. *Langmuir*, 12(23):5704, 1996.

[200] Abraham Marmur. Wetting on hydrophobic rough surfaces: to be heterogeneous or not to be? *Langmuir*, 19(20):8343, 2003.

[201] Abraham Marmur and Eyal Bittoun. When wenzel and cassie are right: reconciling local and global considerations. *Langmuir*, 25(3):1277–81, 2009.

[202] C. L. Martin. Influence of adhesion and friction on the geometry of packings of spherical particles. *Physical Review E*, 77(3), 2008.

[203] G McHale. Cassie and wenzel: were they really so wrong? *Langmuir*, 23(15):8200–5, 2007.

[204] P. McMullen. *Rend Circ. Palermo*, 50:259–271, 1997.

[205] Hendrik Hansen-Goos Mecke and Klaus. Fundamental measure theory for inhomogeneous fluids of non-spherical hard particles. *Physical Review Letters*, 102(1):018302–1, 2009.

[206] K. Mecke. Integral geometry and statistical physics. *International Journal of Modern Physics B*, 12:861–899, 1998.

[207] K. Mecke and C.H. Arns. Fluids in porous media: a morphometric approach. *J. Phys.: Condens. Matter*, 17:503–534, 2005.

[208] Klaus Mecke and Markus Rauscher. On thermal fluctuations in thin film flow. *Journal of Physics: Condensed Matter*, 17(45):S3515, 2005.

[209] Klaus R. Mecke. Additivity, convexity, and beyond: Applications of minkowski functionals in statistical physics. 554:111, 2000.

[210] Klaus R. Mecke and Victor Sofonea. Morphology of spinodal decomposition. *Phys. Rev. E*, 56(4):R3761, Oct 1997.

[211] K.R. Mecke. *Integralgeometrie in der statistischen Physik*. Harri Deutsch (Frankfurt), 1994.

[212] M. M. Mehrabadi and S. C. Cowin. Eigentensors of linear anisotropic elastic materials. *The Quarterly Journal of Mechanics and Applied Mathematics*, 43(1):15, 1990.

[213] N. David Mermin. Thermal properties of the inhomogeneous electron gas. *Phys. Rev.*, 137(5A):A1441–A1443, Mar 1965.

[214] Walter Mickel, Laurent Joly, and Thierry Biben. Transport, phase transitions, and wetting in micro/nanochannels: A phase field/ddft approach. *J Chem Phys*, 134(9):094105, 2011.

[215] Walter Mickel, Stefan Münster, Louise M Jawerth, David A Vader, David A Weitz, Adrian P Sheppard, Klaus Mecke, Ben Fabry, and Gerd E Schröder-Turk. Robust pore size analysis of filamentous networks from three-dimensional confocal microscopy. *Biophys. J.*, 95(12):6072–80, 2008.

[216] A. C. Mitus, F. Smolej, H. Hahn, and A. Z. Patashinski. Q 446 "shape spectroscopy" of local f.c.c. structures in computer simulations of crystallization. *EPL (Europhysics Letters)*, 32(9):777, 1995.

[217] A. C. Mitus, H. Weber, and D. Marx. Local structure analysis of the hard-disk fluid near melting. *Physical Review E*, 55(6):6855, 1997.

[218] B. M. Mognetti and J. M. Yeomans. Capillary filling in microchannels patterned by posts. *Physical Review E*, 80(5), 2009.

[219] B. M. Mognetti and J. M. Yeomans. Modeling receding contact lines on superhydrophobic surfaces. *Langmuir*, 26(23):18162–18168, 2010.

[220] Anatolii V Mokshin and Jean-Louis Barrat. Shear induced structural ordering of a model metallic glass. *J Chem Phys*, 130(3):034502, 2009.

[221] Filip Moučka and Ivo Nezbeda. Detection and characterization of structural changes in the hard-disk fluid under freezing and melting conditions. *Physical Review Letters*, 94(4), 2005.

[222] Florian Müller-Plathe. Scale-hopping in computer simulations of polymers. *Soft Materials*, 1(1):1, 2002.

[223] H.R. Müller. *Rend Circ. Palermo*, 2(1), 1953.

[224] H. Navier. Mémoire sur les lois du mouvement des fluides. *Mémoires de l'Académie Royale des Sciences de l'Institut de France*, VI, 1823.

[225] Alexander V Neimark, Peter I Ravikovitch, and Aleksey Vishnyakov. Bridging scales from molecular simulations to classical thermodynamics: density functional theory of capillary condensation in nanopores. *Journal of Physics: Condensed Matter*, 15(3):347, 2003.

[226] C. Neinhuis and W. Barthlott. Characterization and distribution of water-repellent, self-cleaning plant surfaces. *Annals of Botany*, 79(6):667–677, 1997. arXiv:http://aob.oxfordjournals.org/content/79/6/667.full.pdf+html.

[227] Ran Ni and Marjolein Dijkstra. Crystal nucleation of colloidal hard dumbbells. *J Chem Phys*, 134(3):034501, 2011.

[228] M. Nicolas, P. Duru, and O. Pouliquen. Compaction of a granular material under cyclic shear. *Eur. Phys. J. E*, 3(4):309–314, 2000.

[229] T. Nogawa. private communication. 2010.

[230] Edmund Nowak, James Knight, Eli Ben-Naim, Heinrich Jaeger, and Sidney Nagel. Density fluctuations in vibrated granular materials. *Physical Review E*, 57(2):1971, 1998.

[231] Gerardo Odriozola. Replica exchange monte carlo applied to hard spheres. *J Chem Phys*, 131(14):144107, 2009.

[232] Corey O'Hern, Stephen Langer, Andrea Liu, and Sidney Nagel. Random packings of frictionless particles. *Physical Review Letters*, 88(7), 2002.

[233] Atsuyuki Okabe, Barry Boots, Kokichi Sugihara, and Sung Nok Chiu. *Spatial tessellations: Concepts and applications of Voronoi diagrams*. Probability and Statistics. Wiley, NYC, 2nd edition, 2000. 671 pages.

[234] J. Oliver, C. Huh, and S.G. Mason. Resistance to spreading of liquids by sharp edges. *Journal of Colloid and Interface Science*, 59(3):568, 1977.

[235] T. Onda, S. Shibuichi, N. Satoh, and K. Tsujii. Super-water-repellent fractal surfaces. *Langmuir*, 12(9):2125, 1996.

[236] Didem Öner and Thomas J. McCarthy. Ultrahydrophobic surfaces. effects of topography length scales on wettability. *Langmuir*, 16(20):7777, 2000.

[237] J. Ou, B. Perot, and J. P. Rothstein. Laminar drag reduction in microchannels using ultrahydrophobic surfaces. *Phys. Fluids*, 16(12):4635–4643, dec 2004.

[238] Andreea Panaitescu and Arshad Kudrolli. Spatial distribution functions of random packed granular spheres obtained by direct particle imaging. *Physical Review E*, 81(6), 2010.

[239] Giorgio Parisi. Mean-field theory of hard sphere glasses and jamming. *Reviews of Modern Physics*, 82(1):789, 2010.

[240] Michael Patra and Mikko Karttunen. Stencils with isotropic discretization error for differential operators. *Numerical Methods for Partial Differential Equations*, 22(4):936, 2006.

[241] Y. Peng, Z.-R. Wang, A. Alsayed, A. Yodh, and Y. Han. Melting of multilayer colloidal crystals confined between two walls. *Physical Review E*, 83(1), 2011.

[242] O PENROSE and P FIFE. Thermodynamically consistent models of phase-field type for the kinetic of phase transitions. *Physica D: Nonlinear Phenomena*, 43(1):44, 1990.

[243] John R. Philip. Integral properties of flows satisfying mixed no-slip and no-shear conditions. *Zeitschrift für angewandte Mathematik und Physik ZAMP*, 23(6):960, 1972.

[244] O. Pouliquen, M. Nicolas, and P. Weidman. Crystallization of non-brownian spheres under horizontal shaking. *Physical Review Letters*, 79(19):3640, 1997.

[245] David Quéré. Non-sticking drops. *Reports on Progress in Physics*, 68(11):2495, 2005.

[246] D Quigley and P M Rodger. Metadynamics simulations of ice nucleation and growth. *J Chem Phys*, 128(15):154518, 2008.

[247] Charles Radin. Random close packing of granular matter. *Journal of Statistical Physics*, 131(4):567, 2008.

[248] Aneesur Rahman. Liquid structure and self-diffusion. *The Journal of Chemical Physics*, 45(7):2585, 1966.

[249] S. M. M. Ramos, B. Canut, and A. Benyagoub. Nanodesign of superhydrophobic surfaces. *Journal of Applied Physics*, 106(2):024305, 2009.

[250] Stella M M Ramos, Abdenacer Benyagoub, Bruno Canut, and Cécile Jamois. Superoleophobic behavior induced by nanofeatures on oleophilic surfaces. *Langmuir*, 26(7):5141–6, 2010.

[251] D. C. Rapaport. *The Art of Molecular Dynamics Simulation*. Cambridge University Press, Cambridge, UK, 2nd edition, 2004.

[252] M Rauscher. Ddft for brownian particles and hydrodynamics. *Journal of Physics: Condensed Matter*, 22(36):364109, 2010.

[253] Howard Reiss and Audrey Dell Hammerich. Hard spheres: scaled particle theory and exact relations on the existence and structure of the fluid/solid phase transition. *The Journal of Physical Chemistry*, 90(23):6252, 1986.

[254] Ph Ribière, P Richard, P Philippe, D Bideau, and R Delannay. On the existence of stationary states during granular compaction. *Eur Phys J E Soft Matter*, 22(3):249–53, 2007.

[255] P Richard, A Gervois, L Oger, and J.-P Troadec. Order and disorder in hard-sphere packings. *Europhysics Letters (EPL)*, 48(4):415, 2007.

[256] M. D. Rintoul and S. Torquato. Computer simulations of dense hard-sphere systems. *The Journal of Chemical Physics*, 105(20):9258, 1996.

[257] Yaakov Rosenfeld. Free-energy model for the inhomogeneous hard-sphere fluid mixture and density-functional theory of freezing. *Physical Review Letters*, 63(9):980, 1989.

[258] J. S. Rowlinson and B. Widom. *Molecular Theory of Capillarity*. Oxford University Press, 1989.

[259] M. Saadatfar, A. Kabla, T.J. Senden, and T. Aste. The geometry and the number of contacts of monodisperse sphere packs using x-ray tomography. In H.J. Herrmann and S. McNamara, editors, *Powders & Grains*. Taylor and Francis, London, 2005.

[260] M. Saba, M. Thiel, M. D. Turner, S. T. Hyde, M. Gu, K. Grosse-Brauckmann, D. N. Neshev, K. Mecke, and G. E. Schröder-Turk. Circular dichroism in biological photonic crystals and cubic chiral nets. *Phys. Rev. Lett.*, 106(10):103902, Mar 2011.

[261] J. J. Sakurai. *Modern Quantum Mechanics (Revised Edition)*. Addison Wesley, rev sub edition, September 1993.

[262] L.A. Santaló. *Integral Geometry and Geometric Probability*. Addison-Wesley, 1976.

[263] J. G. Santiago, S. T. Wereley, C. D. Meinhart, D. J. Beebe, and R. J. Adrian. A particle image velocimetry system for microfluidics. *Experiments in Fluids*, 25(4):316, 1998.

[264] S. Sastry, T. Truskett, P. Debenedetti, S. Torquato, and F. Stillinger. Free volume in the hard sphere liquid. *Molecular Physics*, 95(2):289, 1998.

[265] M. Sbragaglia, R. Benzi, L. Biferale, S. Succi, and F. Toschi. Surface roughness-hydrophobicity coupling in microchannel and nanochannel flows. *Physical Review Letters*, 97(20):204503, 2006.

[266] T. Schilling, H. Schöpe, M. Oettel, G. Opletal, and I. Snook. Precursor-mediated crystallization process in suspensions of hard spheres. *Physical Review Letters*, 105(2), 2010.

[267] Michael Schindler. A numerical test of stress correlations in fluctuating hydrodynamics. *Chemical Physics*, 375(2-3):327, 2010.

[268] R. Schneider. *Cic. Mat. Palermo, Ser. II*, 65:1295, 2000.

[269] Erhard Schnell. Slippage of water over nonwettable surfaces. *Journal of Applied Physics*, 27(10):1149, 1956.

[270] Alan H. Schoen. Infinite periodic minimal surfaces without self-intersections. Technical Report TN D-5541, NASA, 5 1970.

[271] Gerd E. Schröder, S. Wickham, H. Averdunk, F. Brink, J.D. Fitz Gerald, L. Poladian, M.C. Large, and S.T. Hyde. The chiral structure of porous chitin within the wing-scales of callophrys rubi. *J Struct Biol.*, 174:290, 2011.

[272] Gerd Elmar Schröder. *Skeletons in the Labyrinth.* PhD thesis, Australian National University, Canberra, Australia, 2005.

[273] G. E. Schröder-Turk, W. Mickel, M. Schröter, G. W. Delaney, M. Saadatfar, T. J. Senden, K. Mecke, and T. Aste. Disordered spherical bead packs are anisotropic. *EPL (Europhysics Letters)*, 90(3):34001, 2010.

[274] Gerd E. Schroder-Turk, Walter Mickel, Sebastian C. Kapfer, Fabian M. Schaller, Boris Breidenbach, Daniel Hug, and Klaus Mecke. Minkowski tensors of anisotropic spatial structure, 09 2010. arXiv:1009.2340.

[275] Matthias Schröter, Daniel Goldman, and Harry Swinney. Stationary state volume fluctuations in a granular medium. *Physical Review E*, 71(3):030301, 2005.

[276] G.E. Schröder-Turk, W. Mickel, S.C. Kapfer, F.M Schaller, M.J.F Hoffmann, Kleppmann N., P. Armstrong, A. Inayat, D. Hug, M. Reichelsdorfer, W. Peukert, W. Schwieger, and K. Mecke. Minkowski tensor shape analysis of cellular, granular and porous structures. *Adv. Materials*, 23(22-23):2535–2553, 2011.

[277] G.E: Schröder-Turk, T. Varslot, L. de Campo, S. Kapfer, and W. Mickel. A bicontinuous mesophase geometry with hexagonal symmetry. *Langmuir*, accepted 2011.

[278] G D Scott and D M Kilgour. The density of random close packing of spheres. *Journal of Physics D: Applied Physics*, 2(6):863, 2002.

[279] V Senthil Kumar and V Kumaran. Bond-orientational analysis of hard-disk and hard-sphere structures. *J Chem Phys*, 124(20):204508, 2006.

[280] Xiaowen Shan and Hudong Chen. Lattice boltzmann model for simulating flows with multiple phases and components. *Phys. Rev. E*, 47(3):1815–1819, Mar 1993.

[281] Monica Skoge, Aleksandar Donev, Frank Stillinger, and Salvatore Torquato. Packing hyperspheres in high-dimensional euclidean spaces. *Physical Review E*, 74(4), 2006.

[282] V. Sofonea and K.R. Mecke. Morphological characterization of spinodal decomposition kinetics. *The European Physical Journal B*, 8(1):99, 1999.

[283] Chaoming Song, Ping Wang, and Hernán A Makse. A phase diagram for jammed matter. *Nature*, 453(7195):629–32, 2008.

[284] Robin Speedy and Howard Reiss. Cavities in the hard sphere fluid and crystal and the equation of state. *Molecular Physics*, 72(5):999, 1991.

[285] Susan Sporer, Christian Goll, and Klaus Mecke. Motion by stopping: Rectifying brownian motion of nonspherical particles. *Physical Review E*, 78(1), 2008.

[286] Todd Squires and Stephen Quake. Microfluidics: Fluid physics at the nanoliter scale. *Reviews of Modern Physics*, 77(3):977, 2005.

[287] Francis Starr, Srikanth Sastry, Jack Douglas, and Sharon Glotzer. What do we learn from the local geometry of glass-forming liquids? *Physical Review Letters*, 89(12), 2002.

[288] F.W. Starr, S. Sastry, J.F. Douglas, and S.C. Glotzer. What do we learn from the local geometry of glass-forming liquids? *Phys. Rev. Lett.*, 89(12):125501, Aug 2002.

[289] Paul Steinhardt, David Nelson, and Marco Ronchetti. Bond-orientational order in liquids and glasses. *Physical Review B*, 28(2):784, 1983.

[290] H. A. Stone, A. D. Stroock, and A. Ajdari. Engineering flows in small devices: Microfluidics toward a lab-on-a-chip. *Annual Review Of Fluid Mechanics*, 36:381–411, 2004.

[291] Michael R. Swift, W. R. Osborn, and J. M. Yeomans. Lattice boltzmann simulation of nonideal fluids. *Phys. Rev. Lett.*, 75(5):830–833, Jul 1995.

[292] Hajime Tanaka. Hydrodynamic interface quench effects on spinodal decomposition for symmetric binary fluid mixtures. *Phys. Rev. E*, 51(2):1313–1329, Feb 1995.

[293] Hajime Tanaka, Takeshi Kawasaki, Hiroshi Shintani, and Keiji Watanabe. Critical-like behaviour of glass-forming liquids. *Nat Mater*, 9(4):324–31, 2010.

[294] Pieter ten Wolde, Maria Ruiz-Montero, and Daan Frenkel. Numerical evidence for bcc ordering at the surface of a critical fcc nucleus. *Physical Review Letters*, 75(14):2714, 1995.

[295] Richard C. Tolman. Consideration of the gibbs theory of surface tension. *The Journal of Chemical Physics*, 16(8):758, 1948.

[296] S. Torquato and F. Stillinger. Jammed hard-particle packings: From kepler to bernal and beyond. *Reviews of Modern Physics*, 82(3):2633, 2010.

[297] S. Torquato, T. Truskett, and P. Debenedetti. Is random close packing of spheres well defined? *Physical Review Letters*, 84(10):2064, 2000.

[298] J. P Troadec, A Gervois, and L Oger. Statistics of voronoi cells of slightly perturbed face-centered cubic and hexagonal close-packed lattices. *Europhysics Letters (EPL)*, 42(2):167, 2007.

[299] Peichun Tsai, Alisia M. Peters, Christophe Pirat, Matthias Wessling, Rob G. H. Lammertink, and Detlef Lohse. Quantifying effective slip length over micropatterned hydrophobic surfaces. *Physics of Fluids*, 21(11):112002, 2009.

[300] A. Tuteja, W. Choi, M. L. Ma, J. M. Mabry, S. A. Mazzella, G. C. Rutledge, G. H. McKinley, and R. E. Cohen. Designing superoleophobic surfaces. *Science*, 318(5856):1618–1622, dec 2007.

[301] Anish Tuteja, Wonjae Choi, Joseph M Mabry, Gareth H McKinley, and Robert E Cohen. Robust omniphobic surfaces. *Proc. Natl. Acad. Sci. U.S.A.*, 105(47):18200–5, 2008.

[302] L-C Valdes, F Affouard, M Descamps, and J Habasaki. Mixing effects in glass-forming lennard-jones mixtures. *J Chem Phys*, 130(15):154505, 2009.

[303] J. D. van der Waals. English translation of thermodynamische theorie der capillariteit in de onderstelling van continue dichtheidsverandering. *Verhandel. Konink. Akad. Weten, Amsterdam*, 1(8):56, 1893.

[304] J. S. van Duijneveldt and D. Frenkel. Computer simulation study of free energy barriers in crystal nucleation. *The Journal of Chemical Physics*, 96(6):4655, 1992.

[305] Olga I. Vinogradova. Drainage of a thin liquid film confined between hydrophobic surfaces. *Langmuir*, 11(6):2213, 1995.

[306] Roman S Voronov, Dimitrios V Papavassiliou, and Lloyd L Lee. Boundary slip and wetting properties of interfaces: correlation of the contact angle with the slip length. *J Chem Phys*, 124(20):204701, 2006.

[307] Roman S. Voronov, Dimitrios V. Papavassiliou, and Lloyd L. Lee. Review of fluid slip over superhydrophobic surfaces and its dependence on the contact angle. *Industrial & Engineering Chemistry Research*, 47(8):2455, 2008.

[308] Hui Wang and Harvey Gould. Homogeneous and heterogeneous nucleation of lennard-jones liquids. *Physical Review E*, 76(3), 2007.

[309] Yanting Wang, S Teitel, and Christoph Dellago. Melting of icosahedral gold nanoclusters from molecular dynamics simulations. *J Chem Phys*, 122(21):214722, 2005.

[310] Edward W. Washburn. The dynamics of capillary flow. *Phys. Rev.*, 17(3):273–283, Mar 1921.

[311] Robert N. Wenzel. Resistance of solid surfaces to wetting by water. *Industrial & Engineering Chemistry*, 28(8):988, 1936.

[312] T. Werder, J. H. Walther, R. L. Jaffe, T. Halicioglu, and P. Koumoutsakos. On the water−carbon interaction for use in molecular dynamics simulations of graphite and carbon nanotubes. *The Journal of Physical Chemistry B*, 107(6):1345–1352, 2003.

[313] Eugene Paul Wigner. *Group theory and its application to the quantum mechanics of atomic spectra / [by] Eugene P. Wigner ; translated from the German by J. J. Griffin*. Academic Press, New York :, expanded and improved ed. edition, 1971.

[314] Tak-Sing Wong and Chih-Ming Ho. Dependence of macroscopic wetting on nanoscopic surface textures. *Langmuir*, 25(22):12851–4, 2009.

[315] L. V. Woodcock. Entropy difference between the face-centred cubic and hexagonal close-packed crystal structures. *Nature*, 385(6612):141, 1997.

[316] L. V. Woodcock. Reply: Entropy difference between crystal phases. *Nature*, 388(6639):236, 1997.

[317] A Wouterse and A P Philipse. Geometrical cluster ensemble analysis of random sphere packings. *J Chem Phys*, 125(19):194709, 2006.

[318] Ning Xu, Jerzy Blawzdziewicz, and Corey O'Hern. Random close packing revisited: Ways to pack frictionless disks. *Physical Review E*, 71(6), 2005.

[319] W-S Xu, Z-Y Sun, and L-J An. Dense packing in the monodisperse hard-sphere system: a numerical study. *Eur Phys J E Soft Matter*, 31(4):377–82, 2010.

[320] Zhenyu Yan, Sergey V. Buldyrev, Pradeep Kumar, Nicolas Giovambattista, Pablo Debenedetti, and H. Stanley. Structure of the first- and second-neighbor shells of simulated water: Quantitative relation to translational and orientational order. *Physical Review E*, 76(5), 2007.

[321] C Yang, U Tartaglino, and B N J Persson. Nanodroplets on rough hydrophilic and hydrophobic surfaces. *Eur Phys J E Soft Matter*, 25(2):139–52, 2008.

[322] Christophe Ybert, Catherine Barentin, Cecile Cottin-Bizonne, Pierre Joseph, and Lyderic Bocquet. Achieving large slip with superhydrophobic surfaces: Scaling laws for generic geometries. *Phys. Fluids*, 19(12):123601, 2007.

[323] Marianna Yiannourakou, Ioannis G Economou, and Ioannis A Bitsanis. Structural and dynamical analysis of monodisperse and polydisperse colloidal systems. *J Chem Phys*, 133(22):224901, 2010.

[324] Xin Yong and Lucy T Zhang. Nanoscale wetting on groove-patterned surfaces. *Langmuir*, 25(9):5045–53, 2009.

[325] Junfeng Zhang. Lattice boltzmann method for microfluidics: models and applications. *Microfluidics and Nanofluidics*, 10(1):1, 2011.

[326] Junfeng Zhang and Daniel Y. Kwok. Contact line and contact angle dynamics in superhydrophobic channels. *Langmuir*, 22(11):4998–5004, 2006.

[327] J. Zimmermann, M. Rabe, G. R. J. Artus, and S. Seeger. Patterned superfunctional surfaces based on a silicone nanofilament coating. *Soft Matter*, 4(3):450–452, 2008.

Acknowledgment

I would like to thank my supervisors T. Biben and K. Mecke for their support during the last three years and for offering me the possibility of this thesis and their great help with the organization of the co-supervision agreement.

Further, I would like to thank G.E. Schröder-Turk for the co-supervision of the local structure analysis subject.

Many thanks also to R. Mascart, S. Kapfer, M. Hoffmann, J. Reinhard and M. Spanner for the IT-support.

Finally I would like to thank S. Kapfer and K. Falk for numerous discussion and mental support during the preparation of this thesis.

Parts of this thesis are published:

- S. C. Kapfer, WM, F. M. Schaller, M. Spanner, C. Goll, T. Nogawa, N. Ito, K. Mecke, and G. E. Schröder-Turk. Local anisotropy of fluids using minkowski tensors. *Journal of Statistical Mechanics: Theory and Experiment*, 2010(11):P11010, 2010. arXiv:1005.4295v1.

- WM, Laurent Joly, and Thierry Biben. Transport, phase transitions, and wetting in micro/nanochannels: A phase field/ddft approach. *J Chem Phys*, 134(9):094105, 2011.

- G. E. Schröder-Turk, WM, M. Schröter, G. W. Delaney, M. Saadatfar, T. J. Senden, K. Mecke, and T. Aste. Disordered spherical bead packs are anisotropic. *EPL (Europhysics Letters)*, 90(3):34001, 2010.

- G.E. Schröder-Turk, WM , S.C. Kapfer, F.M Schaller, M.J.F Hoffmann, Kleppmann N., P. Armstrong, A. Inayat, D. Hug, M. Reichelsdorfer, W. Peukert, W. Schwieger, and K. Mecke. Minkowski tensor shape analysis of cellular, granular and porous structures. *Adv. Materials*, 23(22-23):2535–2553, 2011.

- G.E. Schröder-Turk, T. Varslot, L. de Campo, S. Kapfer, and WM. A bicontinuous mesophase geometry with hexagonal symmetry. *Langmuir*, accepted 2011. doi 10.1021/la201718a

Other publications of the author

- WM, Stefan Münster, Louise M Jawerth, David A Vader, David A Weitz, Adrian P Sheppard, Klaus Mecke, Ben Fabry, and Gerd E Schröder-Turk. Robust pore size analysis of filamentous networks from three-dimensional confocal microscopy. *Biophys. J.*, 95(12):6072–80, 2008.

Summary

This thesis is devoted to several aspects of geometry and morphology in wetting problems and hard sphere packings. In the first chapters the influence of the nanometric surface corrugation on partial wetting contact angles is investigated and the final chapters are dedicated to geometrical effects in amorphous systems.

Superhydrophobicity, i.e. very large contact angles, are of particular interest in the development of micro- and nanofluidics in order to enhance flow rates and reduce friction. This is classically achieved by geometric surface optimization and a proper choice of substrate and liquid chemicals. Simulations of nanorough patterns with macroscopic drops is a notoriously hard task, due to the large gap of lengthscales. The first part is therefore dedicated to the refining and testing of a novel phase field/dynamic density functional theory method. Indeed, this method allows for studying phase transitions in the vicinity of a corrugated substrate and to evaluate the contact angles of infinite large drops. We study static and dynamic properties with our model (wetting and friction). In contradiction with the macroscopic Cassie-Baxter-Wenzel theory the simulations give insight how monovalued surfaces, i.e. surfaces without overhangs, can produce so-called omniphobicity, meaning repellency, no matter the chemical properties of the liquid. We checked systematically the impact of the surface parameters on omniphobic repellency, and we show that the key ingredient are line tensions, which emerge from needle shaped surface structures. Dynamic studies are done to understand the influence of metastability and the resulting slip enhancement as well, showing that needle like structures support air pockets below the drops, which yields large slip and low friction. Recently such omniphobic monovalued structures are found in etched amorphous silica surfaces.

Geometrical effects have also an important influence on glassy or jammed systems, for example amorphous hard sphere systems in infinite pressure limit. Such hard sphere packings got stuck in a so-called jammed phase, and we shall demonstrate that the local structure in such systems is universal, i.e. independent of the protocol of the generation. For this, robust order parameters—so-called Minkowski tensors—are developed, which overcome robustness deficiencies of widely used order parameters. This leads to a unifying picture of local order parameters, based on geometrical principles. Furthermore, we find with the Minkowski tensor analysis crystallization in jammed sphere packs at the random closed packing point.